Geodätisch-geophysikalische Arbeiten in der Schweiz

(Fortsetzung der Publikationsreihe
«Astronomisch-geodätische Arbeiten in der Schweiz»)

herausgegeben von der

Schweizerischen Geodätischen Kommission
(Organ der Schweizerischen Akademie der Naturwissenschaften)

Zweiundsechzigster Band
Volume 62

Solar Spectrometry for Determination of Tropospheric Water Vapor

Bernd Sierk

2001

Adresse der Schweizerischen Geodätischen Kommission:

Institut für Geodäsie und Photogrammetrie
Eidg. Technische Hochschule Zürich
ETH Hönggerberg
CH-8093 Zürich, Switzerland

Internet: http://www.sanw.ch/exthp/geodet/

ISBN 3-908440-04-1

Redaktion des 62. Bandes:
Dr. B. Sierk, Dr. B. Bürki

Druck: Print-Atelier E. Zingg, Zürich

Vorwort

Im vorliegenden Band werden aktuelle Methoden zur bodengestützten Bestimmung des atmosphärischen Wasserdampfgehaltes beschrieben und einer sorgfältigen Fehleruntersuchung unterzogen. Dabei wurde insbesondere ein neues Messsystem entwickelt, das auf Absorptionsmessungen mit einem hochauflösenden Sonnenspektrometer (SSM) beruht. Systematische Vergleiche mit anderen bodengestützten Verfahren, wie Wasserdampfradiometrie (WVR), GPS-Meteorologie und Ballonsondierungen geben Aufschluss, wie weit die Sonnenspektrometrie in der Lage ist, als zusätzliches Schätz- bzw. Kalibrationsverfahren eingesetzt werden zu können.

An Hand der physikalischen Gesetze zur Absorption stellt Herr Sierk zunächst die Beobachtungsgleichungen vor, mit denen der Wasserdampfgehalt bestimmt werden kann. Hierzu gehört die Implementation des Strahlungstransfermodells, welches die Berechnung von Transmissionsfunktionen erlaubt. Die Parameter für die Modellierung von Molekülübergängen stammen aus der Moleküldatenbank HITRAN des Smithsonian Center for Astrophysics. Die Absorptionsmodelle dienen auch der Simulation zur optimalen Linienauswahl und der Spezifikation des Messsystems. Durch Messung von Referenzspektren gelingt Herrn Sierk eine absolute Kalibration der Wellenlängen.

Herr Sierk hat neben der Erarbeitung von theoretischen Grundlagen und von Algorithmen auch Experimente durchgeführt, die fehleranalytische Hinweise auf die Möglichkeiten und Grenzen der Sonnenspektrometrie geben. Ein gezieltes Experiment wurde im Rahmen eines EU Projektes in Hawaii durchgeführt, wo aufgrund eines über grosse Höhenunterschiede verteilten, permanent operierenden GPS-Netzes gute instrumentelle Bedingungen für Vergleichszwecke gegeben sind. Die Leistungsfähigkeit des Spektrometers beurteilt Herr Sierk an Hand von Beobachtungen mit längerer Zeitdauer. Er hat während 40 Tagen einen Datensatz auf der Station Diepoldsau vom Mesoscale Alpine Project (MAP) erhoben, wo neben SSM-, WVR- und GPS-Messungen auch über 100 Ballonsondierungen durchgeführt worden sind.

Wichtig ist die systematische Fehleranalyse, in der Herr Sierk zeigt, dass der grösste Fehleranteil auf die Unsicherheit in den Absorptionslinien-Parametern zurückzuführen ist. Die eigentlichen Messfehler können dagegen als vernachlässigbar angesehen werden. Ein besonderes Interesse betrifft die Höhenverteilung des Wasserdampfes, eine Frage, die gegenüber der Bestimmung des integralen Wasserdampfgehaltes als wesentlich schwerer einzustufen ist. Herr Sierk hat hierzu systematische Untersuchungen durchgeführt. Es bestehen jetzt konkrete Pläne für die Weiterentwicklung in Zusammenarbeit mit NOAA in Boulder, Colorado, USA.

Die SGK dankt Herrn Dr. B. Sierk für diesen wertvollen Beitrag zur Geodäsie in der Schweiz, mit dem er Pionierleistungen auf dem Gebiet der Sonnenspektrometrie und deren Anwendung in der Bestimmung des troposphärischen Wasserdampfes erzielt hat. Herr Dr. B. Bürki, ETH Zürich, hat sowohl in wissenschaftlicher wie auch in entwicklungstechnischer Hinsicht sehr zum Gelingen der Untersuchungen beigetragen. Die Herren Dres. M. Cocard, A. Geiger, E. Favey und Y. Peter begleiteten das Projekt mit kritischen und hilfreichen Ratschlägen. Dank gebührt auch den Herren Dres. St. Florek und H. Becker-Roß vom Institut für Spektrochemie und Angewandte Spektroskopie, Berlin und den Herren Dres. W. Schlüter und M. Becker vom Bundesamt für Geodäsie und Kartographie, Frankfurt/Main, Deutschland.

Der ETH Zürich danken wir für die finanzielle Unterstützung des Projektes. Die Schweizerische Akademie für Naturwissenschaften (SANW) hat die Druckkosten übernommen, wofür die SGK ihren grossen Dank ausspricht.

Prof. Dr. H.-G. Kahle
ETH Zürich
Präsident der SGK

Dr. h.c. E. Gubler, Direktor
Bundesamt für Landestopographie
Vizepräsident der SGK

Préface

Dans le présent fascicule les méthodes actuelles de détermination du contenu de la vapeur d'eau atmosphérique dans la troposphère au sol sont décrites et une étude soignée des erreurs y est conduite. De plus et en particulier un nouveau système de mesure a été développé, basé sur des mesures d'absorption par un spectromètre solaire à haute résolution.

Une comparaison systématique avec d'autres méthodes comme la radiométrie de la vapeur d'eau, la météorologie par GPS et les données des ballons sondes montre combien la spectrométrie solaire peut être mise en oeuvre comme méthode complémentaire de calibration. Sur la base des lois physiques de l'absorption, M. Sierk présente ensuite les équations d'observation avec lesquelles le contenu en eau peut être extrait. L'implémentation d'un modèle de transfert des radiations qui permet le calcul de la fonction de transmission fait aussi partie de ce chapitre. Les paramètres pour la modélisation de passage des molécules concordent avec ceux de la banque des données moléculaire HITRAN du "Smithsonian Center for Astrophysics". Les modèles d'absorptions servent aussi à la simulation du choix optimal de la ligne spectrale d'absorption et des spécifications du système. A partir de spectres de références M. Sierk a réussi une calibration absolue des longueurs d'ondes.

A côté du développement des bases physiques et des algorithmes, M. Sierk a procédé à des mesures et donné des indications, basées sur une analyse des erreurs, des possibilités et des limites de la spéctroscopie solaire. Une expérience dédiée à ce problème a été conduite dans le cadre d'un projet de l'Union Européenne, à Hawaii où grâce à un réseau GPS permanent régulièrement distribué sur un grande différence d'altitude, de bonnes conditions expérimentales existent pour une comparaison.

La capacité du spectromètre a été évaluée sur la base d'observations de longues durées. M. Sierk a érigé un ensemble de données de 40 jours de la station Diepoldsau du projet MAP(Mesoscale Alpine Project) où à côté des mesures SSM, WVR et GPS, plus de 100 sondages par ballons ont été exécutés. L'analyse systématique des erreurs conduite par M. Sierk a montré que la plus grande partie des erreurs est due aux incertitudes des paramètres des lignes d'absorption. Au contraire les erreurs propres peuvent être considérées comme négligeables. Un intérêt particulier concerne la distribution en altitude de la vapeur d'eau: en comparaison à la détermination du contenu intégral de la vapeur d'eau cette distribution verticale est beaucoup plus difficile à quantifier. Monsieur Sierk a conduit une étude systématique de ce problême. Il existe maintenant un projet pour une continuation du développement de ce système en collaboration avec le NOAA, Boulder, Colorado, USA.

La Commission Suisse de Géodésie remercie Monsieur Sierk pour cette contribution de valeur à la géodésie suisse. Cette contribution représente un travail de pionnier dans le domaine de la spectrométrie solaire appliquée à la détermination de la vapeur d’eau troposphérique. Monsieur le Dr. Beat Bürki du Laboratoire de Géodésie et de Géodynamique de l'EPFZ a contribué d’une façon significative, tant scientifiquement que techniquement, à la réussite de cette recherche, ce dont nous le remercions vivement. Messieurs les Dres. M. Cocard, A. Geiger, E. Favey et Y. Peter ont prêtés leur assistance à la réalisation du projet avec des remarques critiques et utiles. Des remerciements s’adressent aussi à messieurs les Dres. St. Florek und H. Becker-Roß de l’institut de spectrochimie et spectroscopie appliquée à Berlin et à messieurs les Dres. W. Schlüter et M. Becker du Bundesamt für Geodäsie und Kartographie, Frankfurt/Main, Allemagne.

Nous remercions aussi l'EPF-Zürich pour son soutient financier à ce projet. Les coûts d'impression de ce fascicule ont été supportés entièrement par l'Académie Suisse des Sciences Naturelles, la Commission Suisse de Géodésie lui exprime ici sa gratitude.

Prof. Dr. H.-G. Kahle
ETH Zürich
Président de la CGS

Dr. h.c. E. Gubler, Directeur
de l’Office fédéral de topographie
Vice-président de la CGS

Foreword

This volume reports the development and application of new ground-based methods for determining atmospheric water vapor content. It includes an overall summary of recent methods to estimate integral precipital water vapor (IPWV) accompanied by an extensive error analysis. The particular goal was to develop a new measuring system which is based on the absorption of solar radiation (solar spectrometry, SSM). Systematic comparisons with other methods, such as water vaper radiometry, GPS meteorology, and radio sounding are being made to clarify to which extent SSM can be used as additional estimation and calibration tool.

First, Dr. B. Sierk presents the physical laws of solar absorption. These are extensively discussed in terms of observation equations. It includes the implementation of a numerical radiative transfer model which enables to compute transmission functions. The corresponding parameters for the transitions were taken from the the database HITRAN of the Smithsonian Center for Astrophysics. The model also served for selection of the absorption lines and specification of the measuring system.

In addition to the theoretical foundation of SSM Dr. Sierk has also conducted dedicated experiments which enabled to validate the usefulness of SSM. One of these experiments was carried out in the high-density GPS network on the Big Island of Hawaii, USA. The good knowledge of ground truth data along a large height range between sea level and Mt. Kilauea enabled to compare the SSM data with other methods. Another measuring campaign was aimed at validating the long-term behavior (participation in the Swiss Mesoscale Alpine Project, MAP) in comparing a 40 days SSM data set with WVR, GPS and more than 100 radio soundings.

An important result of the work is shown in the error analysis. Dr. Sierk reveals that the largest error arises from uncertainties in the absorption line parameters. The measuring errors themselves are negligible compared to these uncertainties. Of particular interest is also the question whether changes of water vapor as a function of height can be deduced from the absorption spectra. However, the low sensitivity did not allow to derive profiles of humidity. Further studies are presently conducted in collaboration with NOAA in Boulder, Colorado.

The Swiss Geodetic Commission thanks Dr. Sierk for his highly valuable contribution to geodesy in Switzerland. It represents a pioneer work in the field of Solar Spectrometry applied to retrieval of tropospheric water vapor. Dr. B. Bürki of the Geodesy and Geodynamics Lab (IGP ETHZ) has significantly contributed to the work in all practical, editorial and scientific aspects. Dres. M. Cocard, A. Geiger, E. Favey and Y. Peter assisted at various stages and gave critical and helpful advice during the project. Thanks are also due to our colleagues Dres. Florek and Becker-Ross from the Institute of Spectrochemistry and Applied Spectroscopy, Berlin, and to Dres. M. Becker and W. Schlüter, Bundesamt für Kartographie und Geodäsie, Frankfurt, Germany.

We are furthermore grateful to the ETH Zurich for financial support. The Swiss Academy of Sciences (SAS) has provided funds for printing this volume. This support is also gratefully acknowledged.

Prof. Dr. H.-G. Kahle
ETH Zürich
President of the SGC

Dr. h.c. E. Gubler, Director
Swiss Federal Office of Topography
Vice President of the SGC

Abstract

This study reports the development of a new instrumental approach to ground based remote sensing of tropospheric water vapor. It is based on the Differential Optical Absorption Spectroscopy (DOAS)-technique using high-resolution absorption spectra of solar radiation in the visible and near infrared spectral region. The investigations include theoretical aspects of the measurement process, simulations for optimizing instrumental parameters, design and construction of the spectrometer system, as well as validation of the technique by comparisons with independent methods. The first step was the implementation of a numerical radiative transfer model which simulates the process of molecular line absorption in the troposphere. It computes theoretical transmission functions of the atmosphere by calculating superposed inividual transitions on a line-by-line basis. The line parameters of the vibration-rotational transitions were taken from the molecular database HITRAN. The model was used for determining the specifications of the spectrometer system, such as the optimum spectral intervals for the DOAS measurements. On the basis of these simulations a dedicated DOAS system was developed, which comprises a Sun tracking telescope with integrated pre-monochromator and a high-resolution Echelle grating spectrometer called SAMOS (Solar Atmospheric MOnitoring Spectrometer). The spectrometer prototype is characterized by a high spectral resolution of better then 2 picometers over the entire measurable range and an integrated absolute wavelength calibration based on simultaneous measurements of neon reference spectra. The algorithm for processing SAMOS spectra is based on a least squares fit of the radiative transfer model to the measured spectra by adjusting the parameter for the precipitable water vapor (PW). First results revealed offsets between retrievals from different spectral intervals, implying significant errors in the HITRAN line parameters. Therefore line strength parameters were estimated using a dataset of radiosonde soundings and simultaneous SAMOS measurements, which greatly enhanced the redundancy of the retrievals. The new instrument was deployed in several field campaigns with collocated water vapor radiometers (WVR) and Global Positioning System (GPS) receivers, in which the feasibility of the solar spectrometry technique was proven. The comparison of SAMOS results with PW estimates from GPS data yielded a statistical agreement within 1 kg/m^2. However, systematic deviations were observed which are likely to arise from inherent effects of the GPS meteorology technique. The accuracy analysis of the solar spectrometry approach revealed that the largest fraction of retrieval error arises from uncertainties in the line parameters. The low sensitivity to model assumptions on meteorological profiles enables accurate retrievals of PW, but was found to render the possibility of deriving vertical humidity profiles from SAMOS spectra impracticable. The new technique can contribute to the validation and calibration of GPS water vapor estimates for meteorological applications.

Zusammenfassung

Diese Arbeit befasst sich mit der Entwicklung eines neuen instrumentellen Ansatzes zur bodengestützten Fernerkundung von troposphärischem Wasserdampf. Die Untersuchungen beinhalten theoretische Aspekte des Messprozesses, Simulationen zur Optimierung instrumenteller Parameter, Entwurf und Konstruktion des Spektrometer-Systems, sowie die Validierung der Technik durch Vergleiche mit unabhängigen Methoden. Im ersten Schritt wurde ein numerisches Strahlungstransfermodell implementiert, das den Prozess der molekularen Linienabsorption in der Troposphäre simuliert. Es berechnet theoretische Transmissionsfunktionen der Atmosphäre durch Modellierung einzelner überlagerter Molekülübergänge. Die Parameter der einzelnen Vibrations-Rotations-Linien wurden der Moleküldatenbank HITRAN entnommen. Das Modell wurde zur Bestimmung der Spezifikationen des Spektrometersystems, wie z.B. der optimalen spektralen Messintervalle, verwendet. Auf der Grundlage dieser Berechnungen wurde ein dediziertes DOAS-system entwickelt, dass aus einem nachführenden Sonnenteleskop mit integriertem Vormonochromator und einem hochauflösenden Spektrometer namens SAMOS (Solar Atmospheric MOnitoring Spectrometer) besteht. Der Spektrometer-Prototyp zeichnet sich durch eine hohe spektrale Auflösung von besser als 2 Pikometern über den gesamten Messbereich und einer absoluten Wellenlängen-Kalibration durch simultane Messung von Neon-Referenzspektren aus. Der Auswerte-Algorithmus für SAMOS-Spektren basiert auf einer iterativen Anpassung des Strahlungstransfermodells an die Messspektren nach der Methode der kleinsten Fehlerquadrate. Dabei wird der Parameter des abscheidbaren Wasserdampfes (PW) angepasst und bestimmt. Erste Resultate ergaben Offsets zwischen den Ergebnissen von verschiedenen Messintervallen, die signifikante Fehler in den HITRAN-Linienparametern implizieren. Unter Verwendung eines Radiosonden-Datensatzes mit simultanen SAMOS-Messungen wurden daher Parameter der Linienstärke für die Messbereiche bestimmt, was die Redundanz der Ergebnisse deutlich verbesserte. Das neue Instrument wurde in mehreren Messkampagnen zusammen mit Wasserdampf-Radiometern (WVR) und Global-Positioning-System (GPS-) Empfängern eingestzt. Hierbei konnte die Durchführbarkeit der Sonnenspektrometrie-Methode gezeigt werden. Der Vergleich der SAMOS-Resultate mit PW-Schätzungen aus GPS-Daten ergab eine statistische Übereinstimmung innerhalb 1 kg/m^2. Die Genauigkeitsanalyse der spektrometrischen Methode zeigte, dass der grösste Anteil des Bestimmungs-Fehlers auf Unsicherheiten in den Linienparametern zurückzuführen ist. Die geringe Sensitivität auf Modellannahmen über meteorologische Profile ermöglicht eine genaue Bestimmung des PW, verhindert jedoch die Möglichkeit zur Ableitung vertikaler Feuchte-Profile aus SAMOS-Spektren. Die neue Methode kann Beiträge zur Validierung und Kalibrierung von Wasserdampf-Schätzungen aus GPS-Daten für meteorologische Anwendungen leisten.

Contents

1 Introduction

1.1 Water vapor in the climate system

1.1.1 Significance in climatology

In the beginning of the new millennium there are growing concerns about antropogeneous influences on the Earth´s climate. Scientific discussions about implications and consequences of global warming and the greenhouse effect are receiving widespread public attention. As a consequence of the worldwide public interest in these issues, research efforts have been intensified to investigate the atmospheric greenhouse effect and the workings of the hydrological cycle.

Water in the gaseous phase, water vapor, is a key element in both of these. There are many atmospheric greenhouse gases, some naturally occurring and some resulting from industrial activities, but water vapor is readily recognized to be the most important one. The reason for this is that water vapor is involved in an important climate feedback loop: As the temperature of the Earth's surface and atmosphere rises as a consequence of an increased concentration of carbon dioxide, the atmosphere is able to hold more water vapor due to a higher saturation pressure. This additional water vapor absorbs energy that would otherwise escape to space and so causes further warming. It therefore acts as a greenhouse gas itself. In addition to this feedback, there are important interactions between water vapor, clouds, atmospheric motion, and radiation, both directly from the Sun and reflected by the surface. In a sense, one can think of atmospheric water vapor as a thermostat on global temperatures. On one hand increased amounts of atmospheric water vapor might lead to further warming due to its absorption characteristics. On the other, the presence of more water vapor enhances the formation of clouds which reduces the amount of incident solar radiation, thus cooling the global temperature. The complex interactions and the fact that water vapor is the most variable constituent of the atmosphere give rise to its complicated role in climate change studies, and some aspects of this role are still not well understood. Part of the uncertainty to the role which water vapor plays in global climate change is due to the lack of necessary observations to test theoretical models.

Water vapor is the only atmospheric constituent, which occurs in all three phases. The hydrological cycle describes its movement within and between the Earth's atmosphere, oceans, and continents. In the vapor phase, water moves through the atmosphere and redistributes energy associated with its evaporation and re-condensation. The energy spent in the evaporation process is released when the gas condensates, sometimes hundreds and thousands of kilometers away. Water vapor acts as a carrier of latent heat energy in the atmosphere and huge amounts of energy are transported this way over very long distances, like with no other energy transport process in the atmosphere. An example for this is the El Niño event, the phenomenon of ocean current warming in the South East Pacific. It is usually accompanied by strong atypical weather events and disasters in distant areas. The destructive force of weather disasters such as floods and heavy thunderstorms have their origin in the energy contained in the warm ocean currents during El Niño. This energy is transferred over long distances through atmospheric moisture, and has a strong impact on the global climate. The movement of water vapor through the hydrological cycle is strongly coupled to precipitation and soil moisture, which have important practical implications. The basic operation of the hydrologic cycle is well known, but some details are poorly understood, again mainly because there are not sufficient good observations of water vapor.

Because of the extraordinary significance of water vapor, many research efforts are currently aiming on improving the global coverage of observations. Several remote sensing techniques have been developed to measure moisture content and its distribution in the atmosphere. Spaceborne systems are increasingly deployed, but ground-based techniques are still important data sources due to their high spatial and temporal resolution. Some of these ground based techniques will be briefly outlined in chapter 2. It is the purpose of this study to introduce a new technique for ground based passive remote sensing of tropospheric water vapor, based on high resolution absorption measurements of solar radiation. The goals of the project are summarized in section 1.3 at the end of this chapter.

1.1.2 Significance in meteorology

Apart from its long-term impact on climate change, tropospheric moisture is also a highly important quantity in weather forecasting. Water vapor is involved in almost all energy conversion processes in the atmosphere and is a key parameter in the formation of clouds. Consequently, rainfall amounts are directly dependent on how much water content, or precipitable water vapor (PW), is suspended in the atmosphere. Accurate prediction of precipitation amounts has remained a challenging goal for the atmospheric sciences (Emanuel et al. [1995]; Dabberdt and Schlatter [1996]). This important field has not advanced as rapidly as the prediction of other variables. It seems obvious that enhanced knowledge of PW, its temporal development and spatial distribution is likely to improve the accuracy of weather forecasts. However, the impact of introducing measurements of water vapor abundance by remote sensing techniques into numerical weather models is a subject of ongoing studies. Recently Higgins [2000] demonstrated that the assimilation of PW observations significantly improved the forecast results for precipitation in Great Britain. The PW estimates were derived from a continuous receiver network of the Global Positioning System (GPS). The technique of determining water vapor content from GPS data is called GPS meteorology and will also be examined in this study (see section 2.3 and chapter 7). Its validation is an objective of several international projects (e.g. MAGIC Haase et al. [1999], SuomiNet Ware et al. [2000]). The recently completed EU-project WAVEFRONT (Dodson et al. [1999]) was dedicated to the study of the potential and feasibility of ground based GPS meteorology for operational weather forecasting. Some results obtained within WAVEFRONT will be presented in this study.

In the framework of the WAVEFRONT project the first field campaign reported herein was carried out on the island of Hawaii, USA (see section 7.1). In the preparation of this field experiment, we learned that the greatest danger to life and property on the Hawaiian islands are spring floods due to sudden heavy rainfall. While these weather events are extremely difficult to predict, it is known that rapid changes in tropospheric water vapor content around the islands are precursor signals for these weather events (B. Farrell, personal communication, 1999). These fluctuations cannot be resolved by standard meteorological data sources (surface stations, radiosondes) as they are influenced by local topography and are also difficult to detect by meteorological satellites. Weather Services are therefore interested in remote sensing systems which are capable of monitoring precipitable water vapor on a real-time basis. This is another example motivating the development of new techniques which meet these requirements. As shown in this study, solar spectrometry is a feasible technique for such applications.

1.2 Water vapor in space geodesy

Maybe less obvious, but not less important is the role of tropospheric water vapor in geodesy. Especially in the evolving field of space geodesy, which has been revolutionized by the implementation of the Global Positioning System (GPS), atmospheric humidity has been subject to intensive study. The reason is that water vapor has a strong influence on the refraction of transatmospheric microwave signals. This influence is parameterized by the tropospheric path delay, the excess path length to which the distance between a satellite and a receiver is overestimated due to the refraction delay of the microwave signal. Changes in the water vapor content of the atmosphere during a space geodetic measurement cause path delay fluctuations which result in significant errors of the coordinate solution. Knowledge of the refraction properties of the propagation medium is therefore required to achieve optimum accuracy and to exploit the potential of high-precision positioning to the fullest extent.

With satellite geodetic techniques, it is possible to achieve absolute positioning accuracies of a few millimeters. Especially GPS is nowadays widely used in Geodynamics to monitor tectonic motions (e.g. Kahle et al. [1999], McClusky et al. [2000]). The scientific value of these measurements strongly depends on their precision, especially in applications where the expected signal of crustal motion is on the order of magnitude of the positioning accuracy. Due to the observation geometry the disturbing influence of a variable path delay during a space geodetic measurement mainly affects the vertical component. As a consequence, GPS derived heights are 3-4 times less accurately determined than the horizontal components. Hence the problem of tropospheric refraction often becomes critical in applications where the vertical component is of special interest. An example for this is the determination of sea level changes. The GPS satellites are used to define an absolute reference frame for tide gauge positions and thereby enable the separation of tectonic motions from sea level changes. Such investigations have been carried out within the EU-projects SELF and SELF II Becker et al. [2000], where GPS measurements were performed to determine absolute positions of selected tide gauges at the Mediterranean coast. Since the vertical components of the tide gauge positions were of utmost importance in this application, two microwave water vapor radiometers (WVR) of ETH Zurich were successfully deployed in the SELF field campaigns. The instruments continuously measure the integrated water vapor content during the observation period at the GPS station. The time series of tropospheric path delay are then introduced in the GPS processing in order to correct for the refraction fluctuations during the measurements. It could be shown that the incorporation of these corrections improved the repeatability of the vertical components (Glaus et al. [1994]). The technique of water vapor radiometry will be applied as a comparison reference in this study and is explained in detail in section 2.2.

Because of the rapid development in GPS technology and its increasing use in science and navigation, the costs of GPS receivers have been significantly reduced, which has promoted the trend towards continuously operating networks. In a continuous network the problem of refraction fluctuations due to tropospheric water vapor becomes less severe for statistical reasons. The receiver positions are continuously determined over a long period, and short time variations of the coordinate solutions cancel out. If the absolute position of the observation sites are already accurately determined, it is even possible to revert the problem of tropospheric refraction and use the effect to estimate path delays from GPS data. As will be shown in section 2.1.2, the estimated excess path delay is directly related to the water vapor content in the troposphere. Therefore it is possible to convert the path delay estimates into PW. This technique has become known as GPS meteorology Bevis et al. [1992]. It is in the process of becoming operational for deployment meteorology and is a subject of ongoing research (e.g.Rocken et al. [1997], Dodson and Baker [1998], Kruse et al. [1999], Gutman et al. [2000]). GPS meteorology will be also investigated in this study and used for comparisons with the results obtained with the newly developed solar spectrometer. The GPS meteorology technique is described in section 2.3.

For completeness it should be noted that apart from GPS there are other space geodetic techniques which suffer from varying microwave refraction due to tropospheric water vapor, such as Very Long Baseline Interferometry (VLBI) and Satellite Altimetry. In the context of their applications the problem arising from path delay fluctuations can be only mitigated by independent external measurement of PW time series.

1.3 Goals of this study

In 1997 a project was initiated by the Geodesy and Geodynamics Laboratory (GGL) of the Swiss Federal Institute of Technology (ETH) to establish of a new instrumental approach to passive ground based remote sensing of tropospheric water vapor. The initiative emerged from the requirement of a new complementary technique, which could supplement the methods already deployed at GGL. The research project was a collaboration between GGL, the Institute of Spectrochemistry and Applied Spectroscopy (ISAS) in Berlin, Germany, and the Laboratory for Atmospheric Physics of ETH (LAPETH). The results of this project, entitled ”Development of a high-resolution spectrometer for determination of tropospheric water vapor” are presented in this study.

The technique developed herein is based on a method called Differential Optical Absorption Spectroscopy(DOAS), which has been successfully applied to quantitative determination of trace gas amounts in the atmosphere (see e.g. Platt [1994]). The principle of this technique will be explained in section 2.5. Water vapor abundance has been derived from DOAS spectra acquired from satellite data (Noel et al. [1999], Maurellis et al. [2000]) as well as from ground based measurements (Richter, 2000, personal communication). High resolution infrared spectra acquired by Fourier Transform Spectrometers (FTIR) have been used to determine tropospheric water vapor by Demoulin et al. [1996]. However, to the best of the author´s knowledge, no dedicated DOAS system for continuous field measurements using direct sunlight has been developed up to now.

The objectives of the solar spectrometer project included the entire development process. This includes:

- 1) Simulations of the measurement process
- 2) Determination of optimum instrumental parameters and measurement frequencies
- 3) Development of processing software
- 4) Design and construction of the DOAS system
- 5) First tests of the prototype in field
- 6) Validation and comparison with independent techniques

The timing of the research activities can be roughly divided into three main stages:

- 1) The planning phase, in which theoretical investigations and numerical simulations of the measurement process were carried out. The goal of this first stage was to define the concept and determine the specifications for the new measurement system
- 2) The construction phase, in which the actual instrument is designed and constructed
- 3) The test phase, in which the new system is deployed in various field experiments. The goal of this final phase was to assess the feasibility and performance of the new approach by comparison with other co-located measurement techniques

The new instrument, which is designed as a low-cost transportable remote sensing device, is expected to contribute as a valuable supplement to the spectrum of existing techniques for ground based water vapor determination. Using the physical process of absorption of visible and near infrared (IR) radiation in the troposphere the approach is complementary to other techniques deployed at GGL, such as WVR and GPS meteorology, which exploit emission and refraction properties of water vapor, respectively. The new technique is meant to contribute to the validation of the evolving field of GPS meteorology (see section 2.3). The potential of this technique, especially its feasibility for real-time operation, is a subject of ongoing research at GGL (Kruse et al. [1999]). While extensive comparison studies have been performed using WVR, the deployment of at least one further comparison method is desirable. Since the absolute accuracy of GPS derived PW estimates is in the focus of interest, one goal of the new spectrometric technique was to obtain stable retrievals of PW within 1 kg/m^2 accuracy. With this level of accuracy, solar spectrometry can contribute to clarify discrepancies between WVR and GPS retrievals, which have been observed in previous studies.

One attribute of the spectrometric technique, which makes it well suited for evaluation studies of GPS meteorology is its independence from radiosonde calibration. While WVR usually have to be tuned to the area of operation by calculating so-called inversion coefficients using a statistically representative set of radiosonde observations, (*see* sction 2.2.3) the spectrometric technique relies on spectroscopic line parameters, which can be determined by laboratory measurements. In this sense, the new approach was expected to close a gap in the analysis of GPS meteorology performance.

Another goal of the spectrometry project was to investigate the potential of deriving information on the vertical distribution of water vapor from high resolution solar absorption spectra. As will be outlined in chapter 3, the integral absorption and the line shape of each individual H_2O absorption line measured at the ground is a function of vertical profiles of temperature, pressure and water vapor density. The question arises whether it is possible to infer a density profile of H_2O-molecules from the intensity measurements by some inversion method. This question will be addressed in section 7.5.

Last but not least it was hoped that this study will contribute to build a bridge between geodetic and atmospheric sciences. Dedicated efforts focused on the determination of water vapor in various scientific contexts requires interdisciplinary cooperation. The study is an example of such a collaboration in this demanding field of environmental research.

2 Water vapor remote sensing techniques

2.1 Introduction

In this chapter some existing methods for ground based remote sensing of atmospheric water vapor will be reviewed. The selection is by far not complete and priority was given to the techniques deployed in this study. Active remote sensing techniques like Raman-LIDAR (LIght Detection and Ranging) and Differential Absorption LIDAR (DIAL) are not in the scope of this study and the reader is referred to the literature (e.g. Sigrist [1994]).

The first technique presented in this chapter is passive microwave radiometry, which has become a standard method in Geodesy and meteorology. This well known technique serves as a comparison standard for the results presented in chapter 7. Section 2.3 will outline the characteristics of GPS meteorology, a relatively new approach to estimating PW from GPS data, which has already been mentioned in the introduction. Although not deployed in this study, section 2.4 will give a brief outline of the Sun photometry technique, which is based on low resolution absorption measurement of sunlight. This technique is based on a similar principle as the foreseen high resolution approach, which will be explained at the end of this chapter.

As mentioned in the previous chapter, there is an important relation between atmospheric water vapor content and refraction delay in space geodetic measurements. This relation provides a link between atmospheric and geodetic sciences and the performance of remote sensing techniques will have implications on both fields. Therefore the derivation of the important relation between refraction delay and tropospheric water vapor will be summarized, before the different measurement techniques are presented.

2.1.1 Refraction of transatmospheric microwave signals

The fundamental law for the geometry of radiation paths in a refractive medium is Fermat's principle, which determines the propagation path between two points by minimizing the travel time of the light. If the phase velocity of an electromagnetic wave is defined by $v_p = ds/dt$, the travel time τ of a signal propagating from a satellite to a receiver the ground is found by integrating the infinitesimal path elements ds along the ray path O:

$$\int_{\tau} dt = \int_{O} \frac{1}{v_p} ds. \tag{2.1}$$

With the definition of the refraction index $n = c/v_p$, where c denotes the speed of light in vacuum, we obtain the electric path length L of a radio signal propagating along the path O:

$$L = c \cdot \int_{\tau} dt = \int_{O} n\, ds. \tag{2.2}$$

According to Snellius' law the propagation path will be bended towards optically thicker layers in the atmosphere as indicated in Fig. 2.1. The deviation from the straight line M between satellite and receiver is defined as the total path delay

$$\Delta L = (L - M) = \int_{a}^{b} (n-1)\, ds + S - M, \tag{2.3}$$

if the term $S = \int_O ds$ expresses the geometrical path length along the curved path O. In Eq. 2.3 the refraction effect is split into the first term accounting for the delay due to the lower phase velocity and the second term $S - M$, which denotes the geometrical effect of the ray bending. This latter contribution is usually neglected when considering microwave signal delay.

Instead of the refraction index n, the refractivity N is used, which is numerically more convenient and defined by

$$N = 10^6\ (n-1) \tag{2.4}$$

The refractivity of the neutral atmosphere is approximated by Essen and Froome [1951]:

$$N = k_1\, \frac{P_d}{T} + k_2\, \frac{e}{T} + k_3\, \frac{e}{T^2}, \tag{2.5}$$

where P_d and e are the partial pressures of the dry air and water vapor, respectively. k_1, k_2 and k_3 are empirical constants, which have repeatedly been determined in

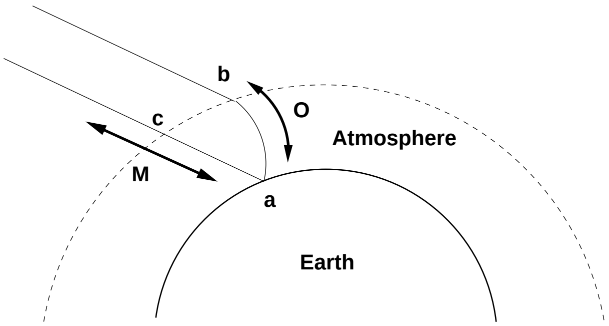

Figure 2.1: Signal propagation of an extraterrestrial radio source (e.g. GPS satellite) to the antenna. The geometrical path length (M) represents the propagation in vacuum (from [Kruse, 2000]).

laboratory studies. It is nowaday common to use the values published by Thayer [1974], which are $k_1 = 77.61 \pm 0.01\ K/hPa$, $k_2 = 64.79 \pm 0.08\ K/hPa$ and $k_3 = (3.776 \pm 0.004) \times 10^5\ K^2/hPa$.

The first two terms of Eq. 2.5 describe the influence of the induced dipole effect, while the third term accounts for the permanent dipole moment of the water vapor molecule. Inserting Eq. 2.5 into Eq. 2.3 yields the total path delay, which can be divided into the hydrostatic or "dry" delay

$$\Delta L_h^z = k_1 \cdot \int_{h_0}^{h_t} \frac{P_d(h)}{T} dh \tag{2.6}$$

and the "wet" path delay due to the refraction influence of water molecules:

$$\Delta L_w^z = 10^{-6} \int_{h_0}^{h_t} (k_2^{'} \frac{e}{T} + k_3 \frac{e}{T^2})\ dh \tag{2.7}$$

where

$$k_2^{'} = k_2 - k_1 \frac{m_w}{m_d} = 22.1 K hPa^{-1}. \tag{2.8}$$

By carrying out the integration over height along the zenith direction from the station altitude h_0 to the limit of the troposphere h_t, we parameterized the delay by its zenith value. The zenith path delay is used to characterize the refraction properties of a homogeneous atmosphere. It is related to the slant path delay in the direction to a specific satellite by using so-called mapping functions, which describe the dependence from the elevation angle (e.g. Herring [1992]).

Although we are primarily interested in the wet component, the hydrostatic path delay is important in the context of GPS meteorology. It can be related with high accuracy to the ground pressure P_0 at the station by Saastamoinen [1973]:

$$\Delta L_h^z = (0.0022768 \pm 0.0000024(m/hPa))\frac{P_0}{f(\Theta,\ H)} \tag{2.9}$$

where

$$f(\Theta,\ H) = 1 - 0.00266\ \cos 2\Theta\ -\ 0.00028H \tag{2.10}$$

describes the variation of the acceleration due to gravity. Θ is the geographic latitude, and H the height in km (above the ellipsoid) of the station. Since the the mixing ratio of the non-polar atmospheric gases can be considered to be constant R.McIlven [1989] the hydrostatic delay can be well modeled from barometer measurements alone using Eq. 2.9. The expression enables the removal of the hydrostatic delay from the total zenith delay estimated from GPS receivers (see section 2.3).

In contrast, the remaining wet component is highly variable due to local conditions such as topography and sea-land interference. In the subsequent section it will be shown, how L_w^z is related to the precipitable water vapor in the troposphere.

2.1.2 Precipitable water and microwave path delay

The integrated water vapor content, or precipitable water vapor PW, is defined by

$$PW = \int_{h_0}^{h_t} \rho_w\ ds. \tag{2.11}$$

where ρ_w denotes the mass density of water vapor or absolute humidity, expressed in kg/m^3[1]. In order to establish a relation between this quantity and the wet path delay L_w the mean weighted temperature T_m, defined by

$$T_m = \frac{\int_{h_0}^{h_t} \frac{e}{T}\ ds}{\int_{h_0}^{h_t} \frac{e}{T^2}\ ds} \tag{2.12}$$

---

[1] Sometimes the water vapor content is expressed in terms of the column height of precipitable water measured in mm. This quantity is identical to the one defined in 2.11 divided by the liquid water density set to 1000 kg/m^3. The absolute value of PW given in kg/m^2 is equal to the column height given in mm

is introduced, which inserted into Eq. 2.7 yields

$$\Delta L_w^z = 10^{-6}(k_2^{'} + k_3/T_m) \int_{h_0}^{h_t} \frac{e}{T}\, ds. \tag{2.13}$$

Under terrestrial conditions water vapor behaves as an ideal gas, so the the equation of state can be used to relate the water vapor partial pressure e to the vapor density ρ_w and the absolute temperature T:

$$e = \rho_w R_v T, \tag{2.14}$$

where $R_v = 461.524\ J\ K^{-1} kg^{-1}$ is the specific gas constant for water vapor. The combination of Eq. 2.7, 2.11, and 2.14 yields

$$\Delta L_w^z = 10^{-6}(k_2^{'} + k_3/T_m) R_v\ PW. \tag{2.15}$$

In order to convert ΔL_w^z into PW or vice versa, the linear relation Eq. 2.15 has to be evaluated. The constant of proportionality contains only constants, except for the mean weighted temperature T_m. Its computation requires information of the vertical profile of water vapor pressure and temperature. However, Bevis et al. [1992] showed that it is possible to determine T_m from the surface temperature T_s by:

$$T_m = 70.2 + 0.72 T_s. \tag{2.16}$$

The constants in Eq. 2.16 were derived from an analysis of 8'718 radiosonde profiles measured 13 stations in the United States. The error introduced by using Eq. 2.16 is estimated to less than 2% Bevis et al. [1992].

With Eq. 2.15 and 2.16 a simple relation between the wet component of the tropospheric path delay in satellite geodetic measurements and the meteorological quantity of the precipitable water vapor PW was found. It allows the conversion from one quantity to the other without introducing considerable errors. It therefore provides a link between geodetic and meteorological problems and is the basis of the GPS meteorology method, which is discussed in section 2.3.

2.2 Microwave Radiometry

2.2.1 Introduction

The radiometric determination of water vapor is based on intensity measurements of radiation, which is emitted by H_2O-molecules due to thermal excitation. The technique utilizes the relation between the water vapor abundance and the thermal radiation emitted at the 22.235 GHz spectral line. Ground based water vapor radiometers (WVR) are increasingly used in Geodesy and Meteorology. Several prototypes of these instruments have been developed at the Geodesy and Geodynamics Laboratory (GGL) of ETH of which three will be deployed in this study for comparisons with the DOAS system. The theory behind this technique is reviewed in the following section in some detail, since it is the basis of the WVR processing software, which was developed in the framework of this study.

2.2.2 Brightness temperatures

The physical description of absorption and emission in a non-scattering atmosphere is expressed by the radiative transfer equation of Chandrasekhar [1960]:

$$I(f,s_b) = I(f,s_a)\exp[-\tau_f(s_a,s_b)] + \int_{s_a}^{s_b} k(f,s), B(f,T)\exp[-\tau_f(s,s_b)]ds \quad (2.17)$$

where f denotes the frequency of the radiation, s the propagation path, $I(f,s)$ the radiative flux density per frequency interval (in Ws/m^2), $k(f,s)$ the absorption coefficient of the medium (in $1/m$) and $B(f,T)$ Planck´s radiation function. The quantity

$$\tau_f(s_a,s_b) = \int_{s_a}^{s_b} k(f,s)ds \quad (2.18)$$

is called the optical depth or opacity. The first term in Eq. 2.17 described the attenuation of the incident radiation due to absorption while propagating from s_a to s_b. The second term corresponds to the emission of the medium along the propagation path given by Planck´s function and attenuated by the absorption factor $\exp[-\tau_f(s,s_b)]$. In the microwave region the following simplifying assumptions can be applied:

- 1) Planck´s law can be replaced by the Rayleigh-Jeans approximation

$$B(f,T) = \frac{2f^2k_BT}{c^2} \quad (2.19)$$

- 2) The intensity $I(f,s)$ can be expressed in terms of brightness temperatures $T_B(f,s)$, which corresponds to the temperature of a black body radiator emitting the equivalent intensity, given by

$$T_B(f,s) = \frac{c}{2k_Bf^2}\cdot I(f,s) \quad (2.20)$$

- The brightness temperature of the cosmic background radiation is assumed to be independent from frequency with $T_{bg} = 2.8K$

Using these assumptions and the abbreviation

$$\tau_\infty = \int_{sa}^{\infty} k(s)ds \tag{2.21}$$

the radiative transfer equation 2.17 becomes:

$$T_B = T_{bg}e^{-\tau_\infty} + \int_0^\infty T(s)k(s)e^{-\tau(s)}ds. \tag{2.22}$$

This non-linear expression has to be modified to be used in radiometry. The exponential terms in Eq. 2.22 lead to saturation effects at high opacities, where the brightness temperature becomes insensitive to changes in water vapor content. In order to correct for these saturation effects, Wu [1979] introduced the "linearized" brightness temperature defined by

$$T'_B = T_{bg} \cdot [1 - \tau_\infty] + \int_0^\infty T(s)k(s)ds \tag{2.23}$$

and the "effective" temperatures for the linearized and non-linearized brightness temperatures, respectively:

$$T_{eff} = \frac{\int_0^\infty T(s) \cdot k(s)e^{-\tau_s}ds}{\int_0^\infty \cdot k(s)(s)e^{-\tau_s}ds} \tag{2.24}$$

and

$$T'_{eff} = \frac{\int_0^\infty T(s) \cdot k(s)(s)ds}{\int_0^\infty \cdot k(s)ds}. \tag{2.25}$$

By inserting Eq. 2.24 into Eq. 2.22 and Eq. 2.25 into Eq. 2.23 we obtain

$$T_B = T_{bg}e^{-\tau_\infty} + T_{eff}(1 - e^{-\tau_\infty}) \tag{2.26}$$

and

	b'_0	b'_1	b_0	b_1
22.73 GHz	62.16	0.7283	1.00004	1.37E-3
31.40 GHz	58	0.738	1.00002	9.80E-4

Table 2.1: Coefficients for relating the effective temperatures T_{eff} and T'_{eff} with the daily maximum temperature (from [Jarlemark, 1997]).

$$T'_B = T_{bg}(1-\tau_\infty) + T'_{eff}\tau_\infty. \tag{2.27}$$

Eliminating τ_∞ in Eq. 2.26 and 2.27 yields:

$$T'_B = T_{bg} - (T'_{eff} - T_{bg}) \ln\left(1 - \frac{T_B - T_{bg}}{T_{eff} - T_{bg}}\right). \tag{2.28}$$

This equation relates the observable of a radiometer, T_B, with the linearized brightness temperature T'_B, which is used to retrieve precipitable water vapor (see next section). Jarlemark [1997] has shown, that the frequency dependent average temperatures of the attenuation medium T_{eff} and T'_{eff} are highly correlated and can be calculated from the daily maximum of the surface temperature $T_{o,max}$ to high accuracy by

$$T'_{eff} = b'_0 + b'_1 \cdot T_{o,max} \tag{2.29}$$

$$T_{eff} = (b_0 + m \cdot b_1) \cdot T'_{eff,f}, \tag{2.30}$$

where m denotes the airmass of the observation.

The coefficients b_0 and b_1 in Eq. 2.29 were obtained by Jarlemark [1997] with a least-squares analysis of a radiosonde dataset. The values he obtained for the measurement frequencies of the WVR at the Onsala space observatory in Sweden are tabulated in table 2.2.2. They can be used for the ETH WVRs, operating at slightly different frequencies, with neglectable error.

2.2.3 Inversion coefficients and observation equation

The observation equation for WVR measurements is obtained by relating the linear brightness temperature introduced in the previous section to the quantity to be retrieved. Such a relation could be derived for the precipitable water vapor PW.

However, for radiometers deployed in geodetic measurements the algorithms are developed to retrieve the wet tropospheric path delay ΔL_w. This quantity can be transformed into PW using Eq. 2.15.

The observation equation used in this study was derived by Elgered [1993]. It is a linear combination of linearized brightness temperatures measured at the two observation frequencies on the vicinity of the H_2O-emission line. The physical reason to use a linear combination is to eliminate the contribution of cloud liquid water to the absorption coefficient. The total absorption coefficient is a superposition of the contributions from water vapor, liquid water and oxygen.

$$k(s,f) = k_v(s,f) + k_l(s,f) + k_{ox}(s,f). \tag{2.31}$$

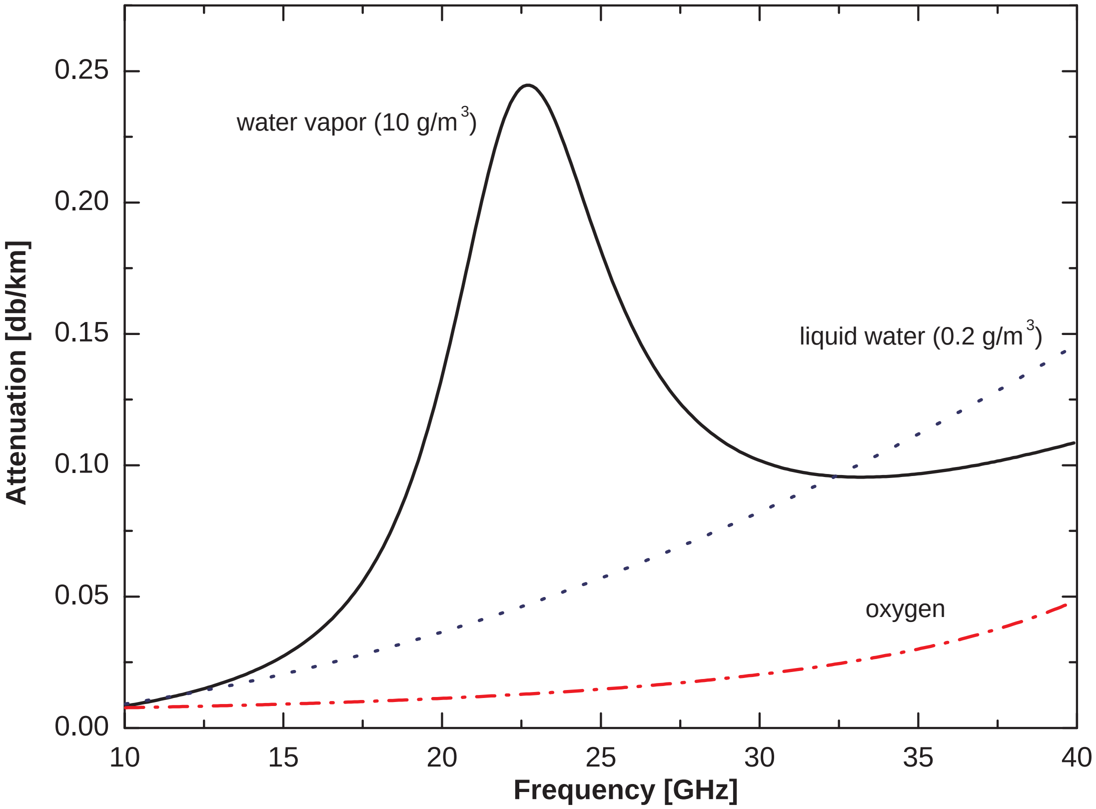

Figure 2.2: Atmospheric attenuation spectra of water vapor, liquid water and oxygen in the vicinity of the 22.235 H_2O-transition (from [Kruse, 2000])

In Fig. 2.2 the atmospheric attenuation of these three components is plotted in the spectral range of the 22.235 GHz water vapor line. As can be seen, the liquid and the gaseous phase of H_2O exhibit a different frequency dependence. The knowledge of these dependences enables to minimize the influence of the liquid component by forming the following linear combination of the measurement frequencies:

$$X = \left[\left(\frac{f_2}{f_1} \right)^2 T'_{B,f_1} - T'_{B,f_2} - T_{bg+ox} \right] . \tag{2.32}$$

Here T'_{B,f_1} and T'_{B,f_2} are the sky brightness temperatures measured by the WVR and linearized using Eq. 2.28. T_{bg+ox} is the combined radiation contribution of oxygen and the cosmic background. It is approximated by the following expression:

$$T_{bg+ox} = \left[\left(\frac{f_2}{f_1} \right)^2 - 1 \right] T_{bg} + \left(\frac{f_2}{f_1} \right)^2 T_{ox,f_1} - T_{ox,f_2}, \tag{2.33}$$

where T_{ox,f_1} and T_{ox,f_2} are the brightness temperatures at the two measurement frequencies. The quantity X given by 2.32 is linearly related to the tropospheric path delay,

$$\Delta L_w = c \cdot X, \tag{2.34}$$

by introducing the constant of proportionality c which depends on the local meteorological conditions at the observation site. After Elgered [1993] it can be parameterized by:

$$\begin{aligned} c = c_{eff} \Big[1 + c_1(P_o - \overline{P}_o) + c_2(T_{o,max} - \overline{T}_{o,max}) \\ + c_3(X - \overline{X}) \Big] \cdot (1 + 6 \cdot 10^{-5} T_{o,max}), \end{aligned} \tag{2.35}$$

which introduces the so-called inversion coefficients for the retrieval of ΔL_w from radiometer data. These are

- P_o: ground pressure at the WVR site
- $\overline{P}_o$: one year average of P_0 at the radiosonde site
- $\overline{X}$: one year average of X at the radiosonde site
- $T_{o,max}$ daily maximum of ground temperature at the WVR site
- $\overline{T}_{o,max}$ one year average of daily maximum of ground temperatures at the radiosonde site

The empirical constants c_{eff}, c_1, c_2 and c_3 are again determined in a least squares analysis of radiosonde data. This procedure has to be performed for every location, where a WVR is operated. If no radiosonde data are available at the exact location, one has to select a dataset from a launch site which represents the climatology of the radiometer site as closely as possible. The algorithm error for retrieving ΔL_w from radiometer data with a noise level of 1 K is estimated to be in the order of 0.7 cm, which corresponds to about 1.1 mm PW. However, this does not include systematic errors of radiosonde sensors, which are likely to propagate into the inversion coefficients. A discussion on the performance of the observation model can be found in Johansson et al. [1993]

2.2.4 The ETH radiometers

After the theory of PW retrieval has been reviewed the question arises how brightness temperatures are determined by a dual channel water vapor radiometer. This will be using the example of the WVR prototypes developed at GGL Bürki et al. [1992]. These instruments have been deployed in the various field campaigns reported in chapter 7. The following description of the instrumental structure and the data handling is the basis for the WVR processing software implemented during this study.

A block scheme of an ETH WVR is illustrated in Fig. 2.3. The radiation emitted by the sky is collected by two horn antennas, each for one of the two measurement frequencies 23.8 and 31.5 GHz. A pin switch behind the the horn antennas selects the radiation source to be conducted to the detector. Besides the antennas these are the calibration reference signals, which are generated by a noise diode. The pin diode switches continuously between the horn antenna, the activated noise diode, and the turned off noise diode, which are measured as the detector voltages V_B, V_A and V_H. Through microwave waveguides the signal is conducted to a frequency mixer, which converts it to 110 MHz. After amplification by 80 dB it reaches the detector, which is read out by an A/D converter.

The detector delivers a voltage signal which varies linearly with the incident radiation power. Since the constant of proportionality depends on the amplification, which is not constant over time, a continuous calibration is necessary during operation. This is achieved by means of the reference loads, generated by the noise diode in each channel. The emitted noise power of the activated and deactivated diode, respectively, represent signals of two different black bodies, whose temperatures are known. For the switched off diode it is equal to the ambient (or cold load) temperature T_A, for the activated diode it is equal to the so-called “hot load temperature” T_H. They relate the corresponding detector readings V_A, V_H and the signal from the horn antenna V_B with the sky brightness temperature defined in Eq. 2.22 by:

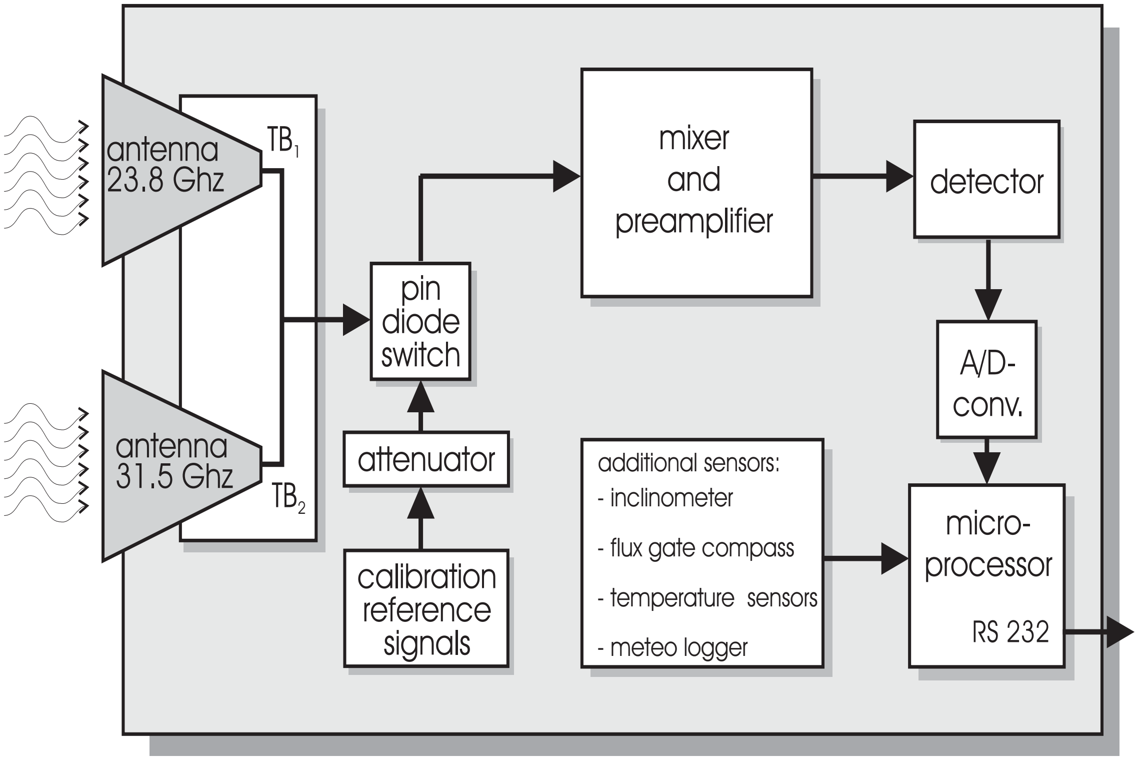

Figure 2.3: Block scheme of the ETH water vapor radiometers. Explanation see text.

$$\frac{T_B - T_A}{T_H - T_A} = \frac{V_B - V_A}{V_H - V_A}. \tag{2.36}$$

or

$$T_B = T_A + \gamma \cdot (T_{Hs} + \Delta T_H - T_A) \quad \text{with } \gamma = \frac{V_B - V_A}{V_H - V_A}. \tag{2.37}$$

In Eq. 2.37 the hot load temperature T_H has been replaced by the sum of a start value T_{Hs} and the so-called hot load correction ΔT_H. This accounts for the fact, that the actual hot load temperature of the noise diode is unknown. It is determined by an iterative technique, which has become known as the “tipping curve”-calibration. It is based on the assumption that the linearized brightness temperature as expressed by Eq. 2.23 depends linearly from the intersected airmass, approximated by the cosine of the elevation angle. This can be seen by plotting the brightness temperatures computed from the radiometer measurements using Eq. 2.37 (assuming $\Delta T_H = 0$ K for the moment) after linearization by Eq. 2.28 against the airmass, as shown in Fig. 2.4. The regression line through the measurements should intersect the abscissa exactly at $T_B(0) = 2.8$ K, since it corresponds to the radiation intensity measured

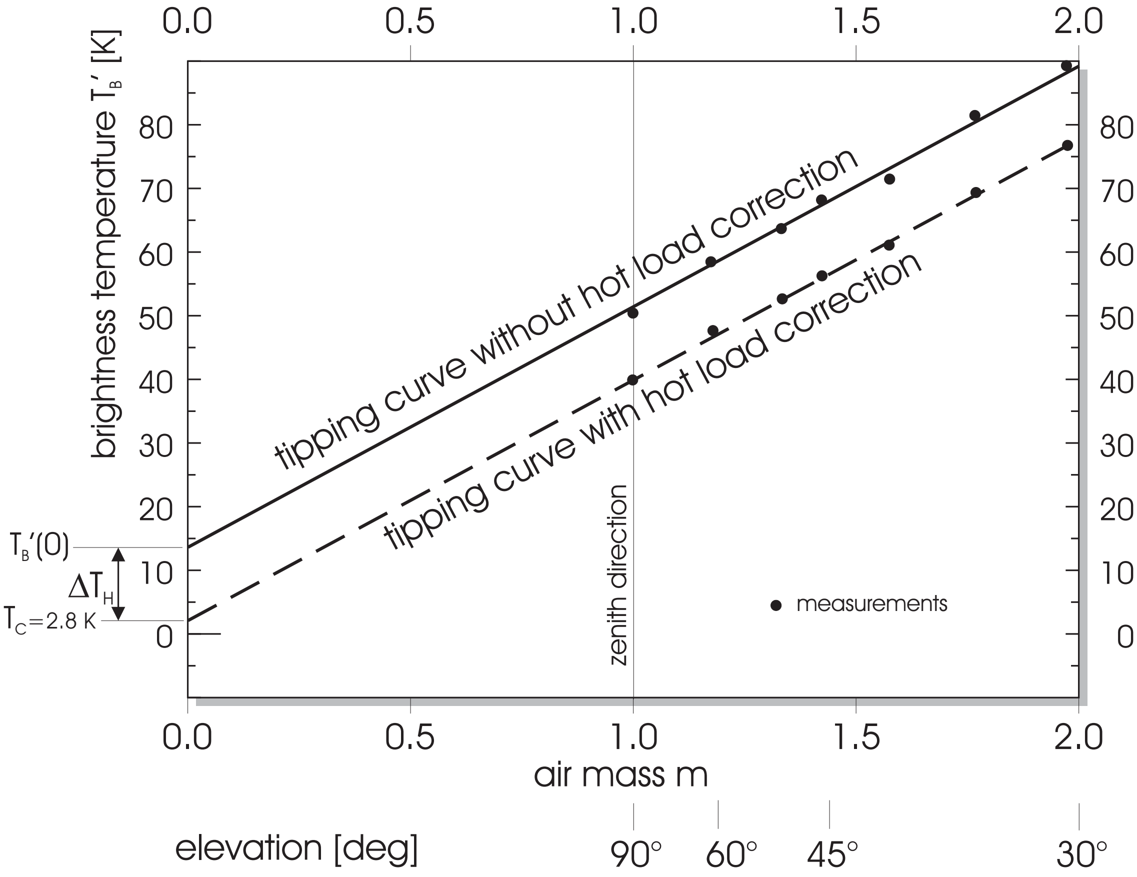

Figure 2.4: Tipcurve analysis for internal radiometer calibration. The regression line of linearized brightness temperatures is iteratively forced to intersect the abscissa at the cosmic background temperature by adjusting the hot load correction ΔT_H

in the absence of the troposphere, which is the cosmic background. Because of the unknown hot load correction, the intersect will at first deviate from this value (as indicated in the figure). ΔT_H is therefore adjusted to obtain the desired intersect. The correction is given by:

$$\Delta T_H = \frac{[T_C - T'_B(0)][T_H - T_A]}{T'_B(0) - T_A}. \tag{2.38}$$

Using ΔT_H all (non-linearized) brightness temperatures have to be corrected by an amount, which can be derived from Eq. 2.36 and 2.38:

$$\Delta T_B = \Delta T_H \Big(\frac{T_B - T_A}{T_H - T_A} \Big) \tag{2.39}$$

The new brightness temperatures $T_B + \Delta T_B$ are again linearized using Eq. 2.28 and a new linear fit according to the procedure outlined above is performed. The process is repeated until the intersect $T'_B(0)$ has approached the cosmic background $T_C = 2.8$ as close as 0.1 K. Usually 3-4 iterations are necessary to reach that point.

2.3 GPS Meteorology

2.3.1 Introduction

Over the past decade a method of determining precipitable water vapor has been developed which reverts the problem of microwave refraction in space geodetic measurements and makes use of the close relationship between PW and the associated refraction delay of transatmospheric signals. This methods uses phase measurements of satellite signals from the Global Positioning System (GPS) acquired in continuous networks of geodetic GPS receivers (the importance of continuity of measurements is explained below). The Global Positioning System is a constellation of 24 active satellites distributed on six orbital planes, inclined by 55° and separated by 60° with respect to the Earth´s equator. The space vehicles move along almost circular orbits with a height of 20000 km above the surface within 11 hours and 58 minutes (corresponding to 12 hours sidereal time). Each satellite sends out so called ´´ pseudo random code´´ signals which are modulated on two carrier waves with the frequencies $f_1 = 1575.42 MHz$ and $f_2 = 1227.60 MHz$. The carriers are generated by rubidium and cesium oscillators which produce the fundamental frequency $f_0 = 10.23 MHz$, which is then multiplied by 154 and 120, respectively.

Originally designed for military navigation purposes, GPS is now widely used in a vast variety of civil navigation applications and has revolutionized the field of space geodesy. It has become a standard tool to determine tectonic motions on regional and global scales with positioning accuracies of several millimeters. Although the high precision determination of site coordinates is to date the most common application of GPS in Earth sciences, this context is not in the scope of this study. For a more detailed description of GPS and its applications the reader is referred to the literature in this field (e.g. Seeber [1993], Teunissen and Kleusberg [1998]).

The problem of varying refractivity of the Earth´s atmosphere (see section 2.1.2) affects GPS positioning like any other space geodetic system using microwave signals. However, GPS has the inherent strength of obtaining large amounts of independent phase observations in a network of receivers which observe the same satellites under different elevation angles. As will be shown below, this capability offers the possibility to separate the atmospheric refraction effect from other unknown parameters provided the station coordinate are already precisely known. If this condition is satisfied, signal path delays can be estimated from GPS data. The GPS derived path delays can then be transformed into estimates of precipitable water vapor using the simple relation 2.15. This technique of determining tropospheric water vapor content using GPS networks has become known as ´´GPS meteorology´´ Bevis et al. [1992] and has been subject of intensive study to evaluate its potential (e.g.Rocken et al. [1997], Dodson and Baker [1998], Kruse et al. [1999], Gutman et al. [2000]). It also plays a major role in the context of this study, since one of the main goals of the newly developed spectrometric technique is the validation of GPS PW estimates. The technique will therefore be described in more detail in the following section.

2.3.2 GPS observation equation

The observable of a geodetic GPS receiver is the phase difference the received carrier signal of the satellite and an oscillation of the same frequency generated within the receiver. This phase difference measured in cycles between the signal of satellite s and receiver r for one of the two channels c is given by the observation equation:

$$\Phi^s_{r,c} = \frac{\rho^s_r}{\lambda_c} + f_c \cdot (\Delta\tau^s - \Delta\tau_r) + N^s_r + \Delta\Phi_{trop} + \Delta\Phi_{ion}, \tag{2.40}$$

where

- ρ^s_r is the geometric distance between receiver r and satellite s
- τ_r and τ^s are the clock offsets of the receiver and satellite oscillators
- N^s_r is the initial phase bias, the unknown number of cycles between satellite and receiver
- $\Delta\Phi_{trop}$ and $\Delta\Phi_{ion}$ are the phase delays caused by refraction in the troposphere and the ionosphere, respectively

- λ_c and f_c are the wavelength and the frequency of the carrier wave

The observation equation is often expressed in units of length rather than in phase difference, which is obtained by multiplying 2.40 with the wavelength $\lambda_c = c/f_c$:

$$\text{Ł}^s_{r,c} = \rho^s_r + c \cdot (\Delta\tau^s - \Delta\tau_r) + \lambda_c N^s_r + \Delta L_{trop} + \Delta L_{ion}, \tag{2.41}$$

which introduce the slant path delays SPD for troposphere and ionosphere into the observation equation, which we already encountered in section 2.1.2. The two components of the path delay would not be distinguishable in single frequency GPS measurements and only their combined effect could be estimated. The reason why the refraction delay is split into two terms in Eq. 2.41 is that ΔL_{ion} can be removed by a linear combination of the measurements at both GPS frequencies. This is possible because the ionosphere is a dispersive medium, which means that the refractivity in this part of the atmosphere depends on the signal frequency. Using the known dispersion relation for microwaves in the presence of free electrons (see e.g. Budden [1961]) it can be shown, that the linear combination

$$\Phi_{L3} = \Phi_{L1} - \frac{f_{L1}}{f_{L2}} \cdot \Phi_{L2} \tag{2.42}$$

eliminates the term for the ionospheric path delay ΔL_{ion} and is therefore called the ´´ionosphere free linear combination´´. The possibility to remove ΔL_{ion} from the observations is the reason why GPS signals are broadcasted on two frequencies. There are other linear combinations which remove the geometrical terms in Eq. 2.40 and 2.41 and allow the determination of ionospheric path delays with the purpose of mapping the electron content of the ionosphere. More details on ionospheric refraction in GPS measurements can be found in GPS literature references above and recently published Ph.D. thesis by Schaer [1999].

Since the troposphere is an non-dispersive medium for frequencies below 40 GHz, ΔL_{trop} cannot be removed by a linear combination of measurement frequencies (which turns out to offer the possibility to determine its value, see below). However, it is possible to get rid of the the satellite and receiver clock biases $\Delta\tau^s$ and $\Delta\tau_r$ by forming differences between observations: The phase difference

$$L^k_{i,j} = L^k_i - L^k_j \tag{2.43}$$

between two receivers i and j simultaneously tracking the same satellite k yields the single difference observation equation

$$L^k_{i,j} = \rho^k_{i,j} + c\Delta\tau_{i,j} + \Delta\rho^k_{i,j,trop} + \lambda N^k_{i,j}, \tag{2.44}$$

where the clock error $\Delta\tau^s$ of the commonly observed satellite has been eliminated. Further differencing the single differences given by Eq. 2.44 between observations to two different satellites k and l acquired at the same epoch also eliminates the differential receiver clock offset $\Delta\tau_{i,j}$:

$$L^{k,l}_{i,j} = \rho^{k,l}_{i,j} + \Delta\Delta L^{k,l}_{i,j,trop} + \lambda N^{k,l}_{i,j}. \tag{2.45}$$

The constellation of receivers i and j and satellites k and l is illustrated in Fig. 2.5

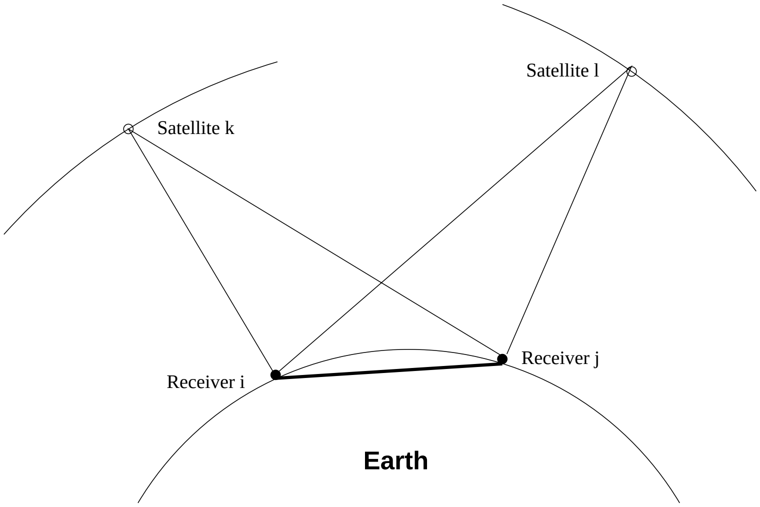

Figure 2.5: Constellation of two receivers and two satellites with their corresponding ray paths. The four observations are used to form one double difference observation. The straight line between the receivers is called baseline. (from [Kruse, 2000])

Looking closer at the remaining unknowns in the observation equation we find the double difference satellite to receiver range $\rho^{k,l}_{i,j}$ which is given by

$$\rho^{k,l}_{i,j} = \rho^k_{i,j} - \rho^l_{i,j} = \rho^k_i - \rho^k_j - \rho^l_i + \rho^l_j. \tag{2.46}$$

Each term in 2.46 is a zero difference range between receiver r and satellite s

$$\rho_r^s = \sqrt{(X_r - X^s)^2 + (Y_r - Y^s)^2 + (Y_r - Y^s)^2} \tag{2.47}$$

and incorporates the geocentric coordinates (X, Y, Z) of receiver and satellite, denoted by the subscripts r and s, respectively. The satellite coordinates can in most cases be assumed to be known, since the International GPS Service (IGS) provides high precision satellite orbits with accuracies better that 5 cm Kouba and Mireault [1998]. The unknowns one is finally left with are therefore the station coordinates of each receiver in the network, the tropospheric slant path delays and the double difference phase bias $N_{i,j}^{k,l}$, the so called integer ambiguity. The latter has the property to remain constant for a pair of satellites and receivers. Further the slant path delays forming the double difference $\Delta L_{i,j,trop}^{k,l}$ are parameterized by the product of the zenith path delay ZPD and some mapping function to account for the dependence on the satellite elevation angle. If the ZPD is assumed remain constant over some time interval, the number of unknowns remains constant, while the number of observations increases as phase differences are continuously measured by the GPS receivers in the network. We therefore obtain an overdetermined equation system, where each epoch and double satellite-receiver pair yields one equation 2.45. With a least squares approach, the unknown parameters can be determined from the observations $L_{i,j}^{k,l}$. The hydrostatic delay can be removed from the estimated total zenith delay using Eq. 2.9 and the latter be transformed into an estimate of PW using Eq. 2.15.

It has been found that zenith path delays can be estimated every 10-30 minutes per receiver using this processing scheme. The higher the frequency of estimating tropospheric parameters is chosen, the greater the noise will be on the results. To reduce the scatter the parameters can be constrained in the least squares adjustment. This, however, reduces the sensitivity to rapid changes of the atmosphere´s refraction properties.

Another problem of the technique is its high correlation between the tropospheric parameters and the height component of the receiver position. Geiger [1987] showed that in GPS positioning a systematic range error, like tropospheric delay, is amplified by a factor of 3 in the vertical component. This means in turn that height errors are mapped into the estimate of zenith delay by 1/3. The absolute precision of the GPS receiver height is therefore a crucial factor for the absolute accuracy of GPS derived PW estimates.

Finally it has to be mentioned that the above considerations assume neglectable errors in the satellite orbits. Highly accurate IGS orbits justify such an assumption but are usually not available in real time. For near real time applications the user has to rely in predicted orbits, which are also provided by IGS. However these are significantly less accurate (50-100 cm) and may be corrupted by poorly modeled satellites. An alternative is to estimate local orbits along with the tropospheric parameters. This requires online access to a large scale network and real time processing facilities, imposing strong requirements on the logistics of network operation. The impact of orbit accuracy on PW estimates has been closely investigated by Kruse et al. [1999].

2.4 Sun Photometry

The first approaches to relate transmission of solar radiation in the near infrared (NIR) to the tropospheric water vapor content date back to the early 20th century (Fowle [1912a], Fowle [1912b]). Foster and Foskett [1945] used a spectrograph to perform measurements inside and outside the H_2O absorption band centered at 940 nm. This approach has been further developed over the years utilizing narrow band interference filters and has become known as Sun photometry (Quenzel [1965], Volz [1974], Tomasi and Guzzi [1974], Thome et al. [1992], Peter and Kämpfer [1992], Ingold et al. [2000]). In Sun photometric measurements, the intensity of incident sunlight is determined in a spectral interval containing H_2O-absorption lines. The average value of solar irradiance over the spectral interval of typically 5-10 nm width is then compared to the intensity measured in a reference channel with no water vapor lines. The ratio of the intensity values of the absorption and the reference channel are a measure of the number of water molecules along the ray path.

For the retrieval of water vapor amount, Sun photometers can be externally calibrated by means of radiosondes. However, numerical radiative transfer models are nowadays utilized to relate the measured voltages to the water vapor abundance. In the so-called modified Langley technique (Reagan et al. [1987], Schmid and Wehrli [1995]) the dependence of the measured transmission from the integrated water vapor amount is determined by model calculations assuming different atmospheric conditions. For the water vapor channel, a non-linear dependence of the optical density from PW is assumed, which is a deviation from the Bouguer-Lambert- Beer law (see section 3.2). The constants of a power law describing this dependence are computed in a two-parameter fit using calculated solar irradiances for different water vapor amounts. In this calibration procedure, the radiative transfer models have to take into account aerosol and Rayleigh scattering, since their impact on sunlight attenuation is different for the water vapor and the reference channels, respectively.

The error budget of the photometric technique has been analyzed in detail by Schmid et al. [1996]: The accuracy strongly depends from the performance of the radiative transfer model used in the Langley-calibration procedure. The best results are found to be achieved when using the line-by-line code FASCOD3P (Clough et al. [1988]), which agree within 10-15 % of PW with WVR and radiosonde measurements. For solar elevation angles below 30° systematic deviations were observed. Part of the error is assumed to arise from incorrect water vapor continuum data, which are commonly applied in all atmospheric transmittance models.

2.5 DOAS - the principle

After the brief review of some existing methods the principle of the approach implemented in this study will be explained. The motivation for developing another technique for water vapor determination arose in the necessity of validating the potential of the GPS meteorology technique. In this context it is desirable to dispose of a technique, whose error budget is fundamentally different from the existing ones. It was therefore decided to develop an instrumental technique which utilizes the absorption properties of H_2O and is therefore complementary to the WVR technique, which measures emission intensities, and GPS, which exploits the refraction properties of water vapor.

The technique described herein is similar to the Sun photometric method described in the previous section. However, instead of measuring the integrated solar irradiance in broad spectral intervals, single H_2O absorption lines including their spectral vicinity are resolved in high-resolution measurements. The retrieval of atmospheric water vapor content from solar absorption spectra is based on the method of Differential Optical Absorption Spectroscopy (DOAS) (Platt [1994]). The basic idea of this approach will be briefly outlined in the following.

When a light beam traverses the atmosphere the radiation is attenuated by scattering at molecules and aerosol particles, as well as by absorption due to atmospheric constituents. In addition, every constituent of the atmosphere absorbs radiation at discrete characteristic wavelengths, given by the energy required for the transition between different vibration-rotation states of the molecule. This results in a spectrum of single absorption lines, which exhibits a band structure corresponding to the vibrational and rotational quantum numbers. The H_2O molecule is an asymmetric rotator giving rise to a complicated absorption band structure of an atmospheric spectrum comprising thousands of individual transitions. Compared to the discrete line absorption, the above mentioned effects of Rayleigh- and Mie-scattering show a broad band behavior slowly varying with wavelength.

The intensity $I(\lambda)$ measured at the ground as a function of wavelength depends on the incident intensity $I_0(\lambda)$ and the superposition of all these attenuation effects, and is quantified by the Bouguer-Lambert-Beer law:

$$I(\lambda) = I_0(\lambda) \cdot \exp\Big[-\int_{s_0}^{\infty} \tau(s) ds \Big], \tag{2.48}$$

where $\tau(s)$ denotes the optical density summarizing the attenuation effects and the integration is carried out along the ray path. While in laboratory spectroscopy it is usually a trivial task to determine the background intensity I_0, this is mostly impossible in atmospheric measurements, since it would involve removing the air from the light path. The general idea of the DOAS approach is to define an intensity level I'_0 describing the part of the absorption, which varies “slowly” with wavelength.

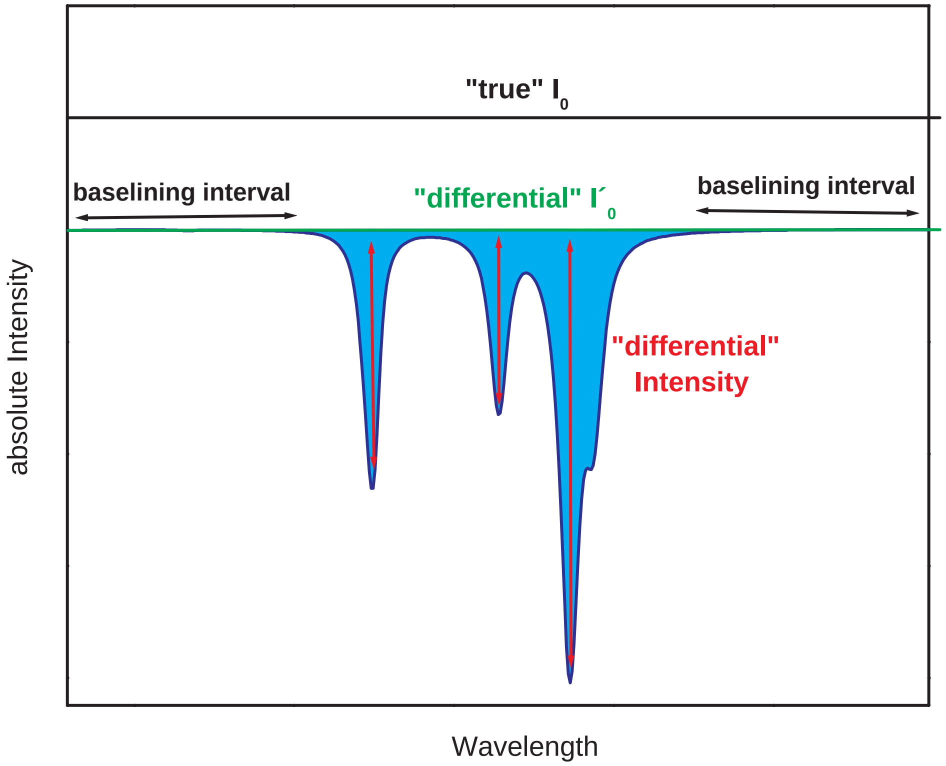

Figure 2.6: Principle of Differential Optical Absorption Spectroscopy. The extraterrestrial intensity I_0 is attenuated in the atmosphere by scattering and line absorption. By interpolation of the measured intensities at either side of the spectrum a "differential" intensity level I_0' can be defined. The integral differential absorption given by the area enclosed by the differential spectrum and I_0' depends only on absorber amount and distribution.

The so-called differential absorption $I'_0(\lambda)/I(\lambda)$ is then determined, which can be defined as the "rapidly" varying part of the total absorption. Fig. 2.6 illustrates this principle of determining differential absorption spectra. The differential background intensity level $I'_0(\lambda)$ can be e.g. defined by interpolating the intensities in spectral regions with neglectable line absorption. These intervals will in the following be called the "baselining intervals" and $I'_0(\lambda)$ the corresponding "baseline".

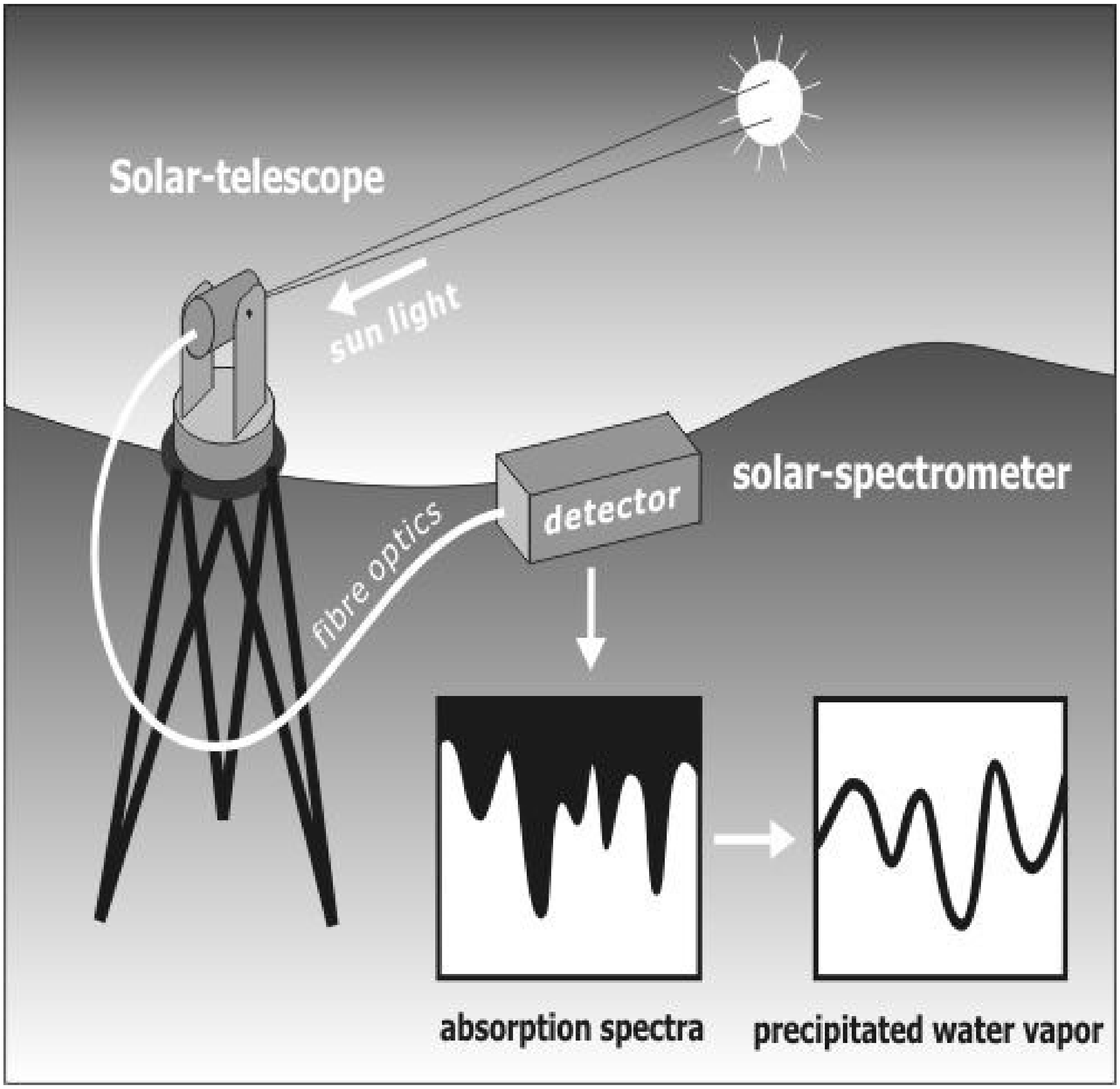

Figure 2.7: Schematic overview on the proposed measurement system. A solar telescope tracks the Sun. The sunlight is conducted via optical fiber cable into a grating spectrometer, which records series of solar absorption spectra. These are processed according to the DOAS approach to yield time series of PW

The advantage of this approach is that the broad band effects including scattering are eliminated and the remaining differential absorption only depends on the amount and the absorption properties of the corresponding molecular species in the atmosphere. As will be shown in chapter 3, the latter can be well described by models of molecular line absorption. Using these models, it is possible to derive the amount of absorbing molecules along the ray path. In chapter 3 it will also be shown that the shape and intensity of differential absorption lines depends on the distribution of molecules along the ray path. The line shape is primarily determined by the collision broadening effect (see section 3.6), which depends on atmospheric pressure. Therefore, the line shapes generated in each height layer of the atmosphere depend on the molecular density and the air pressure in that layer. Furthermore, the line strength is a function of the atmospheric temperature profile. The differential spectra measured at the ground are generated by integration of the absorption line contributions in each atmospheric layer. They should therefore carry some information about the vertical distribution of absorbing molecules. The possibility of retrieving this information under the assumption of known temperature and pressure profiles will be also investigated in this study.

It is obvious that the measured spectral intervals have to be sufficiently narrow to justify the neglection of scattering effects within the interval. In order to define $I_0'(\lambda)$ by interpolation of the spectral intervals, where line absorption can be neglected the individual transitions and their spectral vicinity have to be well resolved. The application of DOAS therefore requires the use of high-resolution spectrometers. The technique has been successfully applied to quantify atmospheric trace gas amounts. DOAS measurements are usually performed using terrestrial light sources, but also spectra of scattered sunlight measured at the ground (e.g.Fiedler et al. [1993]) and by spaceborne instruments have been used (e.g. Noel et al. [1999], Maurellis et al. [2000]).

It is the purpose of this study to develop an instrumental approach for dedicated continuous field measurements of tropospheric water vapor applying the DOAS technique. A spectrometer system will be designed for deployment in geodetic and meteorological field campaigns. Fig. 2.7 shows a basic sketch of the measurement system. A solar telescope continuously tracks the path of the Sun. The collected sunlight is conducted via an optical fiber cable into a high-resolution grating spectrometer, which sequentially records series of solar absorption spectra at a number of selected wavelength intervals. These are processed using the DOAS technique outlined above to yield time series of retrieved water vapor amounts. The technique measures PW only in the slant direction towards the Sun, since the high resolution approach requires strong radiation intensities. For comparison with other techniques the unidirectional retrievals can be mapped the the zenith.

The technical implementation of the DOAS approach is described in chapter 5, where the development of the grating spectrometer and the solar telescope are reported. In the following chapter, the model for atmospheric absorption necessary to retrieve PW from highly resolved solar spectra will be explained.

3 Modeling tropospheric absorption

3.1 Introduction

The basis for any algorithm designed to retrieve information about the troposphere from solar spectra is the model for the radiation transfer. In section 2.5 it was shown that emission and scattering processes can be neglected in the high-resolution approach to be implemented. Therefore the simulation of DOAS spectra will be restricted to the molecular line absorption processes. The theory of vibrational-rotational absorption spectra in the infrared spectral region was developed by Herzberg [1945] and its application to meteorology was decribed by Goody [1964]. This theory is the basis of the radiative transfer model developed in this study and will be reviewed in this chapter.

3.2 The Bouguer-Lambert-Beer law

Absorption of light has been described since the middle of the 18th century, long before the physical origins of the attenuation of electromagnetic waves were understood. Beer and Lambert formalized the exponential law for the radiation intensity I received after propagating along a path of length L in a homogeneous medium, when the initial intensity is I_0:

$$I = I_0 \cdot \exp[-k \cdot l] \tag{3.1}$$

This equation is at the same time the macroscopic definition for the absorption coefficient k of the propagation medium. The quantum mechanical description of k which provides the relation between the microscopic properties of the absorbing molecules and the macroscopic observable I is reviewed in the subsequent sections. While the physics of absorption is summarized in the absorption coefficient, the refraction properties of the medium will determine the length of the absorption path. In atmospheric spectroscopy the propagation medium is inhomogeneous and its properties vary continuously along the ray path. We therefore rewrite the Bouguer-Lambert-Beer law as the path integral of the absorption coefficient along the Sun ray. Furthermore, considering molecular line absorption, we assume linear superposition of the contributions of individual lines l at any given wavenumber $\nu = 1/\lambda$:

$$I(\nu) = I_0(\nu) \cdot \exp\Big[\sum_l - \int_{s_0}^{s_{trop}} \tau_l(\nu, s) ds\Big]. \tag{3.2}$$

The integration is carried out along the ray path and s_0 and s_{trop} denote the station location and the ray intersection with the tropsphere boundary, respectively. The absorption coefficient k is replaced by the optical density $\tau_l(\nu, s)$. This is done, because in the inhomogeneous atmosphere the term ´´monochromatic absorption coefficient´´ is occupied by a quantity, which is defined by

$$\tau_l(\nu, s) = \rho(s) \cdot k_l(\nu, s), \tag{3.3}$$

where $\rho(s)$ denotes the molecular density. The unit for the absorption coefficient depends on those used to express $\rho(s)$. We will use the number density in $[molecule/m^3$ so that $k_l(\nu, s)$ is expressed in $m^2/molecule$. In the following sections, the dependence of the absorption coefficient from absorption path s and wavenumber ν will be considered.

3.3 The absorption coefficient

As pointed out in the previous section, one can define the total absorption coefficient at a given frequency as the superposition of the corresponding contributions of individual transitions k_l. In the following we focus on a general formalism for these transitions and will therefore omit the index l. In the mathematical treatment of molecular spectra the absorption coefficient is split into a factor which describes the intensity of the energy transition (line strength) S and a factor f_ν describing the spectral shape of the absorption line on the frequency axis:

$$k(\nu) = S \cdot f(\nu) \tag{3.4}$$

with

$$\int_{-\infty}^{+\infty} f(\nu) d\nu = 1. \tag{3.5}$$

The line intensity or integral absorption therefore can be defined as

$$S = \int_{-\infty}^{+\infty} k(\nu) d\nu \tag{3.6}$$

Both factors reflect the two different features in solar spectra, which carry information about the distribution of water vapor in the troposphere: Line intensity and line shape, the first one determined by the transition probability and the latter by collision- and Doppler broadening. Both are changing with the varying conditions in different atmospheric layers. For the purpose of retrieving atmospheric parameters from absorption spectra, which reflect the integral of all these effects along the propagation path, requires knowledge of their height and frequency dependence. For a better understanding of the processing algorithm it is useful to analyze the derivation of these dependencies.

3.4 The line intensity

The starting point for deriving an equation which relates the integral absorption 3.6 with quantum mechanical quantities are the Einstein coefficients for induced absorption B_{fi}, induced emission B_{if} and spontaneous emission A_{if}. The Einstein coefficients are a measure for the probability of these processes. The index i always denotes the energetically higher and f the lower molecular state. If the radiation density per wave number ν in a radiation field is u_ν, the probability for a transition from the lower to the higher energy state is given by

$$P_{fi} = B_{fi} \cdot u_\nu / c \tag{3.7}$$

and the corresponding probability for the induced emission

$$P_{if} = B_{if} \cdot u_\nu / c \tag{3.8}$$

The probability for the spontaneous emission is independent from the radiation field and therefore simply equals A_{if}. In thermodynamic equilibrium Planck's radiation law can be written in terms of u_ν as:

$$u_\nu = \frac{4\pi}{c} \cdot B_\nu(T) = \frac{8\pi h \nu^3 c}{\exp[hc\nu/k_B T] - 1} \tag{3.9}$$

In this case, the amount of transitions from the lower level f to the higher i equal those from i to f. Since the number of transitions is the product of the transition probability and the the number of molecules in the corresponding levels N_i and N_f, it follows from 3.7 and 3.8:

$$N_f B_{fi} u_\nu = N_i (A_{if} \cdot c + B_{if} \cdot u_\nu), \tag{3.10}$$

or resolved to u_ν:

$$u_\nu = \frac{cN_iA_{if}}{N_fB_{fi} - N_iB_{if}} \tag{3.11}$$

The ratio of occupation numbers in equilibrium are given by the Boltzmann- distribution:

$$\frac{N_f}{N_i} = \frac{g_f}{g_i} \cdot \exp\Big[-\frac{E_f - E_i}{k_BT}\Big] = \frac{g_f}{g_i} \cdot \exp\Big[-\frac{hc\nu_{fi}}{k_BT}\Big]. \tag{3.12}$$

Here g_f and g_i are the statistical weights or degenerations of the energy levels. The combination of 3.11 and 3.12 yields for the energy density:

$$u_\nu = \frac{c \cdot A_{if}}{B_{fi} \cdot \frac{g_f}{g_i} \cdot \exp\left[\frac{hc\nu}{k_BT}\right]} \tag{3.13}$$

A comparison with 3.9 yields:

$$\frac{A_{if}}{B_{if}} = 8\pi h\nu^3 \cdot \frac{g_f}{g_i} \tag{3.14}$$

and

$$B_{fi}g_f = B_{if}g_i \tag{3.15}$$

The effective number of transitions $f \rightarrow i$ induced by interaction with the radiation field per unit time and volume, n_{fi}, is the difference of the molecule density in both states multiplied by the corresponding transition probabilities:

$$n_{fi} = (N_fB_{fi} - N_iB_{if}) \cdot \frac{u_\nu}{c}, \tag{3.16}$$

and in equilibrium follows with 3.11:

$$n_{fi} = N_i \cdot A_{if} \tag{3.17}$$

When the radiation intersects a differential mass layer dm, the differential form of the Bouguer-Lambert-Beer law can be expressed in terms of the radiation density $B_\nu = u_\nu c/4\pi$ by:

$$dB_\nu = -B\nu k_\nu dm = -\frac{c}{4\pi}u_\nu k_\nu dm, \tag{3.18}$$

where k_ν is the absorption coefficient. The energy per unit mass absorbed in dm over the frequency interval $d\nu$ is $(dB_\nu/dm)d\nu$. Therefore

$$-4\pi\frac{dB\nu}{dm}d\nu = cu_\nu k_\nu d\nu \tag{3.19}$$

is the energy absorbed by transitions of molecules in the lower state f to the higher state i. The number of transitions n_{fi} induced by the photons of energy $hc\nu$ is obtained by integrating over the entire frequency range:

$$n_{fi} = \int_{-\infty}^{+\infty} \frac{u_\nu k_\nu}{h\nu} d\nu \tag{3.20}$$

In the spectral interval $\delta\nu$, where absorption of the single transition $f \rightarrow i$ occurs, u_ν can be assumed as being constant and 3.20 can be simplified to:

$$n_{fi} = \frac{u_\nu}{h\nu_{fi}} \cdot \int\limits_{\nu_{fi}-\delta\nu}^{\nu_{fi}+\delta\nu} k_\nu d\nu \tag{3.21}$$

Equation 3.16 relates n_{fi} with the Einstein coefficients. By comparing 3.16 and 3.21 and the definition of the line strength 3.6 we obtain:

$$S = \frac{h\nu_{fi}}{c} N_f B_{fi} \Big[1 - \frac{N_i B_{if}}{N_f B_{fi}}\Big] \tag{3.22}$$

and with 3.12 and 3.15

$$S = \frac{h\nu_{fi}}{c} N_f B_{fi} \Big[1 - \exp\Big[-\frac{hc\nu}{k_B T}\Big]\Big] \tag{3.23}$$

Inserting 3.14 yields

$$S = \frac{1}{8\pi c\nu^2}\frac{g_i}{g_f} N_f A_{if} \Big[1 - \exp\Big[-\frac{hc\nu_{fi}}{k_B T}\Big]\Big]. \tag{3.24}$$

The total number of molecules N is the sum of molecules in the allowed quantum states. The number N_f of molecules in quantum state f is related with N by the total partition sum

$$Q = \sum_j g_j \exp\Big[-\frac{E_j}{k_B T}\Big] \tag{3.25}$$

in the following way:

$$N_f = \frac{1}{Q} N \cdot g_f \cdot \exp\Big[-\frac{E_f}{k_B T}\Big], \tag{3.26}$$

which is inserted into 3.24 to give

$$S = \frac{1}{8\pi c\nu^2} \frac{g_i}{Q} N \cdot \exp\Big[-\frac{E_f}{k_B T}\Big] \cdot A_{if} \cdot \Big(1 - \exp\Big[-\frac{hc\nu_{fi}}{k_B T}\Big]\Big) \tag{3.27}$$

In quantum mechanics the Einstein coefficients are expressed by the matrix elements of the molecular dipole moment. For the spontaneous emission this relation is

$$A_{if} = \frac{64\pi^4\nu^3}{3h} \frac{g_f}{g_i} |R_{fi}|^2, \tag{3.28}$$

with $R_{fi} =< i|\mu|f >$ being the matrix element of the dipole moment operator μ. By replacing the Einstein coefficient we obtain the expression for the line strength:

$$S = \frac{8\pi^3 N\nu_{fi}}{3hc} \frac{g_f}{Q} |R_{fi}|^2 \exp\Big[-\frac{E_f}{k_B T}\Big]\Big[1 - \exp\Big[-\frac{hc\nu_{fi}}{k_B T}\Big]\Big] \tag{3.29}$$

This equation relates the line strength or intensity with quantum mechanical quantities transition frequency, dipole moment and Energy of the lower state. Furthermore it describes the dependence of S with the temperature T. In the present form, however, equation 3.29 is not practicable for the analysis and simulation algorithm. In particular it still lacks the description of the temperature dependence of the partition sum Q. Before we continue to study this effect for the water molecule, some notations should be introduced for consistency of the definitions: The wave number ν_{fi} corresponds to the characteristic frequency of the absorption line center. Since in the following we will deal only with the transition and not with its energy levels, we will write ν_0 for this frequency. Furthermore it is common to use the notation E_l' for the lower energy level of a transition l (instead of E_f). With these changes the line strength formula becomes:

$$S_l = \frac{8\pi^3 N\nu_{0,l}}{3hc} \frac{g_l'}{Q} |R_l|^2 \exp\Big[-\frac{E_l'}{k_B T}\Big]\Big[1 - \exp\Big[-\frac{hc\nu_0}{k_B T}\Big]\Big]. \tag{3.30}$$

Eq. 3.30 is the correct relation which we could use to model the line strength if the quantum mechanical parameters $\nu_{0,l}$, E_l', g_l', Q, and $|R_l|$ are known. In practice, the absolute value of the dipole moment matrix operator is difficult to determine, since it would require knowledge of the wave functions of the upper and lower state (which means solving the Schrödinger equation). Instead, the line intensity is determined in laboratory measurements (see section 6.3.4) while keeping the sample gas under a fixed reference temperature T_{ref}. The model expressed by Eq. 3.30 is then used to transform the reference line intensity value $S_l(T_{ref})$ to any other temperature. This can be achieved by rationing the expressions 3.30 for T_0 and an arbitrary temperature T:

$$\frac{S_l(T)}{S_l(T_{ref})} = \frac{Q(T_{ref})}{Q(T)} \frac{\exp[-E'/k_B T]}{\exp[-E'/k_B T_{ref}]} \frac{(1 - \exp[hc\nu_0/k_B T])}{(1 - \exp[hc\nu_0/k_B T_{ref}])}. \tag{3.31}$$

Given the line parameter $S_l(T_{ref})$, this expression can be used to calculate line strengths for different temperatures in different height layers of the atmosphere. It will be used in our radiative transfer model.

3.5 The total internal partition sum (TIPS)

The total internal partition sum (TIPS) Q of a molecule is defined as the direct sum of the factors $\exp(-hcE_s/k_B T)$ over all states s, when E_s denotes the total energy of the state. In most practical cases it is impossible to carry out the summation over all molecular states (electrical, vibrational and rotational), since energy levels are usually not known to high enough states. In this case an approximation for Q has to be found. If for the ground vibrational state the rotational energy levels are known, but those for excited vibrational states are not available, the product approximation can be applied:

$$Q(T) = \sum_{s_{vib}} d_{vib} \exp\frac{-hcE_{vib}}{k_B T} \times \sum_{s_{rot}} d_{rot} \exp\frac{-hcE_{rot}}{k_B T}, \tag{3.32}$$

where d_{vib} and d_{rot} denote the degenerations of the vibrational and rotational states respectively and the summation is carried out over all states s_{vib} and s_{rot}. Gamache [2000] has calculated TIPS as functions of temperature for a large variety of molecules. Taking into account centrifugal distortion corrections for the asymmetric rotor H_2O they approximated these functions by a third order polynomial expression in T, which reproduces the partition sums to a high degree of accuracy:

$$Q(T) = a + b \cdot T + c \cdot T^2 + d \cdot T^3. \tag{3.33}$$

The coefficients are given for each molecule in three temperature ranges. For the temperature range from 70-500 K the values for the water molecule are $a = -4.4405$, $b = 0.27678$, $c = 0.12536 \times 10^{-2}$, and $d = 0.48938 \times 10^{-6}$. [1] The above equation is used to calculate $Q(T)$ for each height layer in the simulation program to be inserted into Eq. 3.31.

---

[1] These values are valid for the most abundant isotope, whose lines are exclusive used in this study. Values for the other isotopes are also given in Gamache [2000]

3.6 The line shape

Heisenberg's uncertainty relation prevents all spectral lines from being infinitely narrow (if they were, it would be impossible to detect them). However, this natural line width is still extremely narrow, of the order of $\gamma = 10^{-11} cm^{-1}$. While this effect is so tiny, that it lies beyond the resolution power of optical spectrometers, there are two further broadening effects that by far exceed natural line broadening. They will be treated in the following two subsections.

3.6.1 Pressure broadening

For atmospheric pressures as found in the troposphere molecular absorption line shapes are essentially determined by collision-induced broadening. Collisions of H_2O molecules with each other as well as with those of other atmospheric constituents (mainly nitrogen) slightly shift the molecular energy levels both in the upper and lower direction. As a consequence, the collided molecules absorb at lower and higher frequencies around the line center ν_0. Since the number of collisions depends on the molecule density it is obvious that this effect depends on atmospheric pressure.

A simple expression for the shape of a pressure broadened absorption line can be derived even from classical considerations of attenuated oscillation of an electric charge. The molecular collisions are represented by attenuation coefficients and a homogeneous distribution of the velocity and acceleration vectors after the collision are assumed. This way the following expression was found 1906 by Lorentz:

$$f(\nu) = \frac{\gamma_L}{\pi(\nu - \nu_0)^2 + \gamma_L^2}. \tag{3.34}$$

Here, γ_L is the halfwidth of the symmetric shape, the index L denoting the Lorentz- or pressure broadening effect. Since the beginning of the 20^{th} century pressure broadening of spectral lines has been investigated in many theoretical studies. But even after the development of quantum theory the first model 3.34 has proven to be reliable and is still widely used. Deviations from real pressure broadened lines are noticeable only in the far line wings. Vleck and Huber [1974] take into account, that the molecules are distributed over the different quantum states according to Boltzmann statistics and use the same statistics for the velocity and acceleration after the collision. By averaging over all directions they obtain:

$$f(\nu) = \frac{\nu}{\pi\nu_0}\Big[\frac{\gamma_L}{(\nu + \nu_0)^2 + \gamma_L^2} + \frac{\gamma_L}{(\nu - \nu_0)^2 + \gamma_L^2}\Big]. \tag{3.35}$$

In the near infrared spectral regions, where $\nu >> \gamma_L$, Eq. 3.35 approaches the Lorentz line shape near the line center, where $\nu = \nu_0$.

3.6.2 Doppler broadening

The second physical process resulting in line broadening is the Doppler effect arising from the thermal motions of the absorbing molecules. Depending on amount and direction of the translational molecular motion a Doppler-shift of the incident solar light is observed in the inertial system of the molecule. Therefore it will absorb photons whose wavelength deviate from the center wavelength of the transition in the inertial system of the ground observer. If again thermodynamic equilibrium is assumed associated with the Maxwell velocity distribution, the following expression is obtained for the spectral line profile:

$$f(\nu) = \frac{1}{\sqrt{\pi}\gamma_D} \cdot \exp\Big[- \Big(\frac{\nu - \nu_0}{\gamma_D}\Big)^2 \Big], \tag{3.36}$$

where

$$\gamma_D = \frac{\nu_0}{c} \cdot \sqrt{\frac{2k_B T ln2}{m}} \tag{3.37}$$

is the Doppler-halfwidth, T the absolute temperature and m the mass of the molecule. Hence γ_D is a function of ν_0, m and T, the latter implying a height dependence in the troposphere. Like the collision broadening, the Doppler effect decreases with temperature and therefore with height, but with a lower rate. This means that the fraction of the Doppler- halfwidth in the total line shape halfwidth increases with height and the effect becomes more important in the upper atmospheric layers. In the visible and NIR spectral regions, where our DOAS system is supposed to measure the collision effect prevails in the entire troposphere. However, we used the Voigt regime in our absorption model, which combines both line shapes It will be described in the next section.

3.6.3 The Voigt profile

Doppler and collision broadening occur simultaneously under real conditions but differ substantially at different altitudes, since Doppler broadening is not a function of pressure. A line shape that combines both effects is the Voigt profile. It is obtained by the convolution of the Lorentz (Eq. 3.34) and the Doppler shapes (3.36) (e.g. Zuev [1974]):

$$f(\nu) = \frac{f_0 \cdot A}{\pi} \cdot \int_{-\infty}^{+\infty} \frac{e^{-t^2}}{A^2 + (B - t)^2} dt, \tag{3.38}$$

where

$$f_0 = \frac{1}{\gamma_D} \cdot \sqrt{\frac{ln2}{\pi}}, \qquad A = \frac{\gamma_L}{\gamma_D} \cdot \sqrt{ln2}, \qquad B = \frac{\nu - \nu_0}{\gamma_D} \cdot \sqrt{ln2}. \tag{3.39}$$

This expression cannot be evaluated analytically like Eq. 3.34 and Eq.3.36, but various methods have been developed for efficient numerical computation of the Voigt regime. In our radiative transfer model, we implemented an optimized algorithm proposed by Humlicek [1982].

3.7 The pressure broadened halfwidth

As intermolecular collisions are the physical process causing the line broadening, the Lorentz-halfwidth γ_L introduced in Eq. 3.34 will depend on atmospheric pressure as well as temperature. For the radiative transfer model it is important to describe this dependence on p and T. In Lorentz´ derivation of 3.34 the simplest model of a harmonic oscillator was used, in which γ_L is the damping constant. In this model it can be expressed by the mean molecular collision frequency $\hat{f}$ (Yamamoto et al. [1968]):

$$\gamma_L = \frac{\hat{f}_c}{2\pi c}. \tag{3.40}$$

An estimate of the mean number of collisions can be given in the following way: If m_1 is the mass of the absorbing molecule and m_2 the mass of the collision partner, their mean relative velocity towards each other is according to the gas kinetic theory:

$$\hat{v} = \sqrt{\frac{8k_bT}{\pi}\Big(\frac{1}{m_1} + \frac{1}{m_2}\Big)}. \tag{3.41}$$

If the optical cross section of a molecules is σ then the volume it passes through within one second is $\pi\sigma^2\hat{v}$. Thus, collisions between the two different kinds of molecules occur in the volume $\pi(\sigma_1' + \sigma_2')^2\hat{v}$. If the number density of colliding molecules is N_2, this yields a collision frequency

$$\hat{f}_c = N_2 \cdot \pi(\sigma_1' + \sigma_2')^2\hat{v} = N_2\sigma_{12}^2\hat{v}, \tag{3.42}$$

which introduces the quantity $\sigma_{12}^2 = \pi(\sigma_1' + \sigma_2')^2$ as the optical cross section for line broadening collisions between molecules of species 1 and 2. Inserting 3.42 in 3.40 and summing over all constituents of a gas mixture, yields the Lorentz halfwidth for absorption lines of an absorbing gas, which in our case we denote by the subscript w:

$$\gamma_L = \sum_i N_i \sigma_{iw}^2 \sqrt{\frac{2k_B T}{\pi^2 c^2}\Big(\frac{1}{m_w} + \frac{1}{m_i}\Big)}. \tag{3.43}$$

Since in all gas mixtures the number density N_i is proportional to the pressure, there is a linear dependence of the halfwidth from p. The quantity σ_{iw}^2 depends not only from the molecular species of the collision partner, but also on the energy levels and rotational quantum number. This introduces another dependence on temperature which is therefore not just proportional to $\sqrt{T}$. According to Eq. 3.42 the optical cross sections of all constituents in the gas mixture have to be known to calculate γ_L. In order to get an expression which is more practicable for the radiative transfer model the following simplifications are introduced according to Rothman et al. [1998]: First the sum over the gas constituents is substituted by a single term expressing the effective cross section and velocity of the dry air:

$$\gamma_L(p,T)\ N(p,T) \cdot \hat{v}_{eff}(T) \cdot \sigma_{eff}(T). \tag{3.44}$$

with $N(T)\ N_0/T$ and $\hat{v}_{eff}(T) = \sqrt{\frac{8k_bT}{\pi\mu}}$.

Here N_0 is the number density under certain norm conditions and $\mu = (m_w m_d)/(m_w + m_d)$ with m_w being the mass of the H_2O-molecule and m_d the mean mass of the dry air molecules (mainly nitrogen). The temperature dependence of the cross section is described empirically by

$$\sigma^2(T)\ \sigma_0^2 \cdot T^m, \tag{3.45}$$

where σ_0^2 is assumed to be independent from T. By forming the ratio of the Lorentz halfwidth at arbitrary temperature and at norm temperature

$$\frac{\gamma_L(p_0,T)}{\gamma(p_0,T_0)} = \Big(\frac{T}{T_0}\Big)^{-\frac{1}{2}} \Big(\frac{T}{T_0}\Big)^m \tag{3.46}$$

we obtain

$$\gamma_L(p_0,T) = \gamma_L(p_0,T_0)\Big(\frac{T_0}{T}\Big)^n, \tag{3.47}$$

with $n = 1/2 - m$. As found in Eq. 3.42, γ_L depends linearly from pressure. Thus for a constant temperature we analogously get

$$\gamma_L(p, T_0) = \gamma_L(p_0, T_0)\frac{p}{p_0} \tag{3.48}$$

and with $\gamma_{L0} = \gamma_L(p_0, T_0)$ the expression for the transformation of the Lorentz halfwidth from norm conditions to arbitrary p and T:

$$\gamma_L(p, T) = \gamma_{L0}\frac{p}{p_0}\left(\frac{T_0}{T}\right)^n. \tag{3.49}$$

The exponent n as well as the halfwidth at norm conditions $\gamma_{L0} = \gamma_L(p_0, T_0)$ are individual parameters for each molecular transition. They are contained in the molecular database described in section 3.10.

3.8 Absorption path geometry

Another important part of the absorption model is the assumed geometry of the absorption path. The simplest model is a flat layered atmosphere, in which the layers are characterized by values of constant pressure, temperature and humidity. This first approximation can be used for measurements near the zenith. For solar absorption measurements down to elevations near sunset it is obviously not appropriate. Therefore we implemented the next simplest model of a homogeneous spherically layered atmosphere, which is illustrated in Fig. 3.1. While the meteorological parameters are a function of height in this model, the integration is carried out along the absorption path s, neglecting the ray bending due to refraction. For the numerical integration the path elements ds_i have to be determined, which denote the path lengths of the Sun ray when propagating through the i-th atmospheric layer. If s_i denotes the path from the station to the intersection with the a i-th layer in height h_i, the following relations can be deduced from Fig. 3.1:

$$ds_i = s_i - s_{i-1}, \tag{3.50}$$

with

$$s_i = \sqrt{R^2 + (h_i + R)^2 - 2 \cdot R \cdot (h_i + R) \cdot \cos(\gamma)}, \tag{3.51}$$

where R denotes the Earth radius and γ is related to the solar elevation angle θ by:

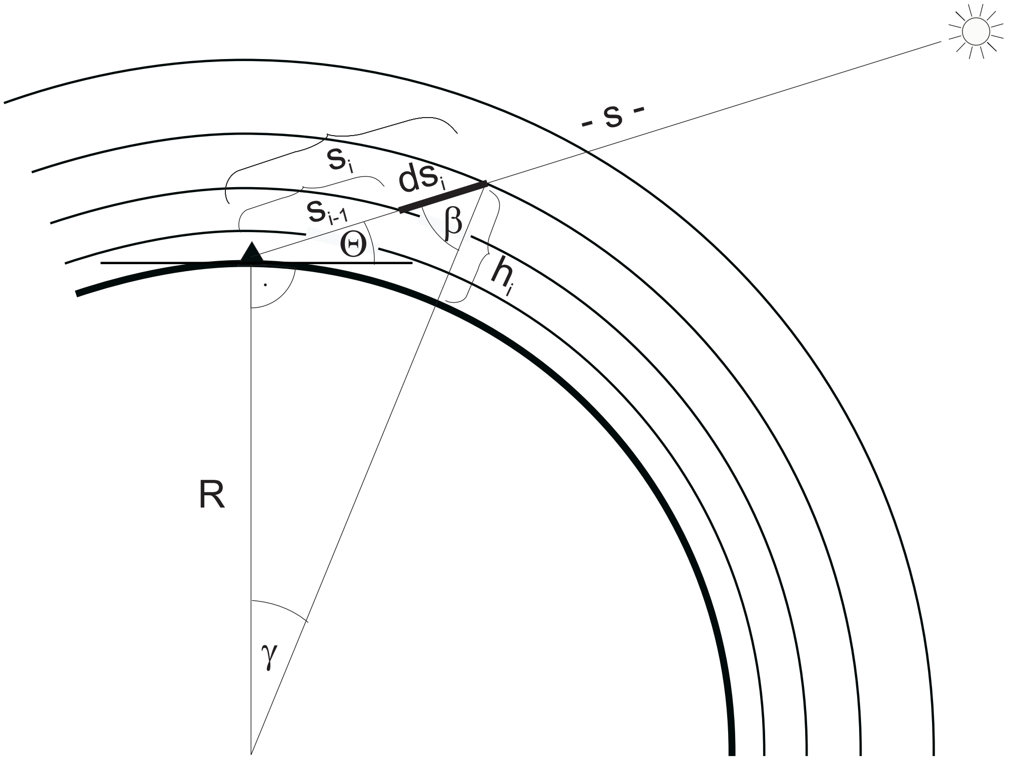

Figure 3.1: Absorption path geometry. The atmosphere is assumed to be spherically layered and homogeneous. The path lengths ds_i for the numerical integration are determined in dependence from layer height by Eq. 3.51 and 3.52.

$$\gamma = \theta - \arcsin\Big(\frac{R}{s_{trop}} \cdot \sin(\theta + \pi)\Big). \tag{3.52}$$

Using Eq. 3.51 and 3.52 the path elements ds_i are computed in the radiative transfer model, which are required to calculate the path integral of the absorption cross section along the ray path (see Eq. 3.2).

3.9 Models of meteorological profiles

From Eq. 3.31, 3.33, 3.37 and 3.49 it is obvious that the intensity measured at the ground at a given wavenumber depends on the vertical profiles of temperature and pressure along the propagation path. Furthermore there is a dependence of the optical density $\tau_l(\nu, s)$ from the molecular density $\rho(s)$ expressed by 3.3. Therefore models of the molecular height distribution and meteorological parameters have to be included in the radiative transfer code. In forward calculations, like e.g. simulations, as well as for the purpose of adjusting line parameters (as will be shown in section 6.3.4.2) this information can be obtained from radiosondes. In the retrieval of precipitable water no such information is usually available and the models become assumptions. The impact of meteorological model errors on the accuracy of PW retrieval is analyzed in section 7.4.

The simplest models that can be applied for the meteorological profiles in the troposphere is a linear decrease of temperature $T(h)$ with height and an exponential decrease of total and partial pressure $p(h)$ and $e(h)$:

$$p(h) = p_s \cdot \exp\left[\frac{h-h_s}{H_p}\right], \quad e(h) = e_s \cdot \exp\left[\frac{h-h_s}{H_w}\right], \quad T(h) = T_s - \beta \cdot (h-h_s), \tag{3.53}$$

where the index s denotes the surface values, H_p and H_w the scale heights for total and partial pressure and $\beta = \text{const}$ the temperature lapse rate. The assumed values are $H_p = 8$ km, $H_w = 1.5$ km and $\beta = 6.3\ K/\text{km}$.

While this simple model is usually adequate for the total barometric pressure, the true temperature and even more extreme the partial pressure for water vapor can deviate substantially from the model assumption. In order to obtain the best possible approximation to the truth, it is desirable to incorporate some further information, if available. The way chosen to achieve this is following an approach described by Robinson [1986] and Peter and Kämpfer [1992]. It is based on the assumption that with increasing height a temperature (or humidity) distribution is better described by a nominal profile, which can be e.g. derived from statistical evaluation of radiosonde soundings. Closer to the ground the actual profile is rather reflected by the measured surface value T_s, which should be associated a greater weight in the lower layers of the model profile. A simple formula which ensures this is given by

$$T(h) = T_n(h) + (T_s - T_n(0)) \cdot \exp\left[\frac{h}{H_T}\right] \tag{3.54}$$

where $T_n(h)$ denotes the nominal profile and H_T its scale height, for which Robinson proposes the value of 3 km. The physical background of this approach is that the warm ground has a stronger influence on the lower temperature profile which decreases with height. The same approach can be applied for the absorber density distribution:

$$\rho_w(h) = \rho_n(h) + (\rho_s - \rho_n(0)) \cdot \exp\left[\frac{h}{H_\rho}\right]. \tag{3.55}$$

In chapter 7 the results of several field campaigns with the water vapor DOAS system are presented. For one of these campaigns, presented in section 7.2, nominal profiles for $T(h)$ and $\rho_w(h)$ have been calculated and used as described above.

3.10 The HITRAN molecular database

Utilizing the expressions derived in sections 3.2 - 3.7 one could start to calculate differential solar absorption spectra. The derivation revealed that the individual absorption lines are characterized by several parameters, which have to be known. These are

- the line position or center frequency ν_0 in cm^{-1}
- the line intensity at norm temperature S_0 in $cm^{-1}/(molecule \cdot cm^{-2})$
- the collision broadened halfwidth at norm temperature and pressure γ_{L0}
- the energy of the lower transition level E'
- the exponent of the temperature dependence of the halfwidth n

A standard source of spectroscopic data for atmospheric gases is the database HITRAN. HITRAN is an acronym for HIgh resolution TRANsmission molecular absorption database. The compilation of spectroscopic parameters in HITRAN is used by a variety of computer simulation codes to predict the transmission and emission of light in the atmosphere. It contains the parameters of more than 1 million single transitions. The database is a long-running project started by the Air Force Cambridge Research Laboratories (AFCRL) in the late 1960's in response to the need for detailed knowledge of the infrared properties of the atmosphere. The HITRAN compilation, and its analogous database are now being developed at the Atomic and Molecular Physics Division, Harvard-Smithsonian Center for Astrophysics Rothman et al. [1998]. For our calculations we used the 1996 version, which is freely available on CD-ROM.

The line parameters for H_2O-transitions are in most cases in laboratory measurements utilizing long path absorption cells, in which an incident light beam is multiply reflected within a mirror system before it is analyzed by a spectrograph. Several research groups perform such measurements and tabulate the determined line parameters which are included in HITRAN. The following publications report the measurements of H_2O lines which were used in our radiative transfer model: (Camy-Peyret et al. [1985], Mandin et al. [1986], Mandin et al. [1988], Chevillard et al. [1989], Schwenke [1998], and Giver et al. [1999]). Among the parameters published in HITRAN for each transition there are also accuracy indices for S_0, ν_0 and γ_{L0}. This is particularly useful for analyzing the error of the radiative transfer model. However, systematic errors in the HITRAN line strength parameters have recently been discovered by P.Giver et al. [2000], which far exceed the errors given by the accuracy indices. The corrections proposed by P.Giver et al. [2000] were incorporated in our model. However, as will be reported in section 6.3.4, it was decided to determine ´´own´´ line strength parameters using the radiative transfer model described above and a dataset of radiosondes.

3.11 Summary: Observation equations

At the end of this chapter the equations describing molecular absorption in the atmoshere, which have been derived above, will be assembled to formulate the observation equations for the DOAS measurements and to give a better overview on the relations used in the radiative trabsfer model.

The general observation equation is the Bouguer-Lambert-Beer law. Since for DOAS spectra the extraterrestrial intesity $I_0(\nu)$ is normalized to unity, it takes the form

$$I'(\nu) = \exp\Big[-\sum_l \int_{s_0}^{\infty} \rho(s) \cdot k_l(\nu, s) ds\Big], \tag{3.56}$$

for the the differential intensity $I'(\nu)$ measured at wavenumber ν, whith $\rho(s)$ being the water vapor density and $k_l(\nu, s)$ the absorption coefficient of line l as a function of frequency and wavenumber. The integration is carried out along the absorption path in a spherically layered atmosphere. The absorption coefficient is divided into two factors describing the line intensity $S_l(s)$ and shape $f_l(s)$, respectively:

$$k_l(\nu, s) = S_l(s) \cdot f_l(s). \tag{3.57}$$

The line strength can be calculated by

$$S_l(s) = S_{0l} \cdot \frac{Q(T_0)}{Q(T(s))} \frac{\exp[-E'/k_B T(s)]}{\exp[-E'/k_B T_0]} \frac{(1 - \exp[hc\nu_0/k_B T(s)])}{(1 - \exp[hc\nu_0/k_B T_0])}, \tag{3.58}$$

which requires the line parameters for the line strength S_{0l} at norm temperature T_0 and the line position ν_0. The total internal partition sum $Q(T(s))$ is approximated by

$$Q(T(s)) = a + b \cdot T(s) + c \cdot T(s)^2 + d \cdot T(s)^3. \tag{3.59}$$

with the coefficients calculated by Gamache [2000]. The line shape is described by the Voigt profile

$$f_l(\nu, s) = \frac{f_{0l} \cdot A_l(s)}{\pi} \cdot \int_{-\infty}^{+\infty} \frac{e^{-t^2}}{A_l(s)^2 + (B_l(\nu, s) - t)^2} dt, \tag{3.60}$$

where

$$f_0(s) = \frac{1}{\gamma_{Dl}} \cdot \sqrt{\frac{ln2}{\pi}}, \qquad A_l(s) = \frac{\gamma_{Ll}(s)}{\gamma_{Dl}(s)} \cdot \sqrt{ln2}, \qquad B_l(\nu, s) = \frac{\nu - \nu_0}{\gamma_{Dl}(s)} \cdot \sqrt{ln2}. \tag{3.61}$$

The halfwidth for the Doppler effect γ_{Dl} depends on the temperature as expressed by

$$\gamma_{Dl}(s) = \frac{\nu_{0l}}{c} \cdot \sqrt{\frac{2k_B \cdot T(s) \cdot ln2}{m}} \tag{3.62}$$

and the Lorentz halfwidth from pressure and temparture:

$$\gamma_{Ll}(s) = \gamma_{Ll0} \cdot \frac{p(s)}{p_0} \Big(\frac{T_0}{T(s)}\Big)^{n_l}. \tag{3.63}$$

The last equation requires two additional line parameters: The Lorentz width at norm conditions γ_{Ll0} and the exponent of temperature dependence n_l. For simulating real DOAS spectra, the differential absorption spectrum is finally convoluted with the apparatus function $A(\nu)$, which accounts for the limited resolution power of the measuring instrument:

$$\hat{I}(\nu) = \int_{\Delta\nu} I'(\nu`) \cdot A(\nu - \nu`) d\nu`. \tag{3.64}$$

4 Absorption line selection

4.1 Introduction

The previous chapter explained the models for absorption of solar radiation in the troposphere. On the basis of this model, several simulation calculation were carried out to determine optimum specifications of the measurement system to be developed. The most important non-instrumental optimization is the selection of spectral intervals to be measured. The dedicated spectrometer was designed to be capable of measuring in a broad wavelength region, ranging from visible light at 600 *nm* up to the near infrared at about 940 *nm*. This allows the instrument to detect absorption lines of three vibration-rotation bands of the H_20-molecule spanning in this wavelength interval. These absorption bands comprise a total of more than 8000 single transitions. From this large number it is obvious that a complete scan of the entire measurable spectral area is not practicable. Consequently, a selection of wavelength intervals to be measured by the spectrometer system had to be made. Since the high resolution approach presented here is based on a line-by-line analysis of the recorded spectra, this selection process is basically a choice of optimum absorption lines.

The systematic search of an optimum subset out of a multitude of measurable wavelength intervals is a task which requires two main steps: First the selection criteria have to be defined and translated into a mathematical terms, and second they have to be implemented in a selection algorithm. The selection criteria are the most important issues to be addressed beforehand. These criteria depend on the objectives of the investigation. In our case there were two main goals: First the accurate determination of tropospheric water vapor content and second the investigation of vertical profile retrievals. The corresponding selection criteria for these two objectives can be contradictory: For the PW retrieval one might seek absorption transitions, whose spectral line parameters are most accurately determined in laboratory studies. However these lines might not be an optimum selection for maximizing information content on vertical H_2O-distribution. In the selection process described in the following a way was chosen which is a compromise between both objectives: In two selection steps possible candidate intervals are filtered which fulfill the criteria for the goal of deriving accurate PW estimates from DOAS spectra. In the final selection step, a subset of these candidates was chosen, which maximize the information content of the measurements on vertical humidity distribution.

Before the selection process implemented in this study is described in section 4.3, the theory of information content of spectrometric data will be outlined in the following section.

4.2 Theory: Information content of spectrometric measurements

In this section the term "information content" will be exclusively defined under the aspect of vertical humidity profiles. It presents a concept which is the basis of the theoretical investigation on the possibility of deriving such profiles from the measured DOAS spectra.

The problem to be addressed here is to evaluate the significance of a spectral measurement for the "quality" of a profile retrieval. There are several ways of defining the "quality" of a retrieval. One might want to optimize the vertical resolution of the estimate for the vertical humidity distribution. This was e.g. investigated by Peckham [1974] in a study on optimizing the configuration of a remote sounding radiometer. Alternatively it is possible to optimize the accuracy of the retrieved parameters, which means minimizing their variance, as was done e.g. by Westwater and Strand [1968]. In any case, some figure of merit has to be defined, characterizing the "quality" of a spectral measurement. Problems of selecting optimum frequencies for remote sensing of atmospheric parameters have been investigated in the context of microwave radiometry by spaceborne (Rodgers [1996]), as well as ground based instruments (Solheim et al. [1998]). All of the papers cited above use the expression "information content" to characterize the contribution of a measurement, but all define different quantities associated with this term. We will follow here the definitions given in Rodgers [2000], which are based on the concepts of information theory. These will be briefly outlined in the following section.

4.2.1 Entropy of information

Rodgers approaches the problem by describing the information content of a spectrometric measurement in the framework of the information theory originally developed by Shannon and Weaver [1949]. The information content as defined in this theory is closely related to the thermodynamic entropy S as a function of the probability density function (*pdf*) P:

$$S(P) = -k \sum_i p_i \ln p_i, \tag{4.1}$$

where p_i is the probability of the system being in state i. While in thermodynamics k is the Boltzmann constant, in information theory $k = 1$. In this context the entropy is used as a measure of knowledge about the unknown state x of the system, in the sense that the greater the entropy, the poorer the knowledge about x. If $P_1(x)$ is the *pdf* before the measurement and $P_2(x)$ the corresponding *pdf* afterwards, the information content H of the measurement is defined as the change in entropy on making the measurement:

$$H = S(P_1) - S(P_2). \tag{4.2}$$

If the *pdf* are both Gaussian distributions with covariances S_1 and S_2, it can be shown that

$$H = \frac{1}{2}\log|S_1| - \frac{1}{2}\log|S_2|. \tag{4.3}$$

For further treatment of the problem, we have to know how to calculate covariance matrices after every retrieval of x using new observations. For this, the so-called weighting functions of the measurements are required, which are introduced in the next section.

4.2.2 Weighting functions

The key to identify frequencies carrying information on atmospheric properties in different heights is the so called weighting function $K(h)$. Unfortunately, this term is not consistently used in the literature. For spaceborne radiometric measurements the radiance $I(\nu)$ emerging vertically at the top of the atmosphere at wavenumber ν is

$$I(\nu) = \int_0^\infty B(\nu, T(h))\frac{\partial\tau(\nu, h)}{\partial h}dh = \int_0^\infty B(\nu, T(h))K(\nu, h)dh, \tag{4.4}$$

when $B(\nu, T(h))$ represents Planck´s radiation function and $T(h)$ the temperature at height h. The measured radiance is thus a mean of the Planck profile, weighted with $K(\nu, h)$. It is the frequently used linear integral equation 4.4 which introduced the term “weighting function” for all functions establishing such a relationship between the the observations (in this case the radiances $I(\nu)$) and the quantities to be retrieved (e.g. the temperature profile indirectly determined through the Planck profile, which can be inverted algebraically).

Rodgers [2000] uses a more general definition of weighting functions: If a vector of ideal measurements $\mathbf{y}$ is approximated by a forward model $\mathbf{F}(\mathbf{x})$ as a function of the unknown quantity $\mathbf{x}$ with additional measurement error ϵ,

$$\mathbf{y} = \mathbf{F}(\mathbf{x}) + \epsilon, \tag{4.5}$$

then the linearization of the forward model about some reference state $\mathbf{x_0}$

$$\mathbf{y} - \mathbf{F}(\mathbf{x_0}) = \frac{\partial \mathbf{F}(\mathbf{x})}{\partial \mathbf{x}}(\mathbf{x} - \mathbf{x_0}) + \epsilon = \mathbf{K}(\mathbf{x} - \mathbf{x_0}) + \epsilon \tag{4.6}$$

defines the weighting function matrix, in which each element is the partial derivative of the forward model element with respect to a state vector element:

$$\mathbf{K_{ij}} = \frac{\partial \mathbf{F_i}(\mathbf{x})}{\partial \mathbf{x_j}}. \tag{4.7}$$

If there are m frequencies ν_i and n unknown parameters x_j, the weighting function matrix has the dimension $m \times n$. The linearization of a non-linear model about a reference or a-priori state is justified if $\mathbf{F}(\mathbf{x})$ is linear within the error bounds of the retrieval. For the purpose of discussing information content, the non-linearity of most retrieval problems is not an important consideration.

We now return to the problem of calculating covariance matrices introduced in section 4.2.1. Let x_a be the prior estimate of x and $\mathbf{S_a}$ its prior covariance. Then, again using the model of Gaussian probability density,

$$P(x) = \frac{1}{(2\pi)^{n/2}|\mathbf{S_a}|} \exp\Big[-\frac{1}{2}(x - x_a)^T \mathbf{S_a}^{\mathbf{-1}}(\mathbf{x} - \mathbf{x_a})\Big], \tag{4.8}$$

the posterior estimate $\hat{x}$ also has a Gaussian *pdf*, and the posteriori covariance is

$$\mathbf{S}^{-\mathbf{1}} = \mathbf{K^T}\mathbf{S}_\epsilon^{-\mathbf{1}}\mathbf{K} + \mathbf{S_a}, \tag{4.9}$$

where $\mathbf{S}_\epsilon$ is the covariance of the measurement error. The above relations are used in the next section to elaborate a concept for evaluating the contribution of a measurement.

4.2.3 Degree of freedom for signal and noise

With the information content as defined by 4.2 and 4.3 we have found a scalar figure of merit that can be used to optimize a remote sensing system. However, there is an inherent problem associated with this quantity: Measuring a single component of the state vector to very high accuracy yields the same information content as measuring several components with lower accuracy. In real applications, however, there is usually a limit of useful accuracy and the determination of more parameters at lower accuracy may be preferable.

Therefore, Rodgers introduces another figure of merit, the degree of freedom of the retrieval. The largest number of parameters that could be determined is given by the dimension of the state vector n (or, if smaller, the dimension of the measurement vector m). However, a particular observing system may not be able to resolve all parameters. Formally, the maximum number of parameters that can be determined is given by the rank of the weighting function matrix K, but in the presence of noise, the real degree of freedom might be smaller. Rodgers describes an approach to identifying the number of useful degrees of freedom: The state and the measurement vector are linearly transformed by $\acute{x} = \mathbf{S}_\mathbf{a}^{-\mathbf{1}}\mathbf{x}$ and $\acute{y} = \mathbf{S}_\epsilon^{-\mathbf{1}}\mathbf{y}$.

The components of the state, which correspond to the eigenvectors of the posterior covariance in this coordinate system $\acute{\hat{S}}$ are measured independently. The corresponding eigenvalue λ_i is the factor by which the variance of the component is reduced on performing the measurement and the signal to noise ratio is $[(1-\lambda_i)/\lambda_i]^{\frac{1}{2}}$. If λ_i is close to unity, the corresponding component is poorly determined and is designated a "degree of freedom for noise". Their total number is given by the sum of the eigenvalues, $d_n = \sum_i \lambda_i$. Hence, the total number of degrees of freedom for signal is

$$d_s = n - d_n = n - \sum_i \lambda_i = tr(\mathbf{I} - \acute{\hat{\mathbf{S}}}). \tag{4.10}$$

The quantity defined by 4.10 is another figure of merit to describe the usefulness of an observation. Rodgers uses both the degree of freedom for signal d_s as well as the information content H defined by 4.3 in a procedure to select a subset of measurement channels for the Atmospheric Infrared Sounder (AIRS) aboard the AQUA spacecraft of the Earth Observing System (EOS), scheduled for launch in late 2000 (see also http://www-airs.jpl.nasa.gov/). The purpose was to optimize the retrieval of temperature profiles, but the concept is of general applicability and can be adapted to our problem of ground based water vapor determination. This will be done in the next section.

4.2.4 Concept for evaluating information content

The selection of an optimum subset of measurement intervals out of a large number of possible candidates could in principle be performed by considering and evaluating all possible combinations. It is immediately obvious, that such a "blind" strategy would require enormous computation time and is not feasible. Instead, a simpler process is needed, which is likely to give a reasonable result, even if it might be suboptimal. Such a process is a sequential selection of frequencies: A single channel or interval is selected which maximizes the figure of merit, and than successively new intervals are selected from those not yet chosen that subsequently maximize the figure of merit.

When $i-1$ channels have been selected and the corresponding covariance matrix is denoted by $\hat{\mathbf{S}}_{i-1}^{-1}$, and if furthermore a diagonal covariance matrix $\mathbf{S}_\epsilon$ is assumed (implying uncorrelated measurement error), then it follows from equation 4.9 that adding a measurement interval with the corresponding weighting function matrix $\mathbf{K_i}$ yields:

$$\hat{\mathbf{S}}_i^{-1} = \hat{\mathbf{S}}_{i-1}^{-1} + \mathbf{K_i^T K_i} = \sum_{\mathbf{k=1}}^{\mathbf{i-1}} \mathbf{K_{k,sel}^T K_{k,sel}} + \mathbf{K_i^T K_i}. \tag{4.11}$$

The summation with index k is carried out over the $i-1$ intervals that have already been selected, as denoted by the subscript *sel*. The change in degree of freedom for signal is:

$$\delta d_n = tr(\mathbf{S_{i-1}}) - \mathbf{tr}(\mathbf{S_i}). \tag{4.12}$$

Equation 4.12 is the fundamental characterization criterion we were seeking and the basis for our selection procedure. Out of the group of measurable wavelength intervals we successively select those maximizing δd_n, or equivalently those minimizing the trace of the covariance matrix $\hat{\mathbf{S}}_i$. The numerical implementation of this concept will be outlined in section 4.3.3.

For completeness it should be noted that instead of Eq. 4.12 the information content H could have been used by maximizing

$$\delta H = \frac{1}{2} ln(1 + \mathbf{K_i^T S_{i-1} K_i}). \tag{4.13}$$

In Rodgers [1996] both figures of merit are used. The comparison of selection results proved that the two approaches selected almost the same subset of frequencies, indicating that the criteria are equivalent to a great extent.

4.3 Implementation: Selecting intervals for DOAS

In the literature on optimizing the information content of spectroscopic measurements, the selection of individual measurement channels for remote sensing is described. However, a grating spectrometer with a detector array always simultaneously measures intensities in a spectral interval whose width is determined by the specifications of the instrument (e.g. angular dispersion, width of the photodiode array) and the measured wavelength. In the case of SAMOS, the measured bandwidth varies from 0.5 to 0.9 nm in the wavelength range from 600 to 940 nm. The problem is therefore finding an optimum set of wavelength intervals to be measured rather than selecting individual absorption lines. Given the measurable wavelength range there are still several hundred intervals and their combinations to be evaluated. It is obvious that some selection algorithm has to be implemented to find a subset of measurement windows. The number of measurable windows is limited by instrumental properties of the spectrometer system. In our construction (see section 5.3.1) one limitation is the size of the telescope's filter wheel which was designed to fit 10 interference filters of 25 mm diameter. Theoretically it would be possible to measure up to 10 contiguous intervals within the 10 nm halfwidth of each filter. However, there is also a temporal limitation: Given an acquisition time of 1-2 minutes for each wavelength window, one has to consider the time it takes for a complete scan of selected wavelengths. We regarded 20 minutes as a reasonable limit for a wavelength scan, which means that the number of intervals to be selected should be about 10-15.

In the following we describe a three-step procedure which we implemented to perform this task. Each step is described in the subsequent sections.

4.3.1 Step 1: Filtering intervals suited for DOAS

The first step in the selection procedure is to locate all intervals in the observable spectral region which are potentially suitable to perform DOAS measurements. This is the case if the measured spectrum can be normalized with respect to a differential intensity level $\acute{I}_0(\nu)$ as described in section 2.5. The tool to check wavelength intervals for this quality is the radiation transfer model described in chapter 3. In order to provide a basis for the filter algorithm, we first computed differential absorption spectra for the entire spectral range from 600 to 940 nm using three different atmospheres and observation geometries:

- 1) A zenith observation through a dry atmosphere with only 4 mm PW
- 2) A zenith observation through a humid atmosphere with 40 mm PW
- 3) A slant observation through a humid atmosphere with 40 mm PW and a solar elevation angle of 10 °

The simple models of meteorological profiles introduced in section 3.9 were used for all three atmospheres. One hundred equally spaced atmospheric layers were defined and a troposphere height of 10 km was assumed. A spectral resolution of 1 pm was chosen, which is roughly the expected instrumental resolution of the DOAS prototype system. Considering 8000 single H_2O-transitions over the bandwidth of 340 nm leads to a considerable computational effort. Two cutouts of these broad band calculations of atmospheric attenuation are plotted in Fig. 4.1 and 4.2.

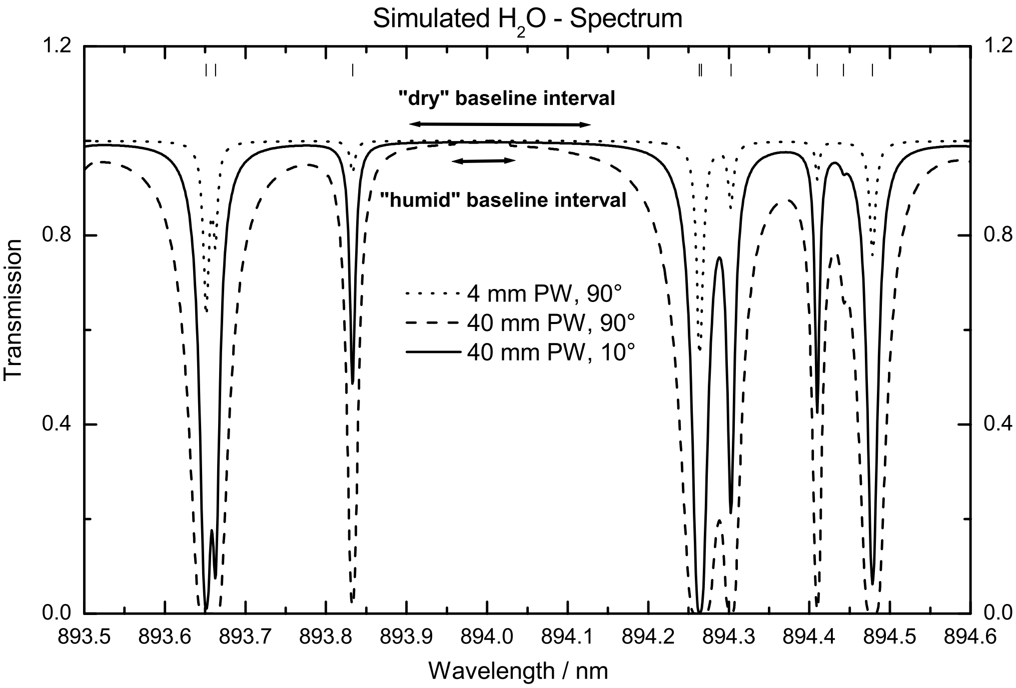

Figure 4.1: Example of a wavelength interval which was considered for measurement window selection. Theoretical transmission spectra are computed for three different observation conditions. For the extreme case of low elevation sounding through a humid troposphere, the baseline interval becomes too narrow. The interval was therefore rejected in the pre-filtering procedure.

Comparing the computed transmissions of the atmospheres gives an idea of the bandwidth of absorption signals to be expected from the DOAS measurements. The difference of transmission between the atmospheres 1) and 2), which have the same observation geometry represents the signal when the total water vapor content changes by an order of magnitude. The difference between 2) and 3) shows the effect of increasing airmass when the Sun passes from the zenith to the horizon.

Both values of PW are rather extreme and represent upper and lower limits of realistic water vapor abundances (40 mm of PW is rarely observed even in tropical climates). Atmosphere 3) simulates the most extreme observation conditions,

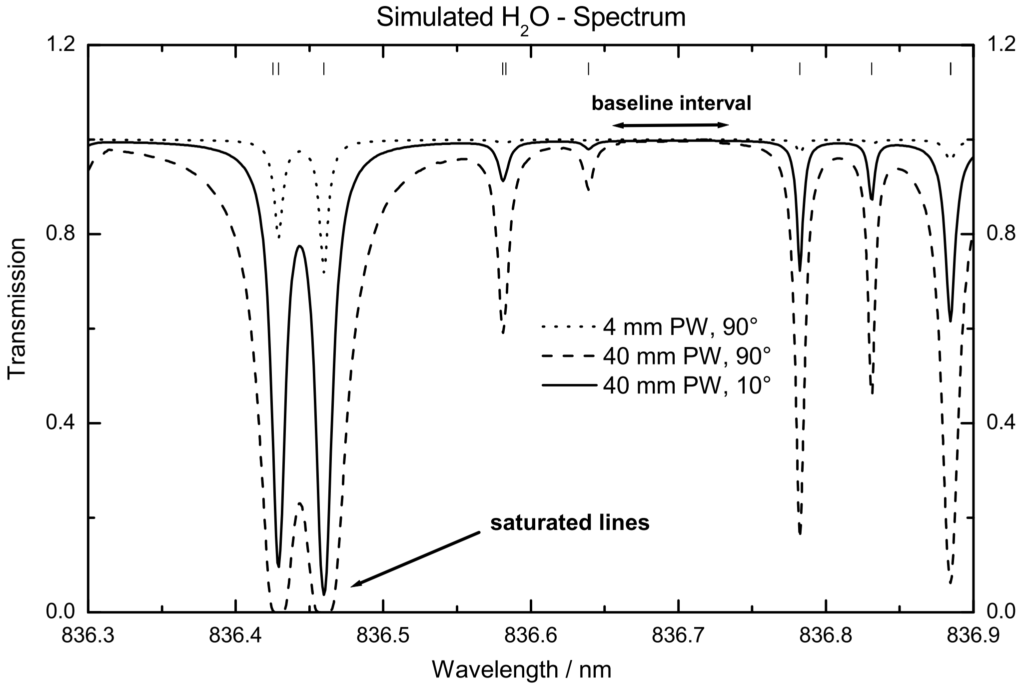

Figure 4.2: Example of a wavelength interval which was considered for measurement window selection. The strong absorption features at 836.42 and 836.46 nm reach saturation for a 10°-slant sounding of an extremely humid troposphere. The interval was therefore rejected in the pre-filtering procedure.

since we arbitrarily defined 10° as our elevation cutoff for spectrometric measurements (however, as will be shown in chapter 7, we achieved PW retrievals down to 2°). The theoretical attenuations calculated using atmosphere 3) surely exceed the amount of absorbed radiation that can be expected under most observation conditions. However, defining extreme threshold conditions as the limit for measurements and verifying the feasibility of PW retrieval under these conditions is a way of reducing the number of candidates in the pre-selection of measurement intervals. In the following, this procedure on the basis of model calculations will be outlined:

The first approach in data reduction is to formulate criteria to reduce the number of candidate intervals. As mentioned above, every candidate interval has to encompass a baseline interval within the measured interval. This is necessary for the normalization of DOAS spectra (see section 6.2.2). Most DOAS approaches interpolate the baseline from both sides of a spectrum Platt [1994]. Since we planned to measure a flatfield spectrum along with each solar spectrum, we decided that one baseline interval would be sufficient. Filtering out intervals with subintervals suited for normalization is therefore the first step in our selection algorithm.

The question arises, what makes a spectral interval suited to be used for baselining. In section 2.5 we pointed out that differential intensity levels $\acute{I}_0(\lambda)$ are usually defined by interpolation of intervals with neglectable line absorption. One could demand that the deviation of transmission from 100 % within the interval be less than the instrument´s noise level. However this might be a too strong constraint: If the line shapes are modeled well enough, even outer line wings could be in principle used for normalization, and the differential absorption of the line is defined with respect to the intensity measured in the line wing.

Another criterion to be defined is the minimum bandwidth of baseline intervals. It is obvious that the wider the interval the more accurate $\acute{I}_0(\lambda)$ will be determined. On the other hand, because of the absence of spectral lines, baseline intervals do not contain information about the absorbing species to be determined. Since the measurable spectral bandwidth is fixed for an adjusted wavelength, the spectral window for measuring absorption lines becomes narrower for wider baseline intervals. The spectral width chosen for the definition of a baseline interval is therefore a tradeoff between a loss of information within the measured solar spectrum and baselining accuracy.

Defining the two criteria for baseline intervals mentioned above is clearly a somewhat arbitrary choice. In the question of baseline interval width we decided that sacrificing 1/4 of the measurable bandwidth for baselining would be a reasonable limit, resulting in spectral ranges of 0.1 to 0.2 nm. We furthermore regarded H_2O-line absorption as neglectable at a given wavelength λ, if the transmission I at λ was greater than 99%.

Thus, given the differential tropospheric attenuations computed from 600-940 nm, the filter program first locates the potential baseline intervals defined by the following conditions for transmission values T in a wavelength interval $(\lambda_{b,s}, \lambda_{b,e})$:

$$T(\lambda) - 1 < \epsilon; \lambda_{b,s} < \lambda < \lambda_{b,e} \tag{4.14}$$

and

$$\lambda_{b,e} - \lambda_{b,s} > \delta, \tag{4.15}$$

where $\epsilon = 0.01$ and $\delta = 0.1$ nm. It is obvious, that the amount of spectral intervals which satisfy 4.14 and 4.15 depends on the model atmosphere used to calculate the transmission spectra. Fig. 4.1 shows an example of a potential measurement interval, which possesses a suitable baseline range at the longer wavelength side of the spectrum for the model atmospheres 1) and 2). However, under the extreme conditions of model atmosphere 3) the spectral width of computed transmissions satisfying the ϵ-criterion defined by 4.14 is narrower than the threshold width $\delta =$ 0.1 nm imposed by 4.15. Since we decided to accept only wavelength windows which fulfill the selection criteria under all possible conditions, such an interval candidate was rejected.

As mentioned above, our realization of DOAS-baselining using flatfield spectra requires only one baseline interval within the measured wavelength window. In the normalization procedure, which will be described in detail in section 6.2.2, the baseline is defined by matching the flatfield and the solar spectrum at either the long- or the short wavelength side of the measured interval. Consequently, every baseline interval identified by 4.14 and 4.15 yields two suitable wavelength windows, given by the simultaneously measurable bandwidth of the instrument to the left and right side of the baseline interval. This is illustrated in Fig. 4.3, where a baseline interval fulfilling the selection criteria is plotted with its spectral vicinity of 1.5 nm width on the short- and long wavelength (left and right) side respectively. Both wavelength intervals, defined by the subinterval satisfying 4.14 and 4.15 and the continuation in either direction (left or right) until the limit of the instruments spectral viewing bandwidth, are potential candidates for measurement intervals.

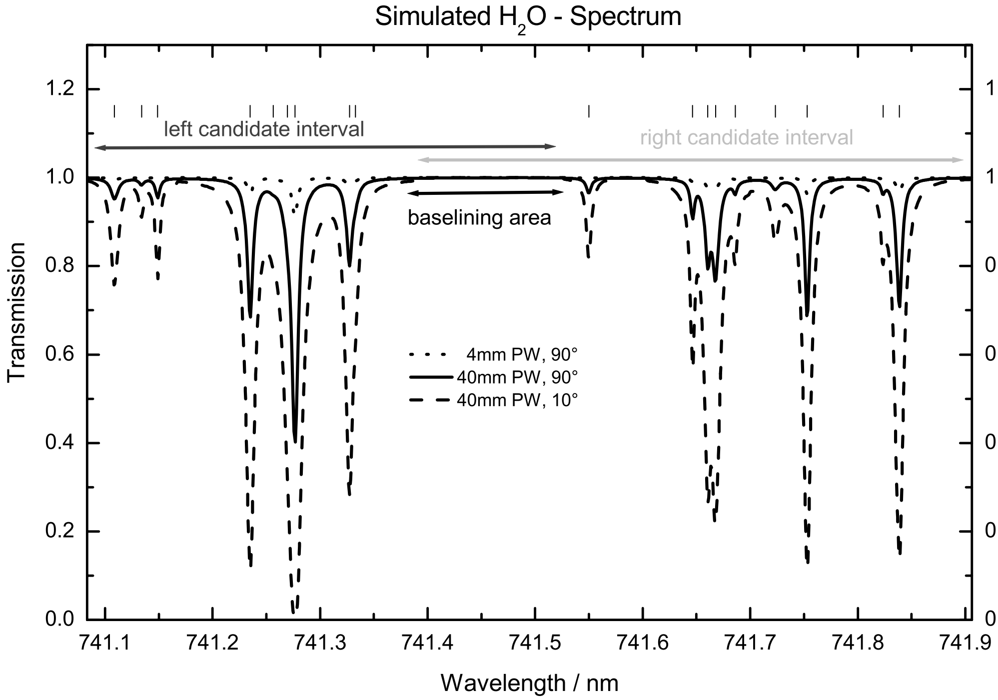

Figure 4.3: Spectral interval fulfilling the baseline criteria. Both the short- and long wavelength (left and right) side of the interval could be used for DOAS measurements

The remaining intervals were checked for a third criterion introduced in the prefiltering stage: The absence of saturated lines, in whose centers all photons are absorbed before reaching the telescope. If a transition becomes saturated, it will not be usable for retrieval of absorber abundance, since the information in the line centers, where the transmission approaches zero, is lost. In principle every independent intensity measurement along the line profile carries information on the amount of absorbing molecules. However, for its retrieval the meteorological profiles (temperature, pressure and absorber distribution) have to be known precisely, since the line shape is sensitive to these functions. Also, the line shapes (see section 3.6) are best modeled in the line centers and model errors become larger with increasing distance from the center wavelength. Applying the same stringent selection rule as in the case of baseline suitability, we therefore rejected interval candidates containing saturated absorption lines under the conditions of atmosphere 3). Fig. 4.2 shows an example interval, which was rejected in the pre-filtering stage for getting saturated under humid tropospheric conditions and low solar elevation angle.

A total of candidate 662 spectral intervals were found to fulfill the criteria of the pre-filtering by the absorption model. These were further validated in the next two steps.

4.3.2 Step 2: Computing weighting functions

The second step in the selection algorithm is merely a preparatory stage, in which no further candidate intervals are sorted out. Instead, the weighting functions introduced in section 4.2.2 will be computed for each of the 662 candidate intervals identified in the previous step.

We will adapt the definitions given above to calculate the weighting functions for DOAS measurements of water vapor lines in the visible and near infrared using the forward model described in chapter 3. For this it is necessary to express the observation equation 3.56 as a function of a finite set of unknown parameters, which means discretizing the meteorological profile to be retrieved. Therefore we parameterized the troposphere by defining $m = 20$ equally spaced layers j of thickness Δh_j with constant T_j, p_j and absolute humidity ρ_j. The discrete observation equation 3.56 then becomes:

$$I_i' = \exp\Big[-\sum_{j=0}^{m} \rho_j \cdot k_{ij} \cdot \Delta h_j \Big]. \tag{4.16}$$

In Fig. 4.4 a vertical profile of absolute humidity and its discretization according to 4.16 is plotted. We only considered weighting functions as partial derivatives of the observation equation with respect to the absolute humidity:

$$\mathbf{K_{ij}} = \frac{\partial \mathbf{I_i'}}{\partial \rho_\mathbf{j}} = \mathbf{I_i'} \cdot \Big[-\mathbf{k_{ij}} \cdot \Delta \mathbf{h_j} \Big]. \tag{4.17}$$

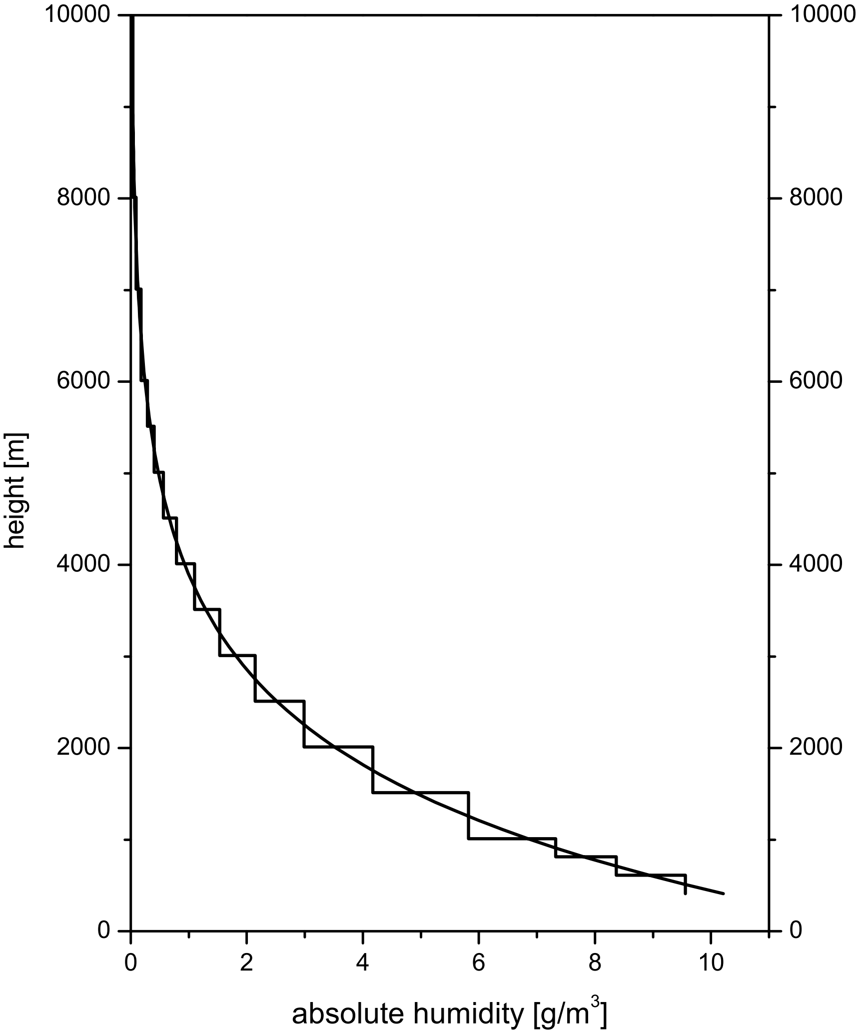

Figure 4.4: Discretization of the absolute humidity profile ρ_j for computation of weighting function matrices. The troposphere is divided into 20 equally spaced layers with constant meteorological parameters.

Weighting function matrices K according to 4.17 were computed for all spectral intervals judged to be suitable for measuring in the filtering stage outlined in the previous section. The same spectral resolution of 1 pm as in 4.3.1 was used. Therefore, given the assumed viewing bandwidth of the spectrometer of 0.7 nm, 816 K-matrices of dimension 700×20 were computed. They were the data basis for the final selection stage, which is described in the next section.

4.3.3 Step 3: Final selection

In the last stage a subset of 10-15 intervals has to be selected from the 416 candidates filtered out in the first stage (section 4.3.1) and characterized in the second stage (section 4.3.2). Here, the optimization concept described in section 4.2.4 and expressed in 4.12 is applied.

The first wavelength which is chosen is the one with the smallest trace $tr(\mathbf{K_1^T K_1})^{-\mathbf{1}}$. Once the "number one" is selected, all the other candidates are evaluated by adding their weighting function matrix inverse covariance matrix $S_{i,cand}^{-1}$ to the total inverse covariance and computing the trace of the inverse:

$$\mathbf{S_{i,cand}^{-1}} = (\mathbf{S_{i-1,sel}^{-1}} + \mathbf{S_{i,cand}^{-1}})^{-\mathbf{1}} = \sum_{\mathbf{k=0}}^{\mathbf{i-1}} \mathbf{K_{k,sel}^T K_{k,sel}} + \mathbf{K_{i,cand}^T K_{i,cand}}, \tag{4.18}$$

and then computing the trace of the inverse

$$d_{n,cand} = tr(S_{i,cand}). \tag{4.19}$$

The subscript *cand* denotes matrices which are not yet selected. The above computation is repeated for every single remaining candidate interval. The one producing the minimum trace $d_{n,cand}$ is then selected. In the next round the cycle starts again.

The behavior of the trace $d_{n,sel}$ after selection of a new interval is plotted in Fig. 4.5. It can be seen that $d_{n,sel}$, as a measure for the degree of freedom for noise, decreases rapidly (presumable exponentially) at the beginning of the process with every new wavelength window. With increasing number of selected observation windows the contributions of new intervals decreases constantly. After about 12 measurement intervals have been selected, adding more observations does not improve the information content of the data. Such saturation of information content has also been observed in similar investigations on finding optimum channels for microwave remote sensing Twomey [1977].

In the last section of this chapter, the chosen candidate measurement intervals are presented.

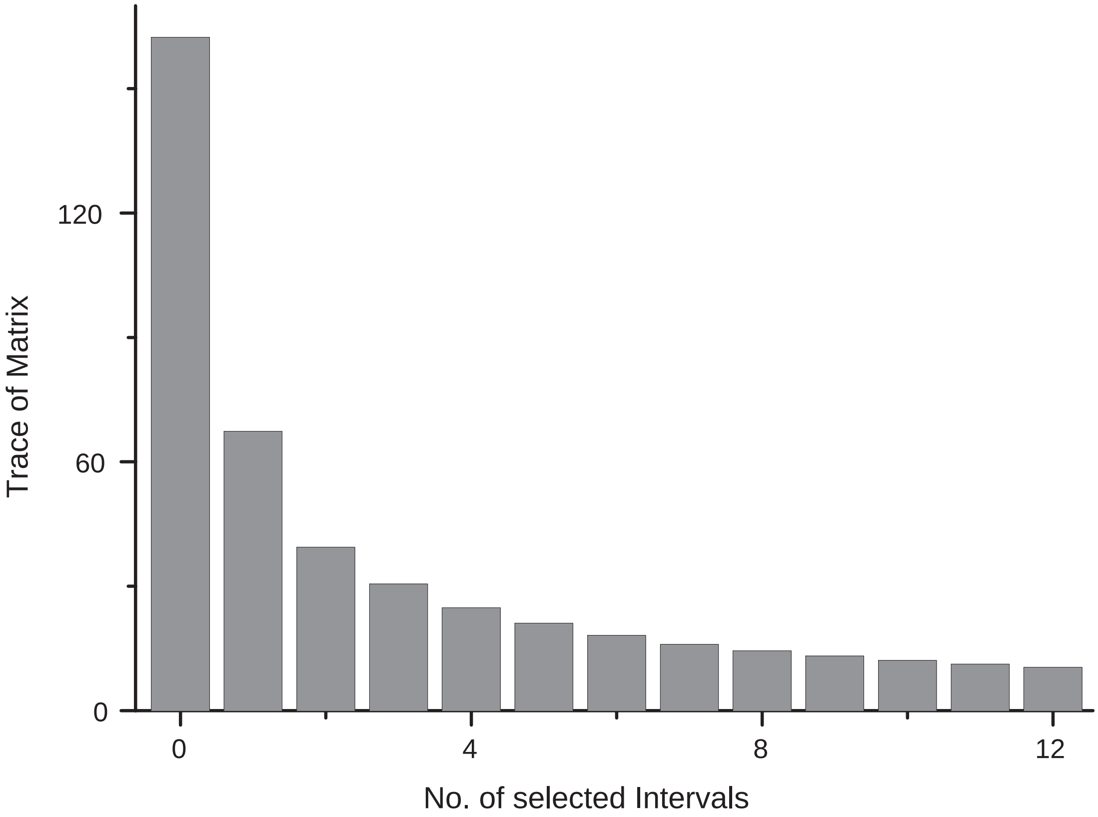

Figure 4.5: Trace of the inverse posterior covariance matrix $\hat{S}_i$ as a function of the number of selected measurement intervals. The trace is a measure for the degree of freedom for noise and seems to decrease exponentially when including more spectral intervals to the observations. The more intervals are selected, the smaller the contributions of new ones, and no further significant gain of information can be obtained after about 12 steps.

Interval Nr.	λ-range [nm]	width [nm]	lines
1	795.66 - 796.38	0.72	12
2	837.62 - 838.25	0.63	17
3	802.12 - 802.62	0.50	9
4	804.18 - 805.01	0.83	19
5	839.32 - 839.88	0.56	13
6	740.90 - 741.48	0.58	14
7	834.04 - 834.78	0.74	23
8	838.18 - 838.79	0.61	10
9	787.52 - 788.10	0.58	7
10	834.67 - 835.40	0.73	17
11	651.77 - 652.25	0.48	18
12	789.53 - 790.05	0.52	8
13	892.60 - 893.33	0.73	6
14	825.18 - 825.78	0.60	7

Table 4.1: Selected measurement intervals. The number corresponds to the iteration step in the selection algorithm.

4.3.4 Selection results: Chosen measurement intervals

The 14 intervals that were chosen in the selection process are listed in table 4.1. They correspond to the sequence of intervals decreasing the trace of the posterior covariance matrix plotted in Fig. 4.5. The spectral range as well as the number of individual lines within the spectral window (according to HITRAN96) are also tabulated. Corresponding transmission spectra calculated using a model atmosphere are plotted for all intervals along with measured spectra are plotted in section 6.3.1

For a better understanding of the selection results it is instructive to look closer at the weighting functions of the selected wavelengths. Figs. 4.6 and 4.7 show surface plots of the weighting function matrix as defined by Eq. 4.17, but with a higher resolution (50 layers of with 20 m thickness each instead of 20 layers with 50 m thickness). According to Eq. 4.17 the surface reflects the absorption features as a product of the absorption cross section $\sigma(\lambda, p, T)$ and the transmission $I(\lambda)$. It is therefore a function of the temperature and pressure profiles. The height dependence of weighting functions $K_i(h)$ for given λ_i are cognizable by the grid lines along the height-axis. These curves are a measure of the sensitivity of the intensity measurement T_i to absorber abundance in different heights.

The comparison of the two example plots reveals a generally different dependence of the weighting functions from height for the two intervals, as well as for individual transitions. The $K_i(h)$-curves for the center wavelengths $\lambda_i = \lambda_{0l}$ of the lines can well be distinguished from the line wings by following the edges of the absorption

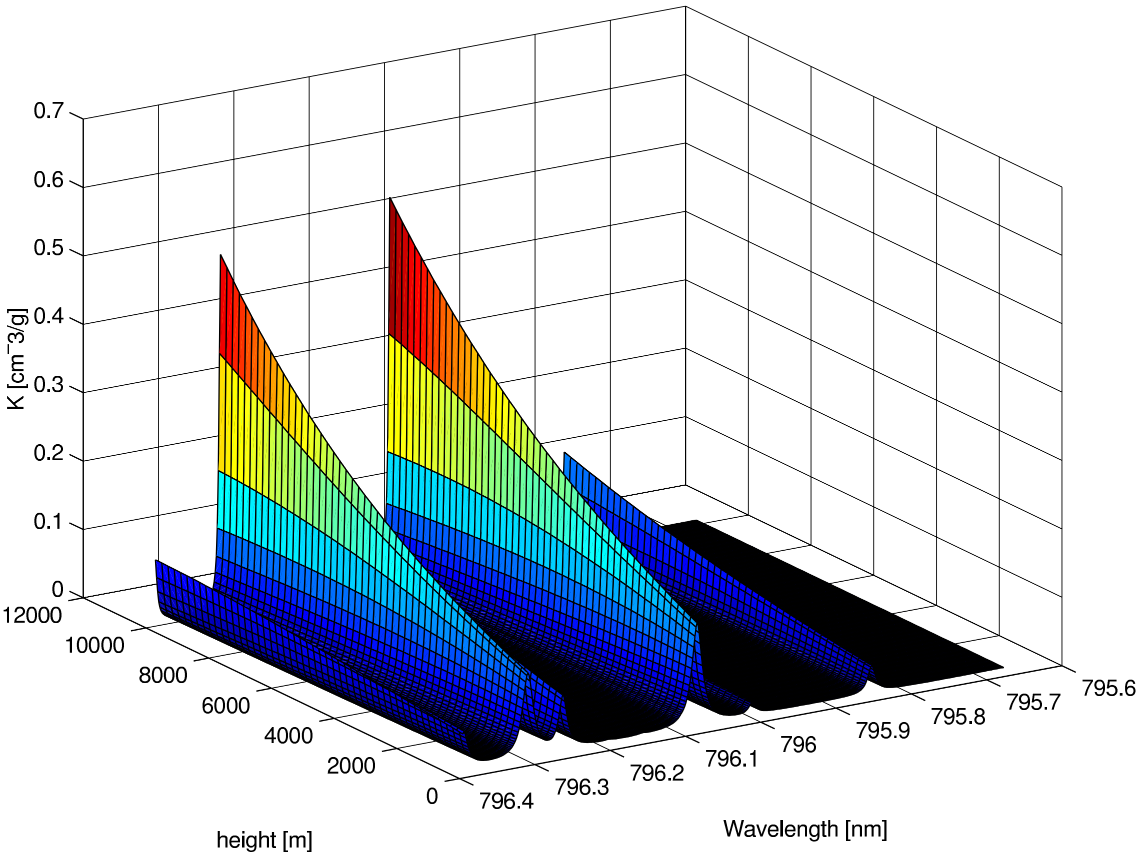

Figure 4.6: Surface plot of the weighting function matrix for the wavelength interval 795.66-796.38nm

features. They reflect the dependence of line intensity I_i from temperature, as expressed by Eq. 3.30. The different signature of these curves arises mainly from the first Boltzmann-term in Eq. 3.30, since the lower energy levels E_l'' are significantly different for the two intervals ($E'' = 920.17\ cm^{-1}$ for the strongest line in at 837.9 nm and $E'' = 134.9\ cm^{-1}$ for the line at 796.1 nm). In both intervals, however, the absolute value of the weighting function for the line center wavelengths increases with height.

Following the pressure broadened line wings along the wavelength axis it can be seen that the heights where the weighting function reach their maxima are decreasing. This is further illustrated in Fig. 4.8 and 4.9. The figures show the $K_i(h)$-profiles for seven wavelengths along the line wing of the strongest absorption with decreasing λ_i starting from the center wavelength λ_0. Figs. 4.8a and 4.9a display $K_i(h)$ in g/m^3 as defined by Eq. 4.17. In 4.8b and 4.9b the corresponding weighting functions normalized to their maxima are plotted. With increasing spectral distance from the line center position the maximum sensitivity to water vapor absorption shifts towards the ground. This is a consequence of the pressure broadening effect. The higher pressure at the ground results in a greater fraction of molecules whose energy intervals are shifted due to collisions. Therefore, by scanning the wavelengths from

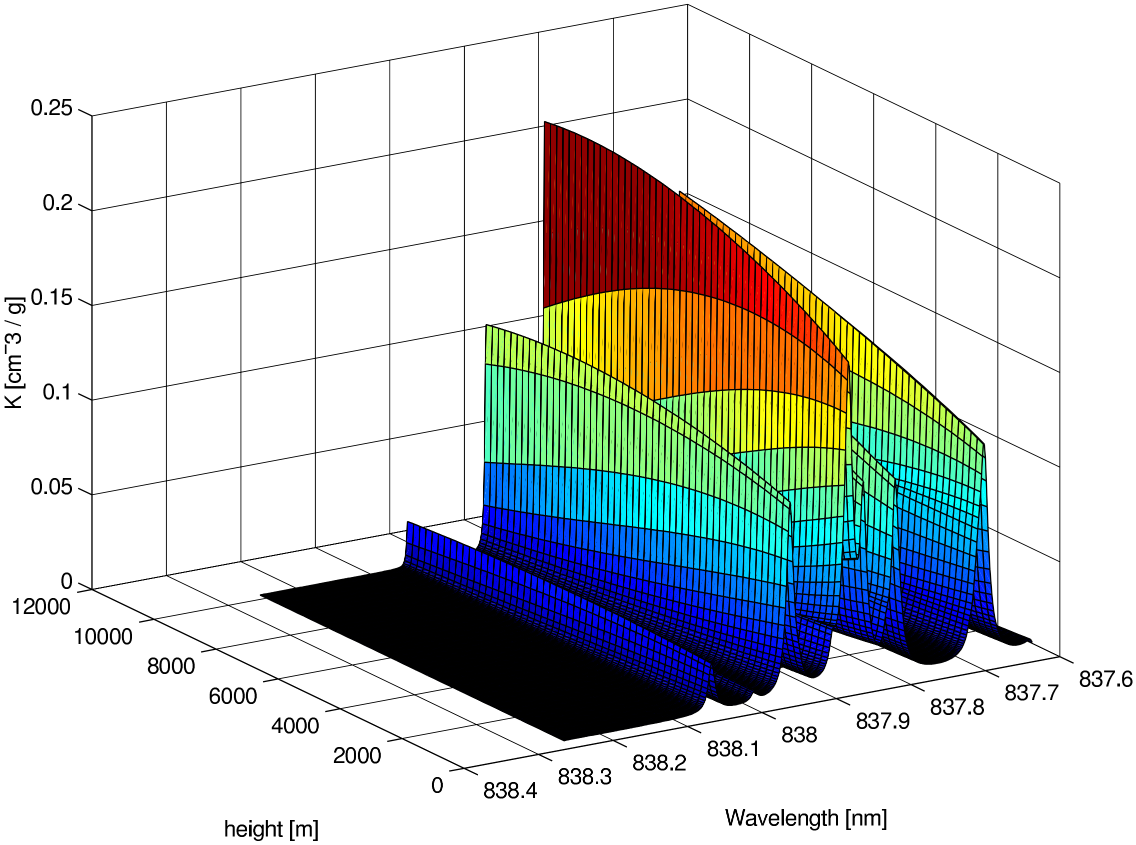

Figure 4.7: Surface plot of the weighting function matrix for the wavelength interval 837.62-838.25 nm.

the line center to the outer wing, a spectrometer is sounding through the atmosphere downwards. However, the weighting functions along the line shape display a significant overlap and their maxima are not well separated.

The strong overlap of the weighting functions indicates that vertical profile retrieval based on observations of the pressure broadened line shape alone will cause numerical problems. The fact that the temperature dependence of absorption lines also depend on the lower energy level $\acute{E}$ however might improve the situation and decorrelate the parameters describing the water vapor density profile. The feasibility of profile retrieval will be investigated in chapter 7.

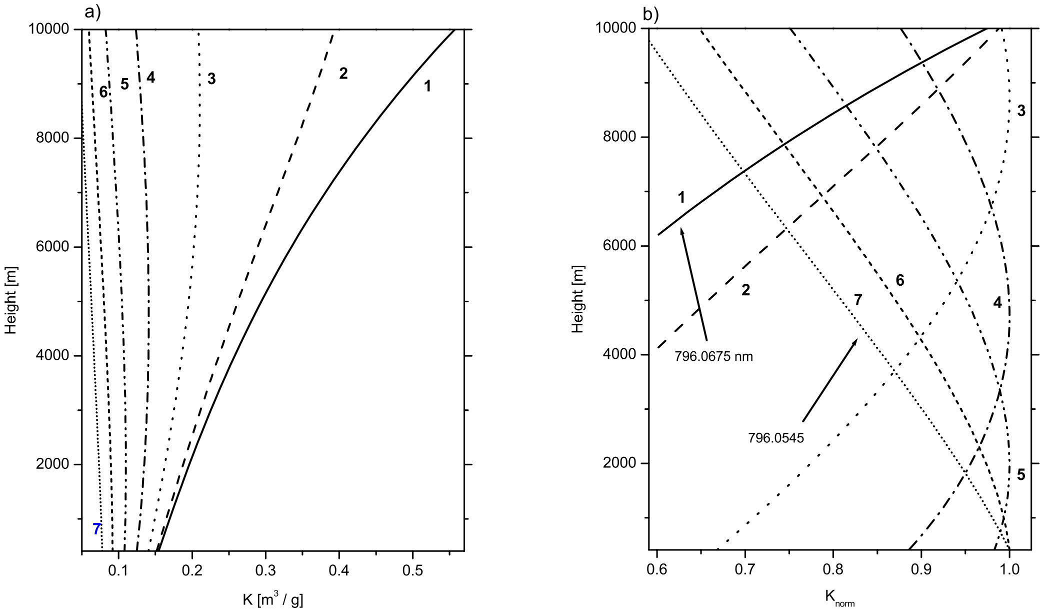

Figure 4.8: Weighting functions for 7 wavelengths along the line wing of the strongest transition of Interval Nr. 2 located at 796.0674 nm.

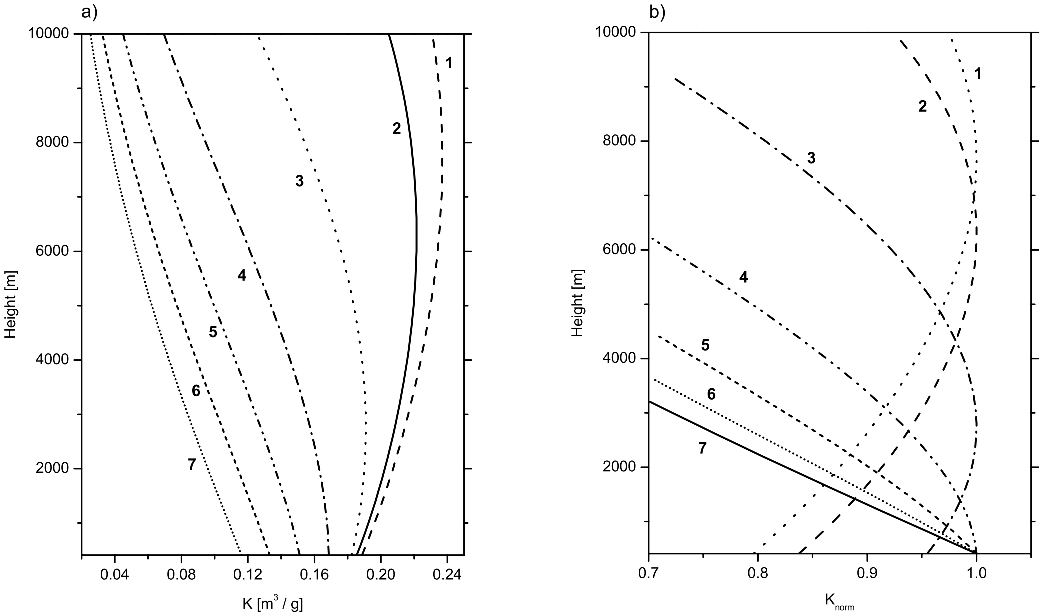

Figure 4.9: Weighting functions for 7 wavelength along the line wing of the strongest transition of Interval Nr. 1 located at 837.8666 nm.

5 Solar spectrometer development

5.1 Introduction

After the detailed description of the DOAS principle and the underlying physics of visible/NIR absorption in the troposphere, this chapter will deal with the instrumental developments performed within this study. They have been carried out in collaboration and partnership with the Institute of Spectrochemistry and Applied Spectroscopy (ISAS), Berlin. The starting point of the instrumental evolution was a prototype which was not designed for DOAS measurements, but for laboratory analysis in Atomic Absorption Spectroscopy (AAS) (Florek and Becker-Roß [1995], Heitmann et al. [1996]). The Double Echelle Monochromator (DEMON) was "misused"in a first DOAS experiment in 1994 (Sierk et al. [1997]). When the ETH-project on solar spectrometry was launched in 1997, the instrument was installed at the Geodesy and Geodynamics Laboratory (GGL) at ETH Zurich to get started with first investigations. Because of a failure in the pre-monochromator stage of the instrument, the acquired data could not be used for quantitative retrieval of precipitable water. However, the spectrometer was deployed to validate candidate spectral intervals in the line selection process. DEMON can be regarded as the predecessor of the dedicated instrument developed within this study. In order to illustrate the instrumental evolution, this prototype is described in the first section of this chapter

The product of the solar spectrometry project is a DOAS system, which is especially designed for high-resolution measurements of water vapor absorption lines using solar radiation. The system, which comprises a solar telescope with pre monochromator and an Echelle grating spectrometer was named the Solar Atmospheric MOnitoring Spectrometer (SAMOS). The telescope system was assembled at the Geodesy and Geodynamics Laboratory at ETH Zurich and will be described in section 5.3.1. The high resolution monochromator was designed and constructed by the spectrometer development group of ISAS in Berlin, which has many years of experience in developing high-resolution spectrometers. The two groups worked in close communication with each other and theoretical and instrumental aspects were investigated simultaneously and mutually. In numerical simulation studies based on the radiative transfer model outlined in chapter 3 the specifics of the the spectrometer system were determined. Since SAMOS was meant as a prototype for studying the feasibility and potential of the new technique, it was designed to fulfill the following conditions:

- The measurable spectral range should be as broad as possible to allow measurement of all individual H_2O lines in the water vapor absorption bands between 600 and 1000 nm.
- The resolution power of the instrument should be high enough to obtain several independent intensity measurements along the line shape in order to exploit the line shape information for profile retrieval.
- It should be capable of switching quickly between selected spectral intervals to be measured, even if separated by hundreds of nanometers.
- The system should be self calibrating in terms of the observable differential transmission.
- The instrument should be capable of measuring under field conditions in a fully automatic mode.

The SAMOS system, which was completed in January 1999, meets all these requirements. The construction and optical scheme are discussed in section 5.3.2. After completion of the prototype a data acquisition software was written which controls the measurement cycle and coordinates the actions of the telescope/pre monochromator system and the spectrometer device. This software is documented in section 9.1. Prior to deployment in the field, the new instrument had to be validated and the apparatus function had to be determined. This was achieved in laboratory measurements using a narrow band titan-sapphire laser, located at the Paul Scherrer Institute in Villigen, Switzerland. The results of these test measurements are reported in section 5.3.3.

5.2 The DEMON spectrometer

In Figure 5.1 the optical scheme of the Double Echelle Monochromator is shown. The instrument is subdivided into the pre monochromator stage with a rotatable prism (upper half of Fig. 5.1 and the Echelle stage with the diffraction grating (lower half of Fig. 5.1). The two components are separated by baffles and each is equipped with an own entrance slit. Two plane mirrors fold the optical path to achieve a compact mounting on a common ground plate of 480 x 280 mm. The “heart” of the spectrometer is the Echelle grating, which is schematically illustrated in 5.2. Such reflection gratings are mirror surfaces ruled with grooves, on which the light is reflected as well as diffracted at the facets of the stair-like structure. The grooves are specially shaped so as to reflect the light into a high order of interference. When the grooves are sharply defined as in Fig. 5.2, the grating is said to be strongly “blazed”. The surface has a steep and a shallow face, corresponding to the short and the long facets of the structure, with the faces being perpendicular to each other. The incoming light strikes the grating at the incidence angle α parallel to the shallow and perpendicular to the steep face. The diffracted light is observed at an angle β nearly equal to α. This condition is known as auto-collimation. Diffracted rays fulfilling the grating equation

$$g \cdot sin(\alpha(\lambda)) + sin(\beta(\lambda)) = m(\lambda) \cdot \lambda, \tag{5.1}$$

with g being the distance between the facets or grating constant, interfere constructively at the detector. The integer number m is the diffraction order. The greater the blaze angle θ_b the greater is the path difference between interfering rays and consequently the diffraction order. Since the angular dispersion $\partial\beta/\partial\lambda$ goes linear with m, as can be seen by differentiating Eq. 5.1, high resolution power can be obtained using strongly blazed Echelles. The grating utilized in the DEMON spectrometer has 75 grooves per mm and a blaze angle of 76° (manufactured by the State Optical Institute (GOI), St. Petersburg, Russia). Compared to an Echelle grating with the more usual blaze angle of 63°, the angular dispersion is increased by a factor of 2. For a more complete discussion of Echelle gratings see e.g. Davis [1970] and Thorne [1974].

The spectral bandwidth of light reaching the Echelle is determined by the pre-monochromator and the intermediate slit (see Fig. 5.1). While it is desirable that the bandwidth be wide enough to cover the entire length of the array detector, it is essential that it be sufficiently narrow to prevent different Echelle orders from overlapping. Therefore the spectral bandwidth at the entrance slit of the Echelle monochromator is limited by varying the prism angle and thereby its linear dispersion. In order to minimize aberrations, the grating is set up in a Littrow mounting with an off-axis parabolic mirror of 400 mm focal length. The orientations of the Echelle grating and the prism are scanned by computer controlled step motors. Despite the compact size of the instrument, a resolution power ($R = \lambda/\delta\lambda$ of up to 140000 is achieved. A detailed description of the DEMON spectrometer is given by Florek and Becker-Roß [1995]. For sunlight reception we used a simple refractor telescope of 30 cm focal length connected to a quartz fiber optics cable conducting the solar radiation to the spectrometer. A parallactic mount was used to track the path of the Sun.

One purpose of deploying DEMON at GGL was to test the new photodiode detector, which was foreseen for the SAMOS prototype and is therefore described in section 5.3.2. Unfortunately, the DEMON spectra could not be used to derive precipitable water vapor. This was due to a temporal instability of the measured spectra, which probably was caused by a technical failure of the pre-monochromator stage. It was suspected that the prism was not perfectly fixed and drifted on its mount, probably due to some damage caused during transportation of the instrument. The effect of a drifting pre-monochromator is a slit function moving along the wavelength scale.

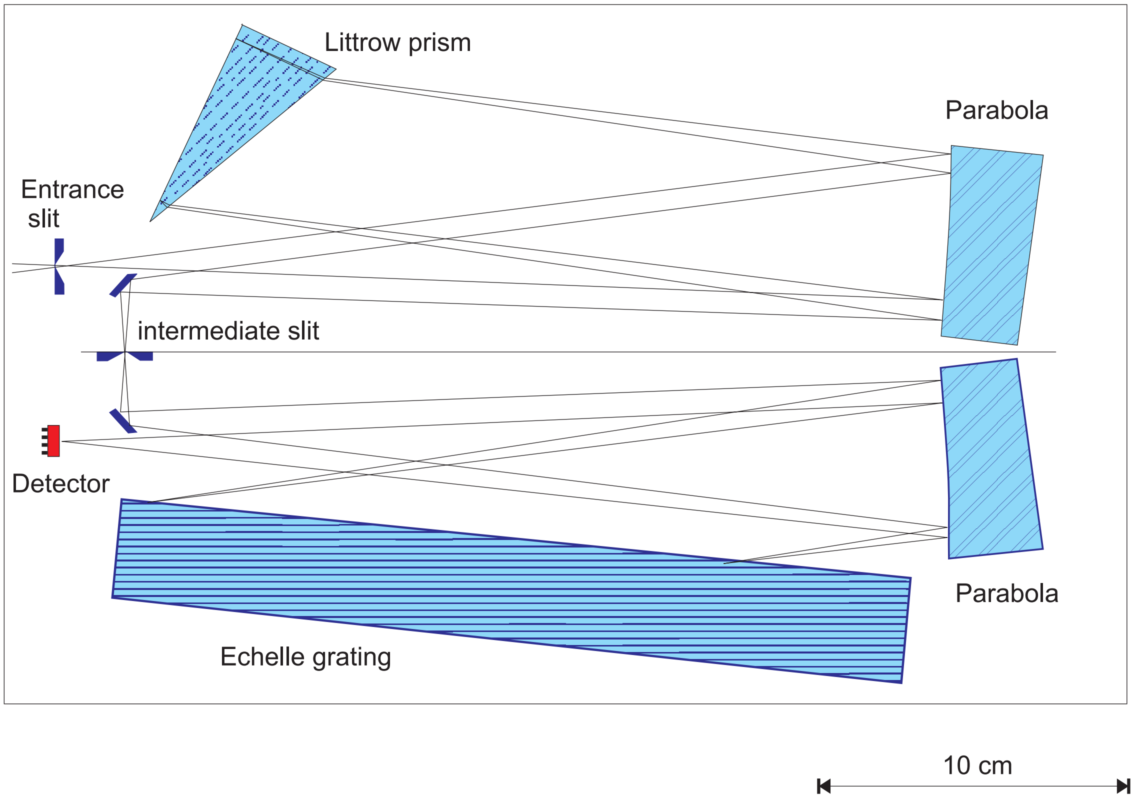

Figure 5.1: Optical scheme of the DEMON spectrometer. A wavelength interval is selected by the the pre-monochromator level above the intermediate slit to separate the diffraction orders. The Echelle level below creates the high resolution spectra.

This becomes critical as the bandwidth measured by the detector approaches the sides of the slit function with decreasing intensity. This results in a variable flatfield in a series of spectra acquired over some period.

Since the DEMON system as described above does not allow the continuous measurement of flatfield spectra, the problem of loose prism renders the solar spectra useless for quantitative analysis. This was not critical, since in the early stage of the project the purpose of deploying DEMON was to perform qualitative test measurements of possible candidate intervals for the future dedicated instrument. Therefore, instead of repairing the old spectrometer, we decided to invest the time in the development of SAMOS, which was already under way. The experience gained with the predecessor DEMON, including the technical problems encountered, turned out to be useful, as it helped to avoid these problems in the construction of SAMOS. One consequence was e.g. the decision, not to use an adjustable prism as a pre-monochromator, but to deploy narrow band interference filters (see section 5.3.1). Another conceptual consequence was the incorporation of a flatfield device to achieve a continuous self calibration of the instrument. These features were integrated into the reception unit of the SAMOS system, which is described in the subsequent section.

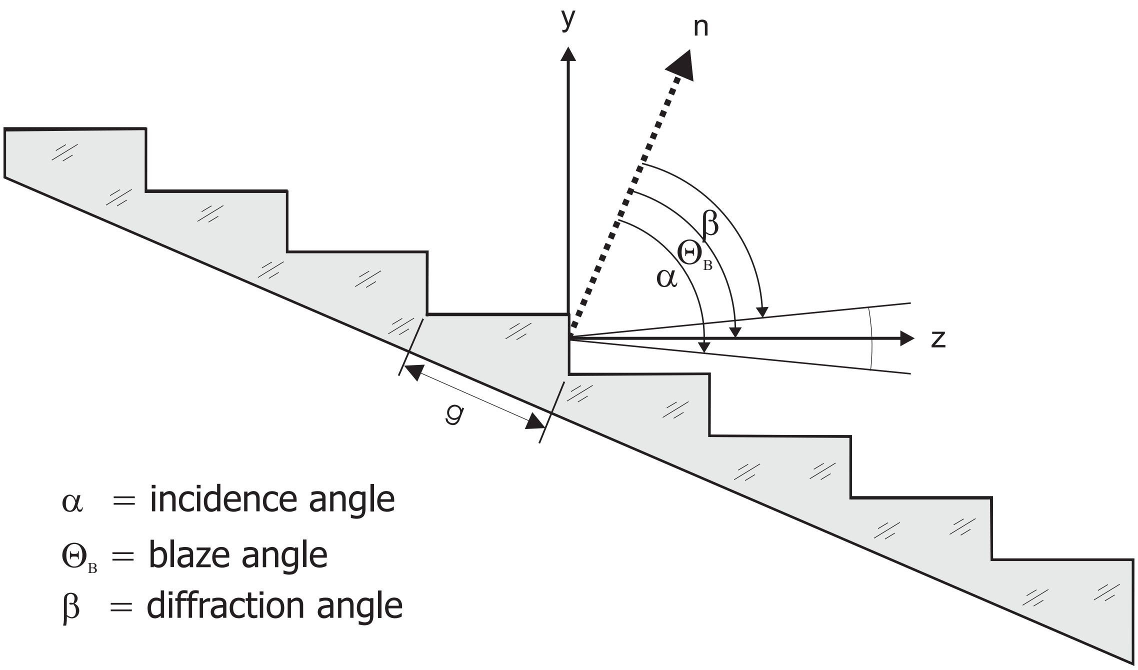

Figure 5.2: Surface structure of en Echelle grating. The light is diffracted at the small facets of the stairs. The large distances between interfering rays creates a high order diffraction spectrum of high angular dispersion.

5.3 The Solar Atmospheric MOnitoring Spectrometer

5.3.1 Solar telescope and pre-monochromator

For the DEMON-spectrometer reception of sunlight was realized by means of a small astronomical telescope on a parallactic mount. This solution has the obvious disadvantage of adjusting the axis to the celestial pole. Therefore the telescope for the SAMOS system was realized on an azimuthal mount which is adjusted to the solar position by computer controlled servo motors. The new telescope is initialized at the beginning of a SAMOS measurements, when the solar position is adjusted by the observer. The notebook computer then computes the path of the Sun from the geographical position and the system time. An alternative approach would be using a quadrant detector to follow the solar motion. Under cloudy conditions, however, the quadrant detector could not deliver motion corrections and the telescope had to be tracked "blindly". For this reason it was decided to realize a blind solar tracking utilizing the control computer. This strategy turned out to be very reliable.

The telescope including the azimuthal mount in a plastic housing is of 30 cm height and displayed in Fig. 5.3. It can be mounted onto a standard geodetic tripod. The servo motors and the mechanical drives fit onto the ground plate of the housing. The telescope itself is located behind the white disk, which can be seen on the picture. It comprises a simple condenser lense of 175 mm focal length and an aperture of 25 mm, mounted inside an aluminum block, which carries the additional components. The lens focuses the sunlight onto an optical quartz fiber with 600 μm diameter, which can be coupled to the telescope using a standard SMA-connector. The position of the connector can be moved along the optical axis using a screw for adjusting it to the focal plane of the lens.

The white disk visible in the picture, is the so called filter wheel. It carries 10 narrow band interference filters, which are used to perform the Echelle order separation (premonochromating). This solution was selected for several reasons: The first is a consequence from the the experiences made with the unstable pre-monochromator of the DEMON spectrometer. Each filter limits the spectral bandwidth to a bandpass with 10 nm half-width around the selected wavelength window to be measured. Therefore they can be fixed once they are adjusted to the corresponding center wavelength. The filter wheel is rotated to adjust the correct filter when measuring at a specific wavelength. Since no optical parts have to be moved, drift effects are avoided. It is an advantage of this approach that the filter in use can be quickly changed by turning the wheel, which allows rapid switching between different wavelength ranges and saves observation time. Furthermore the sensitivity to stray light is reduced by limiting the bandwidth of the incident light before it reaches the spectrometer system.

As already mentioned, the bandpass wavelengths transmitted by the filters have to correspond to the measurement wavelengths which have been selected before (see section 4). It is possible to obtain custom made filters which are designed for any desired wavelength in the visible and near infrared. However, we decided to use the more economical standard filters which are available in 10 nm steps and adjust them to the desired wavelength by tilting them with respect to the incidence angle of the incoming sunlight. This way it is possible to shift the filter bandpass to shorter wavelengths with increasing tilt angle. We were using this effect by mounting the filters on small metal claps, which are attached to the filter wheel through high grade steel springs. The claps can be tilted in a controlled way by adjusting a screw and therefore used to tune the filter bandpass to the desired center wavelength. Although the necessary tilt angle can be roughly calculated, it is advisable to calibrate the pre-monochromators by a low resolution spectrometer. Such a device was kindly provided by the Laboratory of Physical Chemistry (LPC), ETH Zurich. Ten interference filters with diameters of 20 mm fit on the wheel, which were used to measure the 14 selected wavelength intervals (see table 4.1) plus 4 oxygen channels. This is possible because some intervals can be measured with the same pre-monochromator. If the 10 nm-bandpass of the filter is broad enough to cover neighboring measurement intervals (e.g. intervals No. 7 and 10 in table 4.1) the center wavelength is adjusted to the median wavelength between the two neighbor intervals. The only requirement is that the bandpass still be narrow enough to prevent the neighboring diffraction orders, generated by the Echelle grating, from overlapping. An overlap would result in the presence of “ghost lines” within the spectrum - absorption lines which belong to non-suppressed diffraction orders, which are difficult to separate from “real” lines. To prevent these problems, the filter bandpass has to be narrower than the free spectral range F_λ of the Echelle grating, the interval of the spectrum that can be observed without interference or overlapping from other wavelengths in the incident radiation. It can be calculated from the following equation:

$$F_\lambda = \frac{\lambda^2}{2 \cdot g \cdot \sin(\theta_b)}. \tag{5.2}$$

Since the tilting of the filters described above has the side effect of broadening the spectral bandpass, it is necessary to verify if it is still sufficiently narrow to ensure the order separation after the fine adjustment. This could also be done with the low resolution spectrometer provided by LPC. With this instrument it was found that the bandpass was in each case sufficiently narrow, although the specifications given by the manufacturer were almost never reached.

Another detail of the telescope system visible in the photograph is the small box attached to the lower side of the tube. It is the so called flatfield box, which contains a halogen lamp and can be moved in front of the telescope by means of a servo. After the acquisition of a solar spectrum, the flatfield box is turned to the telescope and the halogen lamp is automatically switched on. The lamp serves as the calibration light source, emitting light with an intensity distribution, which can be regarded as constant for the narrow wavelength interval observed by the detector. It plays the role of a “Sun on Earth”, which shall yield the solar spectrum in the absence of the absorbing troposphere. This spectrum is then used for the normalization of the raw spectra. The procedure is described in detail in section 6.2.2. The flatfield box also houses a collimator lens system used to obtain parallel rays from the “artificial” sunlight emitted by lamp located close to the telescope objective (for light coming from the distant Sun this condition is always fulfilled). It is then conducted via optical fiber cable into the high resolution device, which is described in the next section.

5.3.2 High resolution solar spectrometer

While the telescope system described above was constructed at GGL, the spectrometer prototype whose technical features will be outlined in this section was developed at the Institute of Spectrochemistry and Applied Spectroscopy (ISAS) in Berlin, Germany. Design construction and manufacturing was carried out from June to November 1998 in the spectrometer development group by Dr. S. Florek and Dr. H. Becker-Ross. The assembly and adjustment of the instrument was begun in December and completed in early January 1999, when it was “baptized” the Solar Atmospheric MOnitoring Spectrometer (SAMOS).

Figure 5.3: Solar telescope with filter wheel and flatfield box.

SAMOS is an Echelle grating spectrograph set up in a Littrow mounting on a 1100 x 30 mm ground plate. A sketch of the instrumental layout is illustrated in Fig. 5.4. After passing the entrance slit (100 μm width) which is illuminated by the optical fiber the light beam is folded twice by two plane mirrors to reach the parabolic collimator mirror of focal length $f = 2489 mm$. The parabola focuses the light onto the Echelle grating with the extreme blaze angle of 82° and 37.5 grooves per mm. The grating can be rotated in the range of ± 4° to adjust for the wavelength desired to reach the detector. The high resolution spectrum is reflected back onto the parabola and takes the same optical path backwards, while the optical axis is slightly inclined upwards. It finally reaches the detector head which is located right above the entrance slit. [1]. The detector head (Hamamatsu C5964) is a cooled array of 1024 IR-enhanced NMOS photodiodes of 2.5 mm height and 24 μm width.

The instrumental layout of SAMOS looks simpler than the one of DEMON as a consequence of the missing pre-monochromator stage, now integrated into the telescope. Nevertheless, the more extreme grating with the exceptionally high blaze angle and the focal length of 2.5 m imposes strong requirements on the precision and stability

---

[1] "slit array" would be the better expression, as two additional entrance slits were placed on both sides of the center slit (see below and section 6.2.1)

of the optical parts and their positioning. The instrument is surrounded by a highly stable aluminum housing which is designed to absorb vibrations and distortions. A photograph of SAMOS with open housing from a “bird´s perspective” above the spectrometer is shown in Fig. 5.5 on the left hand side. The corresponding optical scheme is shown on the right.

When adjusting a specific wavelength λ one has to determine the diffraction order $m(\lambda)$ for the blaze wavelength. It can be calculated from

$$m(\lambda) = \text{integer}\Big\{\frac{2 \cdot g \cdot \sin(\theta_b)}{\lambda} + O\Big\} \tag{5.3}$$

where O is an arbitrary offset which determined the optimum range of the diffraction angle around the blaze maximum in each order. Its value was chosen to $O = 0.4$ and the grating constant (groove spacing) takes the value $g = 26.66 \mu m$ for the Echelle inside SAMOS. The angle of the diffracted ray follows from the fundamental equation 5.1:

$$\beta = \arcsin\Big(\frac{m(\lambda) \cdot \lambda}{g}\Big). \tag{5.4}$$

The linear dispersion with respect to the detector plane $\frac{dl}{d\lambda}$ is a measure for how wide the spectrum is spread about the detector plane. For the Echelle monochromator this is given by

$$\frac{dl}{d\lambda} = \frac{m(\lambda) \cdot f}{\cos(\beta(\lambda)) \cdot g}. \tag{5.5}$$

Dividing the detector pixel width (25 μm) by this quantity given in mm/nm yields the spectral bandwidth per pixel. This quantity varies between 0.37 pm (at $\lambda = 600 nm, m = 89$) and 0.90 pm (at $\lambda = 885 nm, m = 59$). The theoretical resolution power according to the Rayleigh criterion [2] is given by (e.g. Davis [1970], Thorne [1974]):

$$R(\lambda) = \frac{\lambda}{\delta\lambda} = a \cdot \frac{d\beta(\lambda)}{d\lambda}, \tag{5.6}$$

when a denotes the aperture of the dispersing element (the projection of the grating length in the direction of the diffracted ray) and $\frac{d\beta(\lambda)}{d\lambda}$ is the angular dispersion.

---

[2] The Rayleigh criterion classifies two emission lines as resolved, if the central diffraction maximum of one line falls on the first minimum of the other. See also the references cited.

For a grating spectrometer this simply the product of the diffraction order and the number of interfering apertures N, which in turn is given by the grating constant and the length L of the Echelle:

$$R(\lambda) = m(\lambda) \cdot N = \frac{m(\lambda) \cdot L}{g}, \tag{5.7}$$

with $L = 300\ mm$ and $g = 26.66\ \mu m$ for the Echelle used in SAMOS. For range of diffraction orders given above the resolution power varies from $R = 1001250$ to $R = 663750$, which is about 7 times higher than for the DEMON prototype. However, the theoretical resolution power is never reached by a real instrument. The main limitation arises from the fact, that the wave fronts of the diffracted light are not perfectly plane, which causes aberration effects. It is difficult to determine the degradation of the theoretical resolution power due to this effect, since the grating manufacturer did not provide interferograms quantifying this effect. However it can be assumed that 80 % of the values for R calculated above can be reached. The resulting resolution limits in this case range from to 0.7 to 1.6 picometers.

The equations 5.3 and 5.4 are also used to calculate the step width needed to drive the motor for adjusting the desired wavelength. This coordinate can be deduced from simple geometric considerations. If G_{lever} denotes the lever length of the grating and G_{Motor} the stepper motor increment, then the motor step width is given by:

$$Y(\lambda) = \frac{G_{Lever}}{G_{Motor}} \cdot (\theta_b - \beta(\lambda) + C \cdot (\theta_b - \beta(\lambda)^2 + Y_0, \tag{5.8}$$

where θ_b is again the blaze angle of the grating and C and Y_0 are instrumental constants. Y_0 accounts for the position of the mechanical index switches determining the zero point of the grating rotation. The value for Y_0 is determined by adjusting a known spectral emission line, which is easy to identify, onto the detector center. In our case we used the 643.84696 nm cadmium line produced by a hollow cathode lamp.

The second term in Eq. 5.8 describes the second order dependence of the difference between blaze and diffraction angle. It is possible to determine the unknown parameter C empirically by measuring a group of emission lines, whose center wavelengths are known. By plotting their position on the detector as a function of diffraction angle, the quadratic dependence becomes obvious and can be determined by a square fit. This was actually done with SAMOS, using a group of neon emission lines. The procedure is explained in section 6.2.1. The reason why these laboratory tests are not reported at this point is that the nonlinear correction was not applied when calculating the motor step width using Eq. 5.8 (which means that $C = 0$ was assumed). Instead, the second order dependence was accounted for in the pre-processing of SAMOS spectra, when the measured intensities were associated to the corresponding wavelengths (see 6.2.1).

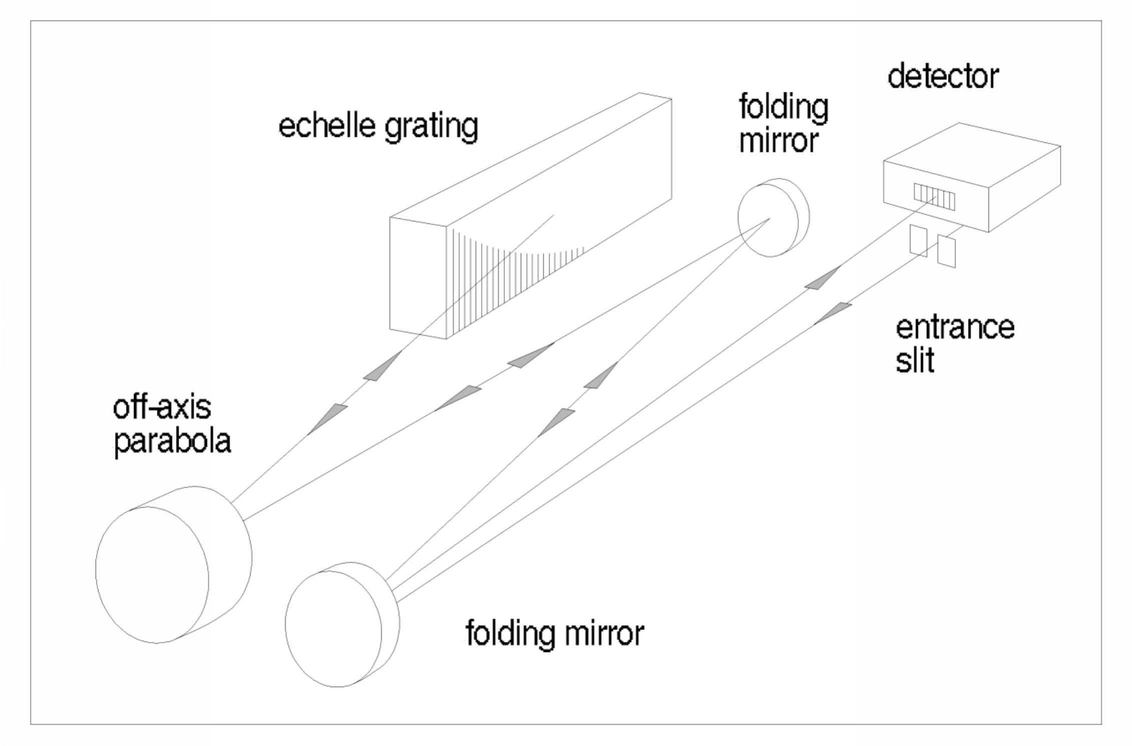

Figure 5.4: Sketch of the instrumental layout of SAMOS. The pre-monochromated light is conducted to the entrance slit and a simple mirror system with 2489 mm focal length focuses the beam on an Echelle grating with the extreme blaze angle of 82°. The high resolution spectrum is reflected back onto the cooled diode detector array, which is located above the entrance slit. Two neon lamps with additional entrance slits (not shown in this figure) are used for an absolute wavelength calibration.

Figure 5.5: Photo with a view inside the SAMOS spectrometer (left) and corresponding optical scheme (right).

5.3.3 Determination of apparatus functions using a Titan-Sapphire-Laser

An important characteristic of any spectrometer is its apparatus or instrument function, taking account the limited resolution power of a non-ideal instrument. It can be defined as the system's spectral response to an infinitely narrow emission line. This response function is used to deconvolute the measured spectra or (like in our case) to convolute the calculated transmission functions according to Eq. 3.64 in section 3.11. A theoretical apparatus function can be derived by calculating the shape of the diffracted image of the entrance slit on the detector. However, it is clear that the verification of this important instrumental quantity by independent measurements is an advantage, if not a necessity.

The most important requirement for measuring apparatus functions is an intensive monochromatic light source whose bandwidth is sufficiently narrow to be regarded as a Dirac-peak for our high resolution device. Although this is quite a demanding requirement, we found such a light source at the Laboratory for Micro- and Nanotechnology (LMN) of the Paul-Scherrer-Institut (PSI) in Villigen, Switzerland. There a tunable Titanium-sapphire ring laser (Coherent-model 899) is operated, which offers a wide tuning range with great output power. The instrument is utilized for investigating the elastical properties of crystals by NIR-Brillouin scattering Gersitz [1998]. While the spectral bandwidth of laser light emitted by such a device would still exceed the pixel bandwidth of SAMOS, the instrument operated at LMN is extended with a passively stabilized solid double etalon assembly, which reduces the lasing single frequency linewidth to approximately 30 MHz. At 800 *nm* this amounts to a bandwidth of 0.07 *pm*, which is an order of magnitude lower than the pixel bandwidth of SAMOS. The solid state laser can therefore safely be regarded as sufficiently monochromatic.

Fig. 5.6 and 5.7 show pictures of the experimental setup during the measurements with SAMOS at LMN/PSI. SAMOS is seen in the background of Fig. 5.6 the Titanium-sapphire laser is the long box the left, which is pumped by an argon laser, seen on the right. Fig. 5.7 shows how the laser light was coupled into SAMOS: After leaving the laser the beam is turned around by a mirror to pass through a perforated glass disk (white, in the center of the picture). The disk is rotated during the measurement by a small electric motor. This is done in order to destroy the coherence of the laser. This usually welcome quality of laser light is not desired for measurements with a grating spectrometer, since any stray light within the instrument would cause unwanted interference effects. The incoherent beam is finally focused on the fiber cable which conducts the radiation into SAMOS.

The wavelength of the laser line can be tuned in the range from 700 *nm* to 850 *nm*. We recorded laser spectra over this range in steps of 10 *nm*. Every adjusted laser line was then scanned over the entire detector array by stepwise rotating the Echelle grating, in order to investigate changes of the line shape under different diffraction angles. Such a detector scan of a monochromatic laser line is shown

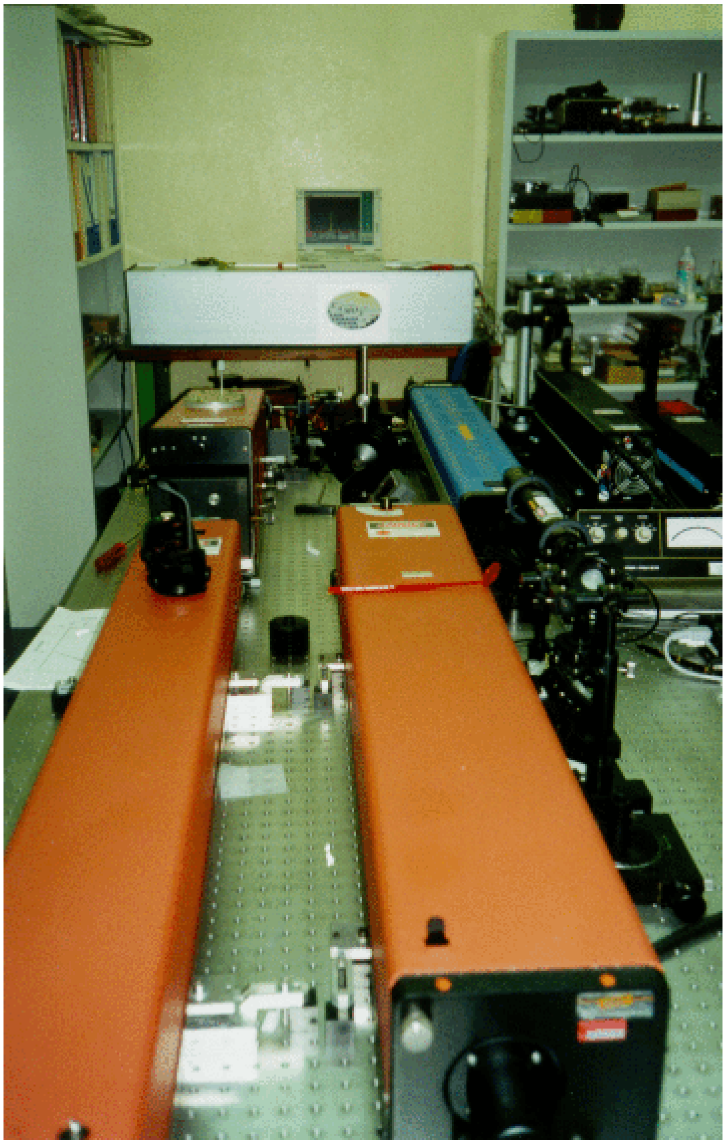

Figure 5.6: Experimental setup for laser line measurements at LMN/PSI. The Titanium-sapphire laser is seem on the left side, the box an the right is the argon pump laser. SAMOS can be seen in the background

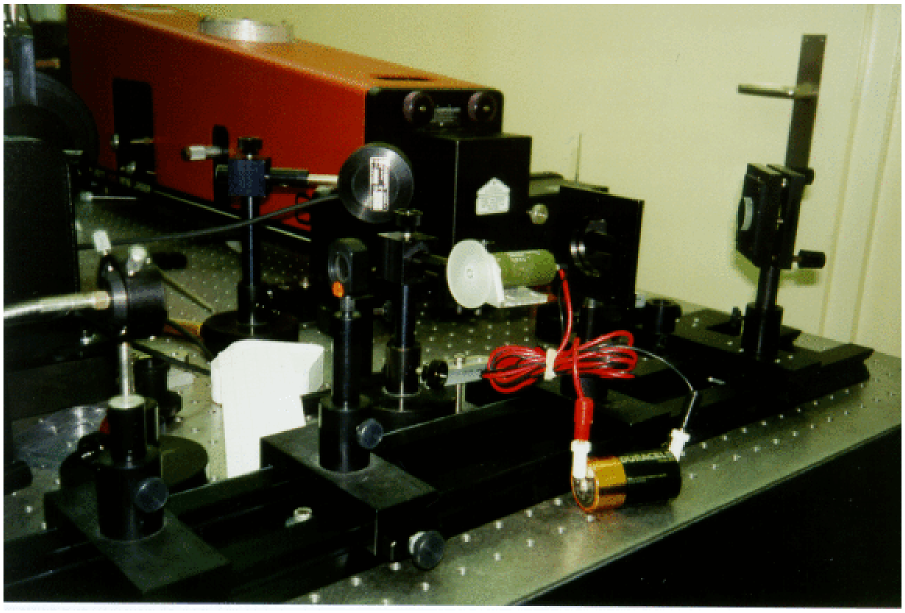

Figure 5.7: Setup for coupling the laser light into the SAMOS spectrometer. The beam is turned around by a mirror to pass through a perforated glass disk (white, in the center of the picture), which is rotated during the measurement. This destroys the unwanted coherence of the light, which is falls onto the optical fiber to be conducted to the entrance slit.

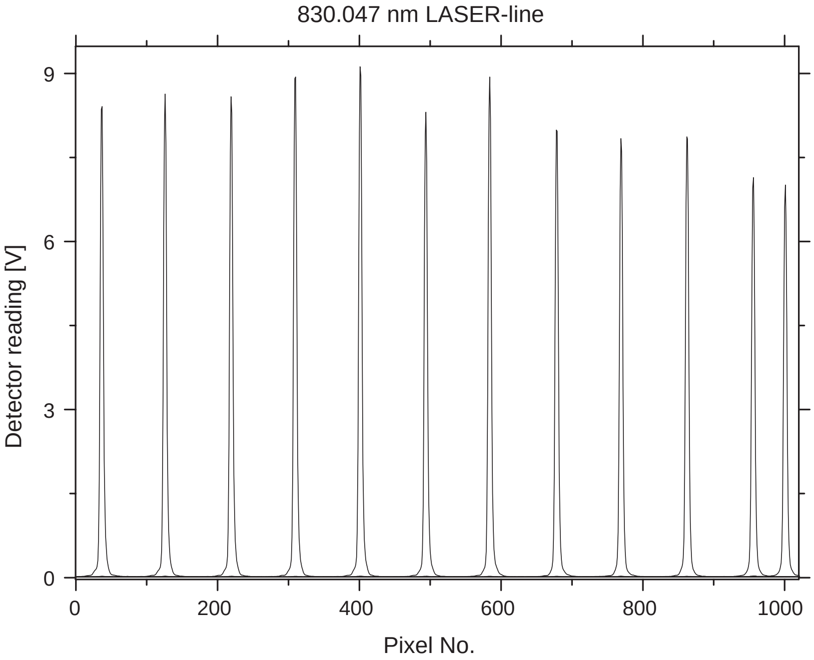

Figure 5.8: Scan of the 830.047 *nm* laser line along the detector array. The line was moved by successivly rotating the Echelle grating.

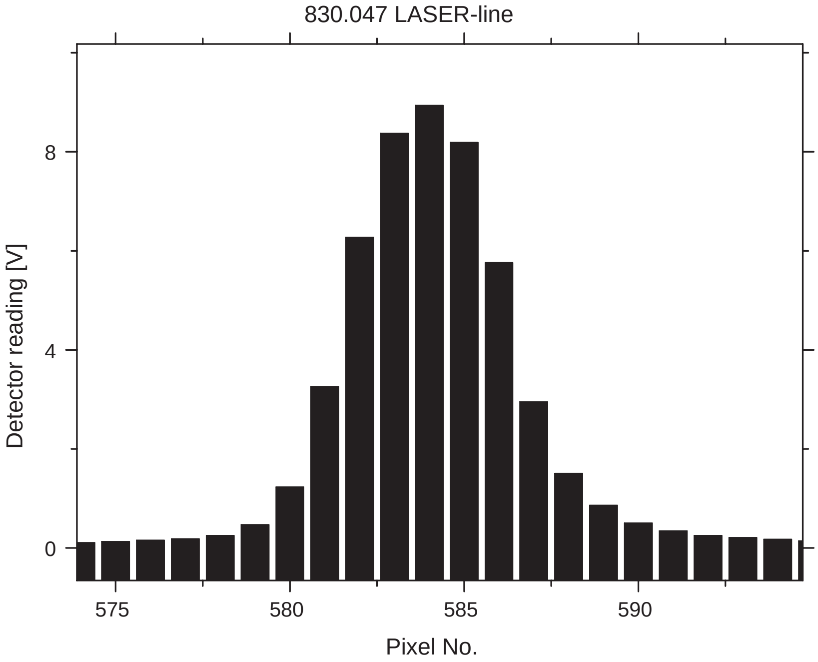

Figure 5.9: Line shape of the 830.047 *nm* laser as measured by SAMOS. This typical pattern was used as the apparatus function for the solar spectrometer.

in Fig. 5.8. It was observed that the apparatus function remained stable over all diffraction geometries and wavelengths. A typical line shape is plotted in Fig. 5.9. The halfwidth of the diffraction pattern is about 5 pixels. Given the width of 25 μm this corresponds to the expected value for an entrance slit width of 100 μm. The measured laser line shape in Fig. 5.9 was used to convolute the transmission functions calculated by the absorption model outlined in chapter 3 for the simulation and processing of SAMOS spectra.

6 Data processing algorithms

6.1 Introduction

This chapter explains and documents the concept and the algorithms developed for processing of the high-resolution solar absorption spectra acquired by SAMOS. It is subdivided into two main sections. The first part describes the pre-processing procedure, which prepares the raw data for the actual retrieval of water vapor parameters. The first task performed within the pre-processing stage is the wavelength calibration, in which each pixel of the raw spectrum is associated to its corresponding λ-value. For the SAMOS prototype a new technique for absolute wavelength calibration using neon emission lines was developed. This procedure is described in detail in subsection 6.2.1. The second step is the normalization according to the DOAS-principle outlined in section 2.5. Our strategy of baselining using flat field spectra is depicted in section 6.2.2. The second part of this chapter presents the algorithms developed to retrieve the precipitable water vapor from the pre-processed spectra using the radiative transfer model described in chapter 3. Comparisons between measured SAMOS-spectra and the modeled transmission functions revealed large discrepancies in the observed line intensities, which had to be corrected before the computation of PW time series. This procedure is documented in section 6.3. Finally, the least squares algorithm for PW retrieval is documented in section 6.4.

6.2 Pre-processing

6.2.1 Absolute wavelength calibration

The first task to be performed in the pre-processing is to associate the photodiodes of the detector array to the wavelength that corresponds to the measured photons (more strictly speaking the wavelength interval that corresponds to the window covered by the pixel width). During the acquisition of a series of spectra, the wavelength scale will not remain constant over time. Temperature fluctuations within the instrument will cause deviations of the grating and mirror positions relative to the detector. The resulting slight changes in geometry will alter the path of a monochromatic ray in the spectrometer. As a consequence, a ray of a defined wavelength might hit the detector array at a different pixel than expected. As the temperature inside the instrument changes continuously, deformation effects are likely to cause a slow-moving drift of the spectrum along the detector array.

Wavelength stabilization of high resolution spectrometers is a non-trivial task. There are several strategies to minimize or correct for the drift of the wavelength scale: One is to stabilize the instrument by operating at constant temperature. This is usually a very expendable procedure since it requires additional hardware for stabilization. For the sake of compactness of the instrument, which was designed to be mobile for field operation, it was decided not to implement such a strategy in the SAMOS prototype. Another approach is to model the influence of temperature and introduce measurements of a thermometer within the instrument. However, the temperature is not always balanced inside the spectrometer and there are some other parameters, such as humidity, air pressure and mechanical influences which can cause a wavelength shift on the detector.

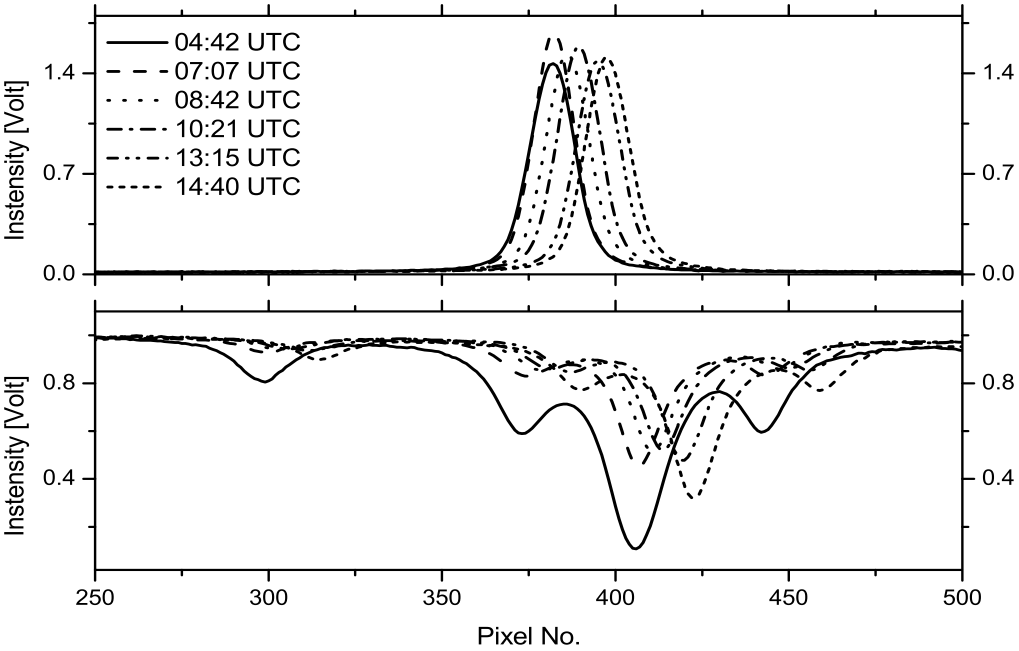

Figure 6.1: Wavelength drift of SAMOS spectra for period over 10 hours. The rightward motion of the solar spectra (upper part) is reproduced by the neon spectra (lower part) which defines the absolute wavelength scale

What is required is an absolute calibration of the wavelength scale for each measured spectrum independent from temperature information or stabilization. To achieve this goal a technique was utilized which is based on the simultaneous measurement of neon emission spectra. In Fig. 6.1 the wavelength drift, as observed during SAMOS measurements, is demonstrated. In the lower part of the figure a series of SAMOS raw spectra acquired over a period of 10 hours is plotted. It can be seen, that the spectra shift toward the right side of the detector array. The upper part of Fig. 6.1 shows the corresponding series of neon spectra, which were recorded immediately after each solar spectrum. The spectra of the well known neon line at 703.241 nm exhibit the same shifts as the solar spectra. This parallel behavior can be utilized not only to correct for the drift, but also to define an absolute wavelength scale for the entire array of detector pixels. To achieve this we exploit the property of the Echelle grating, that different diffraction orders cannot be separated. The method was first implemented in SAMOS, but is of general applicability in analytical spectrometry and has recently been patented [1]. In the following, the procedure will be described in detail.

Two neon lamps were integrated inside the SAMOS, which are alternately switched on after measurement of the solar spectrum. Their emitted light is conducted onto two additional entrance slits located on either side of the main slit used for the sunlight. The neon light containing emission peaks at well known wavelengths propagates along an optical path which is slightly shifted towards the path of the solar light beam. The ray geometry is illustrated in Fig. 6.2.

The white beam represents the optical path of a monochromatic light beam corresponding to the center wavelength of the solar measurement interval λ_{sc}. Because of the autocollimation layout of the instrument, the diffraction angle β_{sc} equals the incidence angle α_{sc} and the diffracted beam should hit the detector at pixel number $P_{sc,theo}$, approximately in the middle of the photodiode array (the calculation of the exact position of center wavelengths will be addressed below). Due to the instrumental drift the solar beam to hits the detector at pixel

$$P_{sc,meas} = P_{sc,theo} + \Delta P_{off}, \tag{6.1}$$

where ΔP_{off} is the shift offset with respect to the theoretical pixel number . It should be noted here that we use real numbers rather than integer numbers to define the pixel scale along the detector array, since the calibration procedure reaches subpixel accuracy. Therefore $P_{sc,theo}$, $P_{sc,meas}$ and ΔP_{off} are real valued quantities. The idea behind the wavelength calibration using neon light is to determine ΔP_{off} indirectly as the shift of a neon emission line along the pixel array. For this, the theoretical neon line position on the pixel scale of the detector has to be calculated and the actual line position has to be measured to determine the correction ΔP_{off}. This task would be trivial if the emission line position ν_{0n} were located within the solar wavelength interval being measured. However this would be rather coincidental and is not the case for all the wavelength intervals selected in 4.3.4. In order to enable neon corrections nonetheless, the new technique exploits the fact that Echelle gratings are unable to distinguish spectra of different diffraction orders, if the light was not pre-monochromated. Because of this, it is possible to map neon lines onto

---

[1] German Patent No.: DE-1954178

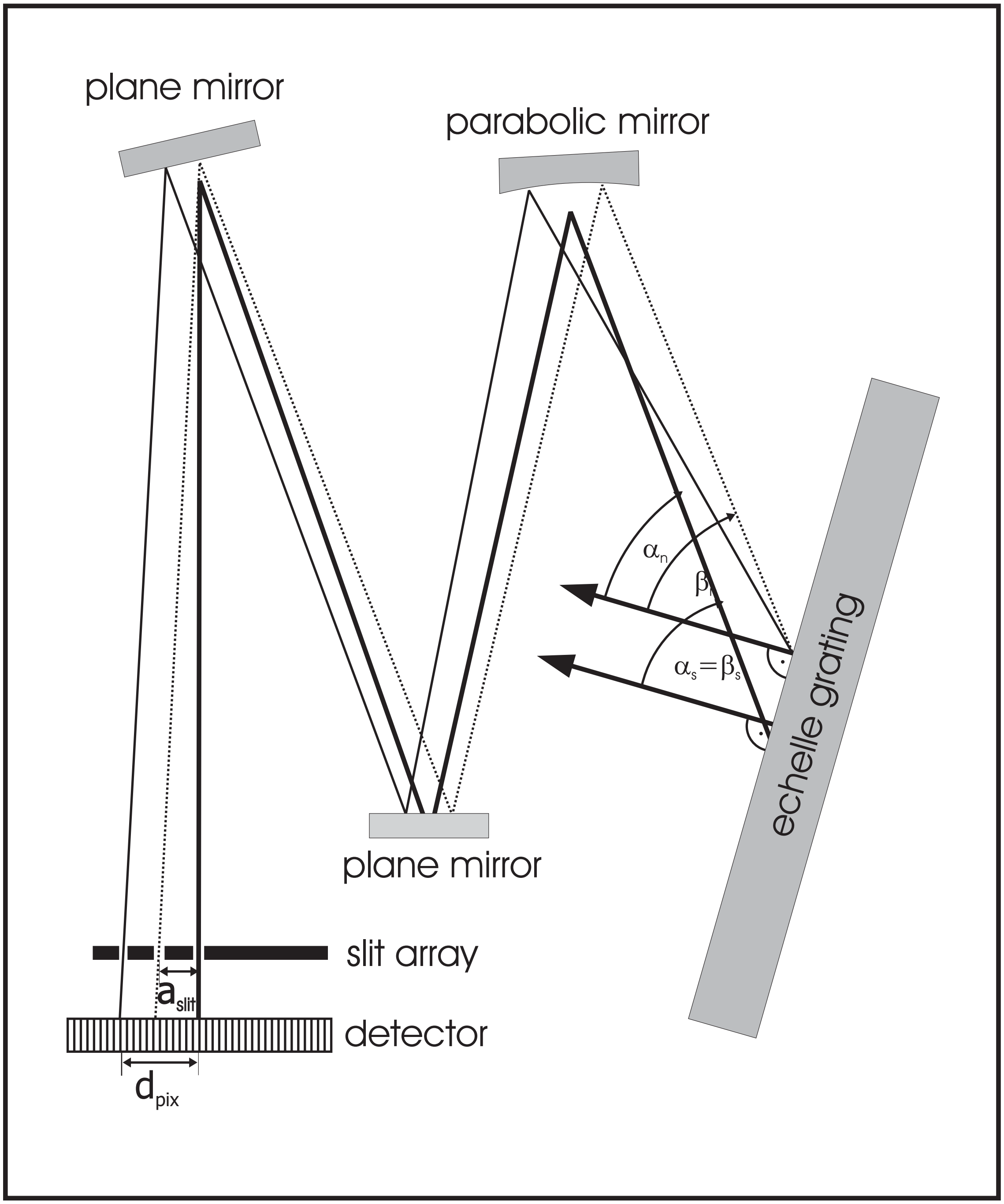

Figure 6.2: Geometry of the absolute wavelength calibration using neon lamps. The ray path of a solar light beam diffracted in autocollimation and a neon light beam entering through a shifted entrance slit are displayed. Using simple geometric relations and the grating equation, the theoretical positions of the diffracted beams on the detector array can be calculated (see text). The deviation of the measured neon line center from the theoretical position is used to correct the drift of the wavelength scale of the solar spectrum.

the detector even if the grating angle is adjusted to a wavelength of a measurement window several hundred nanometers away from the neon wavelength. The following explains how the theoretical neon line positions are calculated:

The general grating equation

$$sin(\alpha(\lambda)) + sin(\beta(\lambda)) = \frac{m(\lambda) \cdot \lambda}{g}, \tag{6.2}$$

where $m(\lambda)$ is the diffraction order and g the grating constant, is the starting point for the calculation of diffraction angles β_s and β_n for solar and neon light respectively. The diffraction order $m(\lambda)$ for the blaze wavelength can be calculated from Eq. 5.3 explained in section 5.3.2.

Because of the autocollimation condition ($\alpha_{sc} = \beta_{sc}$) the diffraction angle for the solar center wavelength becomes:

$$\beta(\lambda_{sc}) = arcsin\Big(\frac{m(\lambda_{sc}) \cdot \lambda_{sc}}{2 \cdot g}\Big). \tag{6.3}$$

The neon light enters through an entrance slit, which is laterally shifted by a distance a_{slit}. With the focal length of the spectrometer f the neon incidence angle is therefore shifted with respect to α_{sc} by

$$\Delta\alpha = \frac{a_{slit}}{f} \tag{6.4}$$

and the neon diffraction angle β_n becomes:

$$\beta(\lambda_n) = \arcsin\Big[\frac{m(\lambda_n) \cdot \lambda_n}{g} - \sin\Big(\alpha_{sc} + \frac{a_{slit}}{f}\Big)\Big] \tag{6.5}$$

Using equations 6.3 and 6.5 it is possible to calculate where the diffracted light beam intersects the detector array. Therefore the theoretical pixel positions $P_{sc,theo}$ and $P_{n,theo}$ can be determined, which detect the wavelengths λ_{sc} and λ_n, respectively. The theoretical position of the center wavelength $P_{sc,theo}$ should in principle lie in the center of the detector array. However, it depends on the instrumental parameters G_{Motor} and Y_0 defined in section 5.3.2 and exhibits a non-linear dependence from the diffraction angle (see Eq. 5.8). Therefore we empirically determined the dependence of the center pixel position $P_{sc,theo}$ from the diffraction angle given by 6.3. This was again done using neon light and the known emission line wavelengths which are tabulated in table 6.1. One of the two neon lines inside SAMOS was

Line No.	Position nm	β degrees
1	585.2488	80.972
2	616.3594	79.213
3	588.1895	78.976
4	717.3939	79.094
5	614.30623	82.126
6	659.8953	81.828
7	597.5534	80.390
8	626.6495	80.743
9	754.4046	81.956
10	692.9468	80.914
11	753.5775	81.523
12	640.2246	79.850
13	609.6163	79.424
14	594.4834	82.769
15	621.72813	82.257
16	878.0622	81.050
17	667.82764	81.581
18	650.6528	81.183
19	724.5167	82.607
20	633.4428	80.333
21	602.9997	79.624
22	703.2413	81.470
23	702.4051	81.027

Table 6.1: Neon line position and corresponding diffraction angles used for absolute wavelength calibration

connected with its fiber cable to the entrance in the middle of the detector array, which normally used for the solar light. The grating angle was successively adjusted to the neon line wavelengths according to Eq. 5.8 and spectra were acquired for all single transitions tabulated in 6.1. The positions of the neon lines on the detector were then determined by calculating the average of pixel numbers along the line shape weighted with the corresponding measured intensities:

$$P_{n,meas} = \frac{\sum_i P_i \cdot I_{ni}}{\sum_i I_{ni}}. \tag{6.6}$$

Fig. 6.3 shows the line center positions determined this way plotted against the diffraction angle defined by Eq. 6.3. Note that the subscript s in 6.3 indicating solar light does not apply for these measurements. The plot clearly shows a quadratic dependence of the pixel position from the diffraction angle. This was expected due to the residual higher order term in Eq. 5.8, which was not yet accounted for. To optimize our model for the center pixel position, we performed a quadratic fit, indicated by the straight line in Fig. 6.3 and used the coefficients for the calculation of $P_{sc,theo}$:

$$P_{sc,theo} = a_0 + a_1 \cdot \beta(\lambda_{sc}) + a_2 \cdot \beta^2(\lambda_{sc}) \tag{6.7}$$

where the coefficients were found to be a_0 = -13001, a_1 = 18872.1, and a_2 = -6595.09.

After the optimization of the model for $P_{sc,theo}$ we return to the problem of calculating the positions of neon lines, whose light passes through the entrance slits at either side of the solar slit. If d_{pix} denotes the pixel width, which is 25μm for our detector array, the theoretical pixel position of the neon emission line with respect to $P_{sc,theo}$ is

$$P_{n,theo} = P_{sc,theo} + \Big(\alpha_{sc}(\lambda_{sc}) - \beta_n(\lambda_n)\Big) \cdot \frac{f}{d_{pix}}. \tag{6.8}$$

Using simple geometric relations and the grating equation the theoretical pixel numbers detecting λ_{sc} and λ_n have now been calculated. The remaining job is to determine the deviations between $P_{n,theo}$ and the measured neon emission line center $P_{n,meas}$. The latter is again determined as the weighted average defined by Eq.6.6. The difference $P_{n,theo} - P_{n,meas}$ then yields the desired correction shift ΔP_{off}, which is applied in 6.1. Therefore by observing neon spectra along with each solar spectrum, we determine the pixel position $P_{sc,meas}$, where light of wavelength λ_{sc} is detected.

At this point there are two possibilities to finally determine a stable wavelength scale: One way is to correct the grating angle in such a way that the solar center

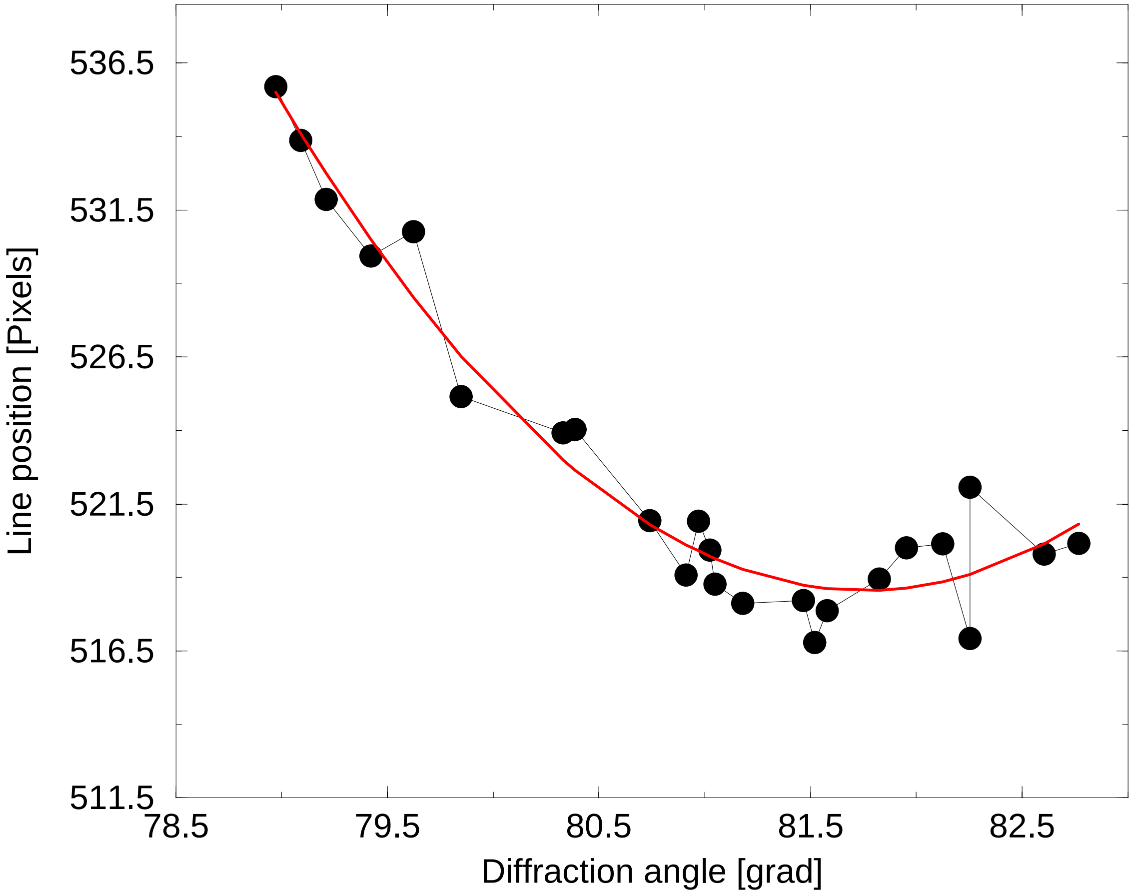

Figure 6.3: Pixel positions of neon lines measured through the center slit as a function of diffraction angle. A quadratic dependence from $\beta(\lambda_{0n})$ is clearly visible. The straight line represents the quadratic fit.

wavelength λ_{sc} really intersects the detector at the theoretically expected position $P_{n,theo}$. This strategy would require an additional movement of the grating every time a solar spectrum is measured. In order to save observation time, we chose a different way for the SAMOS prototype: We allow the observation window to drift along the pixel scale and determine the corresponding wavelength scale "offline" in the pre-processing procedure. For this, the diffraction angle of the solar light beam detected by the i-th pixel is determined geometrically as an offset from the center wavelength diffraction angle $\beta_{sc} = \alpha_{sc}$:

$$\beta_{si} = \beta_{sc} + \frac{P_{si} - (P_{sc,theo} + \Delta P_{off}) \cdot d_{pix}}{f}. \tag{6.9}$$

The grating equation 6.2 finally yields the wavelength λ_{si} associated to the i-th pixel of the solar spectrum P_{si}:

$$\lambda_{si} = \frac{g}{m(\lambda_{sc})} \cdot \big(sin(\alpha_{sc}) + sin(\beta_{si})\big). \tag{6.10}$$

The procedure described above works for a single entrance slit for neon light. The reason that two such additional slits left and right of the center slit were installed was to increase the probability of imaging neon lines onto the detector for all selected measurement intervals. It is possible that for an individual measurement window and a given entrance slit (e.g. the left one) there is no neon emission line diffracted within the range of angles under which rays intersect the detector array. In this case the other entrance slit can be used and even adjusted (by shifting it with respect to the center slit) to force the emission line onto the detector.

It is obvious that for the wavelength scale definition outlined above the lateral distances a_{slit} of the entrance slits with respect to the the center slit must be precisely determined (see Eq. 6.5). This was also achieved by spectroscopic measurements: Neon spectra were recorded for every single emission line listed in table 6.1, using all three entrance slits (including the solar slit in the center of the slit array). Fig. 6.4 shows three neon spectra acquired with the same grating position but each corresponding to a different illuminated entrance slit. As can be seen from the figure, the emission line adjusted to be imaged onto the middle of the detector array using the center slit occurs at the left and right edge of the array, when the right and left entrance slits are used, respectively, although with different intensity (this is partly because different lamps were used as light sources for each spectrum). The pixel difference is a function of the incidence angle offset determined by the slit offset towards the center slit (see Eq. 6.5). By measuring the line center positions for the left, right and center slit spectra and forming their differences, it is possible to determine the left and right slit offsets. This was practically performed by a least squares adjustment of the lateral distances a_{slit} to the model defined by Eq. 6.3 -

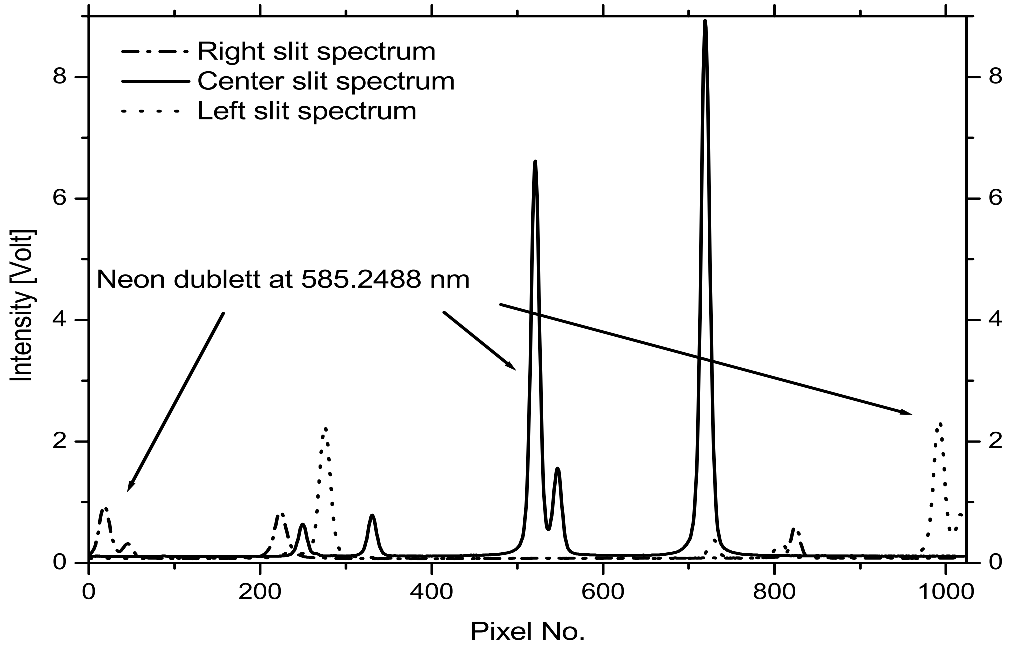

Figure 6.4: Three measured neon spectra using the different entrance slits. The double line at 585.2488 *nm* appears at different pixel positions due to the incidence angle offsets. From the differences of line center position the lateral slit distances can be calculated.

6.8. This procedure yielded values slit distances of 12.88 *mm* for the right and 11.52 *mm* for the left entrance slit with respect to the solar entrance slit in the center.

The accuracy of the wavelength calibration is estimated to better than 1/20 of a pixel width (approx 0.04 *pm* for a bandwidth of 0.7 *pm* per pixel). The technique has been incorporated with slight modifications into several spectrometer prototypes developed at ISAS (Becker-Ross et al. [2000]).

6.2.2 Normalization of solar spectra

As explained in section 2.5 the basis of the DOAS technique is the elimination of broad band attenuation effects by a normalization with respect to a reference interval within a high resolution spectrum. The presence of an appropriate reference interval within the spectral window of a simulated SAMOS spectrum was a criterion for the selection of wavelength intervals to be measured (see 4.3.1). However, the approach of interpolating spectral regions at one or both sides of an absorption line, as outlined in 2.5 is only feasible if attenuation features due to instrumental effects are neglectable (i.e. their wavelength dependence is broad band). For a non-perfect spectrometer such an assumption is rarely justified. In the case of the SAMOS prototype, instrumental effects influencing the intensity distribution of a measured spectrum should be expected. The first source of error is stray light, which is generated wherever radiation is reflected (mirrors and grating) or diffracted (entrance slit, grating). Although considerable care was taken to minimize these effects by a system of baffles, it is inevitable that a certain fraction of stray light will reach the detector. Another, probably more serious problem are interferences that might occur at the detector itself. The array of photodiodes of 25 μm width may act as additional diffraction grating attenuating a fraction of radiation at frequencies with destructive interference. A feasible normalization strategy should be capable to eliminate spectral features created by instrumental effects. The concept of using flatfield spectra, which was realized in this study is outlined in the subsequent sections.

6.2.2.1 Instrumental effects and flatfield spectra

A look at some raw spectra measured by SAMOS, which are plotted in Fig. 6.5 confirmed the expectations for instrumental imperfections. The spectra exhibit strong periodic structures in the baseline intervals and which should normally show a flat intensity distribution. In some cases it is difficult to separate the absorption lines from the structures in the baseline interval.

The plots demonstrate the necessity of a normalization procedure that removes the instrumental effects from the raw spectra. This can be relatively easily performed by using the flatfield spectrum of the halogen lamp attached to the telescope (see 5.3.1). The lamp emits a constant wavelength-independent light intensity over a narrow spectral interval. In this sense, its role can be expressed as the “Sun on Earth”, since the ideal flatfield source would be the original radiation source in absence of the absorbing medium.

A perfect spectrometer would measure a flat spectrum and the structures of the real flatfield measurement identify and quantify the influences of instrumental imperfections. Fig. 6.6 displays various flatfield spectra for different wavelength intervals.

Although periodic features can be observed in all measurement windows, the series also shows that the actual shape of the curves are quite different. This implies the necessity to measure flatfield spectra for each wavelength window. Moreover, the periodic features are also time-dependent, which is demonstrated by fig. 6.7. The two halogen spectra measured at the same wavelength interval at two different times reveals a temporal variation of the flatfield. It becomes obvious, that the measurement of a halogen lamp spectrum has to be performed for each solar spectrum. The main disadvantage of this consequence is the longer time required for measuring a pair of corresponding solar and flatfield spectra. The significance of this loss of time depends on the exposure time needed to measure a flatfield. It is clear that it should be considerably higher than for the solar spectrum, since the solar radiation is more intense by several orders of magnitude. The flatfield exposure time, which can be adjusted at the front panel of the data acquisition software (see appendix 9.1), is a

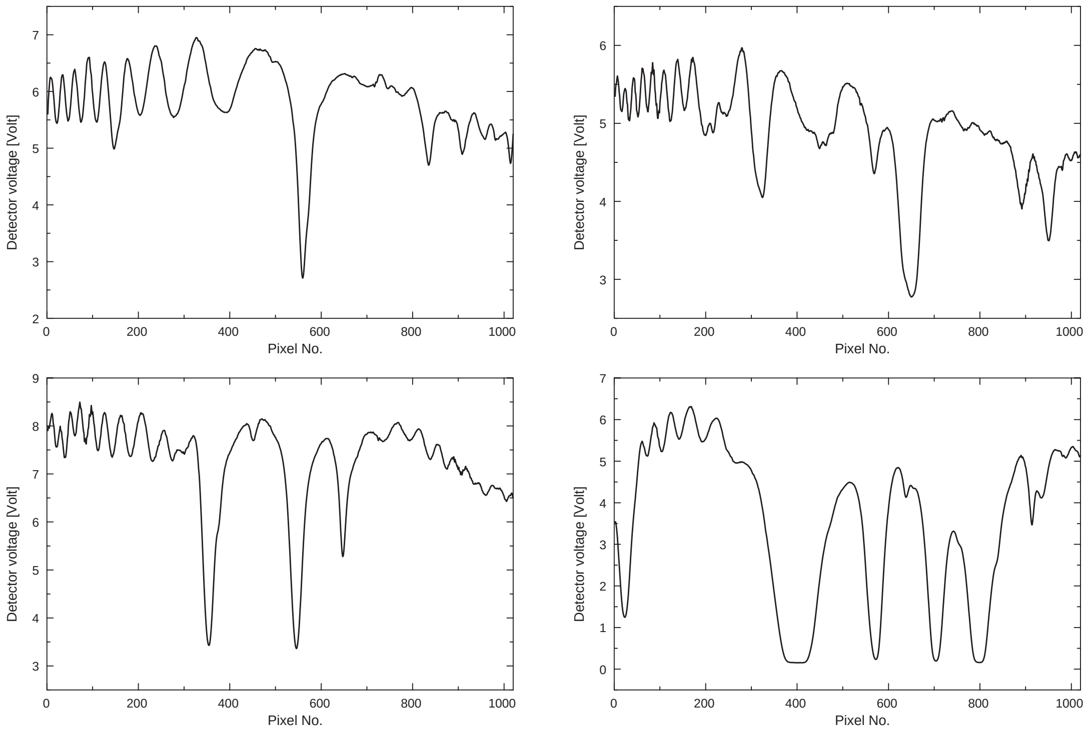

Figure 6.5: SAMOS solar raw spectra measured at different wavelength intervals. Water vapor absorption lines are superposed with periodic features caused by spectrometer imperfections. The two components are separated by means of halogen lamp spectra.

compromise between the acquisition time and the signal to noise (S/N) ratio. The spectra in Fig. 6.7 have been measured with an exposure time of 45 seconds. The maximum value of the detector reading does not exceed 1 Volt. Comparison with the solar spectra of fig. 6.5, which have been acquired within 3-6 seconds close to detector saturation (10 Volt), gives an impression of the large differences in S/N ratio. As a rule of thumb, it takes ten times longer to acquire a flatfield spectrum with a six times worse S/N ratio compared to a solar spectrum. It is obvious that this difference has to be taken into account in the normalization procedure. Another fact is that the flatfield calibration consumes about 90 % of the actual measurement time. This might seem like a limiting factor of the spectrometric method, but considering the relatively slow dynamic behavior of the troposphere, the obtainable time resolution is still high. Under clear conditions, a flatfield- solar spectrum pair takes about one minute to be measured, including the time to measure the neon and the dark current spectrum. For most applications, time series of PW with one minute time resolution are more than sufficient. A scan of all 15 selected measurement intervals, needed for the estimation of a humidity and/or temperature profile requires about 20 minutes.

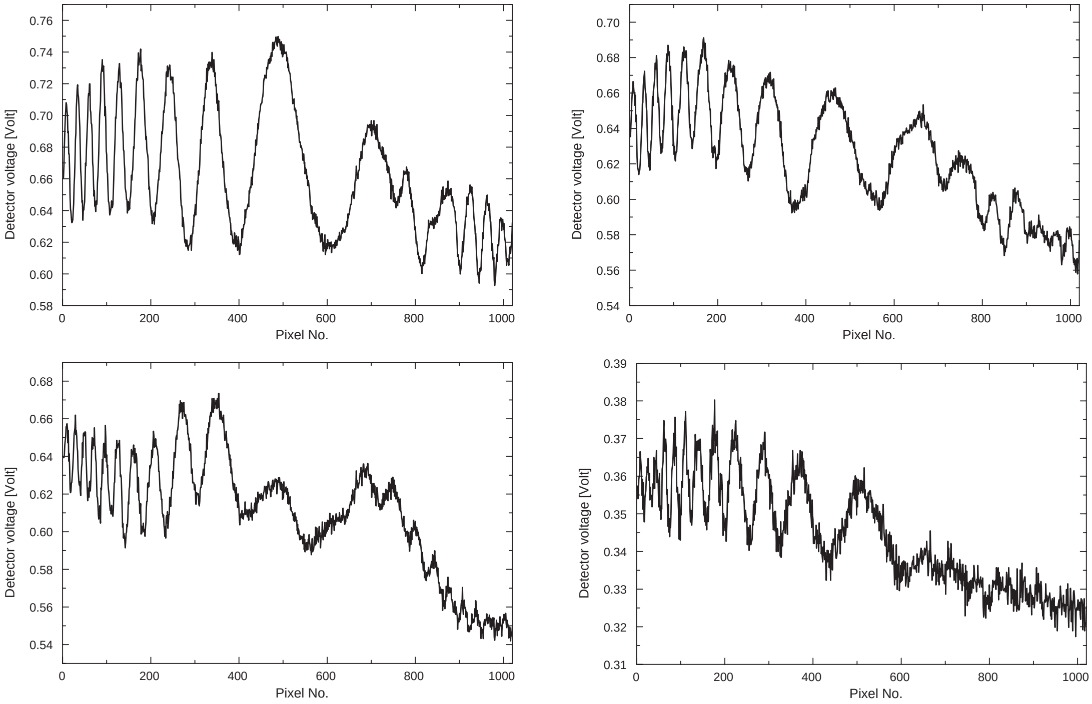

Figure 6.6: SAMOS flatfield raw spectra measured at different wavelength intervals. The periodic structures are different for each measured wavelength window. Therefore flatfield have to be acquired for each selected wavelength

6.2.2.2 Normalization procedure

As mentioned in the previous section a difficulty in normalizing a solar spectrum using the flatfield arises from the large differences in their intensities and S/N ratios. The flatfield spectrum measured has to be modified to represent the differential intensity level I_0', simulating the solar spectrum in the absence of absorbing molecules. The simplest approach is to lift up the flatfield in such a way that the intensities measured in the selected reference interval in both spectra match. This “lifting” by simple multiplication of the entire spectrum with the factor R simulates a flatfield measurement with R-times longer exposure time. The constant R could be calculated as the ratio of the average intensity values of solar spectrum and flatfield within the baseline interval, which begins at pixel b_a and ends at pixel b_e:

$$R = \frac{1}{b_e - b_a} \cdot \sum_{i=b_a}^{b_e} \frac{V_{sun,i}}{V_{flat,i}}, \tag{6.11}$$

where the subscripts sun and $flat$ denote the measured intensities of the solar and the flatfield spectrum, respectively. The differential absorption spectrum is simply calculated as the ratio of the measured voltages of the solar raw spectrum and the uplifted flatfield:

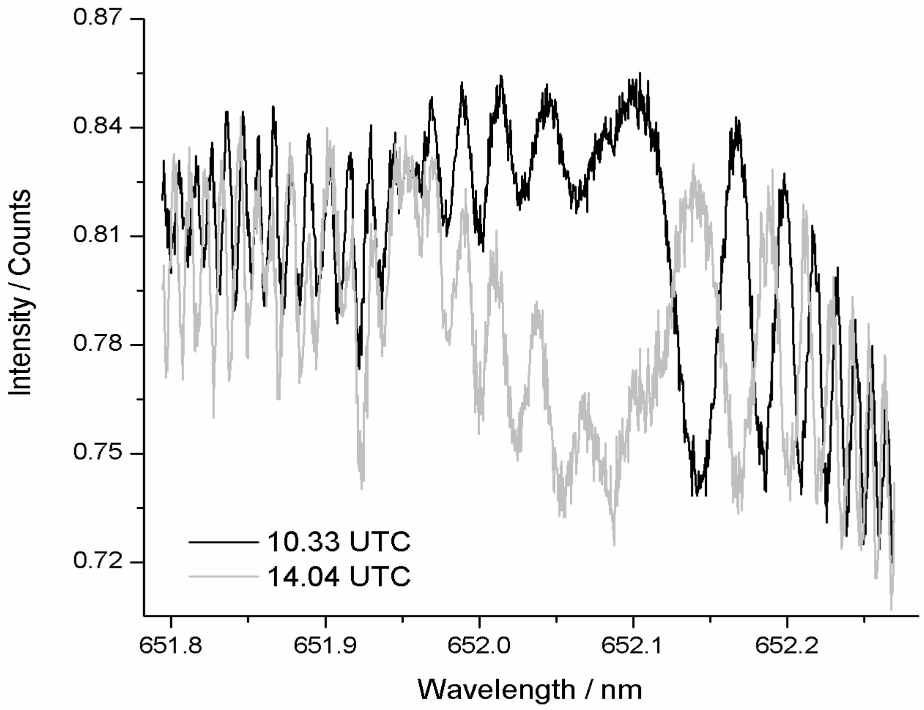

Figure 6.7: Temporal variation of flatfield spectra. The two halogen spectra were measured at the 652 nm interval, with a time lag of 3.5 hours. The temporal variation implies that a halogen lamp spectrum has to be measured for each solar spectrum.

$$I'_i = R \cdot \frac{V_{flat,i}}{I_{sun,i}}, \tag{6.12}$$

with the index i now running over the entire pixel array.

Unfortunately, multiplying the un-smoothed flatfield would also increase the high noise level of the flatfield measurement and propagate the error directly to the normalized spectrum. For this reason it is advisable to smooth the flatfield before its usage in 6.12. Looking at figures 6.6 it seems possible to distinguish the low frequency periodic structures from the superposed white noise. For this purpose an adjacent polynomial filter was applied, fitting a polynomial of adjustable degree (usually 5) in a gliding window of data and replacing the measured voltage by the function value of the estimated polynomial.

The performance of the smoothing is shown in figures 6.8, where a flatfield is plotted before and after smoothing. The smoothed flatfield is regarded as the "best guess" of a solar spectrum in absence of the troposphere and is used for the normalization

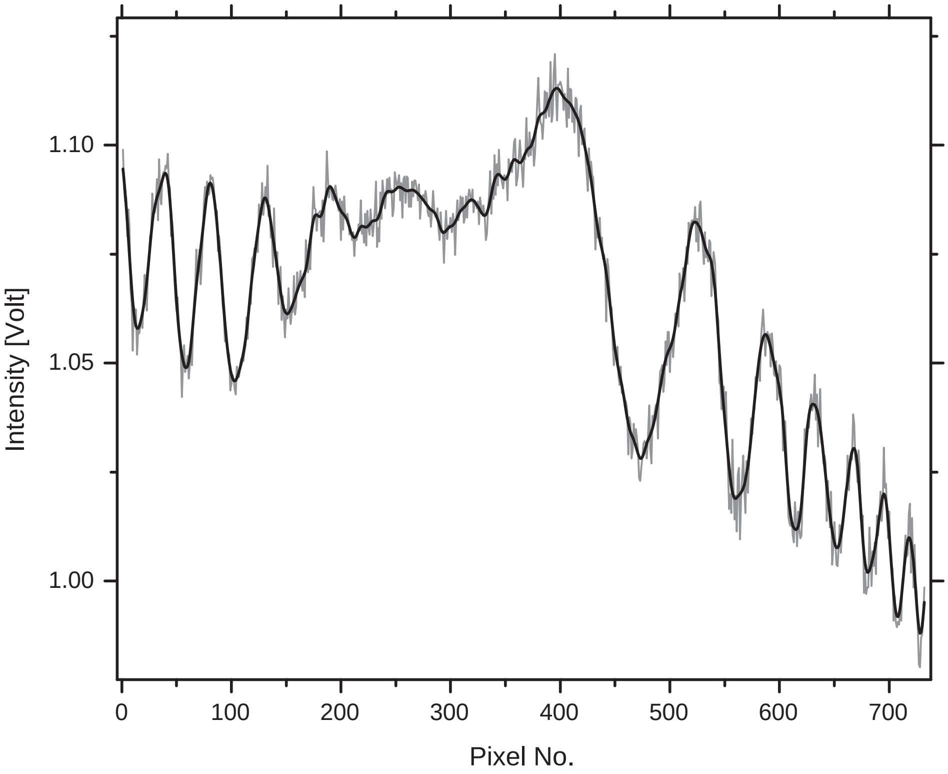

Figure 6.8: Smoothing of the flatfield by adjacent polynomial filtering. The smoothing is performed in order to prevent the high flatfield S/N ratio from propagating into the differential absorption spectrum.

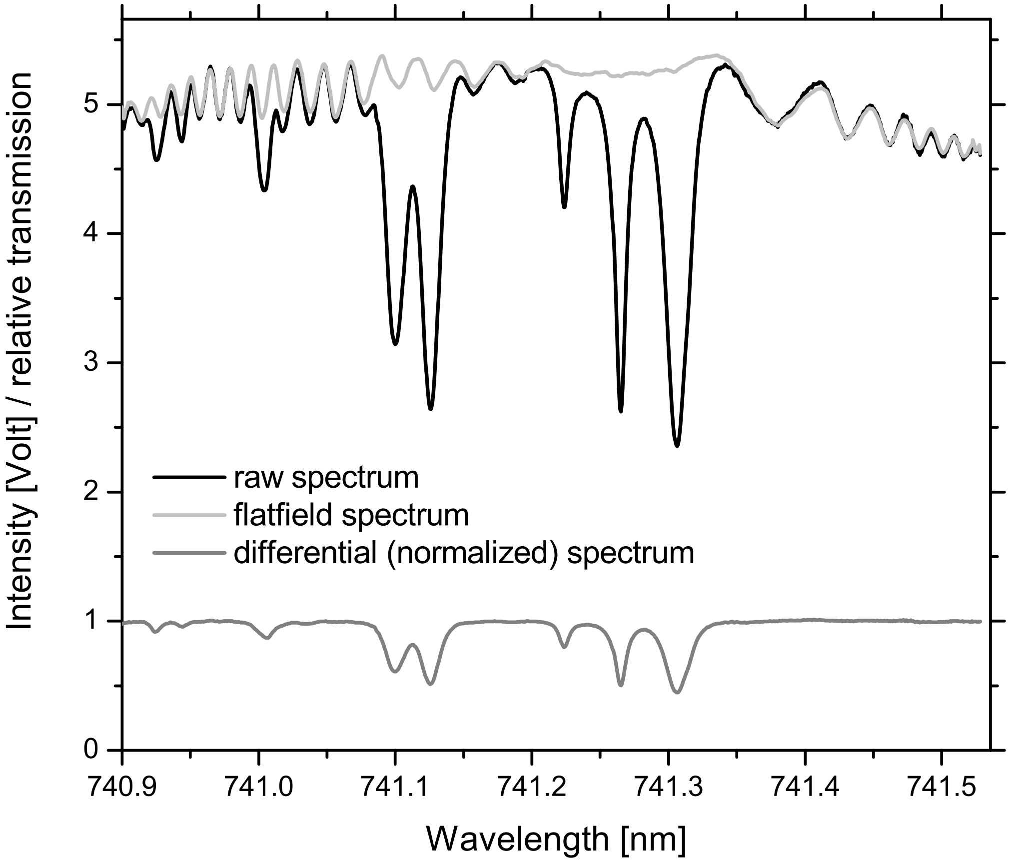

Figure 6.9: Normalization procedure using uplifted smoothed flatfield spectra. The flatfield spectrum is smoothed and lifted up to the intensity level of the spectral region, where line absorption can be neglected (left and right end of measured spectrum). The ratio of these spectra yields the normalized differential solar spectrum which is further processed to retrieve the precipitable water vapor.

following Eq. 6.12. Fig. 6.9 shows the uplifted and smoothed halogen lamp spectrum together with the solar and the resulting normalized spectrum. Note that the units for the flatfield and the raw solar spectrum are given in volts, whereas the result of the normalization is a dimensionless differential transmission spectrum, giving the fraction of light transmitted through the atmosphere.

In this example of a spectrum centered at 741.2 nm it can be seen that solar and flatfield spectrum match each other quite well in the reference interval at the low wavelength side. The normalized, differential spectrum computed using Eq. 6.12 is plotted again as the solid grey line in Fig. 6.10. The plot reveals residual structures which have not been removed. While the normalization yields a satisfactory flat baseline interval on the longer wavelength side of the spectrum, the short wavelength side to the left still exhibits periodic variations in the transmission. The situation is even worse for other wavelength intervals. Fig. 6.11 shows the normalization result for a solar spectrum centered at 837.9 nm. Periodic features are visible in the baseline interval. A possible reason for this could be the presence of additional contributions to the measured intensities of either the flatfield or the solar spectrum or both. Such contributions are likely to arise from stray light effects within the spectrometer, that might be different for the individual wavelength intervals.

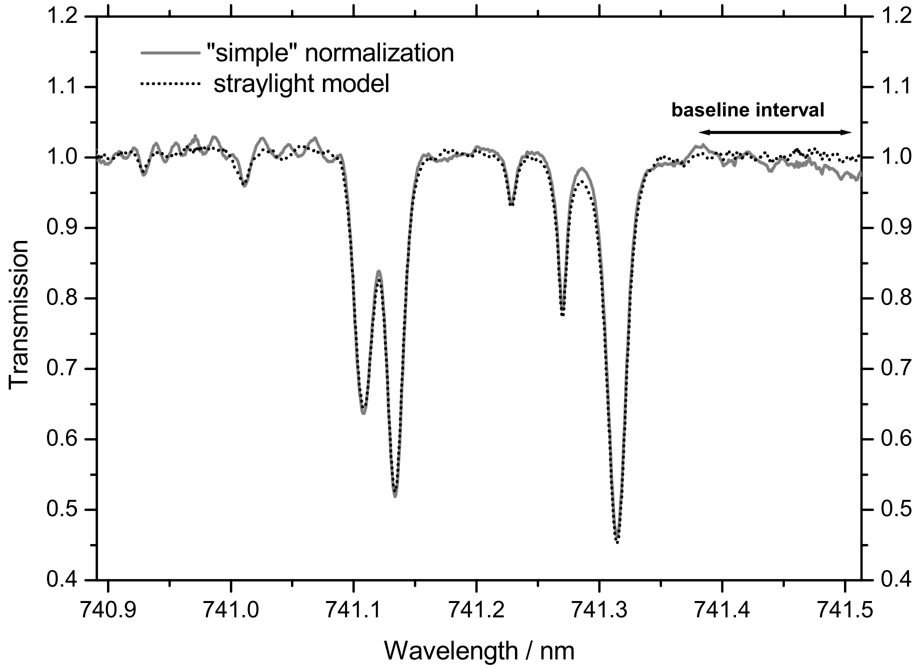

Figure 6.10: Differential absorption spectra at 741.2 *nm* normalized by the "simple" approach using Eq. 6.11 and Eq. 6.12 and the improved procedure using a least squares fit of the stray light model Eq. 6.13.

The examples above indicate, that stray light effects are critical for the removal of interference structures in the raw spectrum and that the normalization procedure outlined above has to be improved to account for these effects. We therefore extended the normalization procedure by a simple stray light model, in which unknown stray light contributions for both, the flatfield and the solar spectrum, are determined. In this model, the relative transmission I_i' at pixel i is calculated by the following equation:

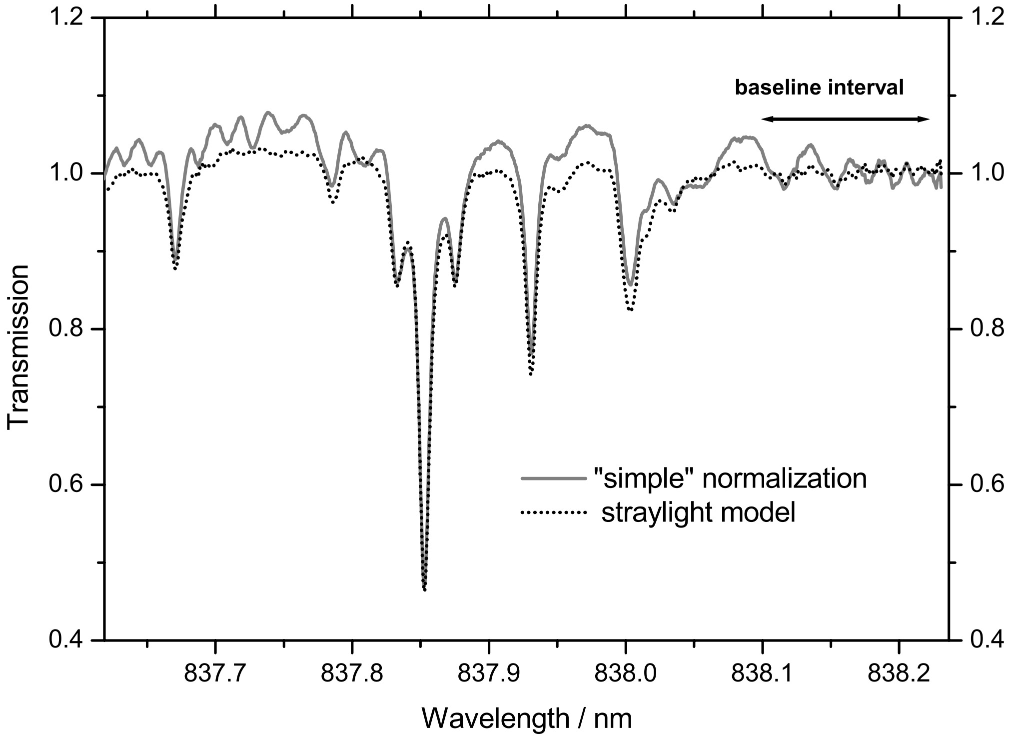

Figure 6.11: Differential absorption spectra at 837.9 nm normalized by the “simple” approach using Eq. 6.11 and Eq. 6.12 and the improved procedure using a least squares fit of the stray light model Eq. 6.13.

$$I'_i = \frac{V_{sun,i} + S_{sun}}{R \cdot (V_{flat,i} + S_{flat})}, \tag{6.13}$$

where $V_{sun,i}$ denotes the measured detector reading at pixel i of the solar spectrum, S_{sun} the constant solar stray light level, while $V_{flat,i}$ and S_{flat} are the corresponding quantities of the flatfield. The “lifting” factor R again accounts for the lower intensity of the flatfield. Since in this model R is no longer the ratio of the average intensities in the reference interval, it is a-priori unknown, as well as the stray light levels S_{sun} and S_{flat}. Within the reference interval, where solar and uplifted spectrum are supposed to match, we can postulate the relative transmission to be 100 %, and with $I'_i = 1$ for all $i\epsilon[b_a, b_e]$ Eq. 6.13 can be written as

$$V_{flat,i} = \frac{V_{sun,i} + S_{sun}}{R} - S_{flat}, i\epsilon[b_a, b_e]. \tag{6.14}$$

With this, we have expressed the flatfield in the reference interval as a function of the unknowns and the measured solar intensity. In the improved normalization procedure, we determine the unknown stray light levels by a least squares fit using Eq. 6.14 as an observation equation. With the partial derivatives

$$A_1 = \frac{\partial V_{flat,i}}{\partial S_{sun}} = 1/R, A_2 = \frac{\partial V_{flat,i}}{\partial S_{flat}} = -1, A_3 = \frac{\partial V_{flat,i}}{\partial R} = -\frac{V_{sun,i} + S_{sun}}{R^2} \tag{6.15}$$

the flatfield spectrum is iteratively adjusted to match the solar spectrum within the reference interval:

$$\Delta \mathbf{S_{i+1}} = (\mathbf{A^T} \cdot \mathbf{A})^{-\mathbf{1}} \mathbf{A^T} \cdot (\mathbf{V_{flat,mod}} - \mathbf{V_{flat,meas}}) \tag{6.16}$$

The elements of the vectors $\mathbf{V_{flat,mod}}$ and $\mathbf{V_{flat,meas}}$ are the modeled and measured values of the flatfield voltages, respectively, measured by the pixels within the interval $[b_a, b_e]$. The two spectra of the previous example pre-processed with the improved normalization procedure are plotted as the dotted lines in figures 6.10 and 6.11. While the 741.0 nm spectrum has not changed significantly, the periodic features in the 837.9 nm spectrum have vanished. The standard deviation σ_{ref} of the transmission values from 100 % within the reference intervals can be regarded as a measure for the performance of the normalization technique. It also gives an estimate for the remaining instrumental noise of the intensity measurement. The average standard deviation of the transmission values from 100 % within the reference intervals was found to be better than 0.008 (0.8 %). This can be regarded as the noise level of the SAMOS measurements of differential intensity.

6.2.3 Stray light correction using oxygen spectra

In every real, non-ideal optical spectrometer, imperfections of optical parts interacting with radiation are sources of stray light. As found in the previous section, consideration of stray light turns out to be essential even in the normalization procedure within the pre-processing stage. It was also found that the stray light levels of both the solar spectrum and the flatfield spectrum, which is used for its baseline normalization, cannot be determined simultaneously in the least squares estimation. Therefore an alternative approach to obtain an estimate of the stray light level of the solar spectra has to be found. In this context, the oxygen spectra measured in four wavelength intervals from 766.0 nm to 766.5 nm proved to be useful. These spectra contain pairs of strong absorption lines which are saturated under almost all observation conditions. In the vicinity of their line centers a perfect spectrometer would measure zero intensity. In the presence of stray light, the intensity measured in the line centers is a measure for its magnitude. It can be determined as a fraction of the total transmission by the ratio of the average voltages measured in the line centers and in the baseline interval. If the spectral region with oxygen saturation is measured by the pixel within the interval $[s_a, s_e]$ and the baseline interval is again defined as $[b_a, b_e]$, then the fraction of stray light in a solar spectrum is approximated by:

$$S_{sun} = \frac{(b_e - b_a) \sum_{i=s_a}^{s_e} V_{sun,i}}{(s_e - s_a) \sum_{j=b_a}^{b_e} V_{sun,j}}. \tag{6.17}$$

Fig. 6.12 shows four normalized oxygen spectra in different wavelengths measured by SAMOS. A stray light contribution is visible in the line centers of the spectra depicted by the solid grey line. The spectra were normalized again after subtracting the average voltage of the saturated area, which corresponds to a percentage of the baseline voltage indicated in each plot. The stray light corrected spectra, indicated by the dotted lines now reach zero transmission in the saturated spectral regions.

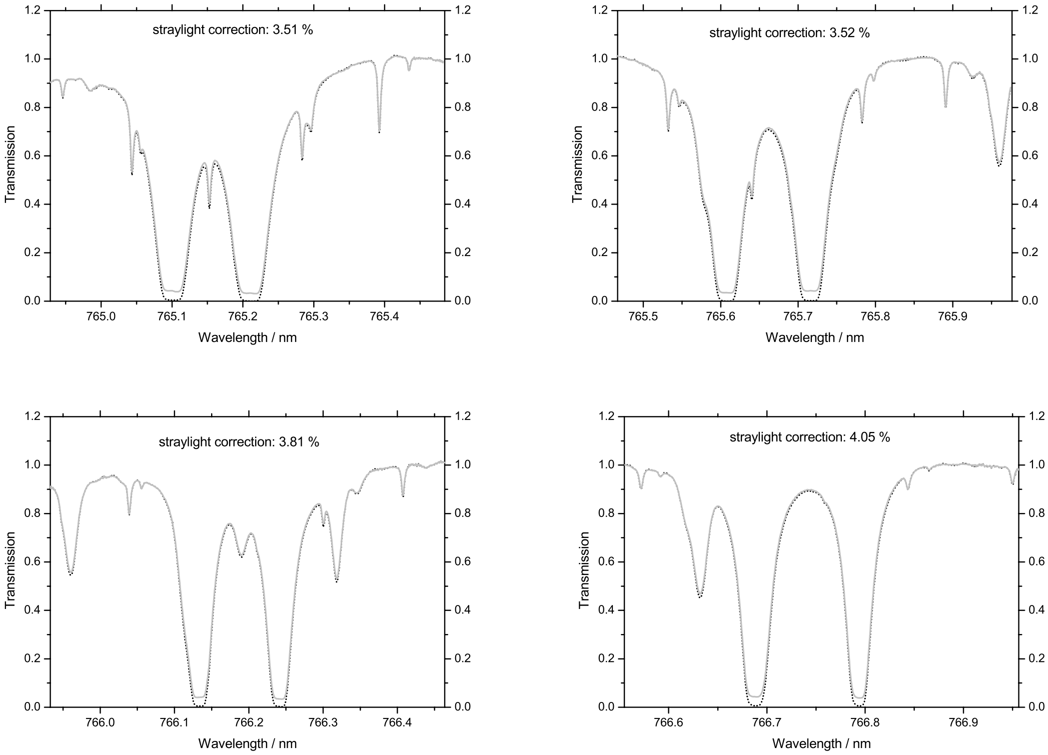

Figure 6.12: Differential oxygen absorption spectra. The strong absorption lines are saturated. The residual voltage measured by the detector in the centers of these lines (grey curve) is a measure of the stray light level within the instrument. If stray light corrections with respect to the intensity level of the baseline interval are applied, the intensity reaches zero (black curve)

The stray light level for the four wavelength intervals ranges between 3.5 % and 4.0 %. According to the experience of the spectrometer developers from ISAS these are realistic values that could be expected for a high resolution device like SAMOS. In the line selection process (chapter 4) it was made sure that the spectral measurement windows contain no saturated H_2O-transitions. Therefore the analysis according to Eq. 6.17 cannot be applied to the water vapor spectra. However, there is no reason for the assumption that the stray light level exhibits a significant dependence on the measured wavelength. Therefore we can regard the corrections determined for the saturated O_2- spectra as the best available model for stray light levels in solar absorption spectra measured by SAMOS (S_{sun} in Eq. 6.13 of the previous section). The differences in correction percentages of the four oxygen-windows is an indication for the accuracy of the stray light determination. The spectra in Fig. 6.12 have been acquired within the same 5 minutes and therefore only represent a single value of S_{sun}. It is reasonable to have a closer look at the temporal dependence of the correction. In Fig. 6.13 the stray light corrections in percent of the baseline intensity is plotted for continuous measurements over one day. The four time series according to the O_2-measurement windows exhibit differences in S_{sun} between 0.3 % - 1%. Towards the end of the day a rapid increase in stray light level can be observed. This observation is typical for SAMOS measurements under low solar elevation angles. The higher stray light level probably arises from higher exposure times needed to measure spectra at near sunset conditions. In summary it can be pointed out that it is possible to derive estimates of stray light from saturated oxygen lines to an accuracy of about 1%.

6.3 Validation and improvement of the absorption model

Once the raw data have been pre-processed as outlined above, they can be compared with simulations based on the radiative transfer model developed in chapter 3, in order to verify if our model of absorption in the troposphere is an adequate description of the reality. This validation is especially important since the “forward model” is the basis underlying the processing algorithms.

6.3.1 Comparisons using radiosonde data and HITRAN

The purpose of a comparison between measured SAMOS-spectra and theoretical transmission functions is to verify if

- the absorption features in the real spectra can be identified and associated to the transitions of the HITRAN database

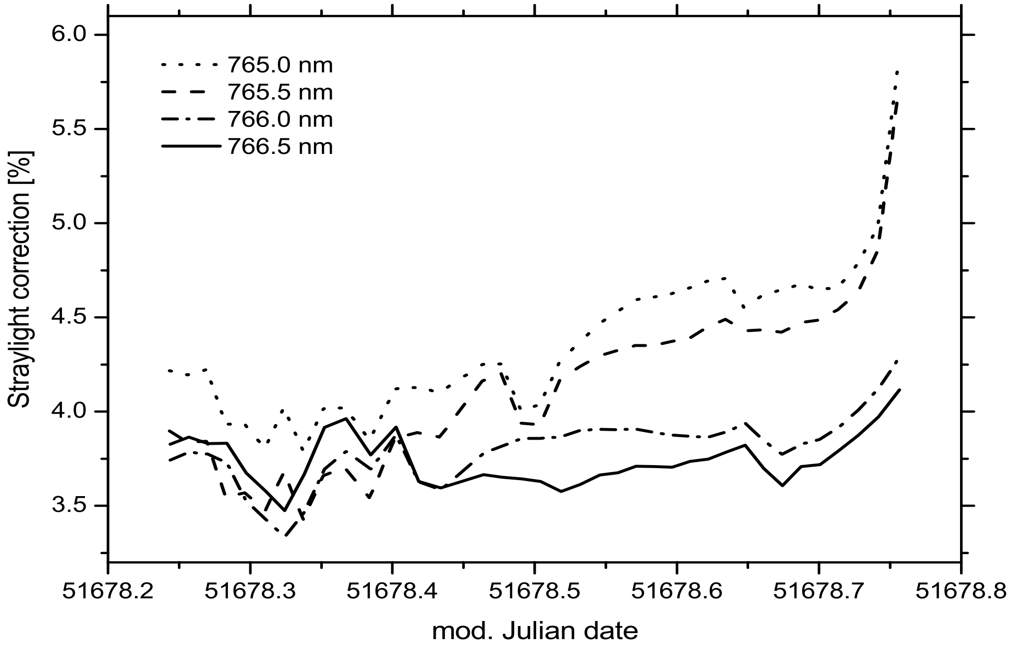

Figure 6.13: Stray light corrections in percent of the baseline intensity plotted for continuous measurements over one day. The differences in S_{sun} range from 0.3-1.0%. Towards the end of the day the stray light level increases rapidly. This behavior, which is observed in all time series is probably due to higher exposure times and lower signal when the sunshine intensity decreases close to sunset.

- unknown absorption features are present in the spectral measurement intervals that are not taken into account in the model(e.g. Fraunhofer lines)
- the measured line positions are consistent with the database values of ν_0
- the integral absorption of the absorption lines corresponds to the theoretical amount of line absorption given the line intensities S_0.
- the line widths of measured and modeled spectra match.

The first three questions could be addressed by comparing the real spectra with model calculations based on standard atmospheres. Investigation of the latter two issues requires knowledge of meteorological profiles, since the line absorption depends on pressure, temperature, and absorber density along the absorption path. This is practically impossible for ground based atmospheric measurements, where the true atmospheric state is unknown. The best source of information available for meteorological profiles are in-situ measurements of p, T and relative humidity acquired by radiosondes. For the following first comparison between real and simulated data we used the dataset of a meteorological field campaign carried out in the framework of the Mesoscale Alpine Project (MAP). During this campaign, SAMOS was operated at a radiosonde launch site in Diepoldsau, Switzerland. A more detailed description of the MAP-campaign and the results are given in section 7.2.4.

In Fig.6.14 to 6.27 SAMOS-spectra for all selected wavelength intervals are plotted together with simulated spectra using the absorption model described in chapter 3. In the model calculation, the assumed vertical profiles of p, T and ρ_w were taken from a radiosonde sounding, which was launched while the SAMOS spectra were recorded.

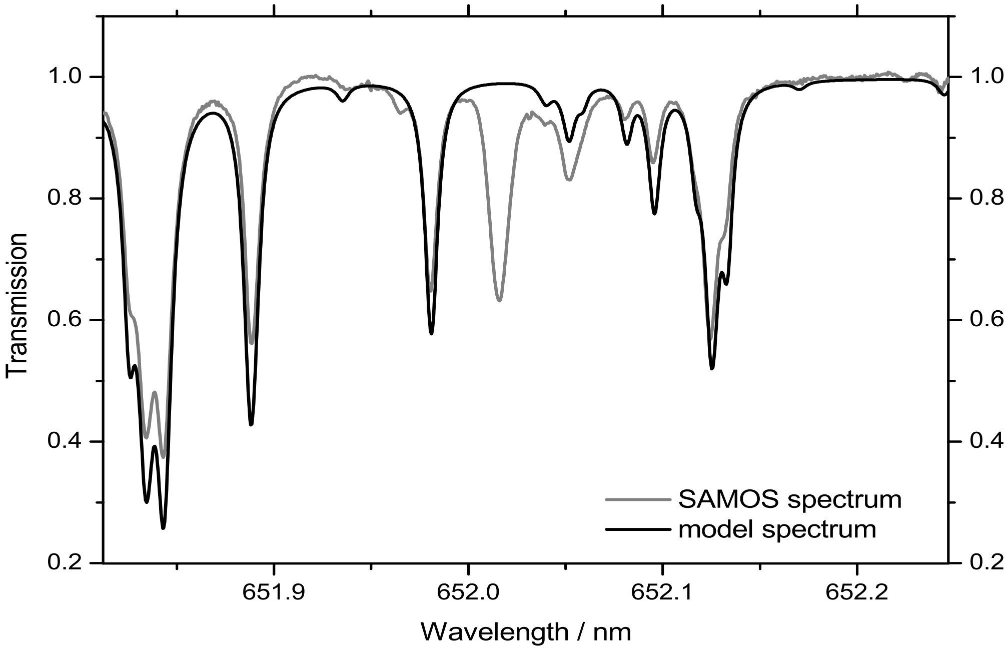

Figure 6.14:

The figures show different levels of agreement for the individual wavelength intervals. The general impression is that the overall absorption is greater for the measured spectra than for the calculated transmission functions. The absorption in some intervals are well reproduced by the model (e.g. 789.5-790.0 nm in Fig. 6.17). Other measurement windows, however, exhibit strong discrepancies in line intensity. The measured lines in Fig. 6.15 in the spectral interval 740.9-741.5 nm are much stronger than predicted by the model. An example for the opposite case is the interval 651.8 - 652.2 nm where the model seems to overestimate the line absorption (see. e.g. Fig. 6.14). It should be noted that the intensity corrections to the HITRAN line strength data was applied as proposed by P.Giver et al. [2000] (see section 3.10).

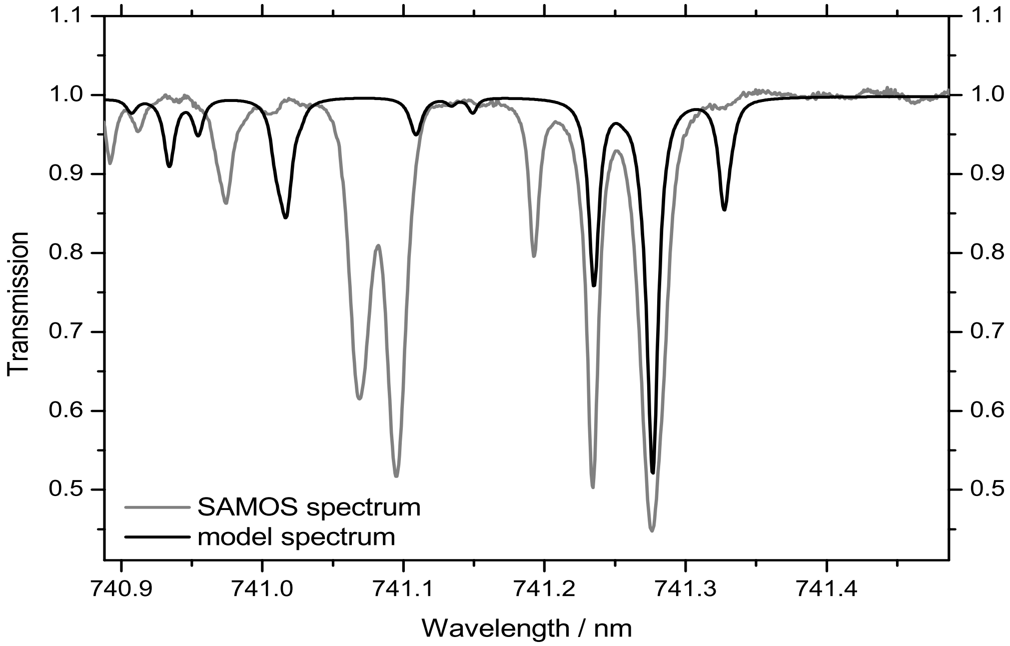

Figure 6.15:

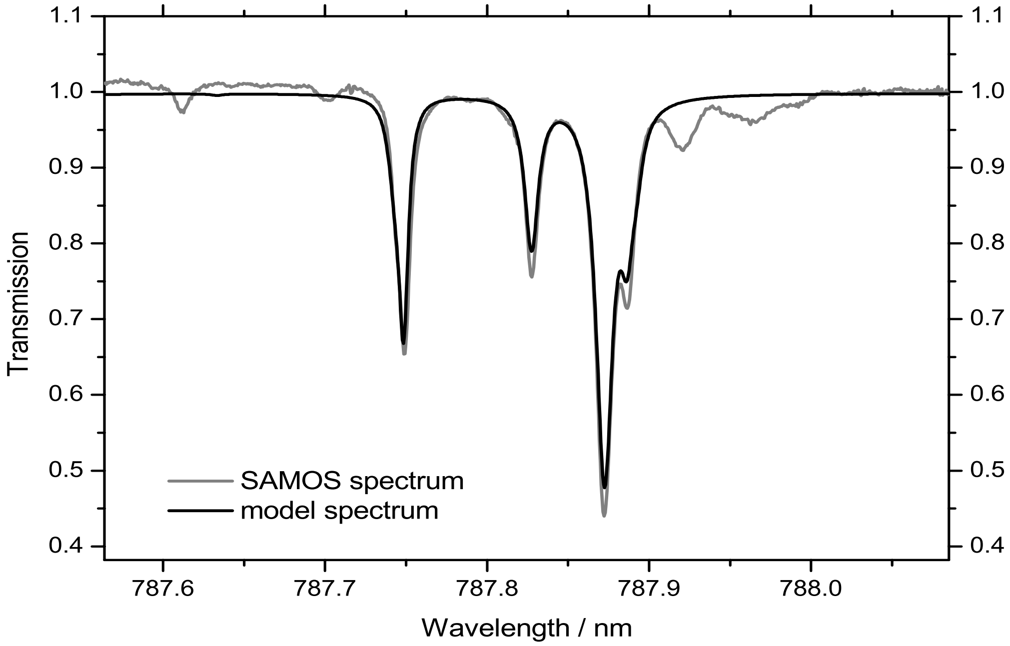

Figure 6.16:

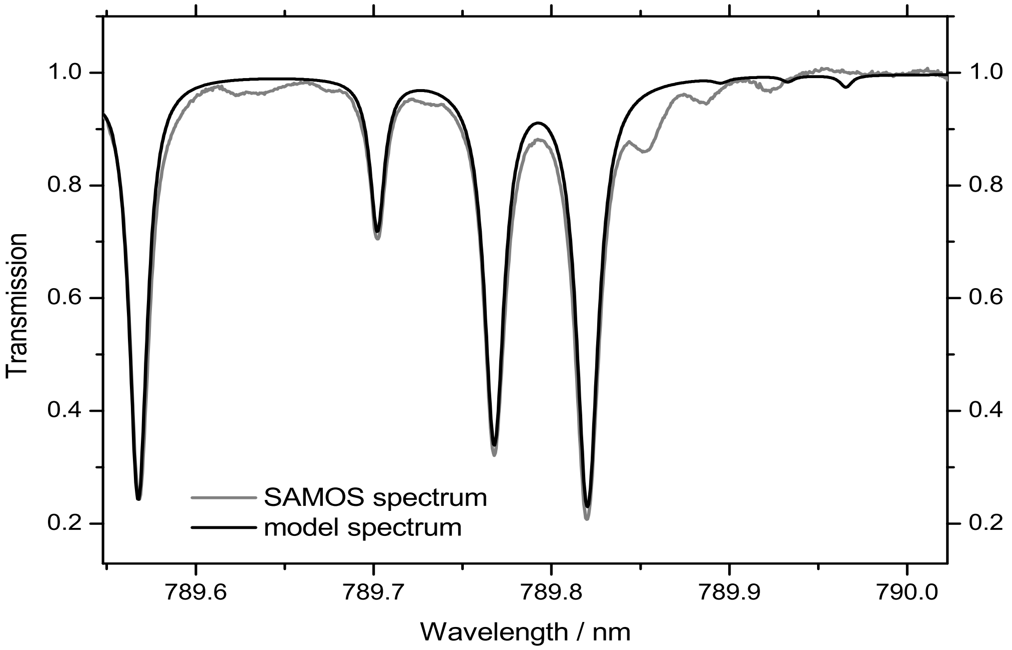

Figure 6.17:

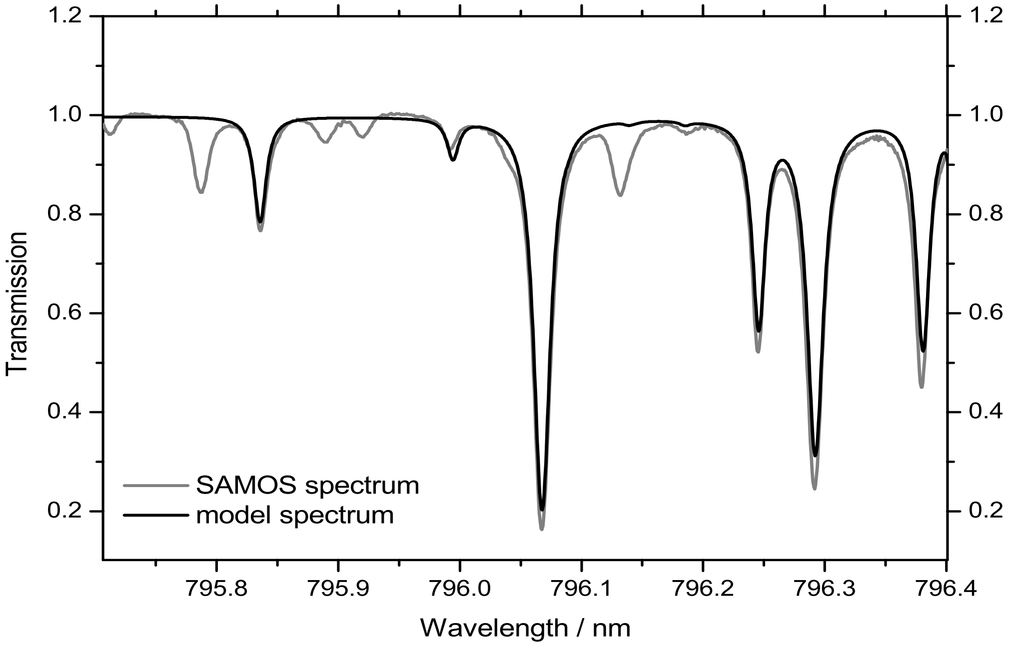

Figure 6.18:

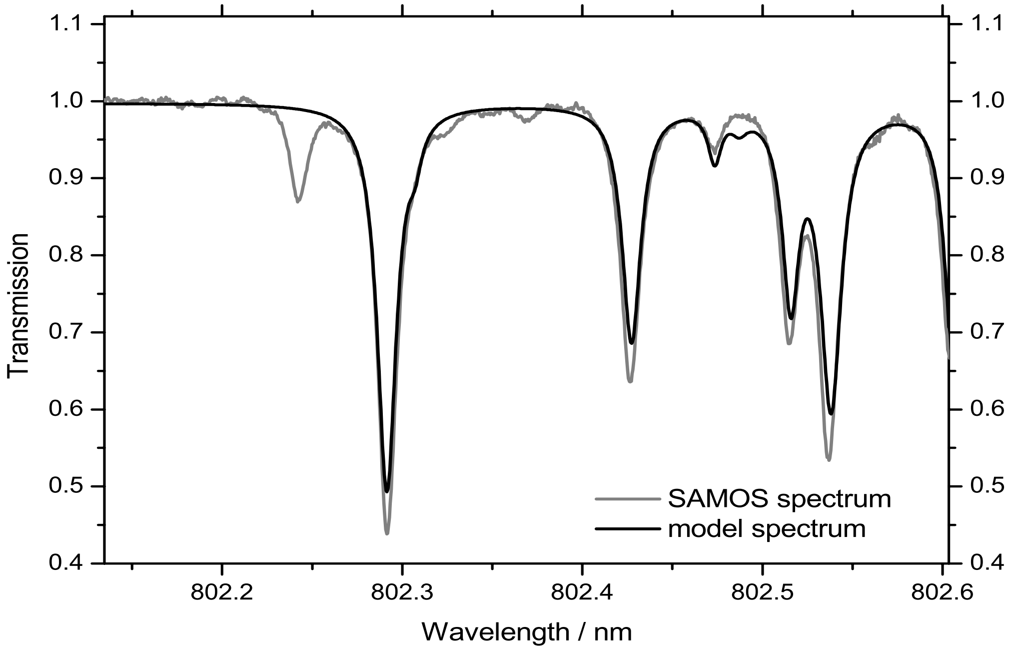

Figure 6.19:

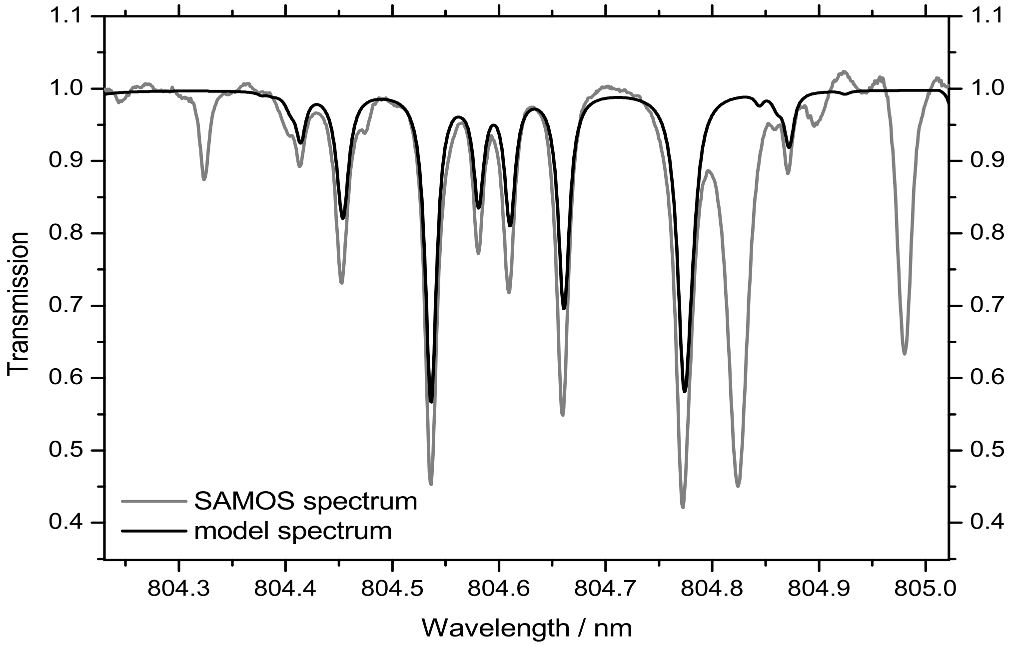

Figure 6.20:

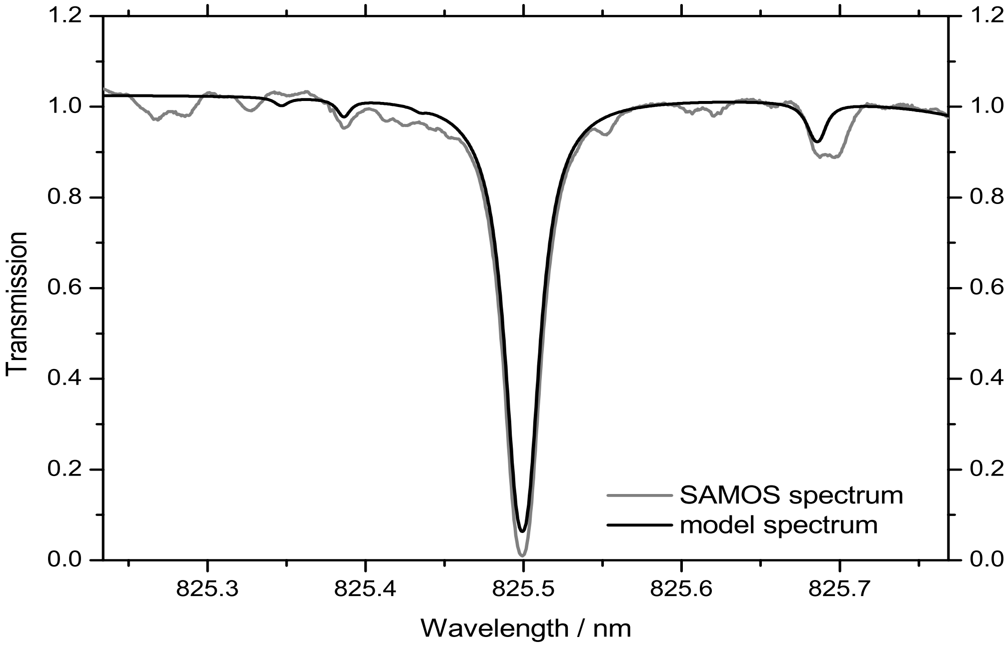

Figure 6.21:

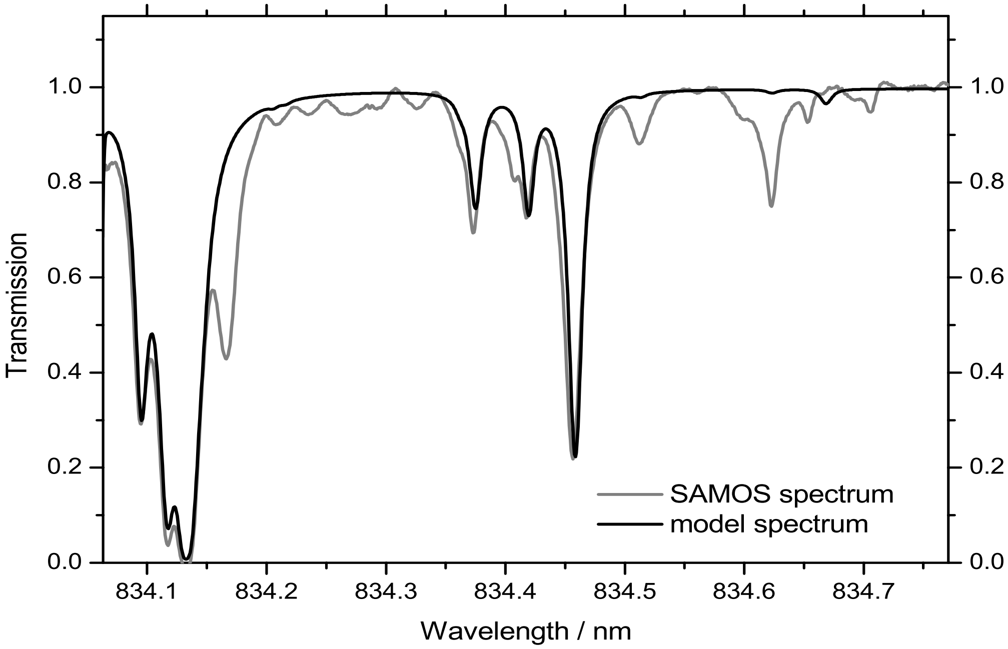

Figure 6.22:

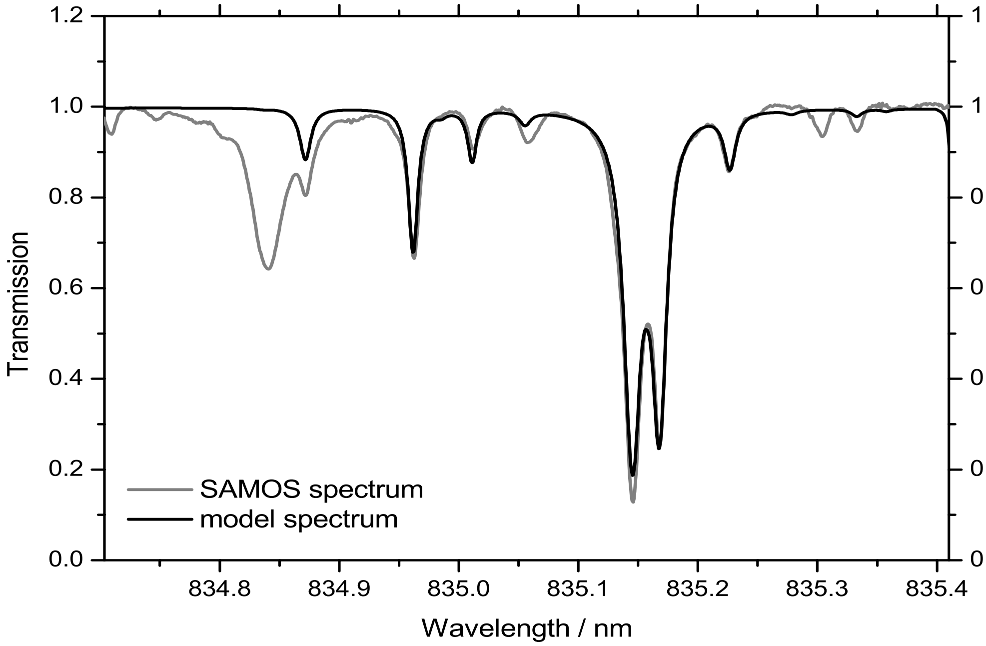

Figure 6.23:

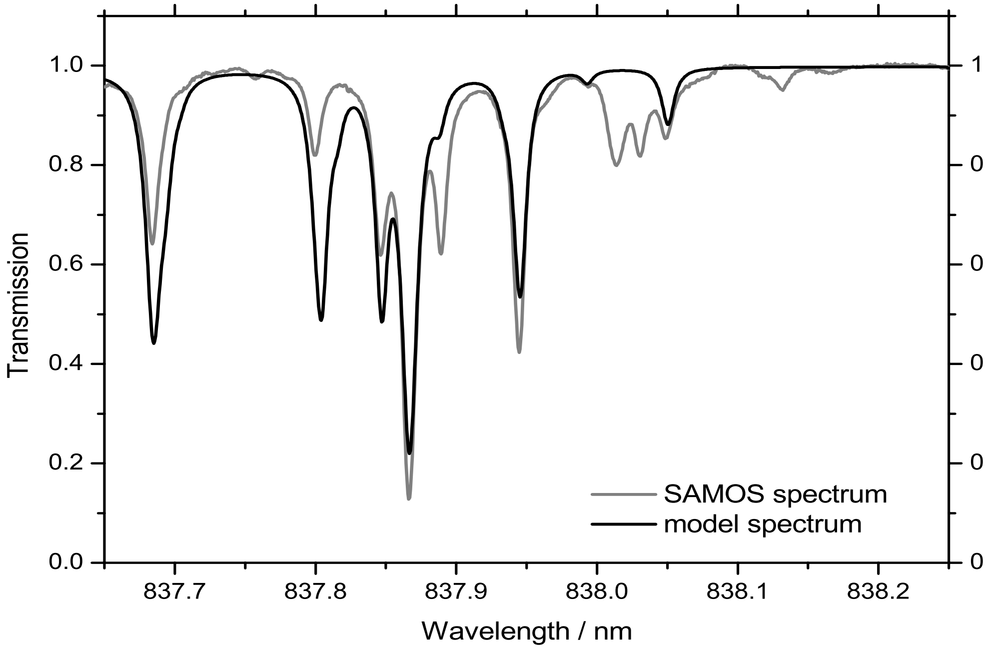

Figure 6.24:

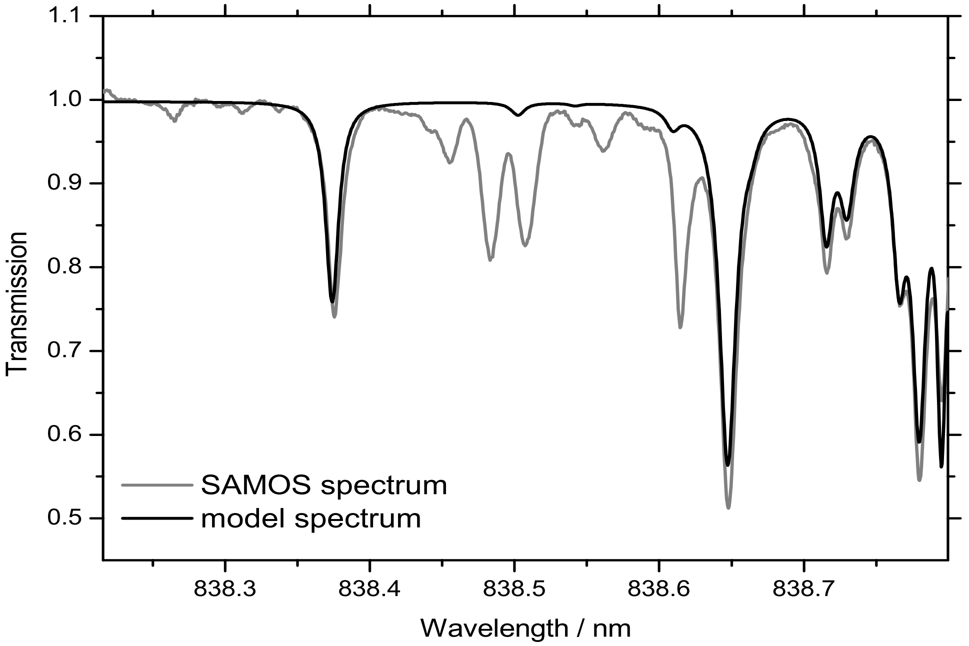

Figure 6.25:

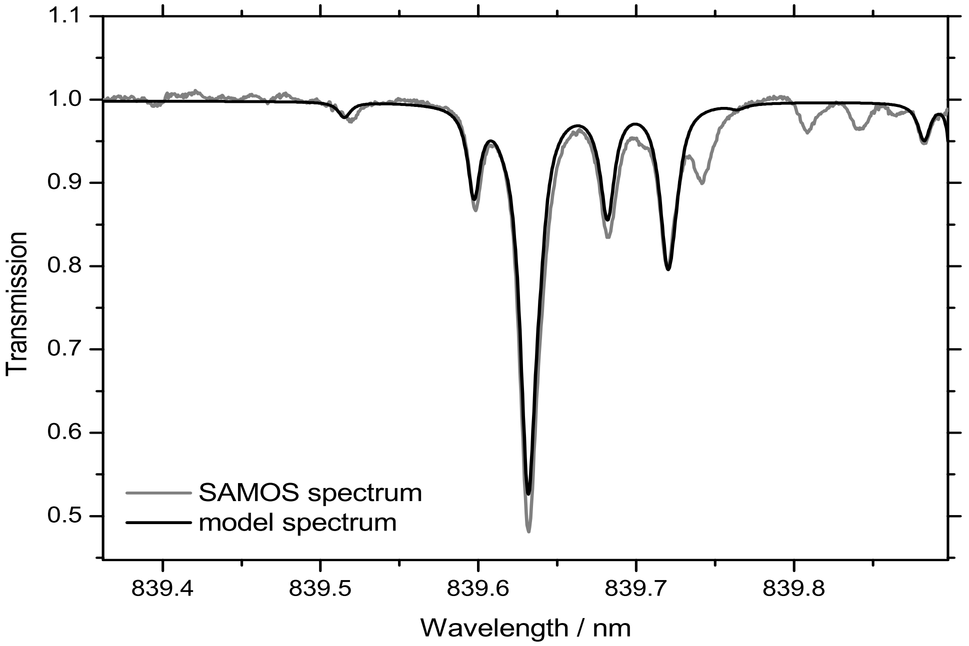

Figure 6.26:

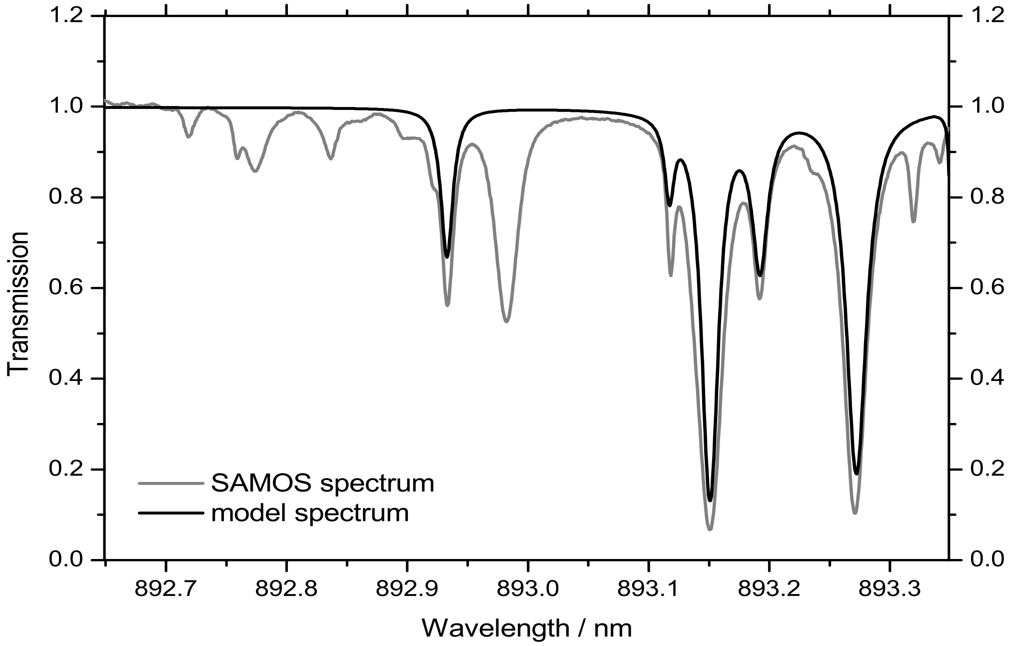

Figure 6.27:

One could speculate about the origin of the differences in line intensity. They could be due to systematic errors in the radiosonde measurements, which are the basis for the model, imperfections of the model itself, which would probably be caused by inaccurate values of the line parameters, and by instrumental measurement error of the spectrometer. Although it is impossible at this point to identify and quantify the error sources, the detailed comparison is important and instructive to identify and address the problems in each measurement interval. The fact that SAMOS is capable of a highly accurate absolute calibration of wavelengths allows a critical review of the line positions given in the HITRAN database. Comparing the line positions, most modeled transitions are well determined with only slight shifts on the wavelength scale. There are also negative exceptions in which the lines can be identified by their shape but occur at different wavelengths far away from the model line positions. This is the case e.g. in Fig. 6.15 for the absorption features between 740.91 *nm* and 741.03 *nm* which appear shifted with respect to the model by as much as 42 *pm*.

6.3.2 Identification of Fraunhofer lines

Another observation is the presence of absorption features in the measured spectra that are not predicted by the model. These are visible e.g. at 741.09 *nm* in Fig. 6.15, and at 893.0 nm in Fig. 6.27. They could arise either from Fraunhofer lines caused by absorption in the solar atmosphere or from unknown transitions not yet included in the HITRAN database (although the latter case is not likely for features as strong as the observed ones). One method to distinguish between solar and terrestrial absorption features is to compare spectra measured at different solar elevation angles. While the total differential absorption of terrestrial transitions depends on the length of the absorption path (airmass), the integral absorption of Fraunhofer lines should remain constant. In Fig. 6.28 - 6.30 SAMOS spectra acquired under different elevation angles at wavelengths with “suspicious” absorption features are plotted. As can be seen, the integral absorption increases rapidly with setting Sun for the already identified H_2O-transitions. The two strong lines at 741.09 nm in Fig. 6.28, in contrast, do not vary while sounding the troposphere at different elevation angles. They can therefore be classified as Fraunhofer lines. The same observation is made at 893.0 nm in Fig. 6.29. The transmission values in spectral regions containing Fraunhofer lines have to be excluded from the data processing. However, it can be seen that these features are narrow enough to be neglected about 50 *pm* distant from their line centers. This means that the neighbor water vapor lines can still be used for processing.

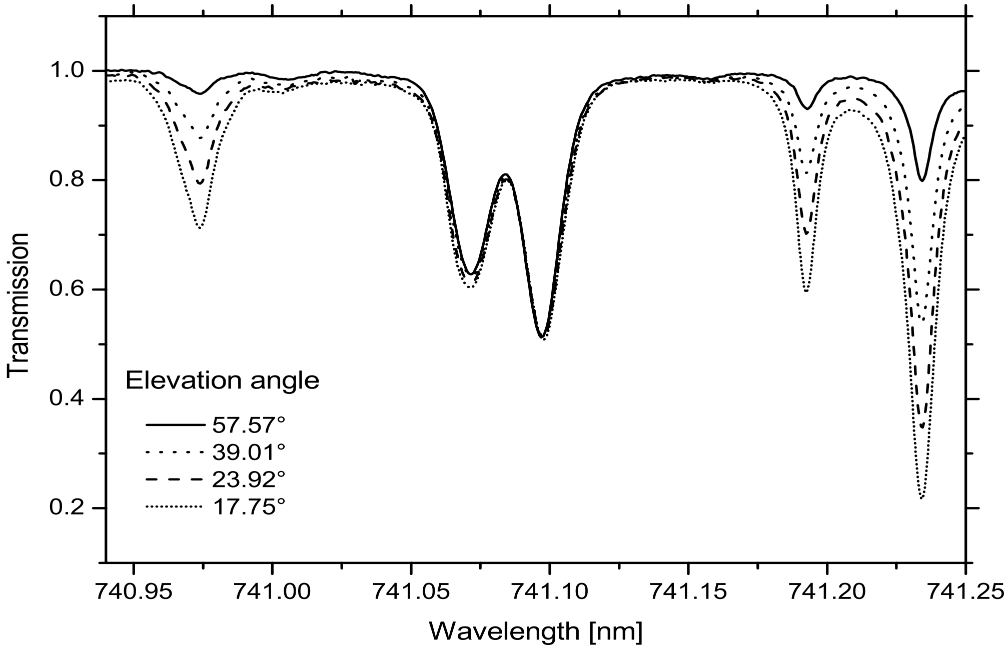

Figure 6.28: Series of SAMOS-spectra acquired over 5 hours under different elevation angles θ. The total absorption of H_2O-lines changes with increasing airmass. The absorption features at 741.09 nm remain unchanged. They can be therefore identified as Fraunhofer-lines

Fig. 6.30 shows another series of SAMOS-spectra acquired while scanning the tropo-

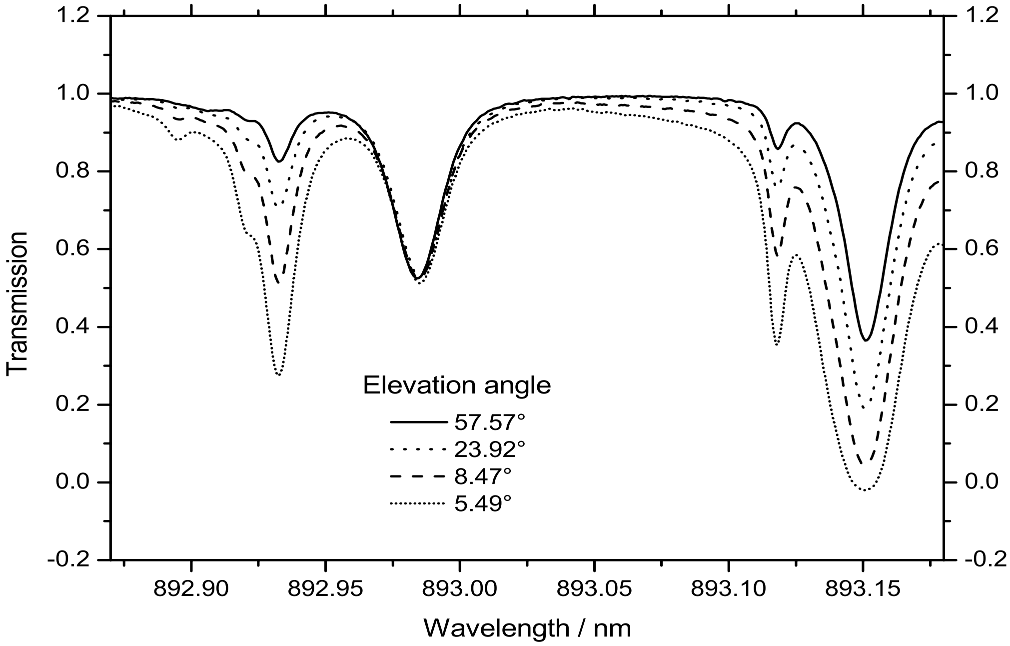

Figure 6.29: Series of SAMOS-spectra acquired over 5 hours under different elevation angles θ. The total absorption of H_2O-lines changes with increasing airmass. The absorption features at 893.0 nm remain unchanged. They can be therefore identified as Fraunhofer-lines

sphere with decreasing elevation angle. In this case the attenuation of the unknown absorption line at 838.6 nm increases like the known transitions as the solar elevation decreases. This dependence from airmass indicates that the absorbing molecule must be a constituent of the Earth´s atmosphere. The HITRAN database does not claim completeness and is constantly updated, the most recently included lines are published on the Internet (www.hitran.com). In our radiation transfer model we used the 1996 edition of the database. We also downloaded the latest version of the H_2O-update (July 2000) in order to verify if the unknown feature at 838.6 nm has been recently incorporated. Since we did not find a tabulated transition at this wavelength, we can not identify the absorption line we found. The spectral region around this line will therefore also be excluded from the processing.

6.3.3 Interpretation of comparison results

At the end of this section, some judgment has to be made about the quality of our absorption model and its suitability for water vapor retrieval: The problem of Fraunhofer lines is probably the least severe. Their effect is a deviation from the constant background Intensity I_0, which would of course falsify the normalization

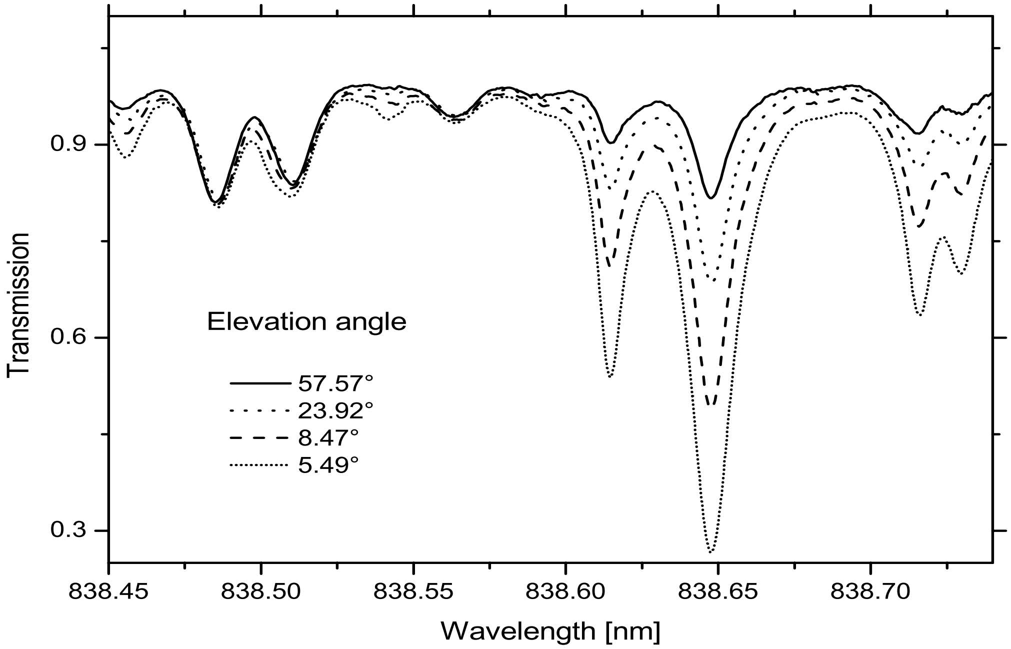

Figure 6.30: Series of SAMOS-spectra acquired over 5 hours under different elevation angles. The absorption feature at 838.6 nm changes with elevation in the same way as the known H_2O-lines. It is therefore likely to be a transition not yet included in the HITRAN database

using flatfield spectra. However, it was shown that such features can easily be identified and their linewidths are comparable to those of the H_2O-lines. Hence they can be avoided by simply excluding the spectral regions with Fraunhofer lines from the processing.

The discrepancies in line position is also a problem relatively easy to solve, since the absolute values of ν_0 do not directly affect the PW retrieval. On the other hand, it is clear that the line centers of the calculated spectra should match the measured ones, when they are adjusted to the real spectra in the processing. To achieve this, it is possible to shift the line positions taken from the HITRAN database so that they are consistent with the wavelength scale of the SAMOS spectra. This adjustment can be regarded as an improvement of the database values, since the absolute wavelength calibration using neon emission lines as described in section 6.2.1 should be more accurate than the precision of the line positions indicated in the database. Even with a calibration error of the SAMOS wavelength scale defined according to section 6.2.1 the relative positions of lines were still measured to high accuracy. We therefore decided to adjust the line position parameters given in HITRAN to the spectra measured by SAMOS. In section 6.3.4.1 the procedure to determine line position corrections will be described in detail .

The most delicate problem revealed by the model comparison are the discrepancies in total line absorption. This is the relevant quantity for determination of water vapor abundance and it depends on the line intensity S_0 as well as on profiles of humidity and temperature. It is not possible to distinguish between an overestimated line strength parameter in the database and too high values of absolute humidity derived from the radiosonde measurements, which can both be the reason for the deviations. Moreover, errors in the model for the temperature dependence of line intensity given by Eq. 3.30 will propagate into the calculated theoretical spectra. However, this model represents our best understanding of the physical process and therefore cannot be improved. Thus, the decision if and how the model can be improved depends on the question, if either the HITRAN values for S_0 or radiosonde measurements account for a greater part of the discrepancies.

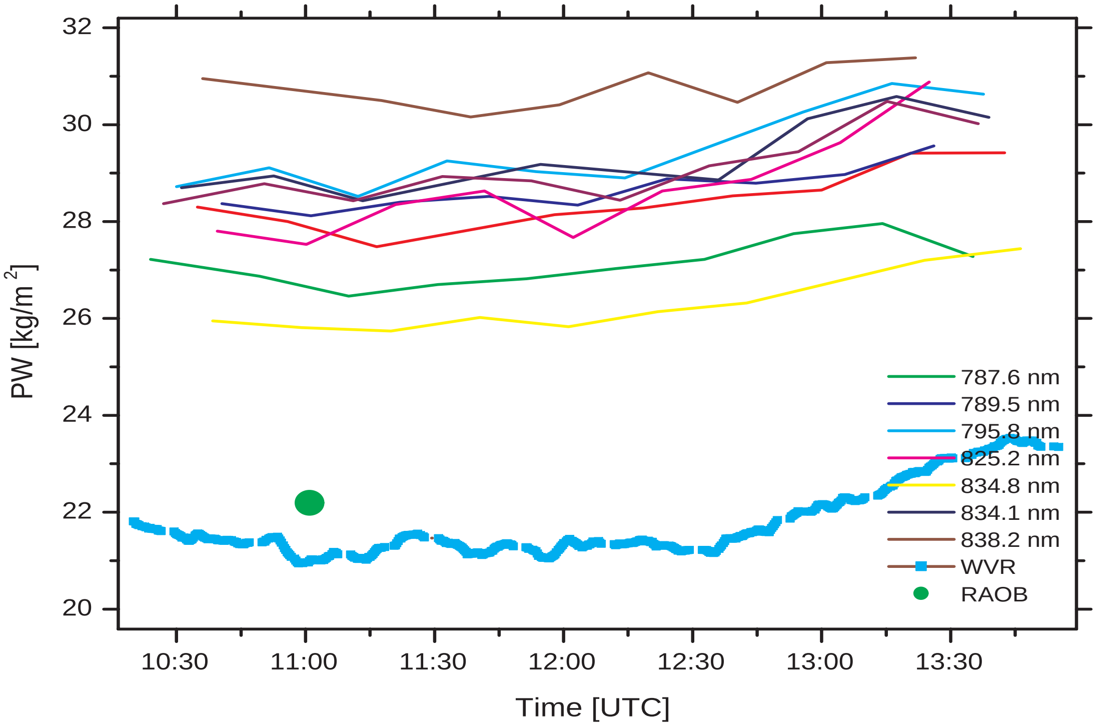

Figure 6.31: Time series of zenith PW derived from solar spectra using the HITRAN line parameters. Huge offsets of up to 5 kg/m^2 are visible between the different measurement windows. The underestimation of absorption by the model yield in higher PW values than observed by the WVR. The circle denotes the integrated humidity profile of a radiosonde observation (RAOB).

In order to get an idea about the impact of these deviations on the resulting PW retrievals, we processed the SAMOS spectra using the HITRAN parameters and the radiative transfer model according to the procedure described in section 6.4. Fig. 6.31 shows the processing results for each selected wavelength interval together with a PW time series measured by a WVR on October 29th, 1999. Also the PW value derived from integrating a radiosonde profile of absolute humidity is plotted. The figure shows huge offsets between the PW time series calculated from spectra of different wavelengths. When compared to the WVR results, the SAMOS results overestimate the water vapor content to an extent which corresponds to the underestimation of total line absorption observed in fig. 6.14-6.27. In the least squares estimation, the discrepancy is compensated by a higher value of precipitable water. The radiosonde observation (RAOB), in contrast, shows a good agreement with the radiometer retrieval. This fact, as well as the large deviations of the SAMOS estimates, as well as the huge offsets between retrievals from measurements at different wavelengths imply that the errors in humidity measurement of the radiosonde are smaller than those in the line strength parameters S_0 from the HITRAN database. A critical review of the line parameter data, based on the accuracy indices given for each individual transition (see 3.10) confirms the suspicion, that parameter errors are the likely cause for the discrepancies between absorption model and SAMOS spectra.

On the basis of these considerations, we conclude that the accuracies of HITRAN line strength parameters are not sufficient for high quality determination of tropospheric water vapor. Instead, they have to be corrected to achieve a better agreement between the radiation transfer model and the measured spectra. This was done using the radiosonde soundings performed during the MAP campaign. The subsequent section describes how this was done.

6.3.4 Line parameter fitting

The accuracy of line parameters for the individual transition within the selected measurement windows are of crucial importance for the spectrometric technique described in this study. Their determination has in this context the significance of an external calibration of the method, which relates the observables, differential intensities or transmissions within a spectrum, with the absorber abundance, which is the quantity to be determined.

Spectral line parameters are usually determined in laboratory measurements using long-path absorption cells, in an which incident light beam is multiply reflected within a mirror system before it is analyzed by a spectrograph. Pressure, temperature and absorber amount are determined by sensors within the absorption cell and kept constant during a measurement. By varying the p and T investigations on pressure broadening and temperature dependence of line strength can be carried out. The longest absorption paths realized within white cells range reach several hundred meters.

The advantage of determining line parameters utilizing this technology is obviously the capability of controlling the conditions under which the absorption takes place. However multiple pass sampling cells have a number of limitations which diminish their effectiveness, especially when determining strength and width of weak transitions.

If the absorption path is not long enough to produce a sufficiently strong absorption signal for line parameter determination, the absorber amount has to be increased. on the other hand increasing the partial pressure of the absorbing gas will result in stronger collision broadening. Thus, with stronger overlap between neighbored transitions it will be increasingly difficult to separate the closely spaced individual lines.

Nevertheless, long path absorption cell measurements of the lines selected in chapter 4 would surely be the best possible external calibration procedure for SAMOS-measurements. Unfortunately, such measurements could not be performed in the framework of this study. They would require a considerable amount of instrumental effort and measurement time in a laboratory equipped with appropriate instrumentation. The selected absorption lines are rather weak (in the order of $10^{-25} cm{-}1/(molecule \cdot cm^{-2})$, as a result of our intention to avoid saturation at low solar elevation angles and high water vapor abundances. There are only few laboratories which are equipped with appropriate absorption cells for accurate determination of such weak transitions. A project aiming at improving the HITRAN parameters was beyond the focus of the SAMOS-project and therefore is left to future investigations. There are several research groups regularly publishing improved laboratory data of H_2O-lines in the visible and NIR regions (Camy-Peyret et al. [1985], Mandin et al. [1986], Mandin et al. [1988], Chevillard et al. [1989], Schwenke [1998], Giver et al. [1999]). It is therefore likely that more accurate parameters for the transitions selected in this study will be available in the future.

However, in order to meet the requirement of improving our model parameters, as found in the previous section, some way had to be found to overcome the actual shortcomings in the currently available data. Therefore we decided to perform line parameters calculations based on radio soundings. This means of course abandoning the advantage of independence from radiosonde calibration, which was claimed in the introduction (see section 1.3). On the other hand the use of radiosonde observations is only restricted to the investigations in this study, in order to cope with the deviations between radiative transfer model and SAMOS-measurements. This does not change the fact that the DOAS-technique itself remains inherently independent from radiosondes. In the following two sections the procedure and the results of the line parameter determination will be described.

6.3.4.1 Correction of line positions

Before the radiosonde data were used to correct the HITRAN line intensities S_0, the line positions λ_0 were adjusted to obtain agreement between the model and the SAMOS-spectra. This could be achieved using the absolute wavelength scale of the SAMOS spectra generated using the neon line procedure (see section 6.2.1). The HITRAN line positions were shifted to match the lines measured with SAMOS. This could of course only be done with well separated lines. In case of a superposed group of lines, the entire group was shifted.

The center of absorption features could be determined as the mean wavelength weighted with the reciprocal transmission measured along the line profile, analogous to the line center determination of neon emission lines by Eq. 6.6. However this simple approach turns out to be not feasible, since the shape of superposed absorption lines is not symmetrical. Instead, the adjustment was performed on the basis of an iterative shift of the line positions λ_0 in the radiative transfer model to match the absorption features in the SAMOS spectra.

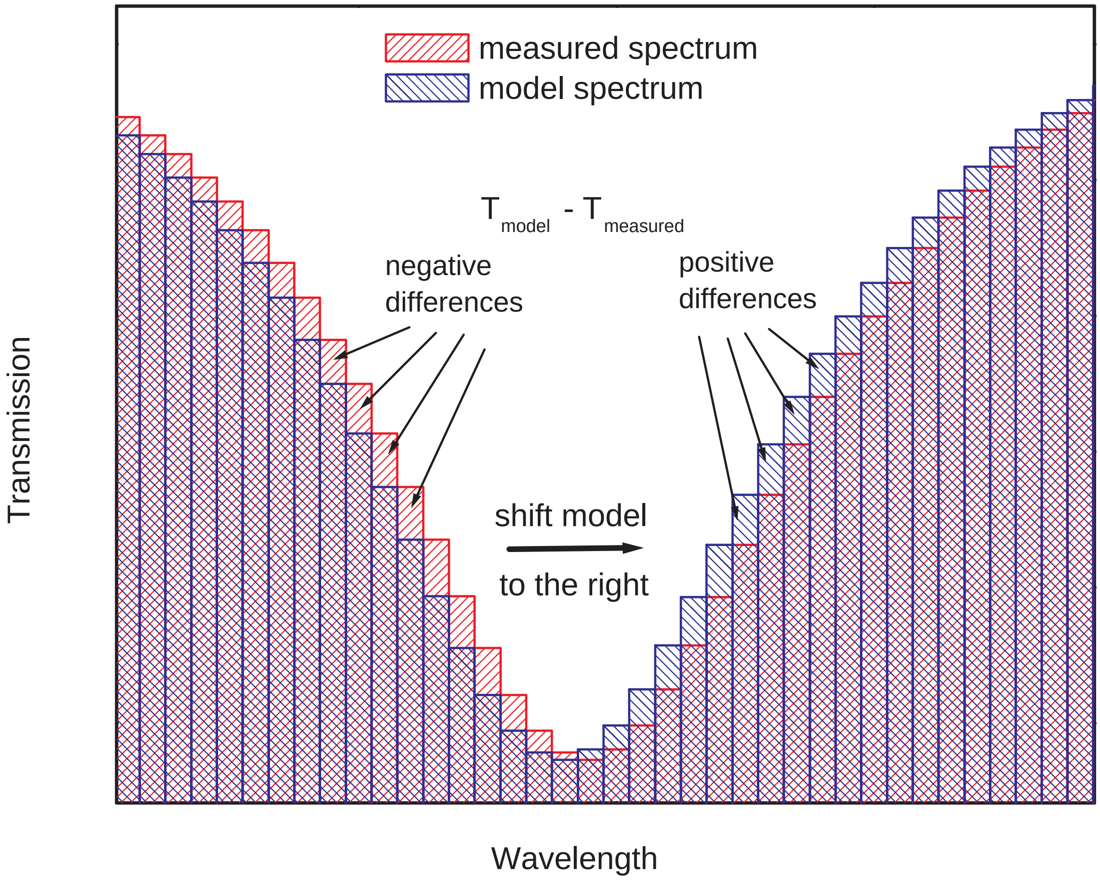

Figure 6.32: Principle of iterative adjustment of line positions λ_0. If the transmission differences between modeled and measured line yield positive values on the right line wing and negative ones in the left, the model is shifted to the right (and the other way round).

The principle of the iterative adjustment procedure is illustrated in Fig. 6.32. Starting with the line position from HITRAN a theoretical absorption spectrum is calculated. The profiles of temperature, pressure and absolute humidity are taken from a radiosonde, which was launched at the time when the SAMOS spectra were acquired (see next section 6.3.4.2). The direction on the wavelength scale, to which the line position is shifted is determined by evaluating the differences between model and measurement on the line wings. In Fig. 6.32 the center wavelength of the model line is too short. Calculating the transmission differences yields positive values for the pixels right (long wavelength side) to the measured line center and negative values to the left (short wavelength side). In such a case the model line position is shifted to the longer wavelength side by a given step width. If the center wavelength of the model line becomes too long, the difference yield positive values on the left line wing and negative ones on the right. In this case the best match has been reached. By reducing the step width and repeating this procedure, the match can be iteratively improved until the desired level of accuracy is reached.

6.3.4.2 Correction of line strengths

A radiosonde sounding represents a snapshot of an atmospheric state averaged over the time of the ascent. Strictly, the validity of this snapshot is limited to the actual (unknown) path the balloon travels along in the atmosphere and the accuracy of the in-situ measurement. However, since atmospheric processes evolve in time scales that are large compared to the time of the ascent, it is usually justified to regard meteorological profiles acquired by radiosondes as a representative picture of the atmospheric state for some time before and after the launch. In the absence of weather fronts the assumption of isotropy of the troposphere also justifies to some extent an extrapolation over space. These assumptions have to be kept in mind when we use radiosonde data to define a "well known" atmospheric state for the purpose of deriving spectral line parameters.

The radiosondes used to define the state of the troposphere for the fit of line strength parameters were launched during meteorological measurement campaign, which was carried out in the framework of the Mesoscale Alpine Project (MAP). This campaign is described in more detail in section 7.2. They were launched by a group of the Swiss Air Force in October and November 1999 in the Rhine Valley at Diepoldsau, Switzerland. The procedure to improve our model parameters using radiosonde observations is analogous to the line parameter determination by long path absorption measurements. However, there are a couple of fundamental differences: The long path cell is the troposphere itself and the absorption path is not folded but the straight slant ray path through the atmosphere. There are no homogeneous absorption conditions, temperature, pressure and absorber amount are not controlled but determined by the radiosonde instead of sensors within the cell.

The line strength parameter $S_{0,l}$ of a transition l is estimated by a least squares adjustment of a model spectrum. The partial derivative of the transmission I_i measured at wavelength λ_i according to the observation equation

$$I(\lambda_i) = \exp\Big[-\sum_l \int_{h=s_0}^{s_{trop}} \rho_w(s) \cdot S_l(s) \cdot f_l(\lambda_i, s) ds\Big] \tag{6.18}$$

with respect to $S_{0,l}$ is with Eq. 3.31:

$$\begin{aligned} A_{ij} &= \frac{\partial I(\lambda_i)}{\partial S_{0,l}} \\ &= I(\lambda_i) \cdot \Big[-\int_{h=s_0}^{s_{trop}} \rho_w(s) \sum_l \frac{S(T(s))}{S_{0l}} \cdot f_l(\lambda_i, s) ds \Big], \end{aligned} \tag{6.19}$$

where

$$S(T(s)) = S_{0l} \frac{Q(T_{ref})}{Q(T(s))} \frac{\exp[-E'' k_B T]}{\exp[-E'' k_B T_{ref}]} \frac{(1 - \exp[hc\nu_0 / k_B T(s)])}{(1 - \exp[hc\nu_0 / k_B T_{ref}])} \cdot f(\lambda_i, s) \tag{6.20}$$

Starting with the original value of $S_{0,l}$ from the HITRAN database, the line strength parameter is iteratively adjusted using:

$$\delta S_{0,l} = (\mathbf{A^T} \cdot \mathbf{P} \cdot \mathbf{A})^{\mathbf{-1}} \cdot \mathbf{A^T} \cdot \mathbf{P}(\mathbf{I_{meas}} - \mathbf{I_{model}}). \tag{6.21}$$

Here $\mathbf{A}$ is the matrix of partial derivatives A_{ij} according to Eq. 6.19, $\mathbf{P}$ is the covariance matrix of the measurements. They are assumed to be independent, which means that $\mathbf{P}$ is a diagonal matrix whose elements are the inverse variances of the differential intensity measurement:

$$\mathbf{P} = \frac{\mathbf{1}}{\sigma_{\mathbf{I}}^{\mathbf{2}}} \cdot \mathbf{I}. \tag{6.22}$$

According to section 6.2.2.2, σ_I takes the value 0.008 (0.8 % transmission). and the elements of the vectors $\mathbf{I_{meas}}$ and $\mathbf{I_{model}}$ are the measured and modeled values of differential transmission respectively. The iteration was stopped, when the convergence criterion was met, which in our case was the case when the improvements fell below the threshold value $\delta S_{0,l}^{thresh} = 1 \cdot 10^{-27} cm^{-1}$. The least squares adjustment is performed separately for individual lines within the SAMOS-spectra. Since the model for the line shape $f(\nu, s)$ deteriorates with increasing distance from the line center, only transmission measurements within the full width half maximum (FWHM) of the transition were used in 6.21. Fig. 6.33 shows the lines fitted to a SAMOS-spectrum at 838.0 nm, which can be compared to the corresponding plot 6.24 for the model spectrum before the parameter adjustment. In the way described above all identified transitions within the SAMOS measurement intervals with intensities greater than $1 \cdot 10^{-25} cm^{-1}$ were adjusted using the 9 radiosonde soundings that were launched during solar spectrometer measurements. The results of the parameter determination are tabulated in table 6.2

λ_0 nm	mean S_0 $\frac{10^{-25}cm^{-1}}{(molecule\cdot cm^{-2})}$	σ_{S_0} $\frac{10^{-25}cm^{-1}}{(molec.\cdot cm^{-2})}$	HITRAN-S_0 $\frac{10^{-25}cm^{-1}}{(molec.\cdot cm^{-2})}$	HITRAN-σ_{S_0} $\frac{10^{-25}cm^{-1}}{(molec.\cdot cm^{-2})}$	Difference $\frac{10^{-25}cm^{-1}}{(molec.\cdot cm^{-2})}$
651.8339	14.65	0.84	19.46	9.73	+4.81
651.8432	16.06	1.08	21.63	10.82	+5.57
652.1243	9.70	0.92	11.30	5.65	+1.6
740.9745	1.95	0.38	2.67	0.05	+0.72
741.2342	10.88	1.17	4.76	0.95	-6.12
787.7490	6.06	0.29	4.21	1.26	-1.85
787.8275	4.30	0.20	3.82	0.19	-0.48
787.8722	13.79	0.41	12.39	0.62	-1.4
787.8869	4.21	0.15	2.84	0.28	-1.37
789.5681	22.10	0.64	20.22	1.01	-1.88
789.7677	19.47	0.88	17.61	0.88	-1.86
789.8198	28.64	1.18	24.24	1.21	-4.4
795.8354	3.58	0.18	4.04	0.20	+0.46
796.0674	32.29	1.58	27.61	1.38	-4.68
796.2451	12.04	1.82	9.30	1.86	-2.74
796.2916	25.29	1.15	21.09	1.05	-4.2
796.3797	11.43	0.67	8.09	2.43	-3.34
802.2916	11.89	1.17	11.96	1.20	+0.07
802.4268	6.76	0.94	6.27	0.63	-0.49
802.5153	4.95	0.78	4.93	0.49	-0.02
802.5372	9.57	0.41	8.98	0.45	-0.59
804.5364	13.55	0.95	12.17	1.22	-1.38
804.5806	4.67	0.49	3.71	0.19	-0.96
804.6094	7.00	0.87	4.77	0.48	-2.23
804.6598	11.44	1.41	8.74	0.87	-2.7
804.7723	15.51	1.44	12.94	0.65	-2.57
825.4991	76.62	3.09	64.79	6.48	-11.83
834.3730	5.66	0.09	4.58	1.37	-1.08
834.4562	29.68	1.91	24.24	1.21	-5.44
834.9624	7.77	1.26	5.10	1.02	-2.67
835.1454	36.72	1.85	30.33	1.52	-6.39
835.1669	6.87	0.41	4.02	0.20	-2.85
835.1685	14.98	1.24	19.02	0.95	+4.04
835.2260	2.88	0.32	2.11	0.11	-0.77
837.6837	3.52	0.22	6.27	0.63	+2.75

Table 6.2: Results of line strength parameter determination using 9 radiosonde soundings and SAMOS spectra. The fit results and their standard deviation are given in columns 1 and 2. In column 4 and 5 the corresponding values from the HITRAN database are tabulated. The last column shows the difference between the fit result and the HITRAN value for line strength. The table in continued in 6.3.

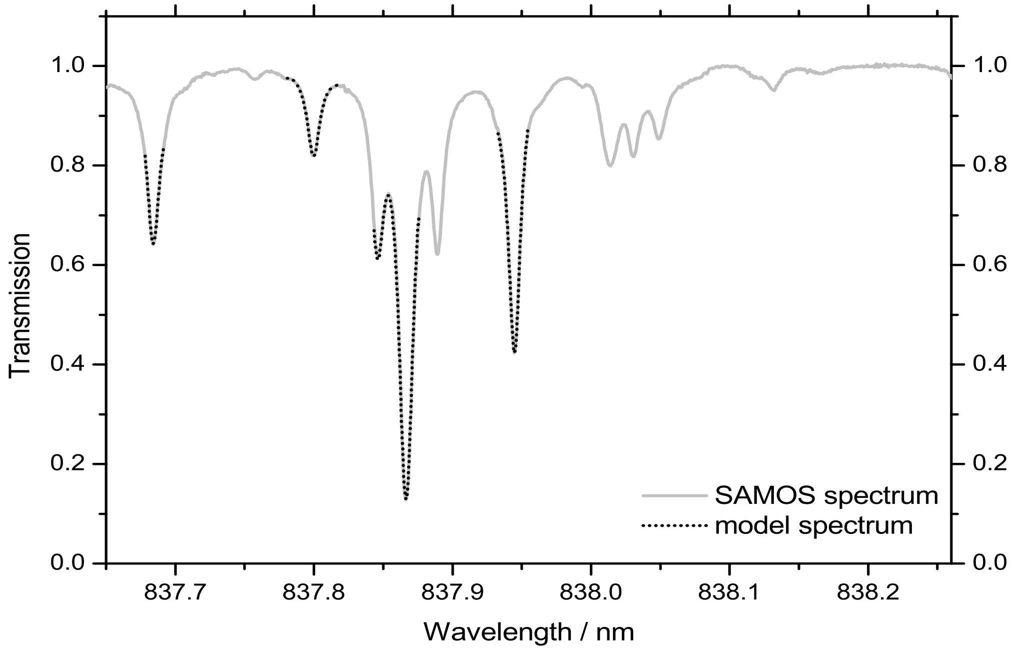

Figure 6.33: Fit of line strength parameters to a measured SAMOS spectrum centered at 838.0 *nm*. The dotted lines depict the adjusted lines. This can be compared to Fig. 6.24, where the original HITRAN parameters were used.

λ_0 nm	mean S_0 $\frac{10^{-25}cm^{-1}}{(molecule\cdot cm^{-2})}$	σ_{S_0} $\frac{10^{-25}cm^{-1}}{(molec.\cdot cm^{-2})}$	HITRAN-S_0 $\frac{10^{-25}cm^{-1}}{(molec.\cdot cm^{-2})}$	HITRAN-σ_{S_0} $\frac{10^{-25}cm^{-1}}{(molec.\cdot cm^{-2})}$	Difference $\frac{10^{-25}cm^{-1}}{(molec.\cdot cm^{-2})}$
837.6844	3.74	0.16	7.07	0.35	+3.33
837.7998	2.70	0.25	2.63	0.13	-0.07
837.8460	5.23	0.71	5.54	1.11	+0.31
837.8666	28.02	2.16	24.24	1.21	-3.78
837.9450	10.36	1.16	8.86	0.44	-1.5
838.6477	11.45	0.21	9.35	0.94	-2.1
838.7155	3.21	0.21	2.42	0.24	-0.79
838.7299	2.30	0.05	1.98	0.10	-0.32
838.7797	8.16	0.14	6.88	0.69	-1.28
839.6315	10.89	0.51	9.14	0.46	-1.75
892.9332	11.00	0.71	7.59	2.28	-3.41
893.1507	62.45	5.73	35.33	10.60	-27.12
893.1921	6.66	1.15	7.53	2.26	+0.87
893.2710	36.59	3.98	30.11	9.03	-6.48

Table 6.3: Continuation of table 6.2

From the table one can see that the difference between the fit results and the HITRAN values (last column in table 6.2 exceeds the error tolerance given by the accuracy indices of the database for 73 % of the transitions, although in most cases only slightly. The standard deviations for the parameters determined by fitting the model to SAMOS spectra are greater for stronger lines, the relative errors range from 2% to 18%. This is in most cases lower than the relative errors of the HITRAN laboratory results, which can be greater than 30 %. The largest corrections are made to the least accurately determined HITRAN values.

It is obvious that all errors induced by approximations of the absorption path geometry (e.g. bended ray path), meteorological conditions along the ray path (deviations from horizontal homogeneity), as well as measurement error of the radiosondes and SAMOS will propagate into the values for the line strength parameters S_0 which are determined. However, it is also evident, that the discrepancies between the atmospheric state defined on the basis of a radiosonde sounding and the true state will affect all the spectral parameters of the measured lines in the same way. A systematic error in the humidity measurement of the radiosonde will e.g. lead to an overestimation of the precipitable water vapor content PW by, say 5 %. This error will propagate directly into the line parameters determined in the least squares estimation with fixed water vapor density profile $\rho_w(s)$ using Eq. 6.18. Any systematic error of a radiosonde measurement used in the parameter fitting will therefore result in an offset of the SAMOS PW retrievals with respect to the true value which should be equal for all corrected transitions. The radiosondes are assigned the role of an absolute calibration device. The main purpose of the parameter determination, however, is the improvement of redundancy of retrievals from different H_2O-lines. The relative accuracy of the line intensities are effectively improved by the procedure described above, since SAMOS measures all transitions with the same accuracy and all error sources originating from the absorption medium (radiosonde observation error, interpolation of meteorological profiles) affect the simultaneously measured lines equally. The improvement of redundancy is demonstrated by a comparison of the PW time series plotted in Fig. 6.31 in section 6.3.3 with the reprocessed time series of the same data in Fig. 6.34. As can be seen the offsets between the time series derived in different wavelength intervals have been significantly reduced.

6.4 Estimation of Precipitable Water Vapor

The processing of SAMOS spectra for retrieval of precipitable water is based on a least squares fit of the radiative transfer model outlined in chapter 3 to the differential absorption spectra after being pre-processed following the procedure described in section 6.2.2.2. The retrieval algorithm works similar to the line parameter fitting described in section 6.3.4.2 with the difference that the line strength parameters are kept fixed in the adjustment and the water vapor content is parameterized and adjusted instead. Another difference is that the vertical profiles $p(h)$, $T(h)$ and $\rho(h)$

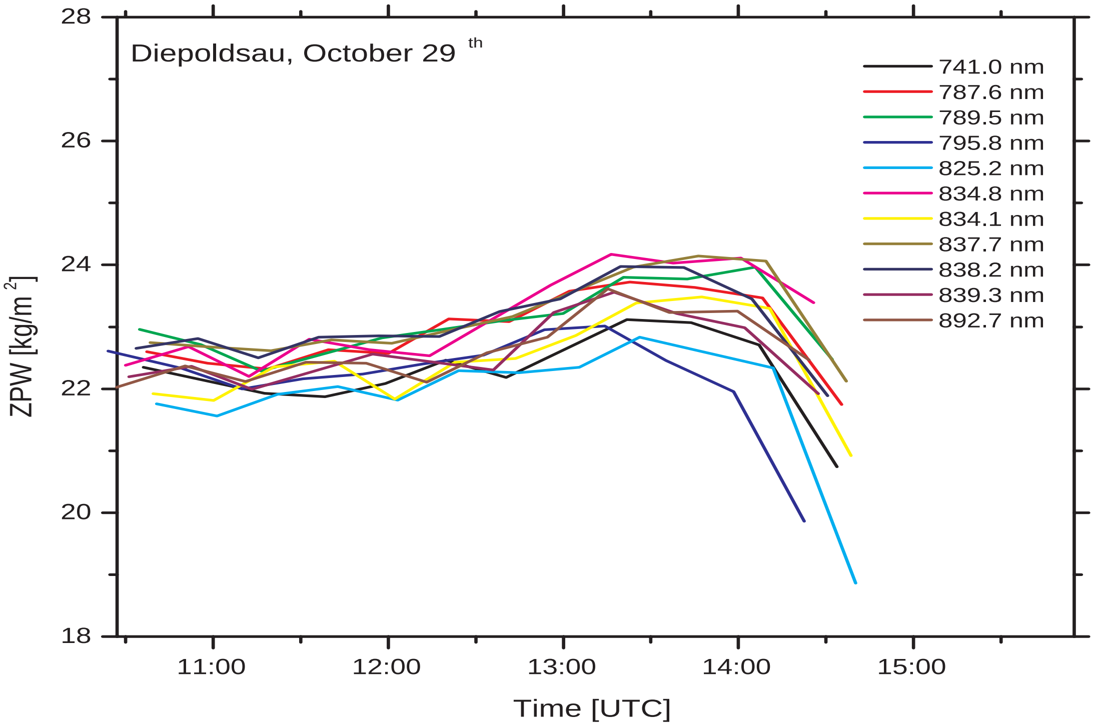

Figure 6.34: Time series of zenith precipitable water (ZPW) from SAMOS spectra using the improved line strength parameters. The offsets between the retrievals from different measurement windows are significantly reduced compared to Fig. 6.31

are unknown and therefore some assumptions on the meteorological profiles have to be made. This is where the meteorological models described in section 3.9 come into play. The way these model are introduced depends on the availability of a-priori information, e.g. from radiosonde observations. The impact of such information will be investigated in section 7.4. Let us first assume the absence of any a-priori information on vertical distributions of meteorological parameters. In this case we use the simple standard models for the vertical profiles given by Eq. 3.53.

In the absence of a nominal profile for the vertical distribution of molecular density the profile of absolute humidity $\rho_w(h)$ is assumed to be exponential:

$$\rho_w(h) = \rho_s \cdot \exp\left[-\frac{h-h_s}{H_w}\right], \tag{6.23}$$

where H_w denotes the scale height for absolute humidity (see section 3.9). Inserting this simple model of the humidity profile into the observation equation 3.56 gives

$$I'(\nu) = \exp\Big[- \rho_s \cdot \int_{s_0}^{s_{trop}} \exp\Big[- \frac{h(s) - h_0}{H_w} \Big] \cdot k_l(\nu, s)\, ds \Big] \tag{6.24}$$

where the integral is calculated along the ray path of the sunlight. Note that the height $h(s)$ is therefore a function of the integral path s given by Eq. 3.51 in section 3.8. In order to express the transmitted intensity in terms of the integral water vapor abundance along this path, we insert the definition for the slant precipitable water vapor SPW:

$$\mathrm{SPW} = \rho_s \cdot \int_{s_0}^{s_{trop}} \exp\Big[- \frac{h(s) - h_0}{H_w} \Big]\, ds \tag{6.25}$$

which yields the observation equation for processing of precipitable water vapor:

$$I(\lambda) = \exp\Big[- \mathrm{SPW} \cdot \frac{1}{\sigma} \int_{s_0}^{s_{trop}} \exp\Big[- \frac{h(s) - h_0}{H_w} \Big] \cdot k(s, \lambda)\, ds \Big], \tag{6.26}$$

where the factor σ in this model is the constant of proportionality between SPW and the surface absolute humidity $\rho_{w,s}$ given by

$$\sigma = \frac{\mathrm{SPW}}{\rho_{w,s}} = \int_{s_0}^{s_{trop}} \exp\Big[- \frac{h(s) - h_s}{H_w} \Big]\, ds. \tag{6.27}$$

Because of Eq. 3.51, σ depends on the solar elevation angle θ_{sun}. It has the significance of a “mapping term”, which relates the slant precipitable water SPW with the zenith value ZPW defined by

$$\begin{aligned} \mathrm{ZPW} &= \rho_{w,s} \int_{h_s}^{h_{trop}} \exp\Big[- \frac{h - h_s}{H_w} \Big]\, dh \\ &= \frac{\mathrm{SPW}}{\sigma} \Bigg[- H_w \cdot \exp \frac{-h - h_s}{H_w} \Bigg]_{h_s}^{h_{trop}} \\ &= \frac{\mathrm{SPW}}{\sigma} \cdot H_w \cdot \Big(1 - \exp\Big[\frac{-h_{trop} - h_s}{H_w} \Big] \Big). \end{aligned} \tag{6.28}$$

In the iterative least squares adjustment the parameter SPW is determined and then mapped to the zenith using Eq. 6.28 to yield the zenith precipitable water. The partial derivative of the measured differential intensity $I(\lambda)$ with respect to SPW is according to 6.26:

$$\frac{\partial I(\lambda)}{\partial SPW} = I(\nu) \cdot \Big[-\frac{1}{\sigma} \cdot \int_{s_0}^{s_{trop}} \exp \Big[-\frac{h-h_s}{H_w} \Big] \cdot k(s,\lambda)\, ds \Big], \tag{6.29}$$

As mentioned in the beginning of this section, SPW is determined in a least squares adjustment of the radiation transfer model to the measured spectra. For this, the vector of partial derivatives $\mathbf{K}$ with elements

$$K_i = \frac{\partial I'(\lambda_i)}{\partial SPW} \tag{6.30}$$

is calculated for the measured wavelengths λ_i as determined in the pre-processing stage (see section 6.2.1). The start value SPW_0 is calculated by Eq. 3.53 using the surface values of temperature, pressure and relative humidity measured by the meteo-sensors at the ground. The fit parameter SPW is then estimated in an iterative procedure, in which the improvement to the previous SPW estimate ΔSPW is given by:

$$\Delta SPW = (\mathbf{K^T} \cdot \mathbf{P} \cdot \mathbf{K})^{\mathbf{-1}} \cdot \mathbf{K^T} \cdot \mathbf{P}(\mathbf{I_{meas.}} - \mathbf{I_{model}}) \tag{6.31}$$

Here, the $\mathbf{I_{meas}}$ and $\mathbf{I_{mod}}$ are the vectors of transmission measurements and their theoretical values calculated by the radiation transfer model using the actual value of SPW. The iteration is performed until the convergence criterion is met. As such we defined the accuracy level $\Delta SPW_t = 0.01$ mm. Typically the improvement ΔSPW fell below this threshold value after 3-5 iterations. The procedure described above is carried out using only the transmission measurements within the processing intervals, given by the full width half maximum (FWHM) of the spectral lines, whose spectral line parameters were improved (see section 6.2.1). Each spectrum was processed separately, forming a single measurement $\mathbf{I_{meas}}$ and model vector $\mathbf{I_{mod}}$ respectively (see Fig. 6.35). In addition to the processing intervals the baseline intervals, whose transmission values were used to normalize the DOAS spectra (see section 6.2.2) were considered in the processing procedure. This is necessary in order to account for the continuum absorption or far line wing contributions which have been eliminated in the pre-processing, but are still present in the model spectra. The problem is illustrated in Fig. 6.35. The baseline interval of the model spectrum is used to normalize the theoretical transmissions $\mathbf{I_{mod}}$ of the processing intervals in the same manner as the measured transmissions with the difference that no stray light parameters have to be determined.

By applying the procedure described above to a continuous dataset of solar spectra, time series of precipitable water are obtained. These time series are the results which can be converted into path delay corrections for transatmospheric microwave signals using Eq. 2.15 (see section 2.1.2). The results obtained from various measurement campaigns deploying SAMOS simultaneously with other techniques are presented and compared in the subsequent chapter.

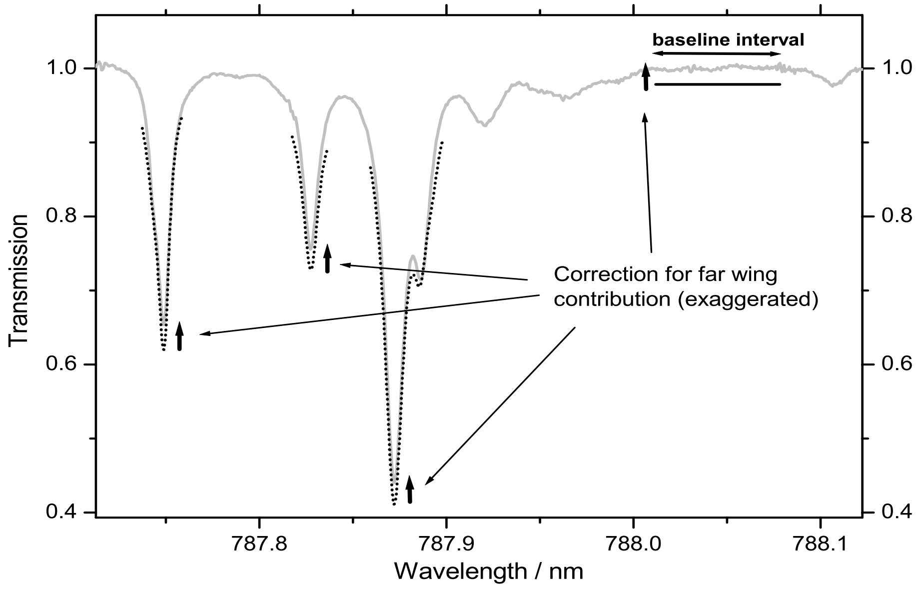

Figure 6.35: Normalization of model spectra in processing intervals using the baseline interval. This is done in order to account for the far wing contributions of line absorption, which are not neglectable in the baseline interval. These contributions have been removed from the measured spectra by the normalization procedure (section 6.2.2). The magnitude of this correction has been exaggerated in the plot for better presentation.

7 Campaigns and results

7.1 The Hawaiian Water Vapor Experiment

7.1.1 Project context

The first time SAMOS was deployed in the field was during an experimental campaign on the Big Island of Hawaii, USA. The international field experiment was initiated by ETH Zurich and was actively supported by several groups collaborating in the EU-project WAVEFRONT (Dodson et al. [1999]). This project was dedicated to study the potential and feasibility of ground based GPS meteorology (see 2.3) for operational weather forecasting. One objective of the WAVEFRONT project was the development of a technique to derive three- and four dimensional distributions of tropospheric humidity from a GPS network using a tomographic analysis scheme. GPS tomography is currently under investigation by a number of groups worldwide (e.g. Kruse [2000], Flores et al. [2000]). This new technique requires a dense network of closely spaced receivers. Large differences in station altitudes are of advantage for decorelation of the three- dimensional water vapor field. These conditions are fulfilled by the continuous GPS (CGPS) network operated in the Mt. Kilauea area by the U.S. Geological Survey, the University of Hawaii and the University of Stanford. The network is located in the Volcano National Park and incorporates 16 receivers in an area of 15×20 km. Fig. 7.1 shows a map indicating receiver positions and the topography in the experiment area. The purpose of the fully automated network is the measurement of tectonic motions caused by volcanic activity. The extraordinary close spacing and extreme fluctuations of tropospheric humidity provide excellent conditions for methodological studies of water vapor determination. In order to validate 3D water vapor distributions derived from GPS, a multitude of different techniques was deployed simultaneously during the Hawaii experiment. Beside SAMOS, the two ETH water vapor radiometers were operated, which were calibrated to the local climate conditions using a radiosonde dataset from Hilo airport. A total of 18 radiosondes were launched within the measurement area. In addition, a network of ten meteorological stations was recording ground values of pressure, temperature and relative humidity in 10 minute intervals. Details on the GPS tomography experiment can be found in the recently published PhD thesis of L.P. Kruse (Kruse [2000]). The GPS results used in the comparison presented below are taken from this thesis.

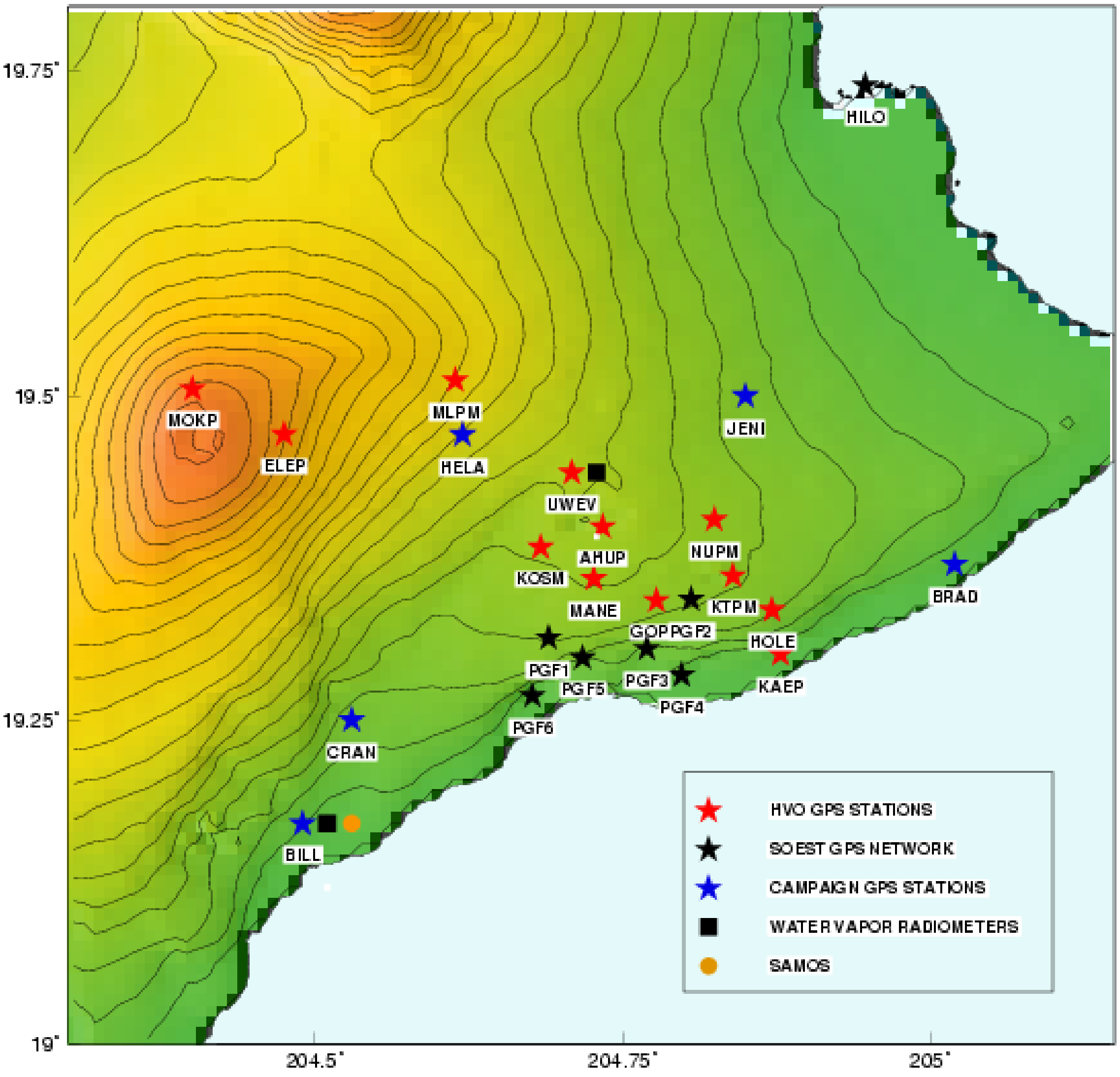

Figure 7.1: GPS stations operated during the campaign. SAMOS was operated at the station BILL in co-location with a WVR and a GPS receiver. Also, seven radiosondes were launched from this site. The permanent CGPS network (*stars*) consists of 6 sites operated by the School of Ocean Earth Science and Technology (SOEST) of the University of Hawaii and 12 stations installed by the Hawaiian Volcano Observatory (HVO, see legend). The altitude difference from the lowest to the highest GPS station (PGF4 - MOKP) is about 4100 meters. The climate of the network region ranges from tropical in the east to arid in the west(from [Kruse, 2000]).

7.1.2 SAMOS measurements on Hawaii

The SAMOS prototype was operated at two locations during the Hawaiian campaign: The first was the "master station" BILL (see Fig. 7.1), where one of the two WVR and a co-located GPS receiver were operated. The instrumentation was installed on the private realty of Mr. William Albrecht of Pahala, who kindly provided his property for the measurements. Also, seven radiosondes were launched from this site. Unfortunately, unfavorable weather conditions were prevailing during the two-week experiment in the south eastern part of the island, with dense cloud cover regularly occurring in the early afternoon. Therefore most PW time series acquired at the station BILL only cover a few hours. In the western part of Hawaii´s Big Island a different local climate prevails and the area around the city of Kona is said to be one of the sunniest places in the United States at sea level. In order to obtain more SAMOS data we transfered the instrument to Kona during a rainy period in the Pahala area. SAMOS was operated for two days at the Natural Energy Laboratories of Hawaii (NELH), about 10 km north of Kona. There we were able to acquire two complete PW time series lasting from sunrise to sunset. During that time, a GPS receiver was installed at NELH and integrated into the campaign network. The GPS estimates of PW derived from this receiver are the only comparison to the SAMOS retrievals at Kona.

One important point to mention before the campaign results are presented is that the wavelength intervals measured during the Hawaii campaign do not correspond to the selection results presented in section 4.3.4. This is because the selection algorithm described there was not fully implemented at the time when the campaign was scheduled. Instead, the measurement windows at that stage of the project were chosen among intervals with wide baseline intervals and covering a wide spectral range. Although not optimum in the sense of the criteria formulated in section 4.3.4, these intervals, which are tabulated in table 7.1, are also suited for retrieval of PW time series. In the same way as for the finally selected intervals listed in table 4.1, the line parameter accuracies turned out to be insufficient to provide redundant PW estimates from all measured intervals (see section 6.3.3). Therefore a line parameter fit was performed analogously to the procedure described in section 6.3.4.2. The difference is that the radiosonde dataset was much smaller and of poorer quality than the MAP dataset[1]. The line strength parameters were determined using just one single radiosonde sounding launched at the station BILL on February 19th, when clear weather conditions allowed the acquisition of a long series of spectra. If a radiosonde profile is sufficiently accurate this calibration procedure is appropriate and the results can be applied without the need of further soundings. However, since there is no statistical information about the accuracy of the parameter fit, the results for the line strengths will not be tabulated here. When comparing the PW time series of SAMOS with those of WVR and GPS, it must be kept in mind that SAMOS was calibrated to match the integrated radiosonde profile of February 19th, which was in good agreement with the GPS estimate of PW (see 7.6). This fact is particularly important for interpreting the bias between the different methods.

---

[1] The MAP radiosondes were calibrated before each launch in special calibration chambers. This effort could not be realized in the Hawaiian field experiment

Interval Nr.	λ-range [nm]	width [nm]	lines
1	601.27 - 601.66	0.39	7
2	659.30 - 659.80	0.50	9
3	738.86 - 739.52	0.66	25
4	819.69 - 820.46	0.77	15
5	825.38 - 825.96	0.58	8
6	834.05 - 834.78	0.73	23
7	836.08 - 836.76	0.68	11
8	835.60 - 836.25	0.65	12
9	839.34 - 839.90	0.56	14
10	845.82 - 846.61	0.79	9
13	892.60 - 893.33	0.73	6

Table 7.1: Wavelength windows measured in the Hawaii-campaign.

7.1.3 Results and comparison of different techniques

The results from the continuous GPS receiver and the WVR operated at the station BILL are plotted in Fig. 7.2 for the entire observation period from February 12th to February 28th, 1999. The plot demonstrates the large fluctuations of precipitable water vapor, with regular daily variations of up to 20 kg/m^2 PW. Although the time series of both methods reflect these variations the difference plot below shows large differences between the two techniques which can reach up to 6 kg/m^2 with a standard deviation of 2.32 kg/m^2. These values are by far higher than the figures reported in other comparison studies (e.g. Rocken et al. [1995]). A closer look at the features in 7.2 reveals that the GPS time series exhibits higher and lower peaks especially after steep increases or drops in water vapor content (e.g. Feb. 12-13 and Feb. 18-20.). The results give the impression that the GPS estimates seem to overestimate the fluctuations by reacting too inert and missing the turning point. The rather bad agreement between GPS and WVR demonstrates that a third independent technique is required to make a judgment about their performance. The results of the SAMOS retrievals are plotted Fig. 7.4 - 7.11. Each point on the SAMOS curve corresponds to an average zenith-mapped value of PW calculated from the 13 measured spectral intervals (listed in table 7.1) of a complete wavelength scan. The offsets between the retrievals from individual wavelength windows range within 0.5 kg/m^2 and are stable like those plotted in Fig. 6.31 in section 6.3.3.

When comparing the spectrometer results with those of GPS and WVR, it must be kept in mind that the retrievals of the solar spectrometer are slant water vapor estimates pointed to the Sun and then mapped to the zenith. A time series of the original slant PW retrievals from solar spectra is plotted in Fig 7.3. It was recorded on February 23rd in Kona, the day with the longest sunshine duration, and can be compared to the corresponding zenith-mapped results plotted in Fig 7.10. In contrast to this unidirectional measurement GPS and also WVR retrievals are averaged over the entire hemisphere. The radiometer scans the sky homogeneously in 8 azimuths and 8 elevations and the single path delay estimates are mapped to zenith. This results in a scattered signal whose bandwidth is determined by the instrument noise and differences which arise from azimuthal anisotropies of the humidity distribution. Using the processing scheme implemented for the ETH radiometers it is impossible to distinguish between these two components. Therefore the WVR curves are smoothed by adjacent averaging over 64 pointings. The averaging effect of GPS retrievals is an inherent consequence of estimating a single tropospheric parameter from phase measurement acquired over a period of time (30 minutes in our case) and using the entire constellation of visible satellites.

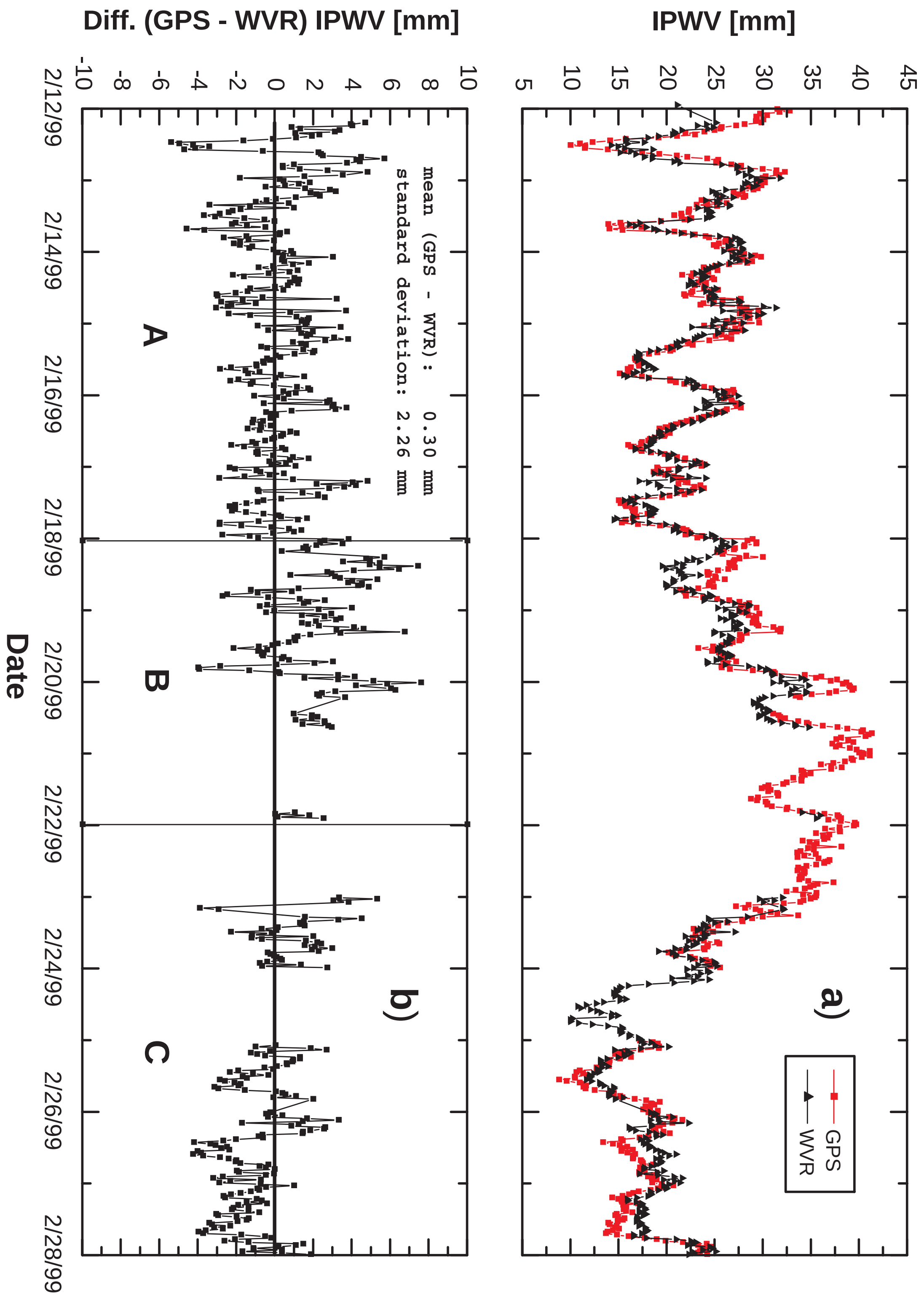

Figure 7.2: a) PW estimates from GPS and WVR and b) GPS - WVR differences as observed at the station BILL. Changes in the offsets between GPS and WVR are marked with vertical lines dividing the time series into three intervals A, B and C (from [Kruse, 2000])

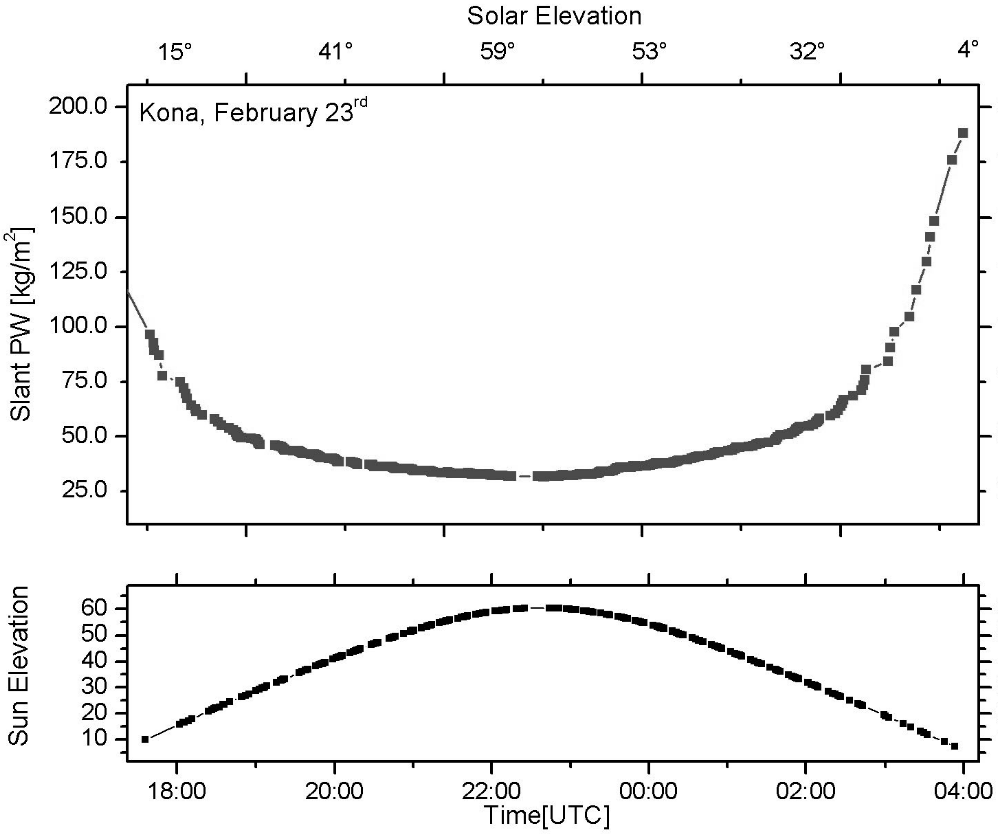

Figure 7.3: Time series of slant precipitable water in the direction towards the Sun recorded on February 23rd in Kona. The lower plot indicates the solar elevation angle. The results are mapped to the zenith as described in section 3.8 to yield the zenith PW time series plotted in Fig. 7.10

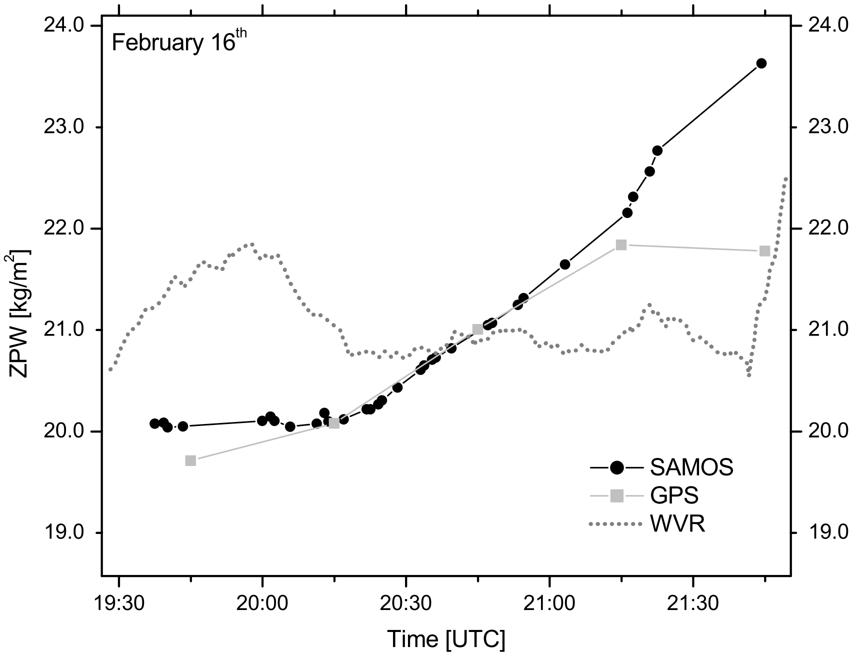

Figure 7.4:

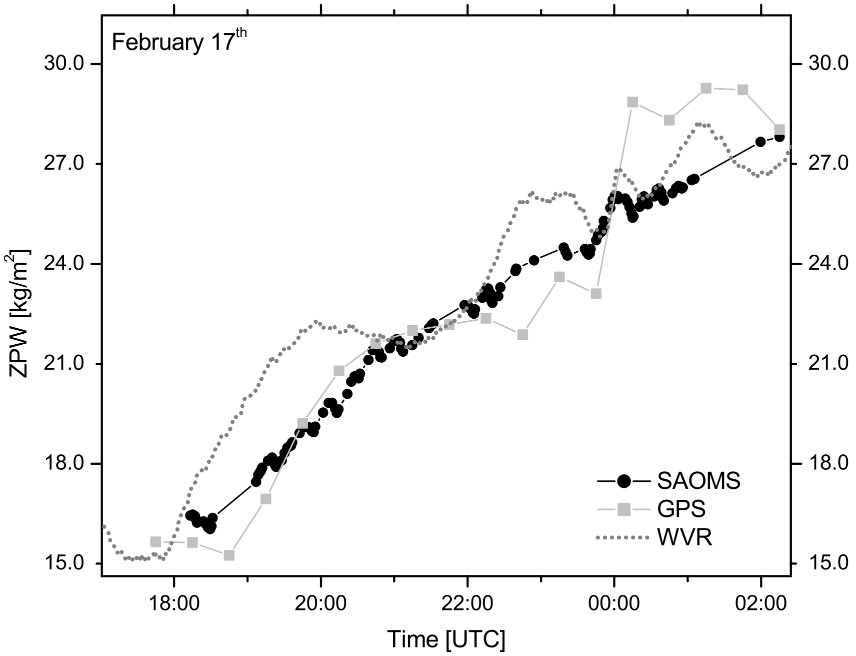

Figure 7.5:

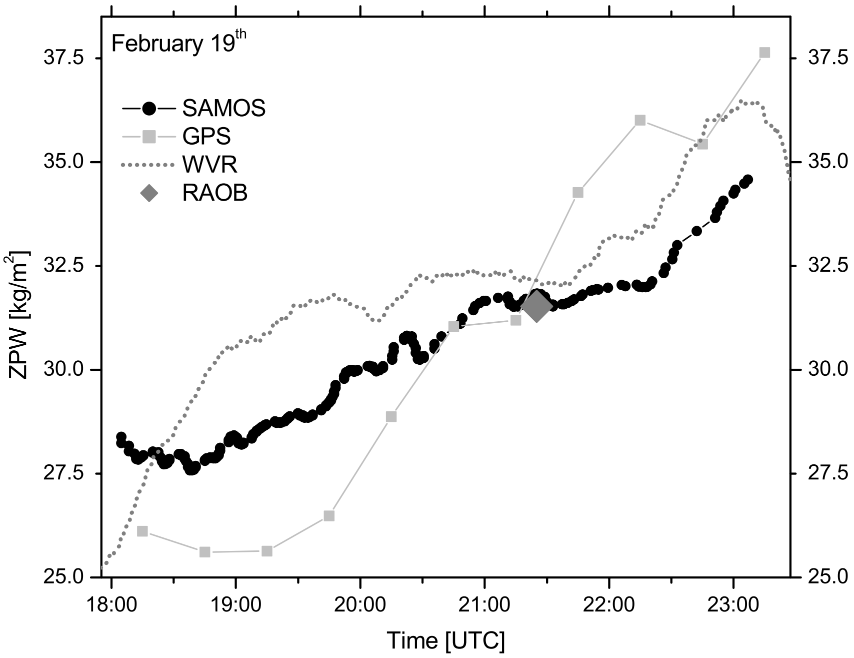

Figure 7.6:

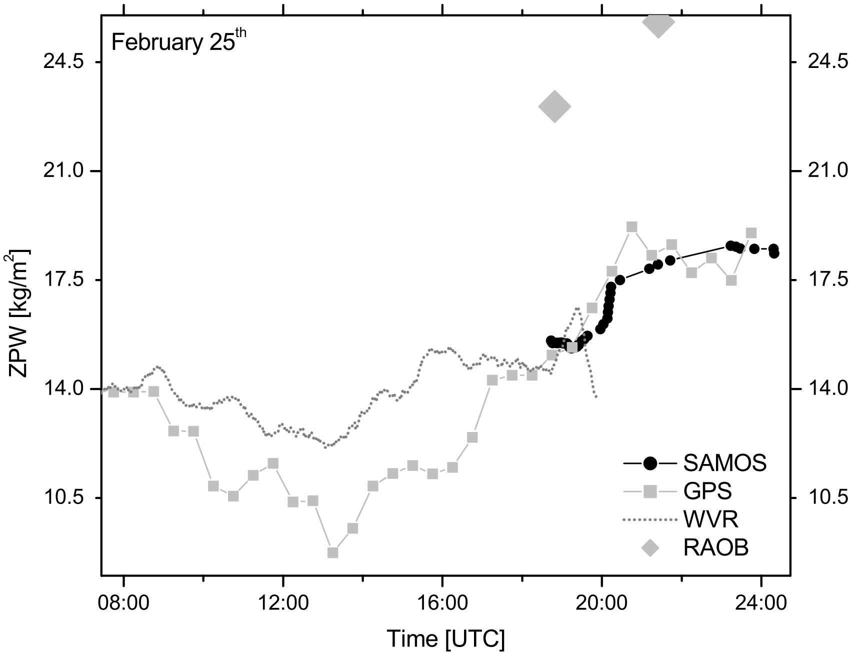

Figure 7.7:

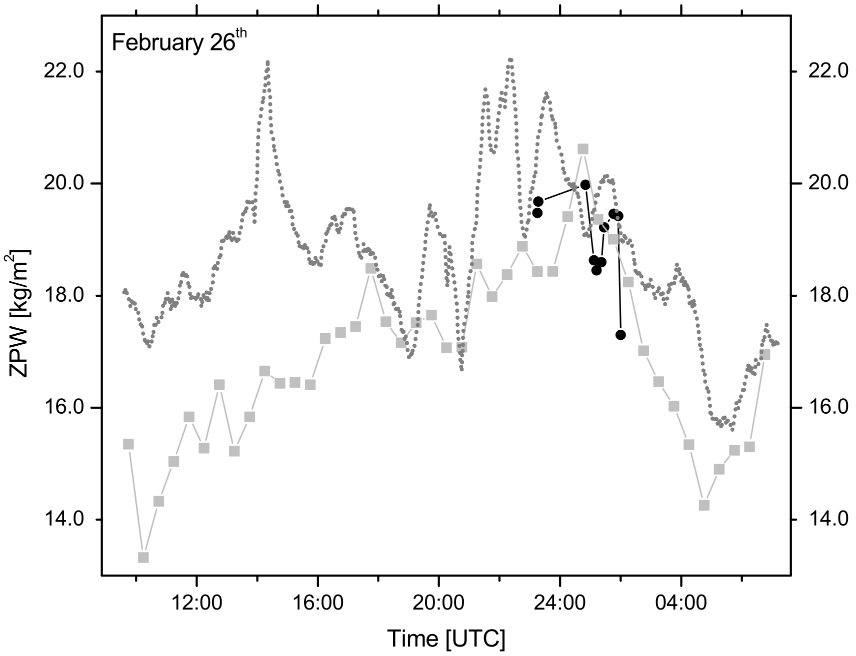

Figure 7.8:

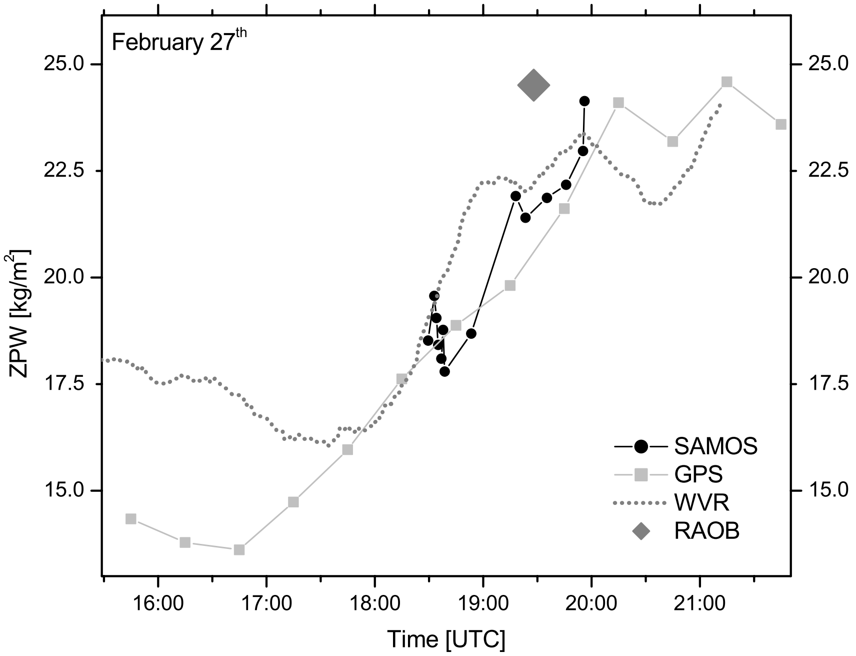

Figure 7.9:

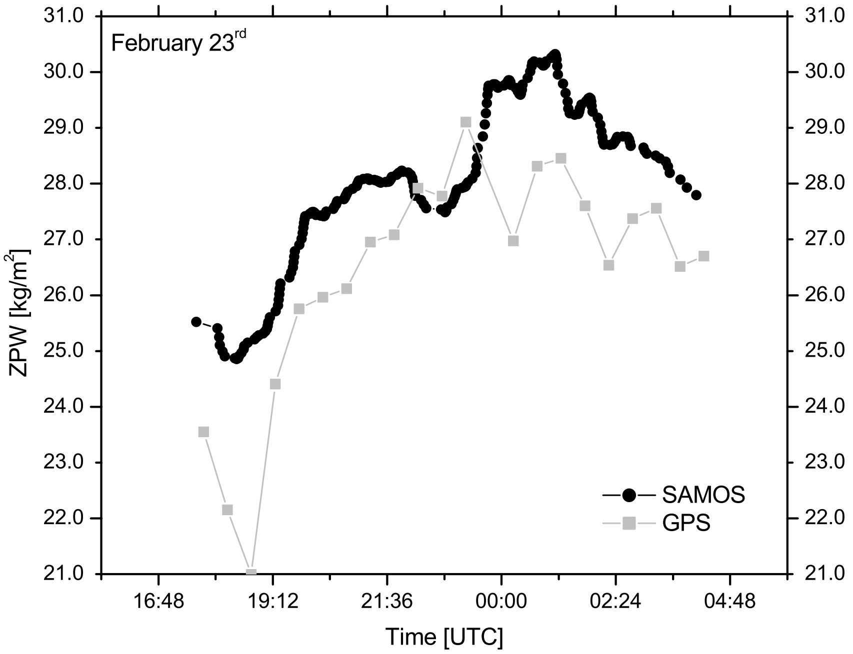

Figure 7.10:

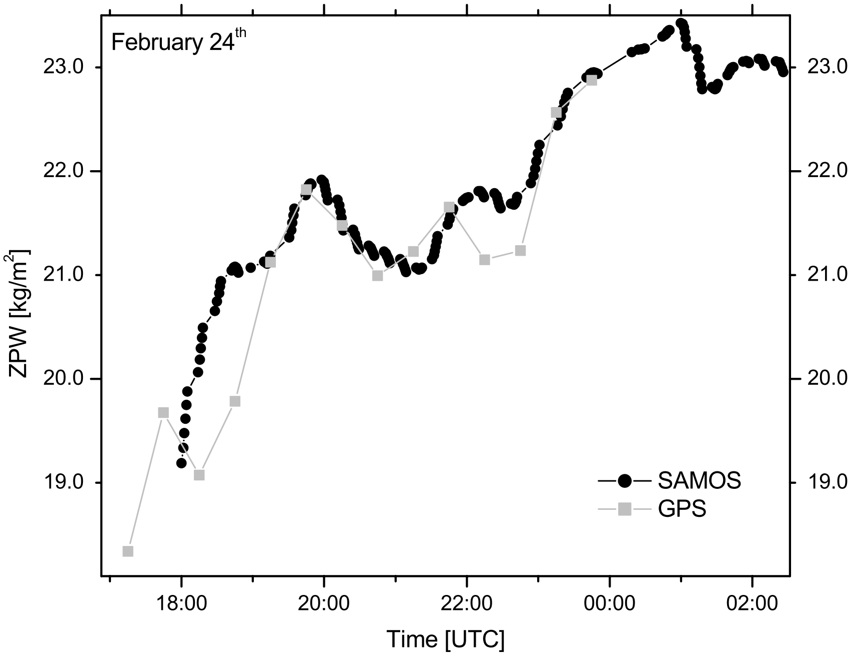

Figure 7.11:

The comparison of time series recorded at station BILL show a good general agreement between the three remote sensing techniques. It is not possible to draw definite conclusion on the origins of the discrepancies observed in Fig. 7.2 As pointed out in the previous section, the February 19 radiosonde was used to determine the line strength parameters for the SAMOS spectra, which is equivalent to an external calibration of the spectrometer. The integrated humidity profile of this particular radiosonde sounding was is good agreement with the GPS estimates at the time of the launch. The use of only one radiosonde forces the SAMOS retrievals onto the PW level of this balloon sounding and the good agreement with GPS at this time leads to a very low bias between GPS and SAMOS. However, comparing GPS with other radiosonde launches (see e.g. Fig. 7.7) the good agreement on February 19 might be coincidental. The comparison of the Hawaii results is therefore only of limited value for the analysis of GPS-WVR discrepancies. Large deviations are also observed between SAMOS and GPS, even on February 19 (Fig. 7.6). The PW amounts retrieved from SAMOS spectra are between the GPS and WVR results in the early morning hours (18:00-21:00 UTC, note the 10 hours time difference to GMT). The increase of humidity detected by GPS is much steeper than the SAMOS curve (with the intersection almost exactly when the radiosonde was launched) and finally reaches the WVR curve. Disregarding the bias, the slope and shape of the SAMOS time series agrees better with the WVR series than with the GPS estimates. Some GPS estimates (e.g. on February 23rd at 18:45 UTC, 00:20 UTC and 02:20 UTC) seem to be outliers, which implies that the temporally large deviations between WVR and GPS are due to errors in the GPS estimates.

In Fig. 7.12 scatter plots for the three comparison pairs are presented. Radiosondes were not included in the comparison because of their small number and the wide distribution of launch locations over the measurement area. Plot a) reveals the good agreement between SAMOS and WVR over the entire range of PW values (note that water vapor abundances up to 40 kg/m^2 have been observed in the tropical climate), but it also exhibits some features which seem to be systematic. These are not present in the SAMOS-GPS comparison but the linear fit yields a slope < 1 (0.93). This tendency is even more extreme for the WVR-GPS comparison (plot c)), (slope $= 0.8$) which suggests that GPS tends to underestimates PW at low levels and overestimates in a very humid atmosphere. This tendency can be classified as an "exaggerating" effect, which will be further investigated in the subsequent sections.

The overall comparison statistics of the Hawaiian campaign are presented in table 7.2. The standard deviation between time series is lowest for the SAMOS-WVR comparison. A good agreement with low bias is also observed between SAMOS and GPS, while the GPS-WVR comparison reflects the large discrepancies seen in Fig. 7.2.

In summary it can be pointed out that SAMOS was operated successfully in its first deployment during the Hawaii´99 experiment. It was proved that the technique is capable of deriving time series of precipitable water from solar spectra. The comparison with WVR and GPS showed a satisfactory agreement. Due to the fact

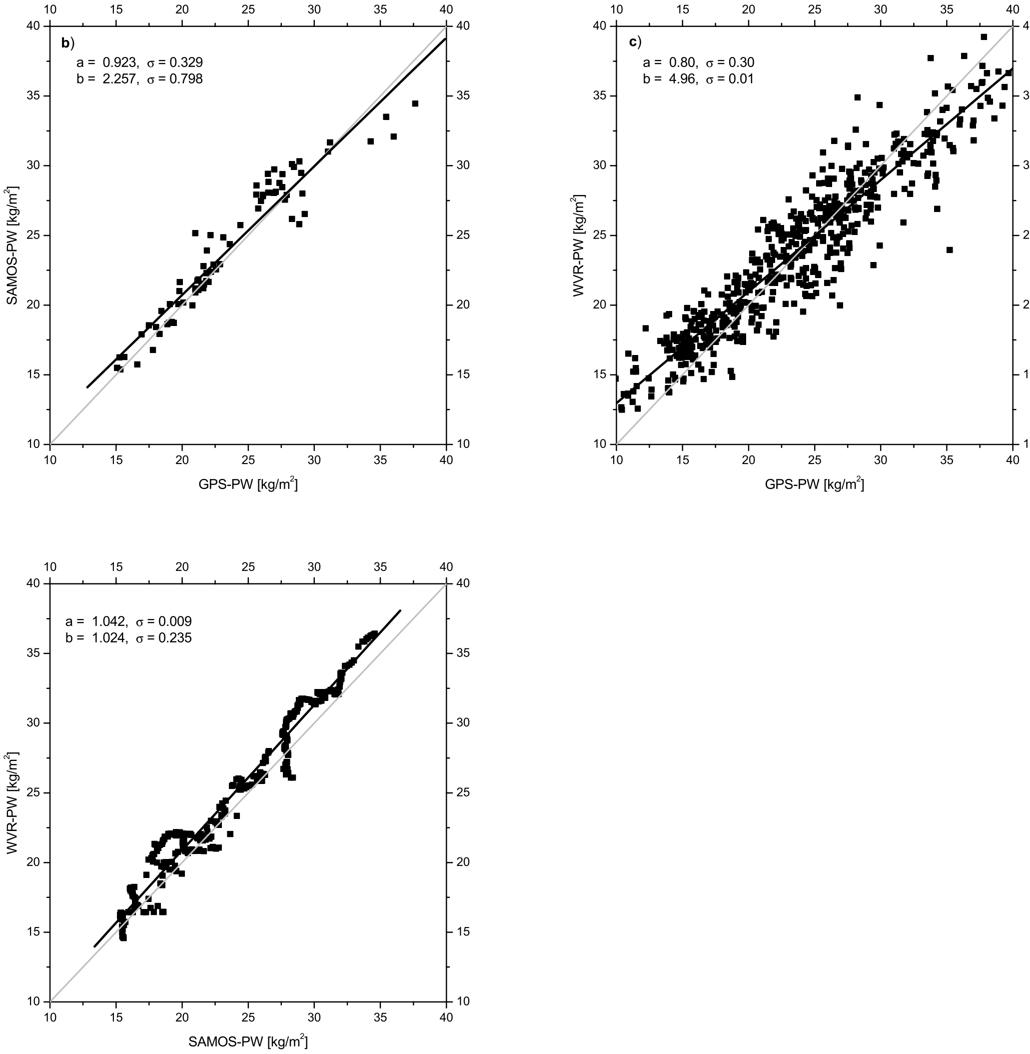

Figure 7.12: Scatter plot for the comparison of PW retrievals during the Hawaiian campaign

Difference	bias kg/m^2	stddev kg/m^2	observations
SAMOS-GPS	0.44	1.47	75
SAMOS-WVR	-1.10	1.12	478
GPS-WVR	-0.30	2.26	540

Table 7.2: Comparison statistics of the Hawaiian campaign. Each observation corresponds to an average PW over 30 minutes of measurements.

that in this first campaign SAMOS was not fully optimized in term of measurement wavelengths and a single radiosonde had to be used to improve line parameters, we are reluctant to draw quantitative conclusions about the performance of the different techniques. This requires more extensive comparisons, which will be carried out in the following sections.

7.2 The Mesoscale Alpine Project

The second field campaign, in which SAMOS was deployed was carried out in October 1999 in the framework of the Mesoscale Alpine Programme (MAP). MAP is an international research initiative devoted to the study of atmospheric and hydrological processes over mountainous terrain. A variety of scientific objectives are addressed in the context of weather and climate over complex topography. The project aims towards a better understanding of meteorological processes in the Alpine region and to contribute to an improvement of current weather forecasting capabilities. For a more detailed overview of the MAP project the reader is referred to the project web page (http://map.ethz.ch).

A large-scale field phase in the Alpine region took place from September 15 to November 15, 1999. A broad variety of measurement systems was deployed all over the Alpine regions, including a network of surface stations, radiosonde launch sites and various remote sensing instruments. This provided an excellent opportunity for a field deployment of SAMOS, in order to validate the technique by comparisons with independent methods. Therefore an additional field experiment was arranged which was conducted in parallel with the activities during the MAP project and will be described in the following sections.

7.2.1 Continuous measurements in the Rhine Valley

A sub-program in the framework of MAP was dedicated to investigation of Foehn-related phenomena. The program called FORM ("Foehn in the Rhine Valley during MAP") was limited to the Rhine Valley area, where numerous weather observation stations were operated during the field phase of the MAP project. A map of the target area with the site locations is shown in Fig. 7.13. The radiosonde launch site at Diepoldsau was installed and operated by the Swiss Army (Wetterkompanie 1). During the so-called Special Observation Period (SOP) high altitude radiosondes type P-760 were launched on a regular basis every 6 hours. The launch frequency was increased to every 3 hours during Intensive Observation Phases (IOP), that were announced during periods with Foehn-winds. In total, 112 balloon soundings were performed at the Diepoldsau station during the period of simultaneous measurements.

With friendly permission of the MAP operation center SAMOS was installed at the Diepoldsau radiosonde launch site from September 24 to November 5, 1999. During

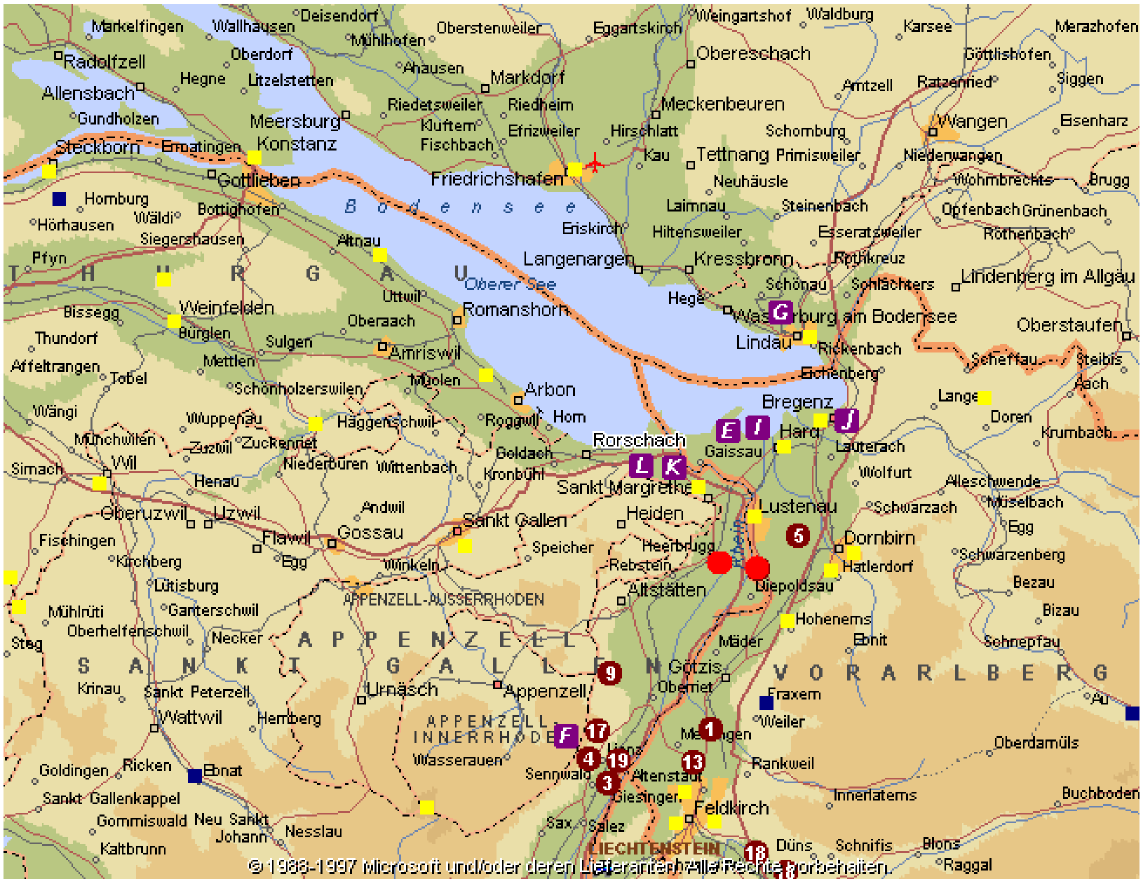

Figure 7.13: Map of the Rhine Valley area. The location of the radiosonde launch site Diepoldsau, where SAMOS was installed, and the position of the GPS receiver in Heerbrugg are marked by circles.

this period, the spectrometer was located in an army field tent to protect it from rain, while the telescope was mounted on a tripod and covered by a glass dome. Fig. 7.14 shows a photograph of the measurement site. The broadband attenuation of sunlight by the glass dome resulted in a loss of approximately 30 % of the light intensity. This was equalized by longer exposure times, which led to a slightly lower S/N-ratio than in uncovered operation.

In addition, the "yellow" Water Vapor Radiometer of the German Bundesamt für Kartographie and Geodäsie (BKG, see also section 7.3), was operated at the Diepoldsau site. The instrument was constructed at ETH and the structure is basically identical to the ETH-WVRs which were described in section 2.2.4. The radiometer was continuously measuring sky brightness temperatures from October 10 to November 5.

Since one objective of the SAMOS project was the validation of GPS meteorology, a GPS receiver had to be operated as well. This task was kindly performed by the Leica-company at Heerbrugg, about 3 km west of Diepoldsau. A Leica AT303 test receiver which is continuously operating on the roof of the company building was in-

Figure 7.14: Photograph of the measurement site in Diepoldsau. SAMOS was located in an army tent, while the telescope was mounted on a tripod covered by a glass dome for protection against rain. In the background the launch vehicle for the radiosondes can be seen.

corporated in the experiment. Because of the short distance between the Heerbrugg receiver and the meteorological measurement station at Diepoldsau, estimates of precipitable water vapor from both sites can be directly compared after transformation of the ground pressure values measured in Diepoldsau to the different station height in Heerbrugg (see 7.2.3). In the following section the GPS processing will be documented.

7.2.2 Radiosondes

The weather balloons launched at Diepoldsau were military high altitude radiosondes (type P-760). They were calibrated before the ascent using a special chamber with adjustable temperature. The accuracy of the measured parameters as given by the manufacturer are about 2 %. In case of the relative humidity measurement a more realistic estimate based on long time experience is 5 %. The heights corresponding to the sonde measurements were calculated using the algorithm suggested by Richner and Viatte [1995].

As described in 6.3.4.2 the radiosonde dataset acquired during the MAP field measurements was the basis for the adjustment of line strength parameters. 9 radio soundings could be used for this purpose since thery were launched during simultaneous SAMOS measurements. The availability of 112 soundings allowed a characterization of the local atmosphere´s statistical behavior offering the opportunity to study the influence of meteorological profile models on the accuracy of SAMOS retrievals. This will be investigated in detail in section 7.4.4. For the processing of SAMOS measurements during the MAP campaign, the radiosonde dataset was used to calculate an average normalized density profile of water vapor density, which is shown in Fig. 7.15. By multiplying the normalized density distribution with PW, the profile of absolute humidity in $[g/m^3]$ is obtained. The profile was introduced as a nominal distribution profile into the forward model as described in 3.9.

7.2.3 GPS processing

In section 2.3 it was explained that it is essential to introduce long baselines into a local GPS network, if absolute values of tropospheric path delay are to be estimated from the data. The usual way to do this, if no distant receivers belong to the network at hand, is to incorporate additional stations from the global network of the International GPS Service (IGS) which are freely available. We chose five such official IGS stationsm Onsala (ONSA), Zimmerwald (ZIMM), Matera (MATE), Gratz (GRAZ) and Wettzell (WTZR) to form a network together with the single receiver located in Heerbrugg (the latter was given the identification code DIPL for Diepoldsau). The coordinates of these stations are accurately known within the ITRF coordinate reference frame, since they are determined on a routine basis by several IGS analysis centers. Other IGS products used are the precise orbits, which are also determined

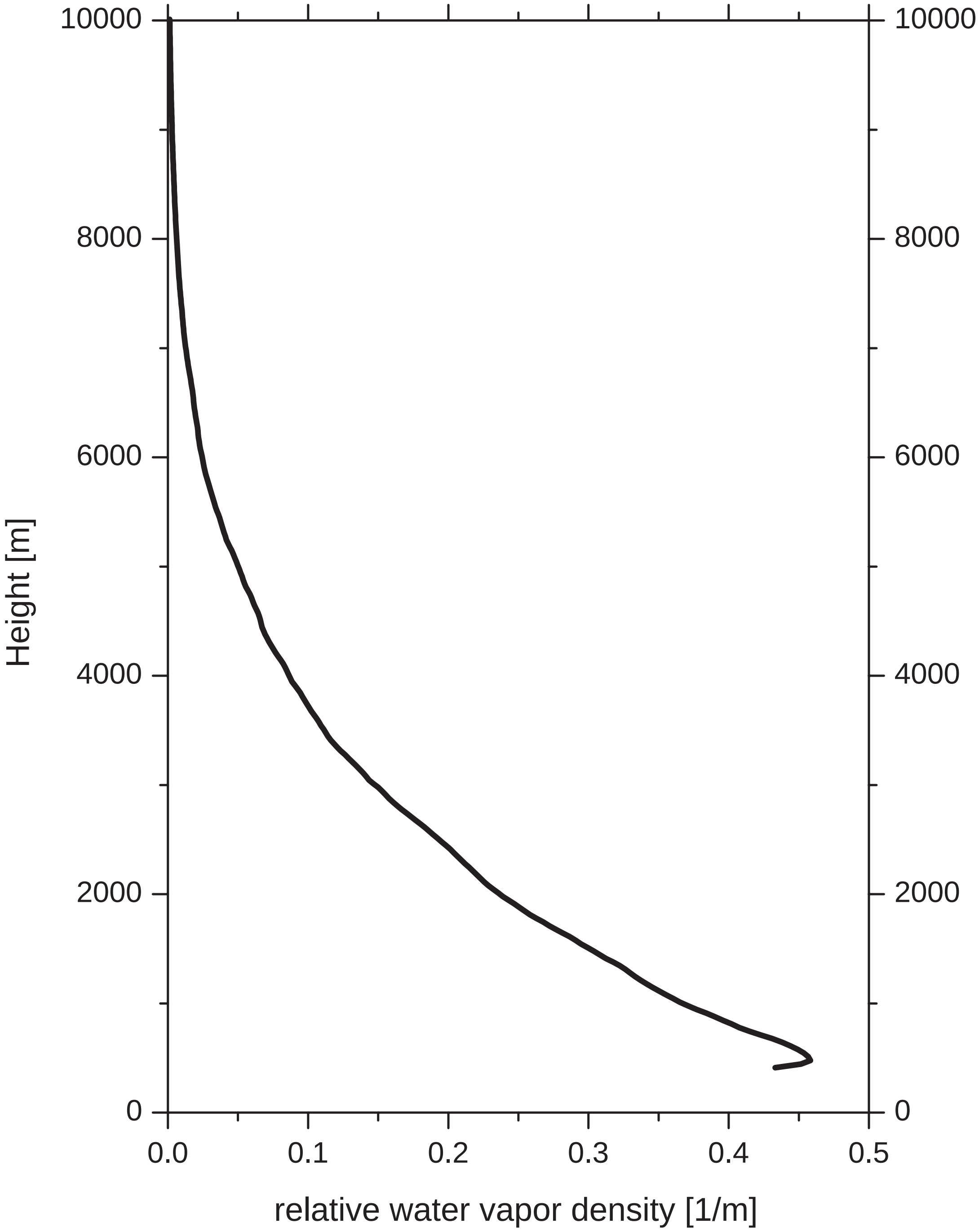

Figure 7.15: Mean water vapor density profile derived from averaging 112 radiosondes launched during the MAP campaign. The profile is used as a nominal distribution of water vapor molecules in the processing of SAMOS spectra (see section 3.9).

on a regular basis and downloaded from the IGS web site (http://igscb.jpl.nasa.gov). Furthermore the official antenna phase center corrections were applied.

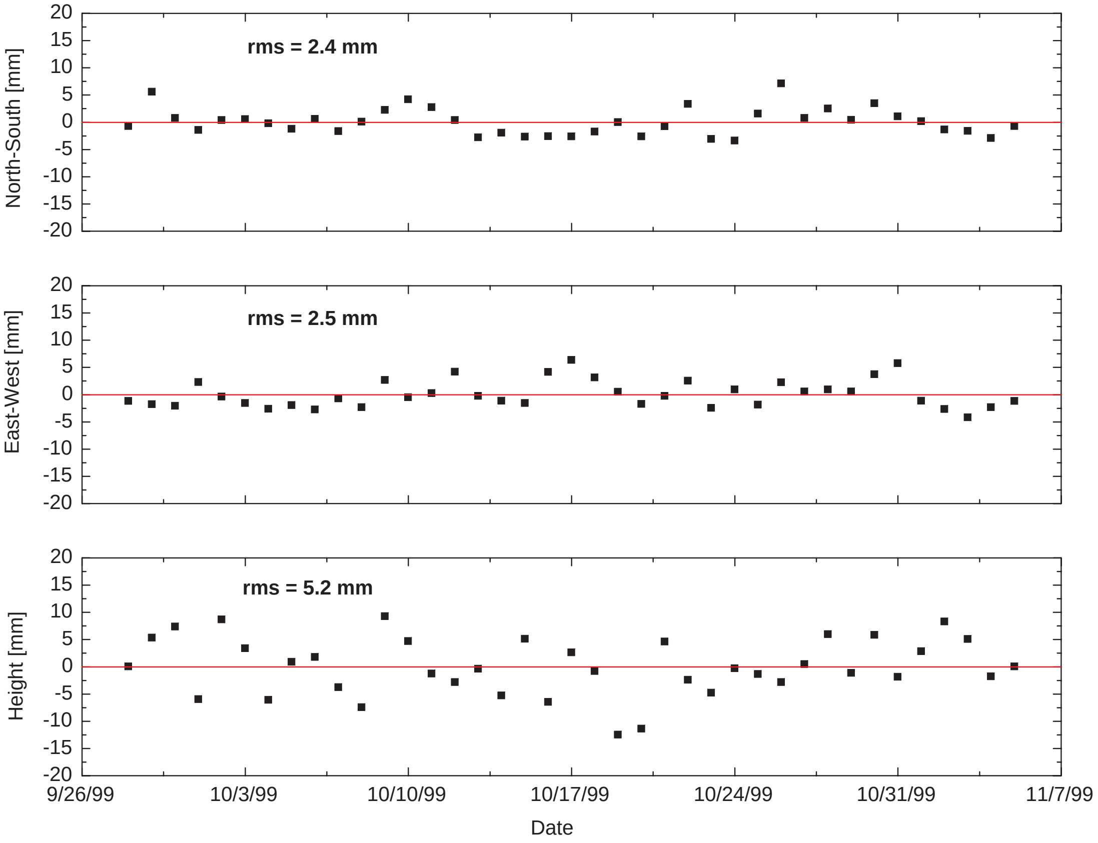

Figure 7.16: Time series of 39 coordinate solutions for the DIPL test site in Heerbrugg during the MAP campaign.

The data were processed with the Bernese GPS Software Version 4.0, which is documented in the User´s Guide Rothacher and Mervart [1996]. The pre-processing corresponds to a standard processing scheme described in detail in therein. The first step towards deriving water vapor abundance from the Heerbrugg receiver was determining its coordinates as precisely as possible. These are kept fixed in the subsequent run and therefore affect the absolute accuracy of path delay estimates. The coordinates of the IGS core stations were fixed on their ITRF97 coordinates calculated for October 15, 1999 by the Center of Orbit Determination (CODE) in Berne. The position of the DIPL station was determined in a first processing run without introducing tropospheric parameters. A total of 39 daily coordinate solutions were calculated this way for the GPS station DIPL, which are plotted in Fig. 7.16. The standard deviations for the two horizontal components are 2.4 *mm* for the North and 2.5 *mm* for the East direction and 5.6 *mm* for the vertical component (which reflects the worse accuracy of the height determination). The average position computed from this time series was taken as the best guess for the site coordinates of the Herrbrugg receiver which were kept fixed in the final processing step.

The last step is the estimation of total zenith delays as the only remaining unknowns in Eq. 2.45 (see section 2.3). In this final run 96 tropospheric parameters per station and day where estimated (15 minute intervals) while all station coordinates were kept fixed. Relative constraints of $\sigma = 1\ mm$ between consecutive tropospheric estimates were applied which reduces the scatter of the PW estimates.

7.2.4 Results and comparison

7.2.4.1 Daily comparison

In this section, the results from four independent methods of determining tropospheric water vapor content are presented and compared. This is done with special emphasis on the validation of the DOAS technique. An overview on the entire dataset acquired during 46 days is given in Fig. 7.17, where all PW retrieval results are plotted. The time series shows a considerable variability of integral humidity during the experiment, although lower than in the Hawaii-dataset. As can be expected, the GPS data are the most continuous, followed by the WVR which exhibit a data gap between October 19th and October 26th due to a technical problem that occurred within the campaign. Compared with the all-weather coverage of GPS and the continuous WVR time series, which is only interrupted in rainy conditions, the SAMOS retrievals indicated by the black circles look like snapshots in this plot. However, a generally good level of agreement between the four different methods is visible. In order to obtain a more detailed picture Fig. 7.18 - 7.35 zoom into the periods, when SAMOS data were available. The results are interpreted in the captions of each plot.

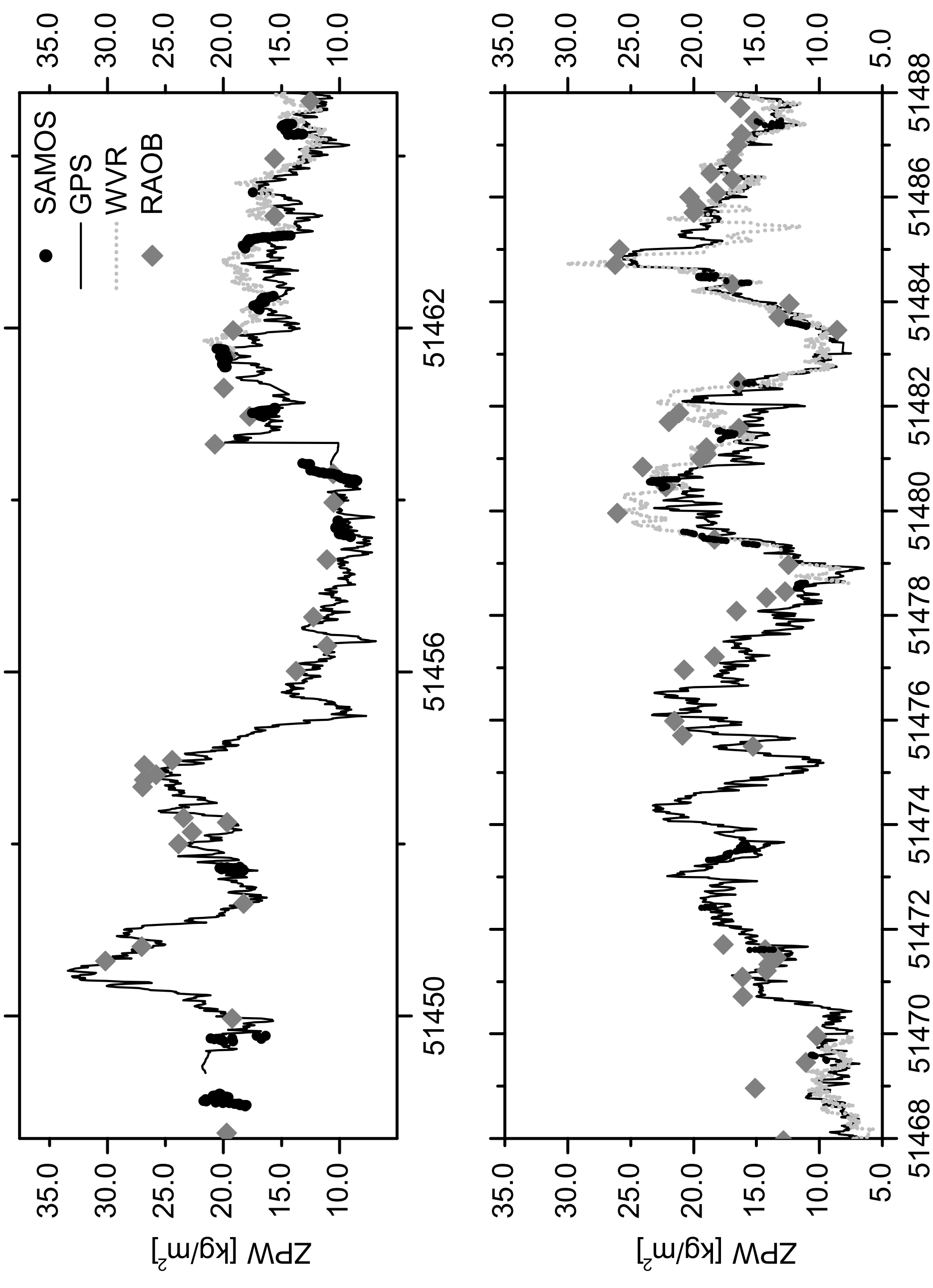

Figure 7.17: PW time series for the entire MAP dataset. The GPS series is the most continuous, followed by the WVR, which was not operated for 7 days from October 19th. A generally good agreement between the three remote sensing techniques and the radiosonde launches can be seen.

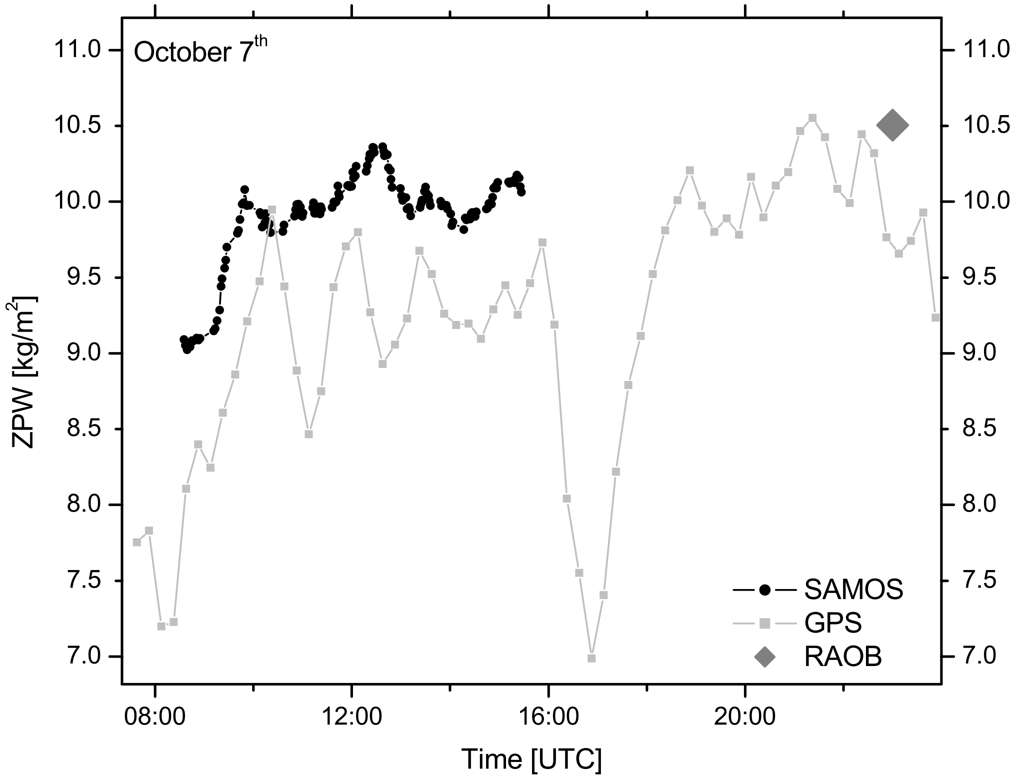

Figure 7.18: The GPS solutions on this day seem to oscillate for unknown reasons (the a-posteriori errors of the estimations do not indicate abnormal behavior). There is also an unexplained outlier period in GPS in the GPS curve, which recovers quickly to obtain good agreement with the radiosonde sonde launched at midnight. The SAMOS curve is much smoother and at a higher level

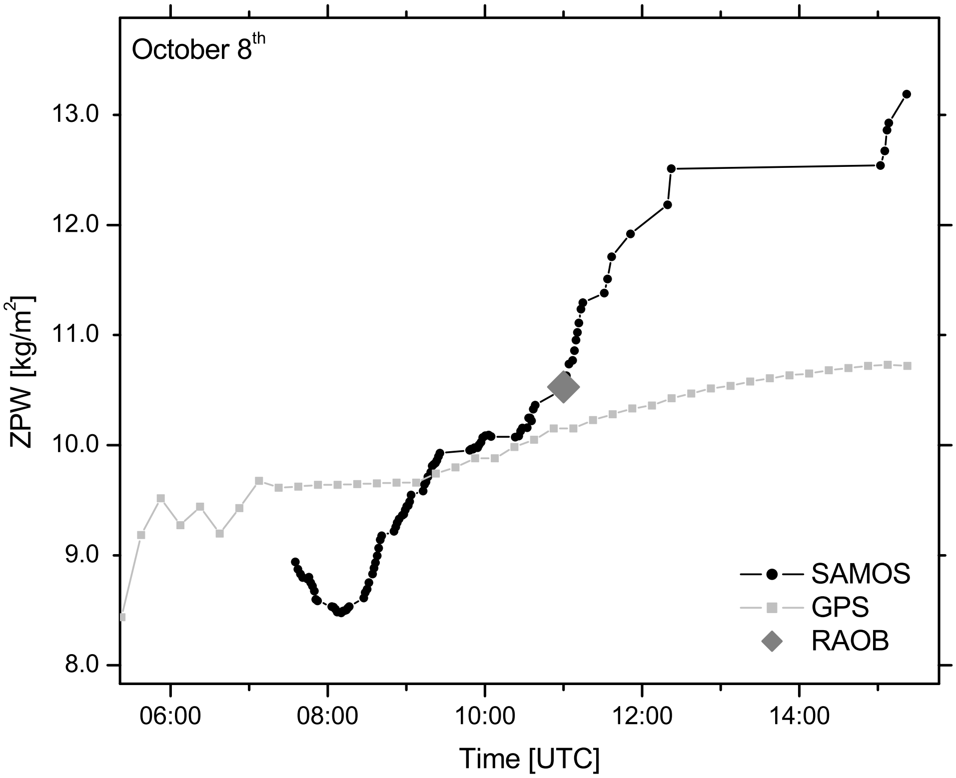

Figure 7.19: The disagreement between SAMOS and GPS in this plot is not real. Instead it demonstrates the effect of a data gap in the GPS data, since the data acquisition was interrupted at 7:00 UTC. Estimates of ZPW are still performed in the processing, since the data of the other network stations (IGS) are continuous. The integrated humidity profile of the radiosonde is in excellent agreement with the SAMOS retrievals.

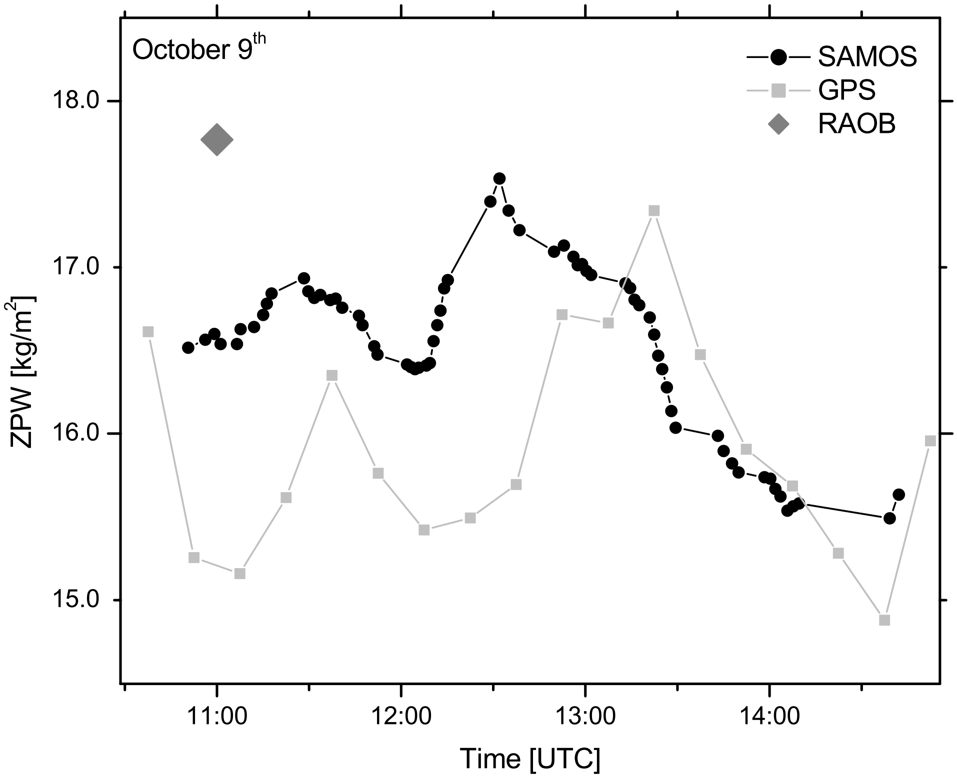

Figure 7.20: Again, an offset between GPS and SAMOS retrievals is present in the first half of the time series, which decreases in the afternoon. The changes of water vapor content detected by SAMOS between 11:00 and 12:20 UTC are also seen by GPS, but seem to be exaggerated. The increase in PW with a peak at 12:30 UTC in the SAMOS curve is seen by GPS almost one hour later (at 13:22 UTC).

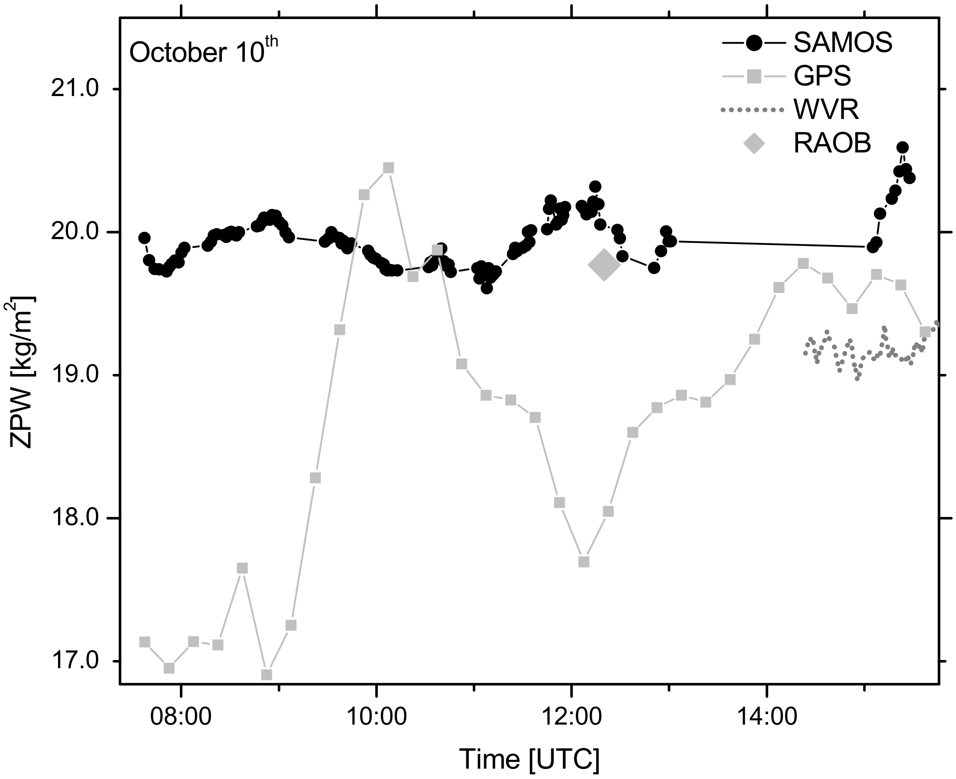

Figure 7.21: On October 10th we observe a large offset of 3 kg/m^2 ZPW between 7:30 and 9:00 UTC, which then rapidly decreases as the GPS estimates jump to approx. the SAMOS level. Neither this increase nor the subsequent drop in PW are observed in the SAMOS curve. Since the latter is well confirmed by the radiosonde observation, the GPS retrievals seem to be erroneous during this period. After 15:00 UTC, the results agree within 1 kg/m^2, with the first WVR measurements lying between the GPS and SAMOS estimates.

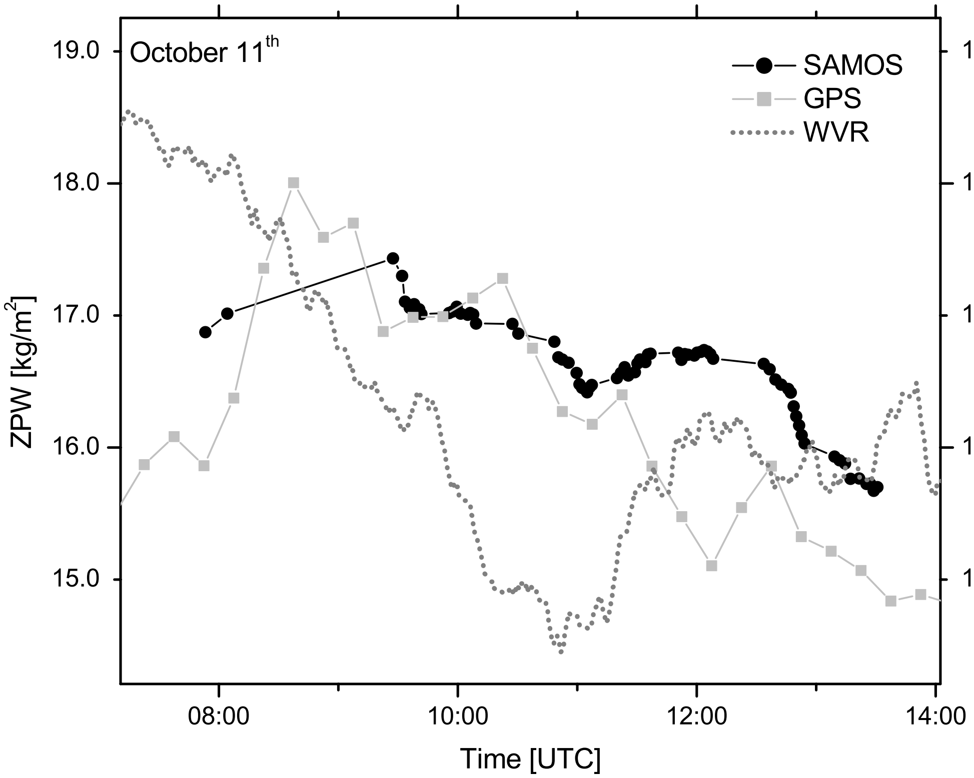

Figure 7.22: On this day, GPS deviates significantly from the other techniques in the early morning hours (3 kg/m^2 lower ZPW) before its estimates increase to agree well with the spectrometer. While WVR and SAMOS both observe an increase after the drop in PW with a peak around moon, GPS yields a minimum at the same time. Again this could be due to some delay in the tropospheric parameter estimation, since a local peak is seen about 40 min. later.

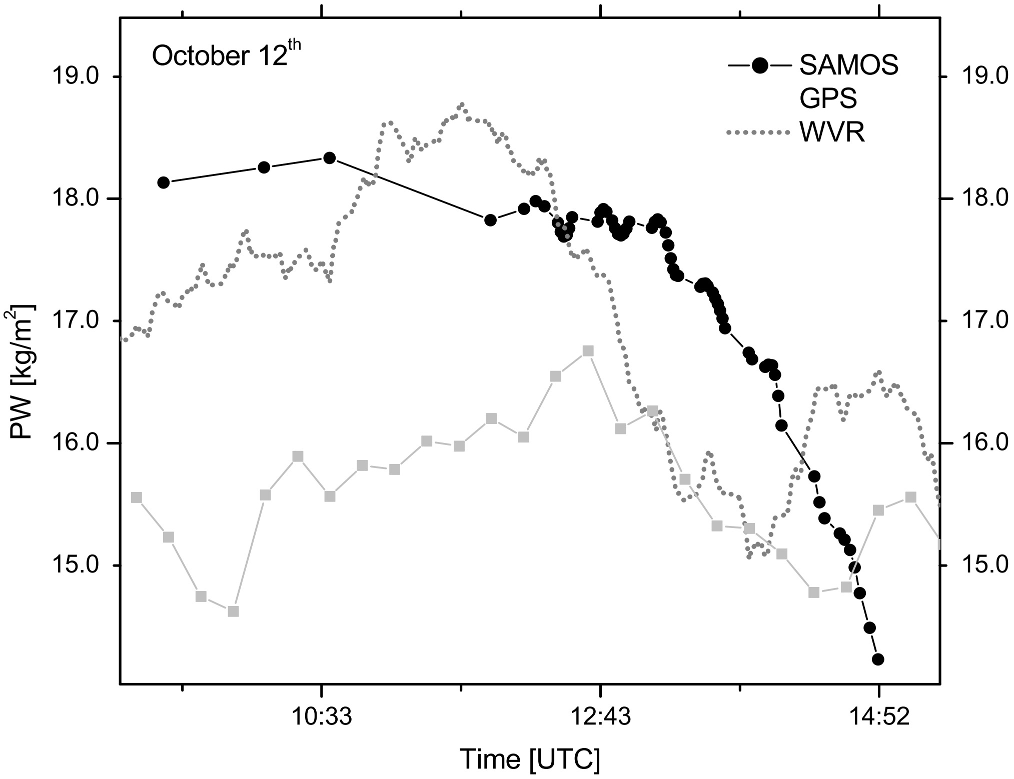

Figure 7.23: On October 12 a decrease in water vapor content after 12:00 UTC is detected by all three remote sensing techniques. However, GPS seems to measure to low before noon (1.9 kg/m^2 negative offset with respect to WVR and SAMOS). WVR and GPS both observe an increase after the drop, again with a 30 minute delay of the GPS curve. This feature is not detected by SAMOS. A radiosonde launch before midnight on that day (not in this plot, see Fig. 7.17, mod. Julian date 51465.95) is closer to the WVR results than to GPS

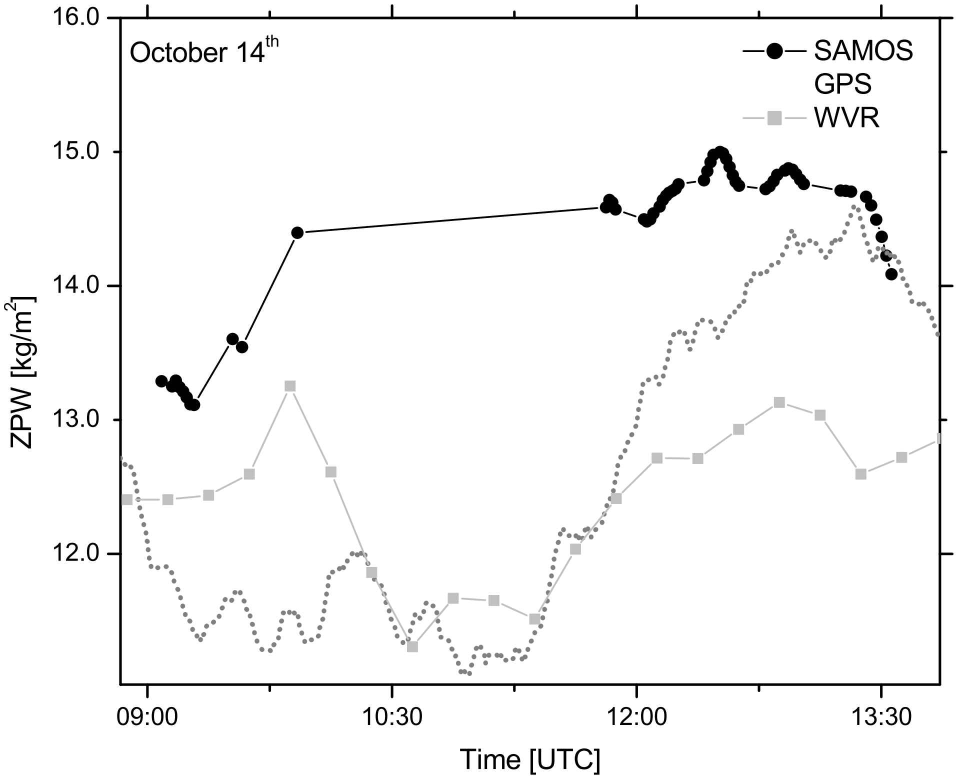

Figure 7.24: This plot is an example for SAMOS retrievals deteriorated by cloud cover, which was present during most of the observation time. The fact that the SAMOS retrievals yield higher water vapor contents may be an indication for anomalous cloud absorption e.g. by multiple scattering effects within clouds (see section 7.4.5). Between 9:55 and 11:55 complete cloud cover causes a gap in the SAMOS time series, while GPS and WVR are in good agreement.

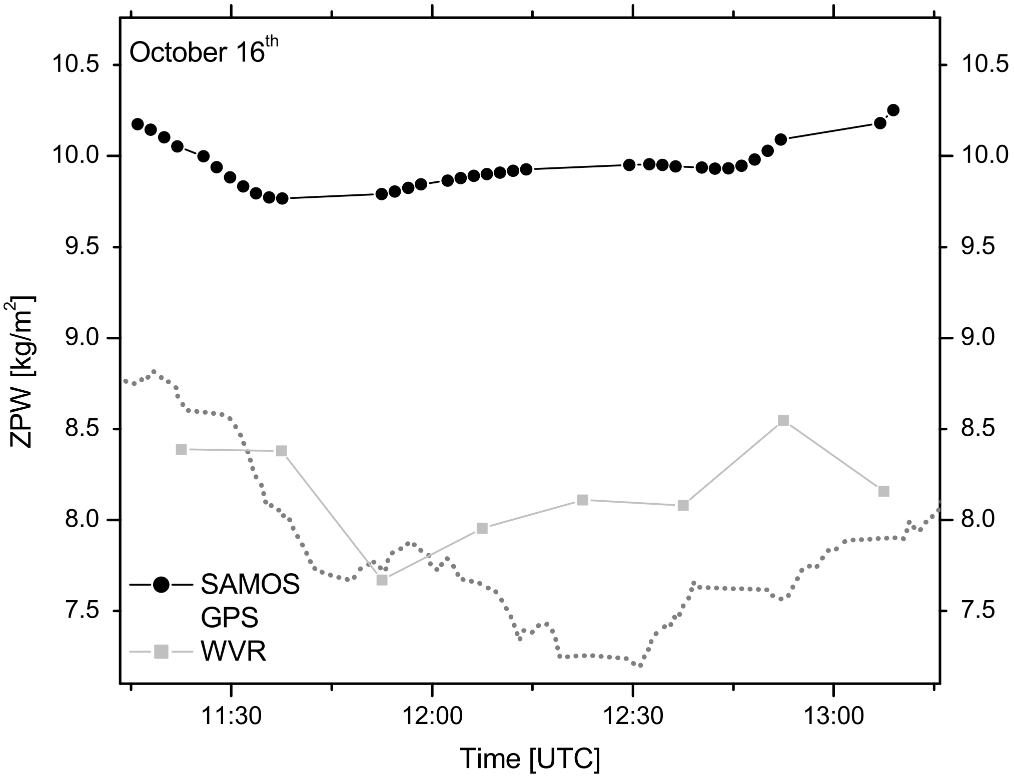

Figure 7.25: This day is an example with a stable water vapor content over time. Like in 7.24 SAMOS seems to overestimate the PW by about 1.8 kg/m^2, since GPS and WVR agree at approx. the same level. However the radiosonde launch in the night at 23:00 (not in this plot, see Fig. 7.17, mod. Julian date 51467.95) yields an even higher PW value (12.9 kg/m^2 whereas GPS and WVR estimate 7.9 and 7.45 kg/m^2 respectively)

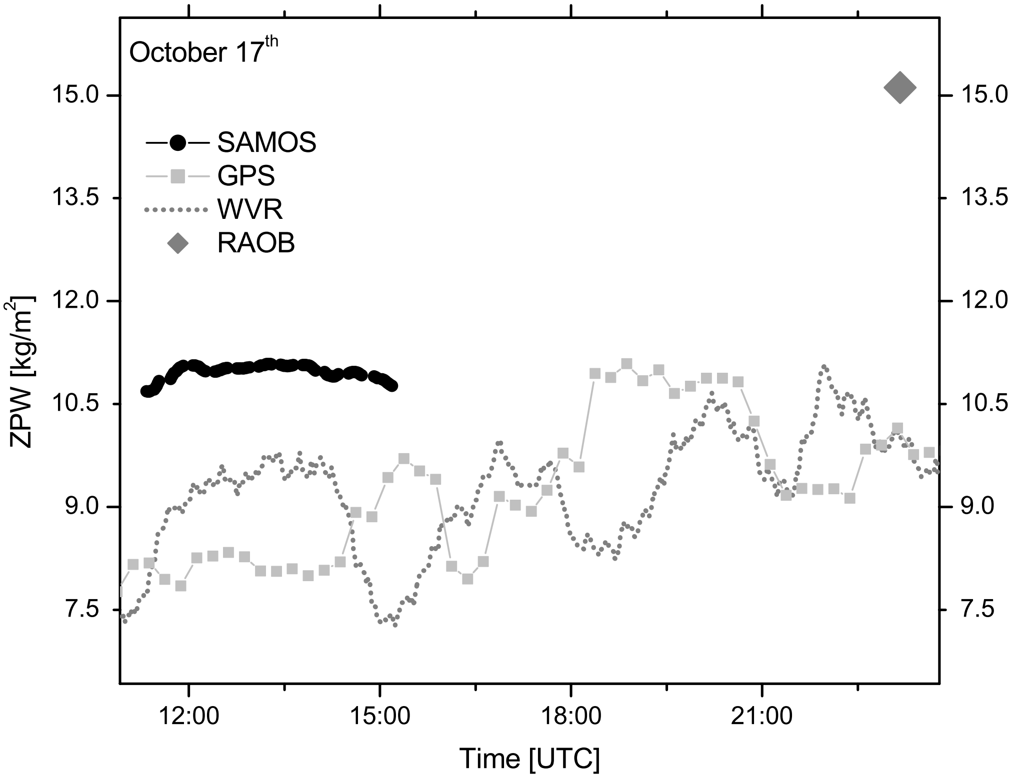

Figure 7.26: October 17th exhibits an almost analogous situation to the previous day. SAMOS measures PW at a higher level (offset 1.3 kg/m^2) than GPS and WVR, but the integrated radiosonde profile yields an even greater difference (5 kg/m^2).

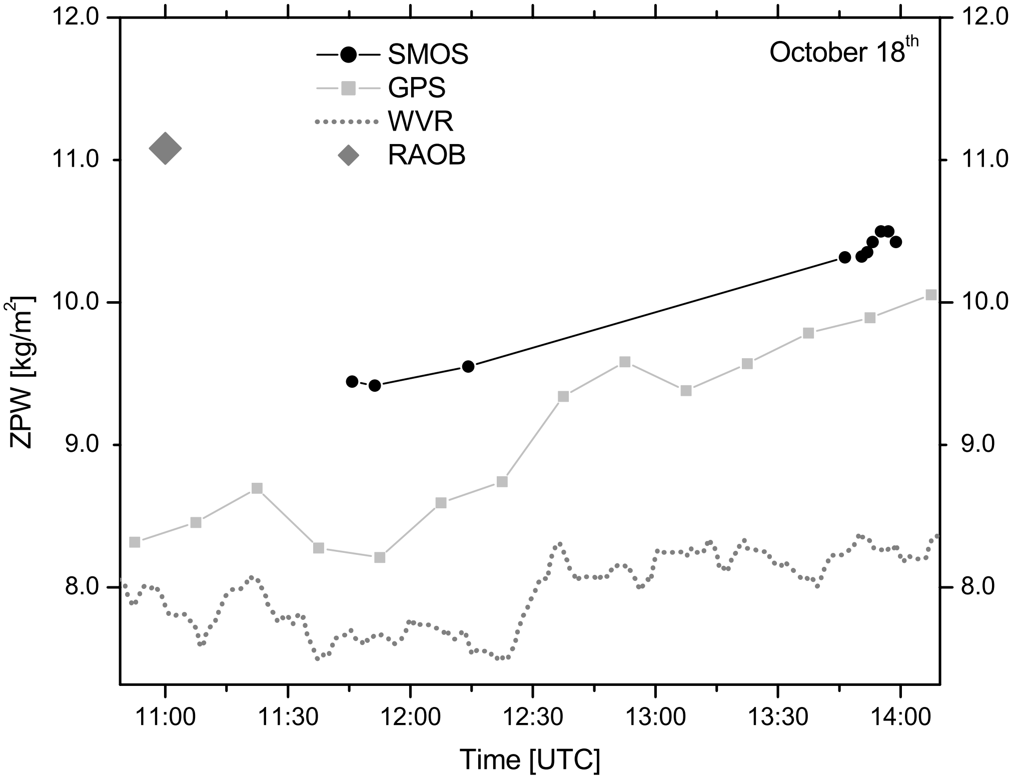

Figure 7.27: This plot shows a better agreement between SAMOS and GPS although only few spectra could be acquired due to unfavorable weather conditions. Both techniques see a slight constant increase which is not reproduced by WVR. The radiosonde observation again seems to overestimate PW.

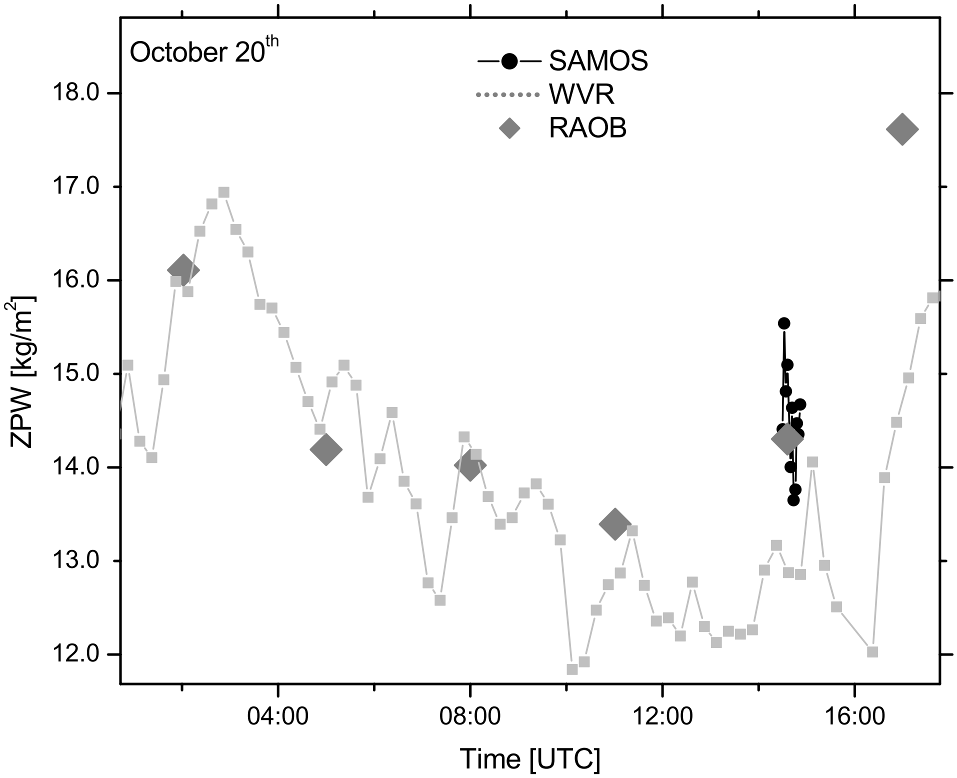

Figure 7.28: On October 20th, the radiosonde launch frequency was increased due to the announcement of an IOP. Only very few SAMOS spectra could be acquired through a cloud hole. However, the SAMOS measurements coincided with a radiosonde launch whose integral agrees well with the spectrometer result. The agreement with GPS is also very good (with the exception of the last launch). Unfortunately, no WVR measurements were available (see text), so it remains unclear, if the PW changes between the radiosonde launches detected by GPS are real.

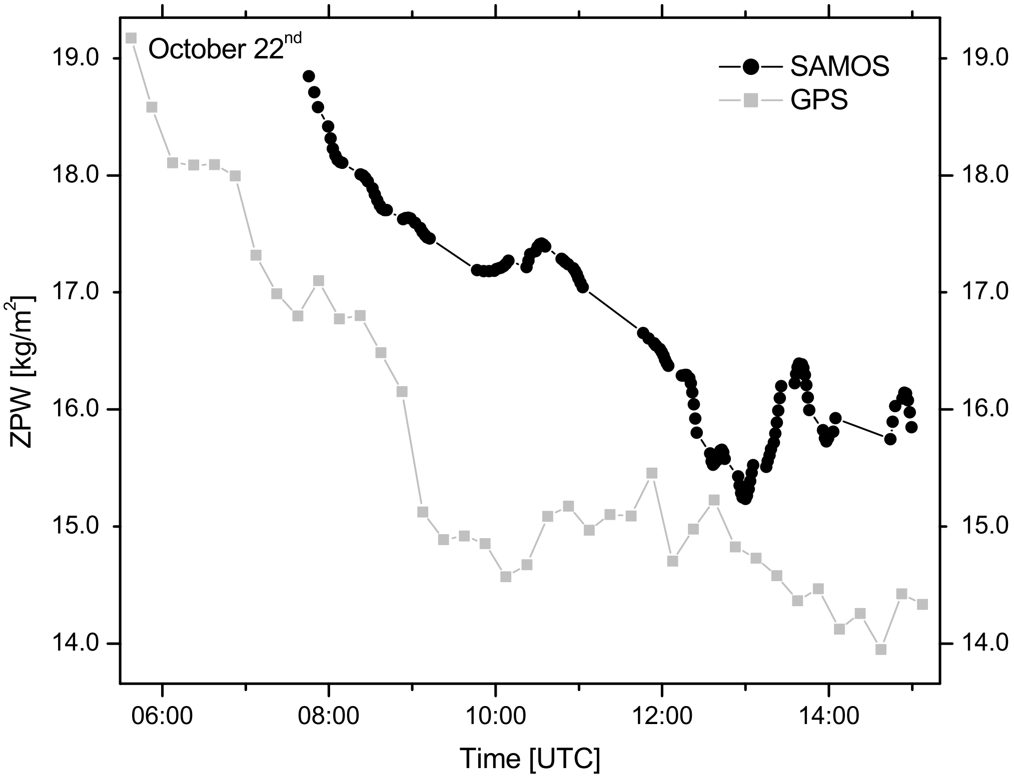

Figure 7.29: Comparing the two techniques operating on October 22nd, both GPS and SAMOS observe a steep drop in PW with an offset varying between 1.2 kg/m^2 and 2.4 kg/m^2. The continued drop in the GPS curve can be interpreted as the "exaggerating" effect which was observed before (see Fig. 7.20). However this cannot be proven without WVR or radiosonde observations

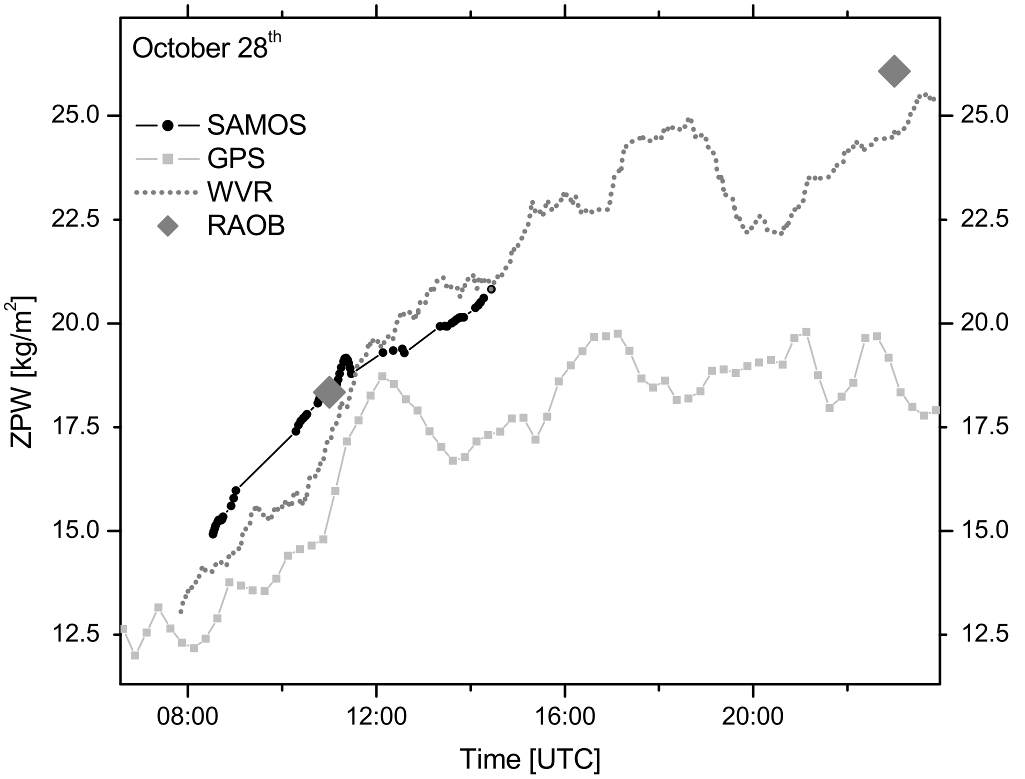

Figure 7.30: On this day, SAMOS is in excellent agreement with WVR and radiosonde, whereas the GPS estimates drift away from the results of the other techniques after a PW maximum at 12:00 UTC. The growing discrepancy thereafter cannot be explained by the unidirectional field of view of SAMOS, since the WVR, like GPS, averages over the entire hemisphere and confirms the SAMOS curve. The radiosonde launch at 23:00 UTC yields a huge bias with respect to GPS (7 kg/m^2 PW), which confirms the WVR results.

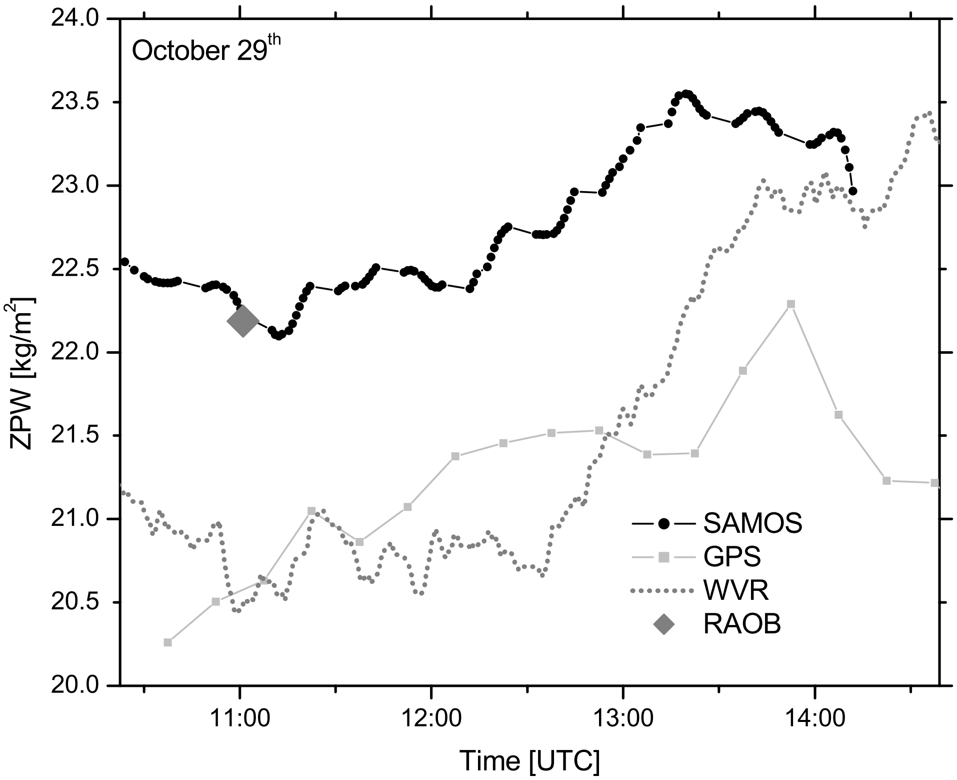

Figure 7.31: This day again shows a perfect agreement between SAMOS and radiosonde, which is of course a result of the fact, that radiosondes were used to determine the line parameters (see section 6.3.4.2). There is an offset of 1.8 kg/m^2 PW with respect to GPS and WVR, which in turn agree well among each other. All three remote sensing techniques see an increase in water vapor content, but GPS again seems to be delayed. GPS and SAMOS both see a sudden drop after the maximum at 13:50 UTC, which is surprisingly not detected by WVR.

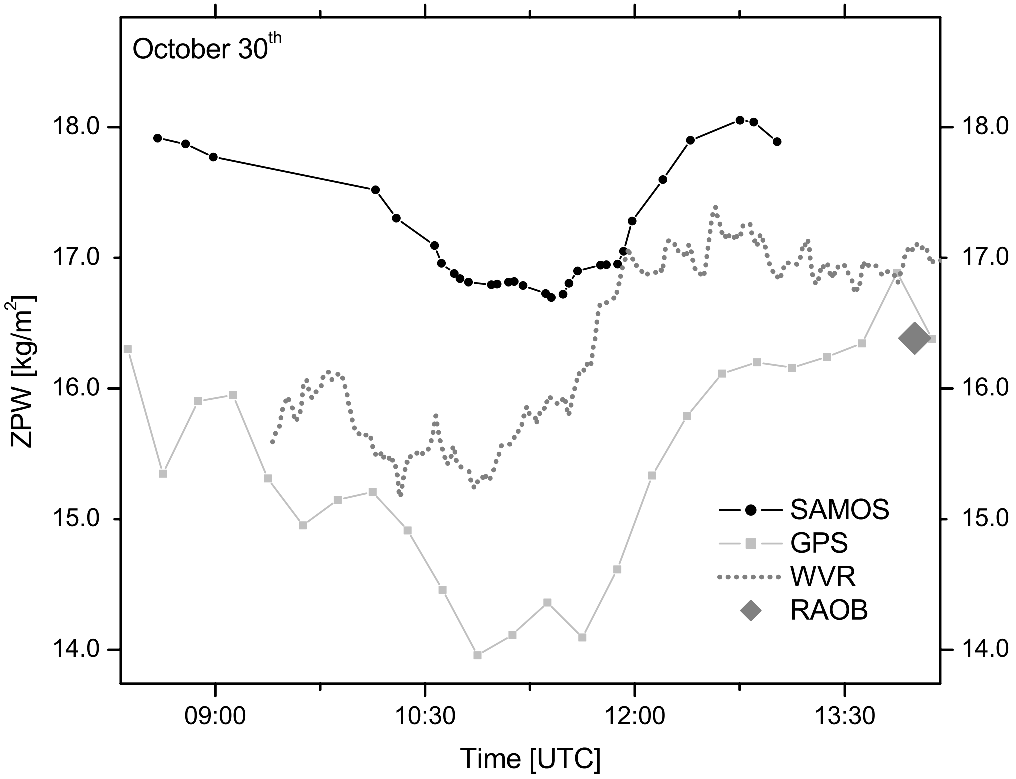

Figure 7.32: On this day offsets between all techniques are visible, although variation in PW is seen similarly. The minimum around 11:00 UTC is more pronounced in the GPS results than in those of SAMOS and WVR. At 13:00 UTC the GPS curve matches the WVR curve and shows obtain a good agreement with the radiosonde.

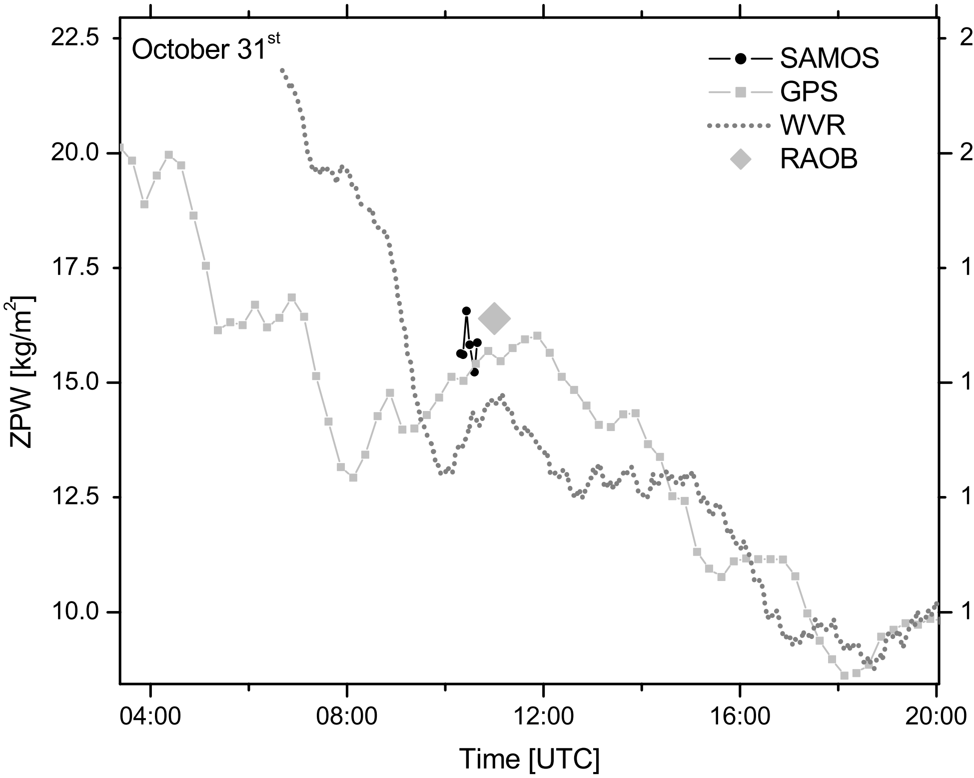

Figure 7.33: This day is an example where the water vapor content in the troposphere falls from more than 20 kg/m^2 to less than 10 kg/m^2 within a few hours. The large discrepancy between GPS and WVR in the early morning hours might arise from raindrops on the WVR antenna lenses, since it has been raining during the night. Shortly before the 11:00 UTC radiosonde launch, a few SAMOS spectra could be acquired through a cloud whole. The SAMOS retrievals are in good agreement with GPS and the integrated radiosonde profile.

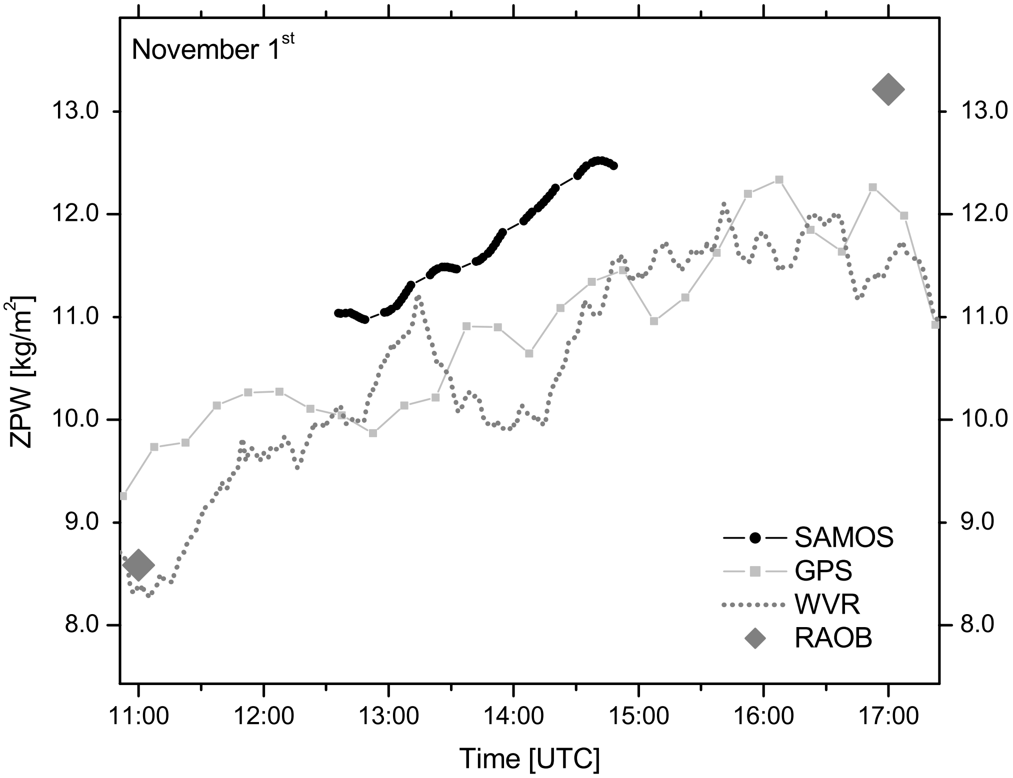

Figure 7.34: The time series acquired on November 1 show a good agreement between GPS and WVR with a standard deviation of about 1 kg/m^2, but neglectable bias. The SAMOS time series is much smoother but with a positive bias of approx. 1 kg/m^2. Again this offset with respect to the two other remote sensing techniques seems to hold for the radiosonde launched at 17:00 UTC. This might explain the SAMOS offset, since the model line parameters were calibrated using the MAP radiosonde launches.

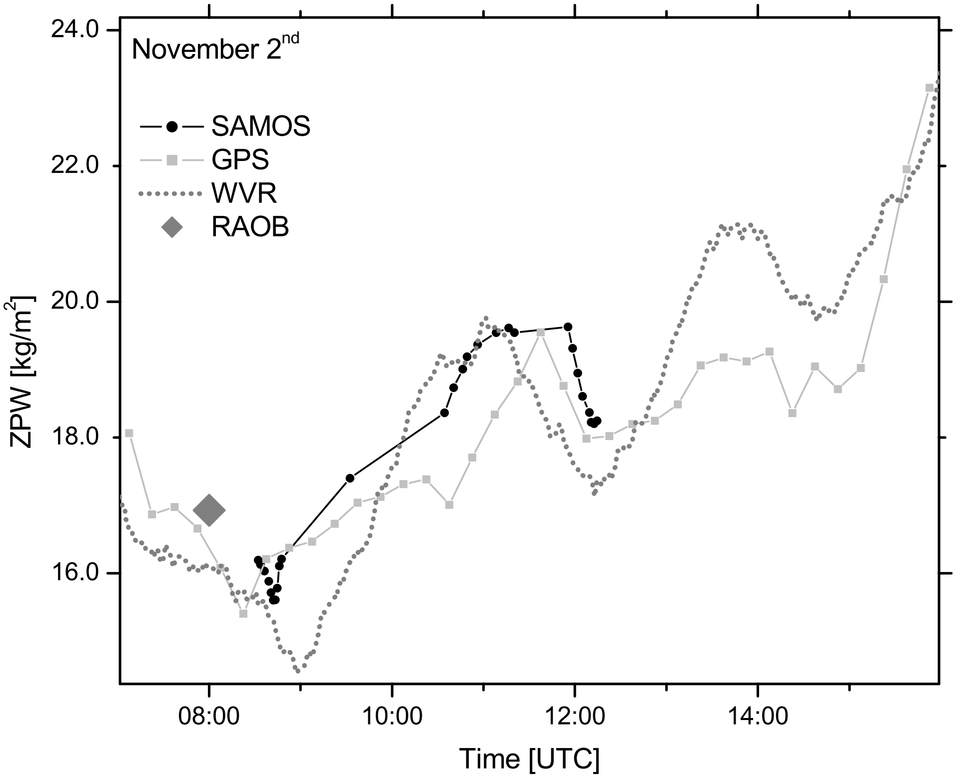

Figure 7.35: On the last day with SAMOS observations there was only a short period with sunshine. However, a considerable fluctuation in water vapor abundance can be observed in excellent agreement with the other techniques. The increase followed by a sudden drop is equally detected by the three methods, although GPS again seems to react too inert.

Difference	bias kg/m^2	stddev kg/m^2	observations
SAMOS-GPS	1.22	0.92	221
SAMOS-WVR	0.11	1.95	676
SAMOS-RAOB	0.04	0.23	9
GPS-WVR	-1.07	2.55	1596
GPS-RAOB	-1.63	1.57	71
WVR-RAOB	-0.74	1.73	36

Table 7.3: Comparison statistics of the MAP campaign.

7.2.4.2 Statistics and interpretation

The comparison of results for every day, closely examined in the previous section, allows some conclusions about the performance of the different methods. The overall comparison statistics for the entire observation period is summarized in table 7.3. The SAMOS retrievals in most cases yielded higher PW values than GPS and WVR. An average bias of 1.22 kg/m^2 with respect to GPS and 0.11 kg/m^2 with respect to WVR was computed. Despite of the larger offset, the agreement in signal signature was much better between SAMOS and GPS, which is indicated by the much lower standard deviation ($\sigma = 0.92 kg/m^2$), compared to the SAMOS-WVR difference ($\sigma = 1.95 kg/m^2$). While the the statistics for the SAMOS-GPS comparison are within the limits, which are usually reported for similar investigations using WVRs (e.g. Rocken et al. [1995]), the standard deviation between our GPS and WVR measurements is surprisingly high ($\sigma = 2.55 kg/m^2$). By far the best agreement was observed between SAMOS retrievals and the integrated radiosonde profiles. The neglectable bias is of course a consequence of the absolute calibration of SAMOS by determining line strength parameters using the MAP radiosondes (see section 6.3.4). However, the very low standard deviation of 0.23 kg/m^2 proves a good stability and redundancy. Since SAMOS and radiosondes exhibit an almost zero bias, the balloon soundings consequently also have positive offsets with respect to WVR and GPS, the latter yielding a larger offset but slightly lower standard deviation.

Apart from the statistics there are a some general observations that can be described but not quantified: One of these impressions is that the GPS estimates of PW often seem to react too “inert” when rapid and large fluctuations of the water vapor content are detected by the other techniques. Examples for this behavior are Oct. 9, Oct. 11, Oct. 12, Oct. 28, Oct 29 and Nov. 2. A similar interpretation was found for the results of the Hawaiian campaign in the section 7.1.3. Occasionally GPS tends to overestimate the changes, which are unlikely to be a real signal of PW fluctuations (e.g. on Oct. 10, Oct. 30). However these observations are somewhat intuitive, since the ”truth” remains unknown and can only approached from the comparison of a multitude of independent techniques. In order to obtain a better impression of the level of agreement and possible systematic differences, Fig. 7.36 displays scatter plots for all comparison pairs. The plots do not imply an "exaggerating" effect of the GPS retrievals as suspected for the Hawaii-results. A systematic difference is rather observed between the WVR measurements and SAMOS, indicated by the inclination of the regression line (slope = 1.125). A slight effect in the same direction is visible in the GPS-WVR plot. Although only few points are available for the comparison with radiosondes, it can be stated that they are in excellent agreement with the SAMOS retrievals.

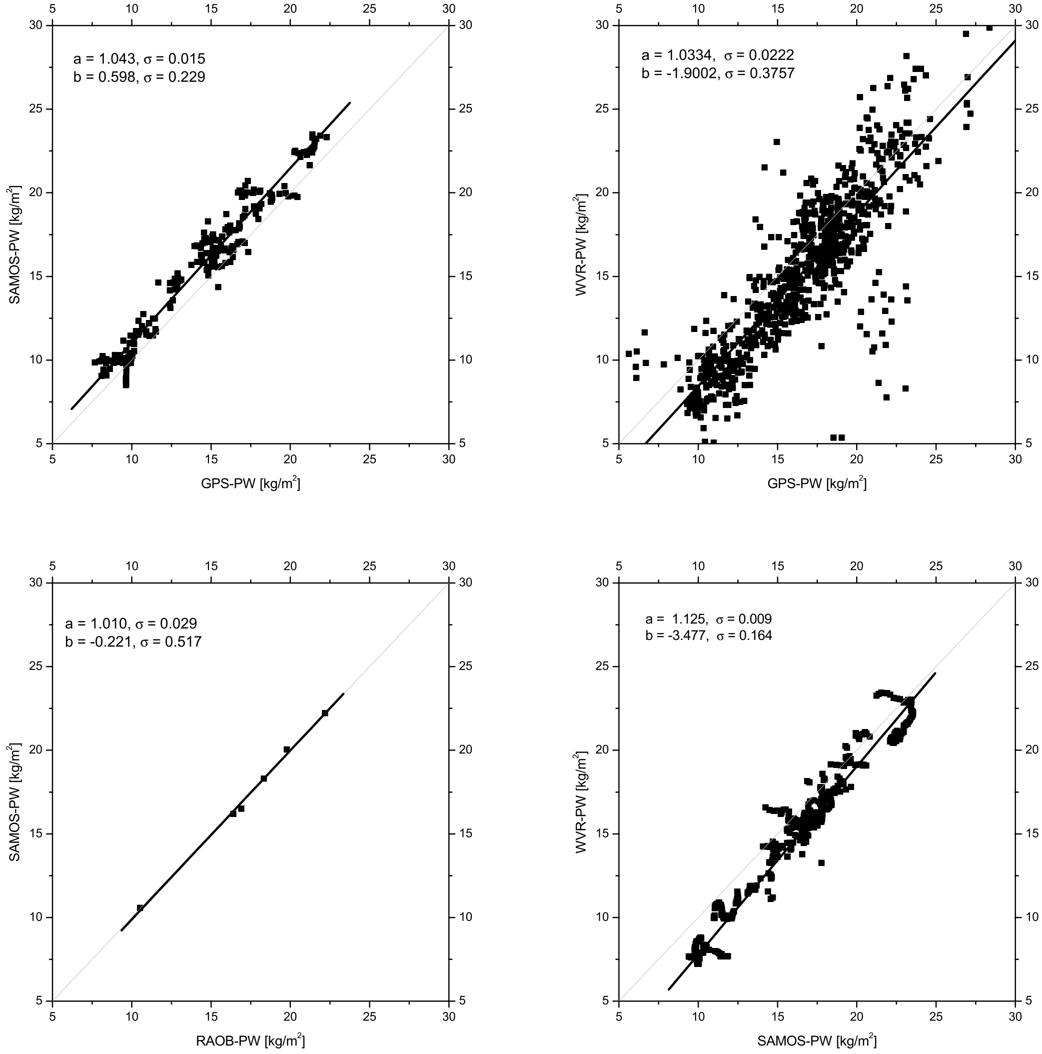

Figure 7.36: Scatter plots for the comparison pairs of the MAP campaign.

7.3 The Wettzell Campaign

7.3.1 The Geodetic Fundamental Station of BKG

The last field deployment of SAMOS reported herein was a two week campaign at the Geodetic Fundamental Station of the German Bundesamt für Kartographie und Geodäsie, located in Wettzell, Germany. The BKG is a federal authority whose task among others is the provision and maintenance of the geodetic reference networks of the Federal Republic of Germany. It is also participating in activities for the determination and updating of global reference systems. This includes the deployment of various relevant surveying techniques. At the Geodetic Fundamental Station in Wettzell a large number of geodetic observations systems are operated, including a radio telescope for VLBI measurements. Also two continuous GPS sites are operated in Wettzell, identified by the code WTZR and WTZT, both being part of the global IGS network. The data are processed on a regular basis by BKG and other analysis centers. The positions of the two GPS sites therefore may be regarded as extraordinary well determined, which is very important in the context of GPS meteorology. Another circumstance which makes Wettzell an favorable place for comparison measurements is the presence of a continuously operating WVR. The instrument is of the same type as the one deployed in the MAP-campaign, which was also provided by BKG. The presence of two CGPS stations and a continuously operating WVR provided a good opportunity for co-located comparison measurements with SAMOS.

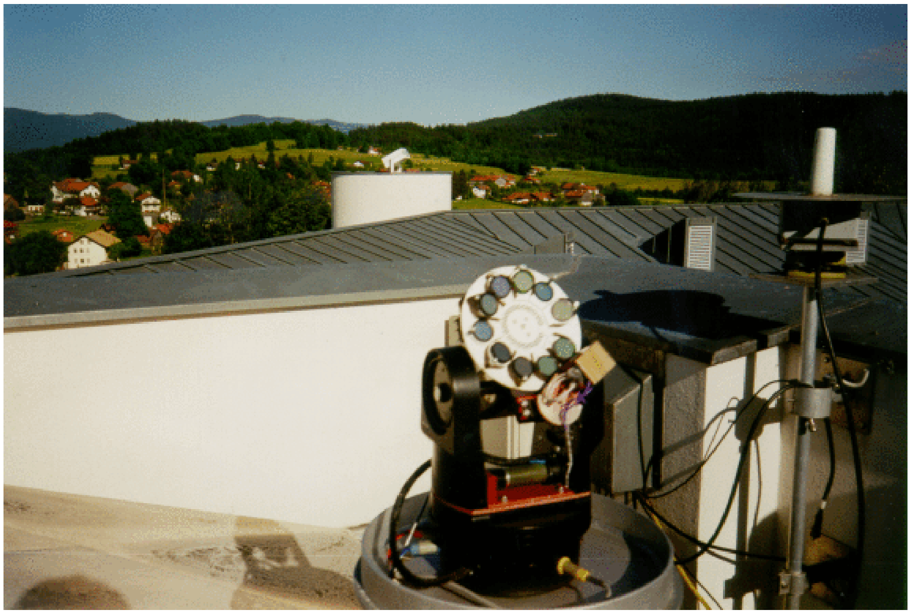

Figure 7.37: Photo of the solar telescope with the WVR on the radiometer tower in the background

Figure 7.38: Photo of IGS station WTZR in Wettzell

Figs. 7.3.1 and 7.3.1 show photographs of the observation tower in Wettzell, where SAMOS was installed. The two GPS receivers are located in two opposite corners of the tower balustrade. The WVR is mounted on a second tower of the same building. The telescope of the solar spectrometer system was mounted on a tripod on the so-called GPS tower and the collected light was conducted via optical fiber cable into the spectrometer located inside the tower.

7.3.2 Results and comparison

The weather during the measurement period from May 13th to May 23rd was quite changeable, but except for the period from May 18 to May 20, solar spectra could be measured every day. Unfortunately the WVR measurements were corrupted during the experiment, yielding very intensive fluctuations of the retrieval results which can for sure be regarded as erroneous. One possible explanation could be disturbing microwave signals from an aircraft radar operated at the SLR facility in Wettzell. The extreme fluctuations in the WVR data rendered them useless for a quantitative comparison with the other techniques and will therefore not presented.

The GPS data were processed by Dr. M. Becker of BKG using the default processing scheme for IGS products with the modification of estimating tropospheric parameters every 30 minutes. The time series of zenith precipitable water vapor content from SAMOS and the two GPS receivers are plotted in Fig. 7.40 to Fig. 7.44. The interpretations for each day are given in the captions of these plots.

Figure 7.39: Photo of IGS station WTZT in Wettzell

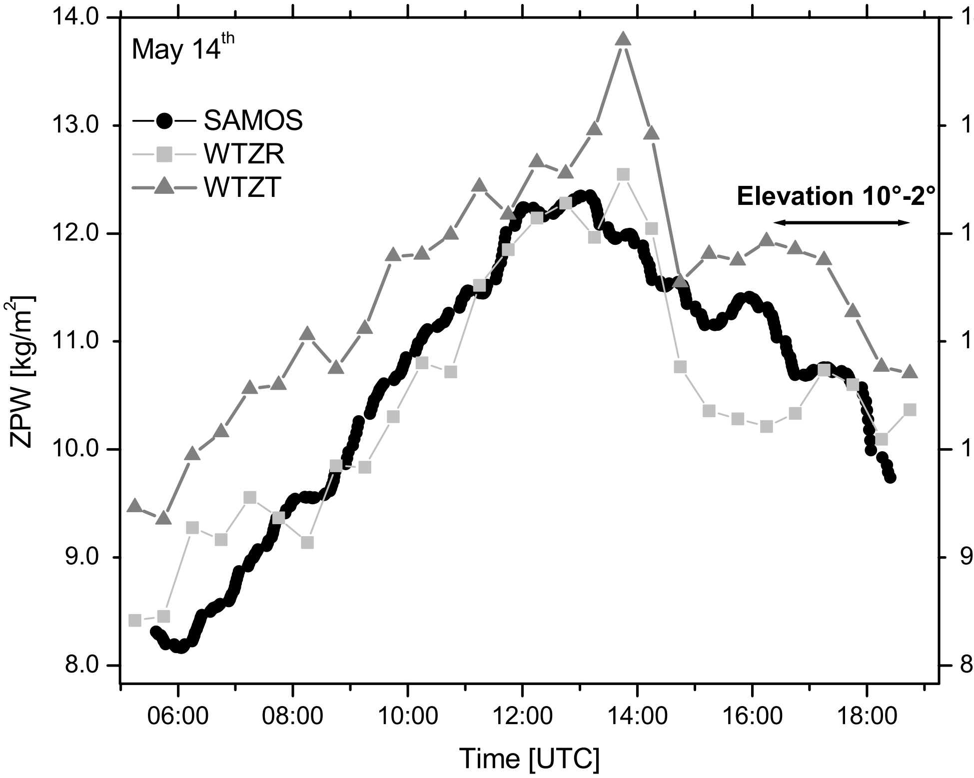

Figure 7.40: On May 14 a complete scan from sunrise to sunset could be measured with SAMOS. The comparison of the zenith PW time series revealed a surprisingly variable offset between the two GPS receivers WTZR and WTZT, which varies between 0.2 and 2 kg/m^2. The situation is particularly interesting between 15:00 UTC and 18:00 UTC. During this period the two GPS curves show opposite trends, one falling while the other one rises. The SAMOS retrievals are therefore particularly interesting to compare with both GPS time series. While SAMOS is in better agreement with WTZR during most of the day, it also sees an increasing structure in the above mentioned period like the WTZT receiver. However, WTZT seems to overestimate the peak, displaying the “exaggerating” effect observed before see 7.1.3. Also the “inertial effect” can be observed, which becomes obvious by comparing the estimated daily maxima. The GPS time series reach the peak simultaneously but 45 minutes later than the SAMOS curve.

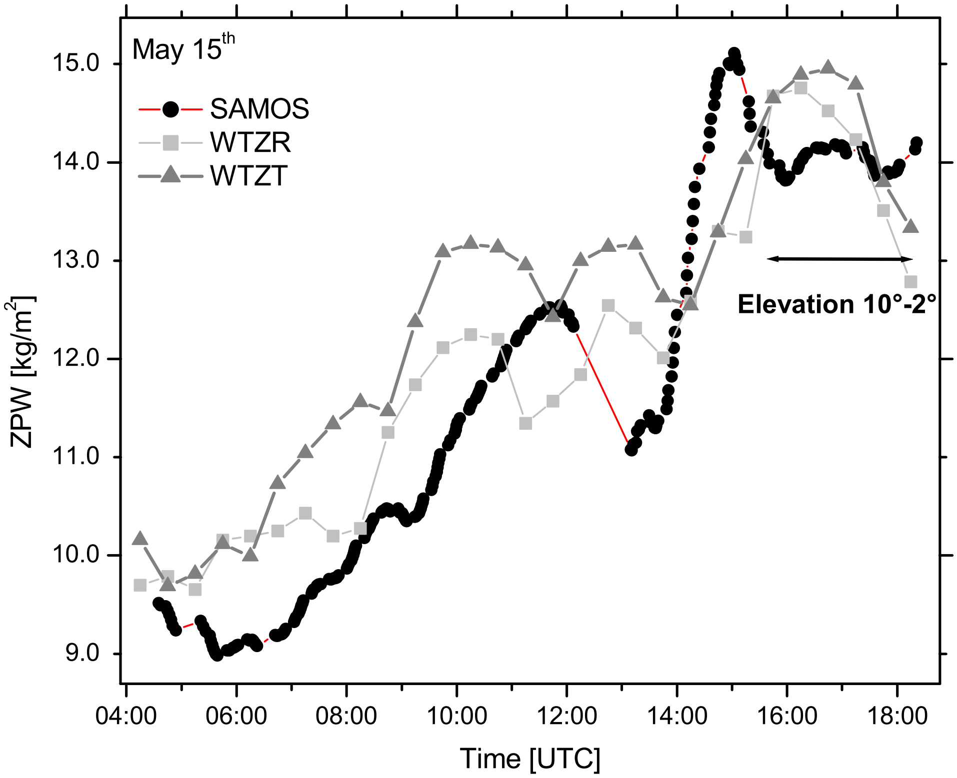

Figure 7.41: On May 15 an increase of atmospheric water vapor abundance was observed by the three instruments. Again there is a variable bias between the two identical GPS receiver, although less pronounced than on the day before. There is a common feature in the GPS time series, displaying two maxima at 10:00 and 13:00 UTC, which is not seen in the SAMOS results. Instead SAMOS detects a sudden drop of PW at noon and the re-increase about one hour later, which is not reproduced by GPS.

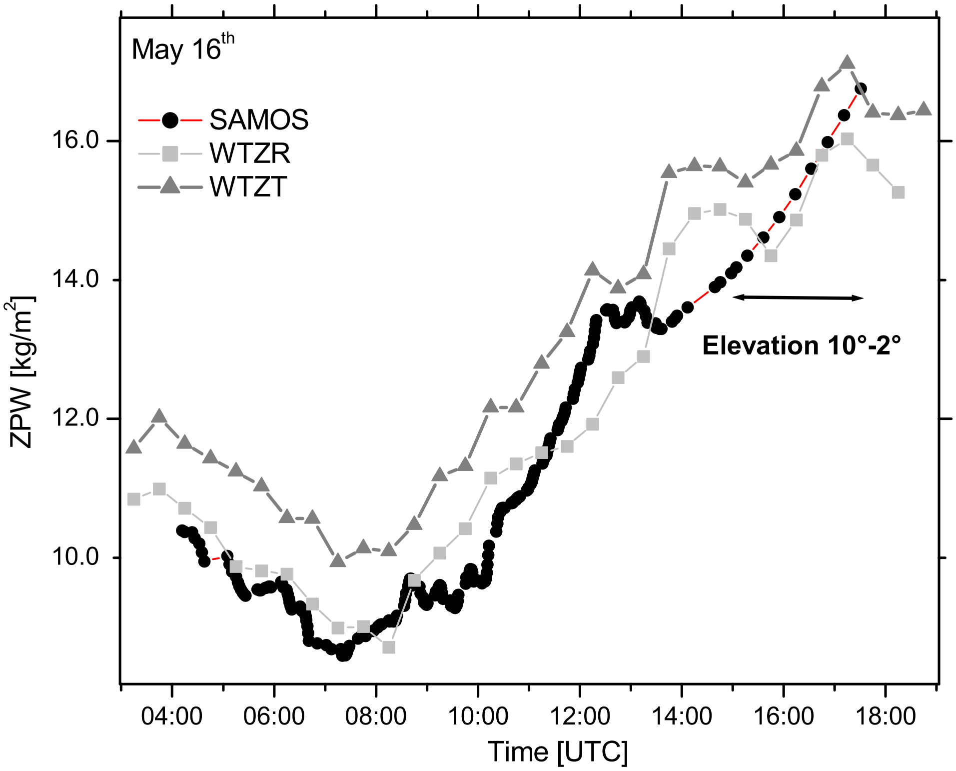

Figure 7.42: This day is another example for a complete SAMOS dataset, with a remarkably good agreement with the WTZR receiver. The results from the two GPS sites again exhibit a variable bias between 1 and 2 kg/m^2. Similarly to previous observations, there is a “hunch” in the GPS time series (at 14:30 UTC), which is not seen in the SAMOS curve. These might arise from multipath effects at the station.

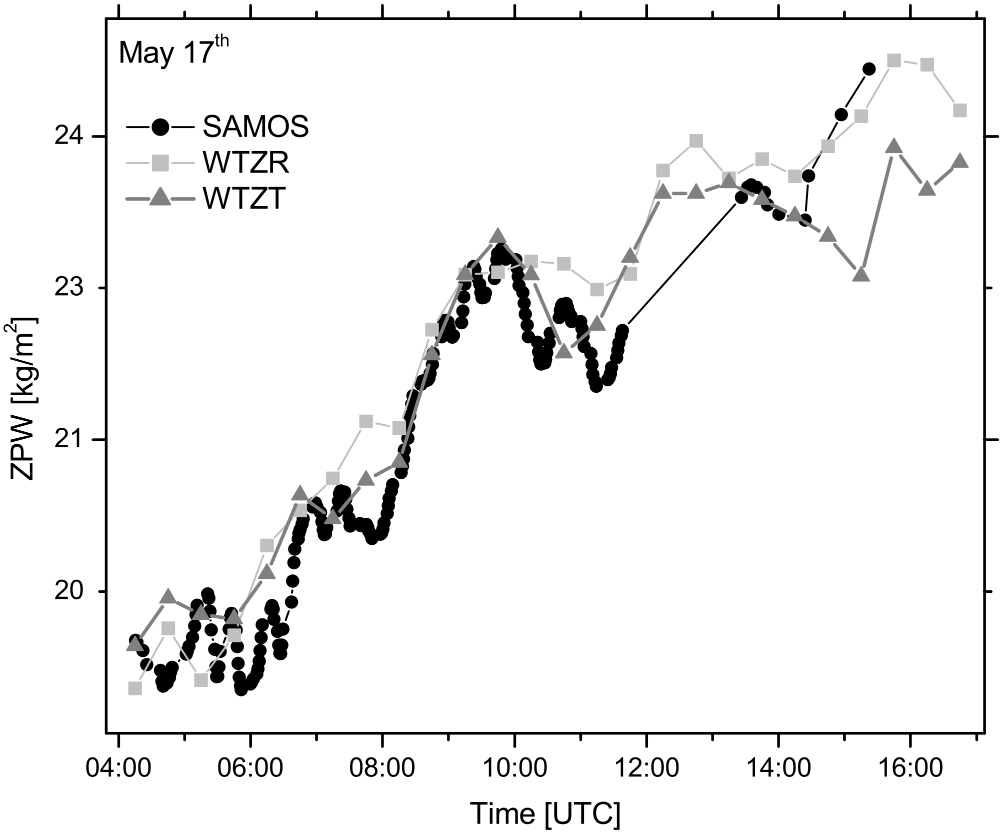

Figure 7.43: On May 17th the bias which was observed between the two GPS receivers seems to have vanished. Both time series agree well with the SAMOS curve with the exception of a sudden drop observed by SAMOS with a peak at 12:20 UTC. It is hard to say if this feature is "real". The discrepancy might arise from comparing the mapped unidirectional SAMOS observation with the averaged GPS estimate. Due to the corrupted WVR measurements this hypothesis could not be verified

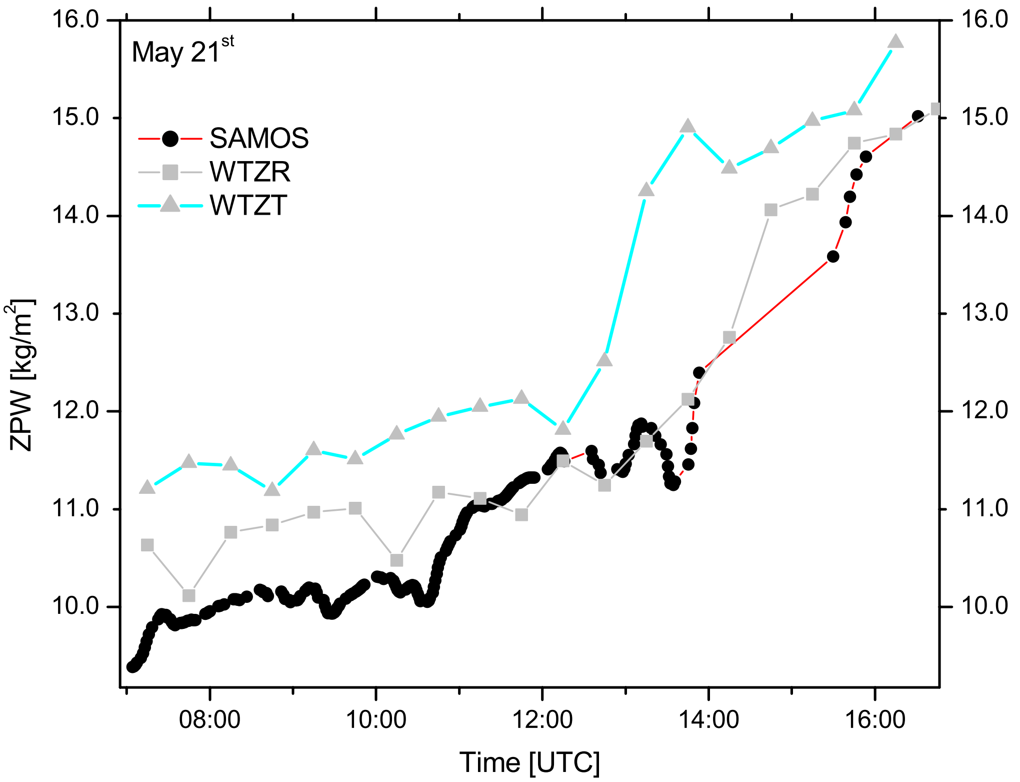

Figure 7.44: The GPS bias with the WTZT site measuring higher PW than WTZR is visible again on this day. It even reaches almost 3 kg/m^2 at 13:45 UTC. Again the SAMOS curve, which is interrupted due to cloud cover between 13:50 and 15:20 UTC, agrees better with WTZR.

Difference	bias kg/m^2	stddev kg/m^2	observations
SAMOS-WTZR	-0.29	0.71	123
SAMOS-WTZT	-0.84	0.93	123
SAMOS-WVR	0.66	1.80	154
WVR-WTZR	0.07	1.69	423
WVR-WTZT	-0.53	2.12	423
WTZR-WTZT	-0.64	0.54	491

Table 7.4: Comparison statistics for the Wettzell measurements. The WVR is included for completeness, but should not be interpreted since the measurements were corrupted (presumably by disturbing microwave sources, see text)

The Wettzell results are particularly interesting with respect to the comparison of the two GPS sites of the IGS network. Although the receiver types, the processing scheme and the observed satellites are identical, varying discrepancies up to 3 kg/m^2 have been observed. This is higher than the level of accuracy usually reported for GPS meteorology using precise GPS orbits (e.g. Rocken et al. [1995], Kruse et al. [1999]). A possible explanation could be multipath effects, which might be responsible for the temporal deviations visible in Fig. 7.40 - 7.43. The conditions at the observation site, characterized by the balustrade shown in Fig. 7.3.1 and 7.3.1 can lead to multipath influences on the two IGS sites. The comparison result demonstrates the need for an independent technique validating estimates from a meteorological GPS network. Although the overall comparison between the GPS sites is within acceptable error bounds (< 1 kg/m^2, see table 7.4), a deviation of 2-3 kg/m^2 over a period of several hours, as observed on May 14, is likely to deteriorate forecast results if introduced into numerical weather models.

With the results presented in Fig. 7.40 - 7.42 it could be clearly demonstrated that SAMOS is capable of measuring PW at very low elevation angles. Retrievals of PW were inferred from spectra which were measured with the Sun almost setting at $2°$ elevation. This quality, which is not provided by the WVR and GPS techniques, is particularly useful for certain applications (see outlook in section 8.2). The comparison statistics for the Wettzell campaign is summarized in table 7.4. The corresponding scatter plots are shown in Fig. 7.45.

7.4 Accuracy analysis for PW retrieval

7.4.1 Introduction

In this section the characteristics of the solar spectrometry technique will be analyzed to obtain an estimate of the accuracy of PW retrieval. Also the contributions

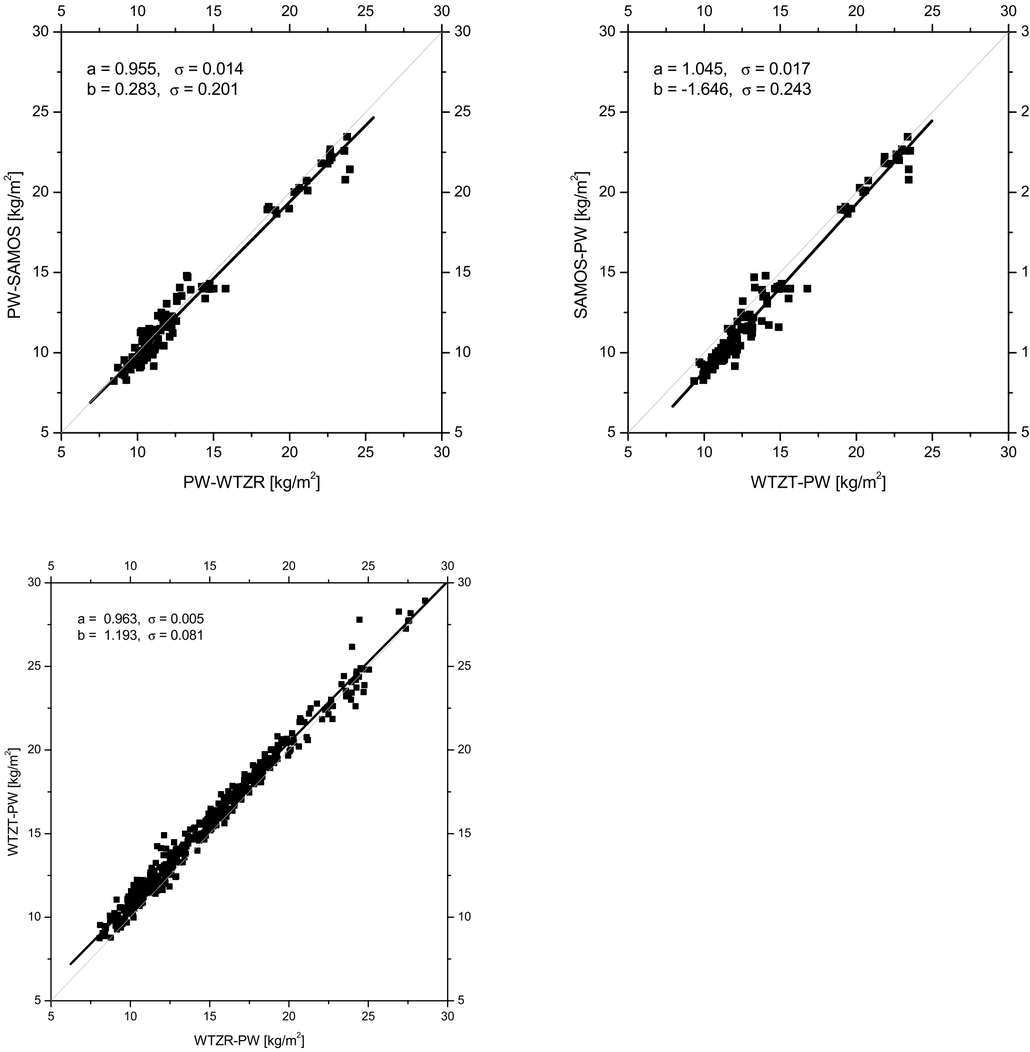

Figure 7.45: Scatter plots for the comparison of SAMOS retrievals with PW estimates at two GPS sites in Wettzell

of the individual error sources to the total uncertainty will be investigated.

The error sources of water vapor DOAS can be classified as measurement errors causing the noise of the differential intensities and errors of the radiative transfer model used in the data processing. The latter category can further be subdivided into the physical model of the absorption process and the meteorological models expressing the assumption on the atmospheric state. The three categories will be treated separately in the following.

7.4.2 Measurement error

The error of the differential intensity measurement can be estimated theoretically by analyzing the characteristics of the detector. The measurement noise of the photodiodes is described by the so-called shot-noise. Its variance is given by the square root of the total number of detected electrons. The exposure time for acquiring the solar spectra is continuously adjusted to work at the maximum detection range of the detector array around 10 Volts. The number of electrons in this case is on the order of 10^6, so that the shot noise is about 10^3 electrons, which corresponds to an error of 0.001 differential transmission. The non-linearity of the detector is about 0.5 % according to the manufacturer, so the total measurement error due to the detector amounts to about 0.006 differential transmission.

Another, more realistic way to estimate the instrumental noise is to determine the variance of the differential intensity values in the baseline interval used in the DOAS-normalization (see section 6.2.2.2). The flatfield has been lifted to match the solar spectrum using a least squares fit of a simple stray light model. With Eq. 6.14 it was postulated that the differential transmission be 1 (100 %) in the baseline interval. The *rms* of the fit result in the normalization procedure reflects the scatter of the normalized transmission values around 100 %. It is therefore a measure for the noise of the differential intensity values. As pointed out in section 6.2.2.2 the *rms* was found to be better than 0.008 (0.8 %) for all selected measurement intervals. For a worst case estimate we assume the noise level of SAMOS measurements to be 1% [2].

In order to determine the impact of the measurement error on the PW retrieval, the error propagation is calculated after Gauss. The standard deviation of the retrieval $\sigma_{PW}^{I'}$ due to independent errors $\sigma_{I'_i}$ of m differential intensities is given by

$$\sigma_{PW}^{I'} = \Big[\sum_{i=1}^{m} \Big(\frac{\partial PW}{\partial I_i} \Big)^2 \cdot \sigma_{I'_i}^2 \Big]^{1/2} \tag{7.1}$$

In matrix notation, Eq. 7.1 can be written as

---

[2] Note that this figure denotes an absolute error of the differential transmission measurement, expressed in percent, not a relative error

$$\sigma_{PW}^{I'} = \sqrt{\mathrm{tr}(\mathbf{K^T P K})^{-\mathbf{1}}} \tag{7.2}$$

where the $\mathbf{K}$ is the vector of partial derivatives $\partial I'(\lambda_i)/\partial \mathrm{PW}$ in the final iteration of the least squares adjustment of PW expressed by Eq. 6.31. $\mathbf{P}$ is the weighting matrix given by the inverse of the measurement error covariance matrix. Assuming independent and constant errors for all pixels of the detector array it becomes

$$\mathbf{P} = \frac{\mathbf{1}}{\sigma^{\mathbf{2}}_{\mathbf{I'_i}}} \cdot \mathbf{I} \tag{7.3}$$

with $\mathbf{I}$ being the identity matrix. In the processing of SAMOS spectra for PW retrieval, the error $\sigma_{PW}^{I'}$ was computed using Eq. 7.3 assuming $\sigma_{I'} = 0.01$ according to the considerations outlined above. The errors were found to vary between 0.02 and 0.03 kg/m^2 of PW for the different wavelength intervals. These figures are extremely low compared to the total error of other techniques. In water vapor radiometry the retrieval error due to uncertainties in the brightness temperature (mainly caused by inaccurate determination of the hot load correction, see section 2.2.4) is estimated to 0.4 cm zenith wet delay or 0.6 kg/m^2 PW (Kruse [2000], Jarlemark [1997]). Optical absorption measurements with SAMOS are much less sensitive to instrumental calibration than microwave emission measurements. Of course the findings above do not represent the total error of SAMOS retrievals. As will be shown in the following two sections, the measurement error can be regarded as negligible with respect to the errors induced by the spectral line parameters and the meteorological model assumptions.

7.4.3 Absorption model errors

The retrieval error due to uncertainties of the absorption model parameters is determined in a similar way as the impact of measurement noise on the PW estimates . However, in contrast to the measurement noise, the influence of inaccurate parameters are truly systematic errors with no time dependence. In the treatment of water vapor content, some spectral line parameters are irrelevant. The line position ν_0 is adjusted to match the measured spectrum as outlined in section 6.3.4.1 and therefore does not propagate into the PW estimation. The halfwidth γ_{L0} affects the shape of the line but not the integral absorption, which is the measure for determining the water vapor abundance. Therefore we only need to consider the line strength parameter S_0, whose errors induces a systematic retrieval error of PW. According to Rodgers [2000] the systematic error in the retrieval due to errors in the line parameters $S_0 l$ is given by:

$$\epsilon_{PW}^{S_0} = (\mathbf{K^T P K})^{-\mathbf{1}} \mathbf{K^T P} \cdot \mathbf{K_{S0}} \cdot \Delta\mathbf{S0}, \tag{7.4}$$

where $\mathbf{K_{S0}}$ is the sensitivity of the forward model to the parameters, given by

$$K_{S0,ij} = \frac{\partial I'_i}{\partial S_{0j}}. \tag{7.5}$$

and $\Delta\mathbf{S0}$ the deviation of our knowledge of the model parameters from their true values. The matrix $\mathbf{K_{S0}}$ for the lines l affecting the processing interval can be calculated straightforward by

$$\begin{aligned} K_{S0,il} &= \frac{\partial I'(\lambda_i)}{\partial S_{0,l}} \\ &= I(\lambda_i) \cdot \Big[-\int_{h=s_0}^{S_{trop}} \rho_w(s) \sum_l \frac{S(T(s))}{S_{0l}} \cdot f(\lambda_i, s) ds \Big], \end{aligned} \tag{7.6}$$

which we already encountered as Eq. 6.19 in the line parameter fit described in section 6.3.4.2. The deviation of the line parameters from the true constant values $\Delta\mathbf{S0}$ are of course unknown. However we have two estimates of their precision: The accuracy indices given in the HITRAN database and the standard deviations of the line parameters determined in section 6.3.4.2. Both were used to estimate their propagation into the PW retrieval in an analogous way to the treatment of measurement error in the pervious section. Every single absorption transition whose line stregth S_0 was determined using the MAP radiosondes and tabulated in table 6.2 is treated separately. The statistic retrieval error $\sigma_{PW}^{S_{0l}}$ due to the estimated error $\sigma_{S_{0}l}$ of line l is given by:

$$\sigma_{PW}^{S_0 l} = \sqrt{\mathbf{H^T} \cdot \mathbf{H}} \cdot \sigma_{S_0 l}, \tag{7.7}$$

where the vector $\mathbf{H}$ is according to Eq. 7.4 given by:

$$\mathbf{H} = (\mathbf{K^T P K})^{-1} \mathbf{K^T P} \cdot \mathbf{K_{S_{0l}}} \tag{7.8}$$

The error influence of the line strength parameters can be estimated using Eq. 7.7, 7.8 and 7.6. The results of this analysis which was carried out for HITRAN and radiosonde fit (RAOB) error estimates are summarized in tables 7.5 and 7.6.

As seen from the tables, the magnitude of the line parameter error contribution is on the order of 0.5 kg/m^2 and does not exceed 1 kg/m^2 except for the most uncertain parameters when the HITRAN accuracy estimates are used. When applying the lower standard deviations of the radiosonde fit results (RAOB) as accuracy estimates $\sigma_{S_0 l}$ in Eq. 7.7, the mean error in PW retrieval is correspondingly lower. However,

λ nm	RAOB σ_{S_0} $\frac{10^{-25}cm^{-1}}{(molec.\cdot cm^{-2})}$	HITRAN σ_{S_0} $\frac{10^{-25}cm^{-1}}{(molec.\cdot cm^{-2})}$	RAOB $\sigma_{PW}^{S_0}$ kg/m^2	HITRAN $\sigma_{PW}^{S_0}$ kg/m^2
651.8339	0.84	9.73	0.12	1.35
651.8432	1.08	10.82	0.15	1.51
652.1243	0.92	5.65	0.38	2.31
740.9745	0.38	0.05	0.06	0.01
741.2342	1.17	0.95	0.43	0.35
787.7490	0.29	1.26	0.19	0.84
787.8275	0.20	0.19	0.20	0.19
787.8722	0.41	0.62	0.09	0.14
787.8869	0.15	0.28	0.03	0.06
789.5681	0.64	1.01	0.11	0.18
789.7677	0.88	0.88	0.19	0.19
789.8198	1.18	1.21	0.18	0.18
795.8354	0.18	0.20	0.17	0.19
796.0674	1.58	1.38	0.19	0.17
796.2451	1.82	1.86	0.71	0.73
796.2916	1.15	1.05	0.19	0.18
796.3797	0.67	2.43	0.22	0.79
802.2916	1.17	1.20	0.38	0.39
802.4268	0.94	0.63	0.55	0.37
802.5153	0.78	0.49	0.23	0.14
802.5372	0.41	0.45	0.12	0.13
804.5364	0.95	1.22	0.28	0.36
804.5806	0.49	0.19	0.48	0.19
804.6094	0.87	0.48	0.61	0.34
804.6598	1.41	0.87	0.54	0.34
804.7723	1.44	0.65	0.37	0.17
825.4991	3.09	6.48	0.17	0.35
834.3730	0.09	1.37	0.07	1.02
834.4562	1.91	1.21	0.27	0.17
834.9624	1.26	1.02	0.81	0.66
835.1454	1.85	1.52	0.17	0.14
835.1669	0.41	0.20	0.04	0.02
835.1685	1.24	0.95	0.12	0.09
835.2260	0.32	0.11	0.48	0.17
837.6837	0.22	0.63	0.13	0.39
837.6844	0.16	0.35	0.10	0.21
837.7998	0.25	0.13	0.37	0.19
837.8460	0.71	1.11	0.43	0.67
837.8666	2.16	1.21	0.24	0.13

Table 7.5: Error influence of individual spectral line strength parameters S_0 on PW retrieval (part 1). The table is continued in 7.6.

λ nm	RAOB σ_{S_0} $\frac{10^{-25} cm^{-1}}{(molec.\cdot cm^{-2})}$	HITRAN σ_{S_0} $\frac{10^{-25} cm^{-1}}{(molec.\cdot cm^{-2})}$	RAOB $\sigma_{PW}^{S_0}$ kg/m^2	HITRAN $\sigma_{PW}^{S_0}$ kg/m^2
837.9450	1.16	0.44	0.40	0.15
838.6477	0.21	0.94	0.08	0.36
838.7797	0.14	0.69	0.05	0.26
839.6315	0.51	0.46	0.19	0.17
892.9332	0.71	2.28	0.28	0.91
893.1507	5.73	10.6	0.36	0.67
893.1921	1.15	2.26	0.65	1.28
893.2710	3.98	9.03	0.42	0.95
mean	1.05	1.88	0.28	0.44

Table 7.6: Continuation of table 7.5

the average of about 0.3 kg/m^2 is probably a too optimistic estimate, since the σ_{S_0} for the radiosonde adjustments only reflect the scatter of the line parameter fit results. Systematic errors of the radiosondes are not represented by this value. The accuracy indices given in the HITRAN database could be too optimistic as well, given that the improvements applied to the parameters in section 6.3.4.2 frequently exceeded these limits. In summary it can be stated that the order of magnitude of the model parameter error contribution could be determined, and a value of 0.6 kg/m^2 can be assumed as a realistic estimate.

7.4.4 Influence of meteorological profiles

The deviations of the models of vertical pressure, temperature and humidity distribution (as outlined in section 3.9) from the true meteorological profiles in the atmosphere during the measurement will cause errors in the retrieved water vapor abundance. While the pressure profile is usually well described by the barometric formula, the temperature profile frequently exhibits significant deviations from a linear decrease, especially in the presence of inversions. The water vapor distribution is known to be even more variable and although the mean profile is usually described by an exponential height dependence (see Fig. 7.15 in section 7.2.2) the actual humidity profile almost never corresponds to this model. It is difficult to analyze the error influence of temperature and water vapor distribution separately, but the combined effect of the meteorological model assumptions can be investigated statistically using the dataset of radiosondes launched during the MAP campaign. These data represent the variability of the atmosphere in the experiment.

For studying the impact of this variability separately from the other error sources in SAMOS measurements, the radiative transfer model will be used to calculate simulated spectra based on the radiosonde profiles. These spectra will be treated as SAMOS measurements and the processing algorithm based on the meteorological model assumptions will be applied to retrieve the precipitable water vapor from these simulations. By comparing the retrieval result with the integrated radiosonde profile of absolute humidity (the true value), the combined error influence of the model profiles can be quantified.

This investigation can be done for each pair of a radiosonde launch and a measured spectral interval, which for the MAP dataset amounts to about 1400 simulated spectra. However, we restricted the analysis to the radiosonde soundings launched at noon time, since they are most representative for the meteorological conditions during sunshine. The 25 noon time launches were used to investigate the error influence of the meteorological model for each of the 14 spectral intervals (which still means performing 350 retrieval simulations). This was done twice: One time the nominal water vapor distribution profile from Fig. 7.15 was used, which was derived as a mean profile from the entire MAP radiosonde dataset. The same analysis was repeated using the standard meteorological model profiles expressed by Eq. 3.53. The comparison of the two simulations reveals the impact of using meteorological models which are improved by using a-priori information on the vertical humidity distribution. The standard deviation of the retrieval results for all selected spectral intervals was computed representing the scatter of the PW solutions. The results are presented in table 7.7.

The statistics of a total of 700 retrieval simulations reveals that the error contribution of meteorological profiles is smaller than those of the spectral line parameters. The usage of an improved nominal height profile of water vapor distribution yields lower errors in PW retrieval. Although the average impact is not large, the retrieval errors do not exceed 0.3 kg/m^2 while they can reach up to 0.5 kg/m^2 when standard models are used. Nevertheless it can be pointed out that the error analysis revealed a low sensitivity of PW retrievals to the vertical distribution of absorbing molecules. While this is a positive result for the determination of column water vapor amounts, it reduces the chances for retrieving information on vertical humidity distributions. This question will be closely analyzed in the section 7.5.

7.4.5 Other error sources

There are some effects which are likely to influence the retrieval of precipitable water, but are impossible to quantify. One of them is the problem of stray light, which was already addressed in section 6.2.3. It was pointed out that the saturated oxygen lines measured around 765 nm can be utilized to determine the stray light level within SAMOS. However, the uncertainty of this technique is estimated to be about 1 % differential transmission. The uncertainty of stray light level affects the measured intensities of a solar spectrum equally. It is therefore a purely systematic influence, resulting in offsets between the retrievals from different wavelength intervals. The effect is likely to be partly responsible for the offsets observed in section Fig 6.34 (see section 6.3.4.2). However, by averaging the retrievals from the different measurement windows the impact on the PW result is significantly reduced.

Date	PW$_{nom}$ kg/m^2	σ_{nom} kg/m^2	PW$_{mod}$ kg/m^2	σ_{mod} kg/m^2
18.9	23.42	0.26	23.63	0.42
21.9	14.51	0.29	14.68	0.38
2.10	22.77	0.29	22.98	0.52
3.10	22.93	0.15	23.14	0.31
5.10	10.25	0.10	10.36	0.17
8.10	9.83	0.05	9.94	0.12
9.10	16.49	0.24	16.67	0.10
18.10	10.31	0.28	10.39	0.21
20.10	12.69	0.30	12.83	0.20
24.10	14.50	0.33	14.65	0.47
27.10	11.65	0.27	11.78	0.17
28.10	17.43	0.08	17.59	0.24
29.10	20.59	0.31	20.80	0.14
31.10	14.94	0.19	15.11	0.15
1.11	8.03	0.14	8.11	0.46
4.11	17.50	0.19	17.69	0.15
5.11	14.16	0.27	14.32	0.15
6.11	12.90	0.11	13.03	0.24
7.11	12.01	0.06	12.14	0.15
9.11	10.78	0.11	11.09	0.06
10.11	10.91	0.10	11.02	0.08
mean	13.88	0.20	14.85	0.24

Table 7.7: Statistics of error contributions of meteorological profiles. The mean PW retrievals and standard deviations σ of the PW results from the different measurement intervals are tabulated. The subscript *nom* denotes the usage of the nominal mean H_2O-distribution profile from Fig. 7.15, the subscript *mod* the meteorological models expressed by Eq. 3.53. Using a-priori information yields only slightly lower errors in PW retrieval.

Another systematic error source comes into play when clouds appear during the SAMOS measurement. The intensity of sunlight is sufficient for recording low intensity spectra with longer exposure times as long as the solar disk is still visible through the cloud layer. However, when the light has to pass through a cloud layer it can be multiply reflected within the clouds. This leads to a longer absorption path and thus stronger absorption. If the effect were broadband within the spectral intervals considered, it would cancel out in the normalization procedure like the scattering effects. Unfortunately the longer absorption path will result in stronger line absorption and therefore affect the PW retrieval under cloudy conditions. There have been indications for this effect in SAMOS data acquired during the field campaigns. Examples for this are e.g. the PW time series acquired at February 16 on Hawaii (Fig. 7.4), as well as those recorded during the MAP campaign at October 10 (Fig. 7.21) and October 14 (Fig. 7.24. The PW retrievals are increasing before and/or after a cloud cover on these days, which could be due to stronger line absorption. However it is not for sure if multiple scattering within clouds are the origin of the PW overestimation.

Multiple scattering effects in clouds and the resulting excess absorption paths are currently under intensive investigation in the efforts to explain the phenomenon of anomalous cloud absorption (e.g. Pfeilsticker et al. [1998], Savigny et al. [2000]). It is possible that reliable models will be available in the future, which are able to quantify these effects and consequently offer a way for corrections of multiply scattered absorption measurements. In the meantime reliable SAMOS retrievals of PW can only be performed under clear weather conditions, while spectra recorded through cloud layers should be handled with care.

7.5 Investigation of profile retrieval

In the introduction it was pointed out that the investigation of the possibility to derive information about the vertical distribution of water vapor from solar spectrometry data was a goal of this study. The line selection procedure described in chapter 4 revealed that the weighting functions of spectral intervals, which were chosen to maximize the information content on vertical distribution, are strongly overlapping and do not exhibit clearly separated maxima. In the previous section the sensitivity of the PW retrieval with respect to changes in the meteorological profiles was found to be relatively low. These facts are indicating that the solar absorption measurements are unlikely to be suited for retrievals of vertical humidity profiles. This question is closer examined in the following.

In order to obtain an impression of the signal for profile retrieval, which is to be expected, the radiative transfer developed in chapter 3 can be utilized again. With “signal for profile retrieval” one can define the residual intensity differences between a SAMOS spectrum measured under real atmospheric conditions and a spectrum corresponding to the model atmosphere characterized by the nominal profile distribution presented in section 7.2.2 but with the same integrated water vapor content. These differences should reflect the deviations of the real profile from the a-priori model. In order to simulate this, we selected two extreme radiosonde profiles from the MAP dataset, representing two contrary distribution profiles. The absolute humidity profiles as measured by the balloon soundings on October 18 and October 24, both launched at noon, are plotted in Fig. 7.46. Along with the real profiles the corresponding model profiles according to the nominal profile presented in Fig. 7.15 scaled to the water vapor abundance measured by the radiosonde. The October 18 sounding is a typical example of a profile characterized by a temperature inversion, while the October 24 is rather unusual because of the increasing absolute humidity at about 5000 m. The two profiles were selected, since they represent opposite distribution situations with respect to the corresponding nominal profiles. On October 18 the model assumption underestimates the humidity in the lower troposphere and overestimates in the upper layers, while in the October 24 profile the situation is reversed. The question is how these two extreme situations are reflected in the spectral data. To investigate this, two model spectra have been calculated for each of the 13 selected wavelength windows listed in table 4.1. The two series of spectra were computed using the radiosonde and the nominal profile, respectively. The differences of the differential transmissions are plotted in Fig. 7.47 a) and b).

The difference spectra are plotted in terms of pixels for a better representation. The plotted curve can also be interpreted as the vector of measurements for profile retrieval. As can be seen from the two plots, the opposite profile characteristics are indeed reflected in the simulated data. The average of the differences have opposite signs. While the transmissions corresponding to the real atmosphere are lower than those for the model atmosphere on October 24, the situation is reversed for October 18. However, the simulation also confirms the expectation mentioned above, that the signal differences are extremely small. Apart from very few peaks of 3 % differential transmission, most differences do not exceed 1 %. The noise level of differential intensity measurements with the SAMOS spectrometer was estimated to 0.8 %. In addition to the instrumental noise one has to take into account the systematic offsets between the different spectral intervals due to different stray light levels and uncertainties in the line strength parameters. From these considerations it becomes clear that the resolution of SAMOS spectra will most likely not be sufficient for retrieval of vertical humidity profiles. However, this will be more closely investigated in the following:

The number of parameters that can be estimated from a set of indirect measurements can be determined from the weighting function matrix $\mathbf{K}$, given by Eq. 4.17 in section 4.3.2, the estimate of the instrumental errors and the knowledge about the a-priori variance of the parameters. Theoretically the number of independent pieces of information is given by the rank of $\mathbf{K}$. However, in the presence of measurement error, the number of parameters that are determined to better than measurement error can be much smaller than the rank of $\mathbf{K}$. In addition the atmospheric inversion problem is well known of being ill-conditioned Eriksson [1999] and as a consequence,

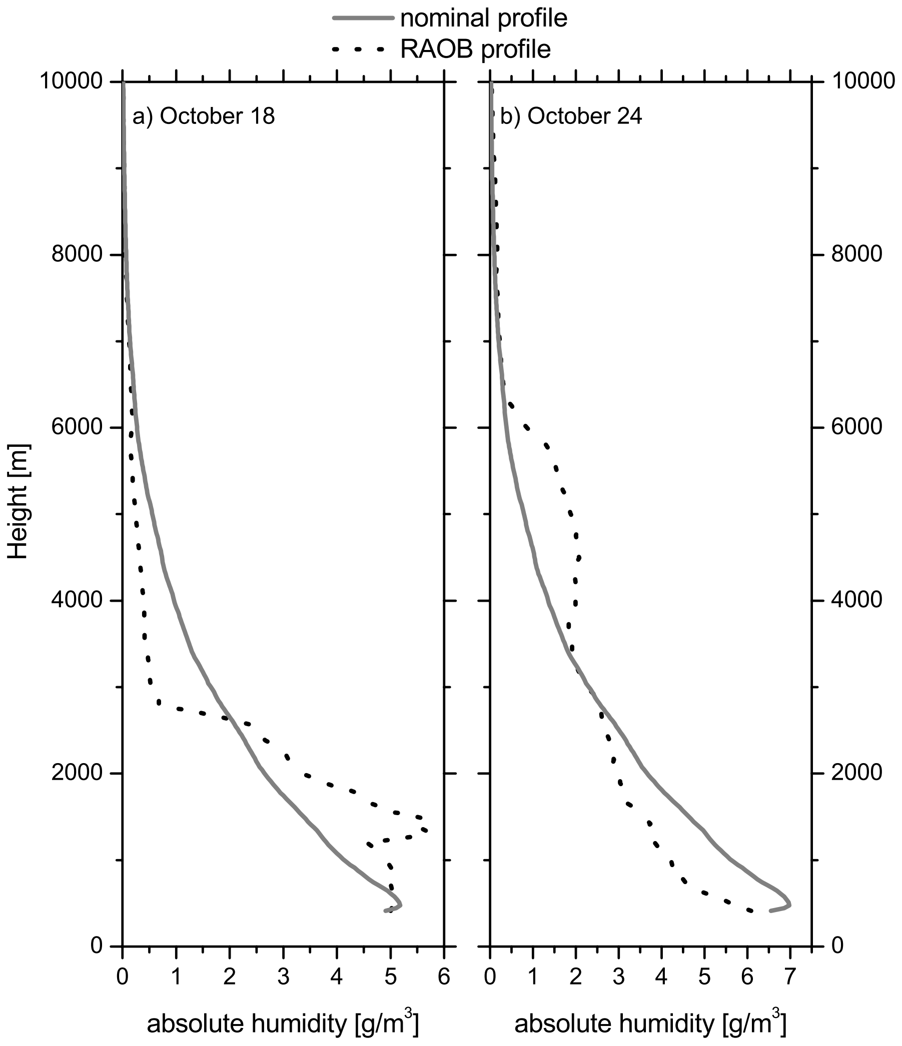

Figure 7.46: Two radiosonde soundings (black dotted line) with extreme deviations from the model profile (grey solid line). While the October 18 launch sees more water vapor in the lower troposphere due to a temperature inversion, the October 24 launch exhibits an increased humidity in the upper troposphere. The four profiles (radiosondes and model) were used to simulate the corresponding differences in the absorption spectra (see Fig. 7.47)

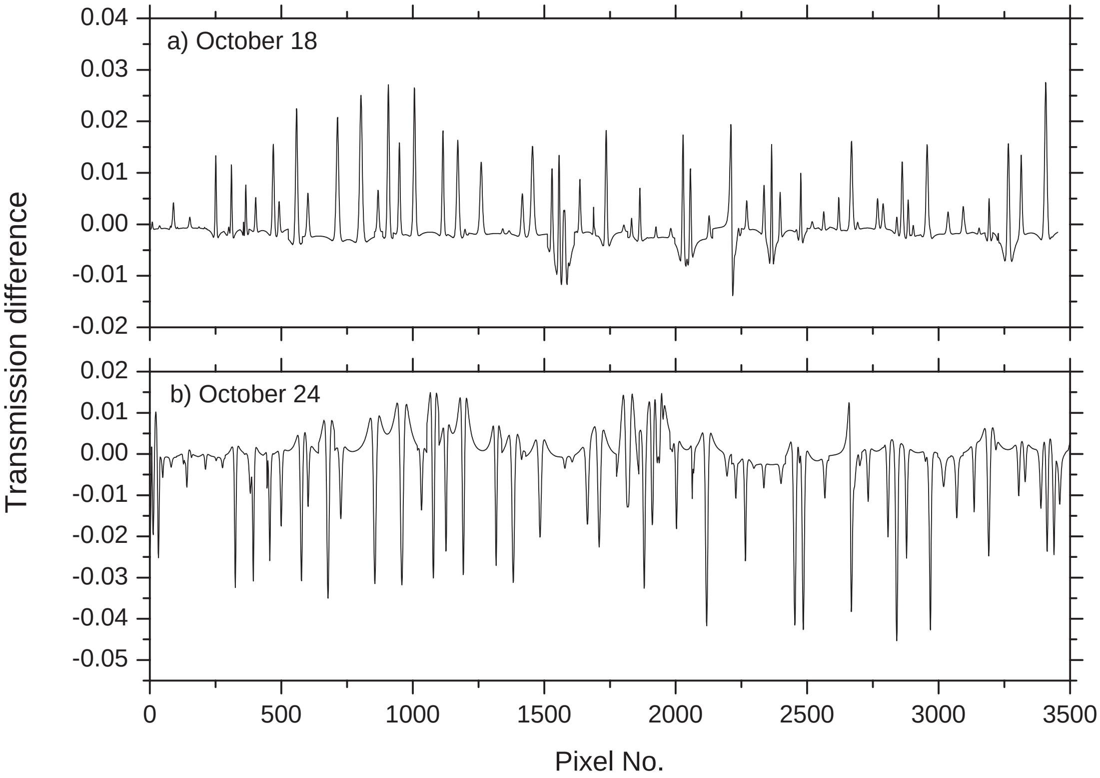

Figure 7.47: Transmission differences between spectra calculated using the radiosonde profiles from Fig. 7.46 and model atmospheres using the nominal distribution profile from Fig. 7.15. The opposite profile characteristics result in opposite signs of the differences.

numerical instabilities might occur which render the retrieval useless. The number of useful independent pieces of information is defined by Rodgers [2000] as the "effective rank" of the problem and the solutions lie in the effective row space, spanned by the linear independent row vectors of **K** which correspond to the retrievable parameters. To identify this subspace the measurement error covariance $\mathbf{S}_\epsilon$ is compared with the natural variability of the parameters expressed by the a-priori covariance $\mathbf{S_a}$. The components whose natural variability is smaller than the measurement error cannot be determined. In order to compare the error covariances $\mathbf{S}_\epsilon$ and $\mathbf{S_a}$ the basis is transformed so that the off-diagonal elements become zero. This is done by transforming the parameter vector **x** and the measurement vector **y** with error ϵ by Rodgers [2000]:

$$\tilde{\mathbf{x}} = \mathbf{S_a}^{-\frac{1}{2}}\mathbf{x} \quad \text{and } \tilde{\mathbf{y}} = \mathbf{S}_\epsilon^{-\frac{1}{2}}\mathbf{y}. \tag{7.9}$$

The transformed forward model then becomes

$$\tilde{\mathbf{y}} = \mathbf{S}_{\epsilon}^{-\frac{1}{2}}\mathbf{K}\mathbf{S}_{\mathbf{a}}^{-\frac{1}{2}}\tilde{\mathbf{x}} + \mathbf{S}_{\epsilon}^{-\frac{1}{2}}\epsilon = \tilde{\mathbf{K}}\tilde{\mathbf{x}} + \tilde{\epsilon}. \tag{7.10}$$

The covariances of $\tilde{\mathbf{x}}$ and $\tilde{\epsilon}$ are both unit matrices in this system. It can be shown that the effective rank of the inversion problem is the number of singular values of $\tilde{\mathbf{K}} = \mathbf{S}_{\epsilon}^{-\frac{1}{2}}\mathbf{K}\mathbf{S}_{\mathbf{a}}^{-\frac{1}{2}}$, which are greater than about unity. The corresponding parameters are the ones which are determined to better than measurement error.

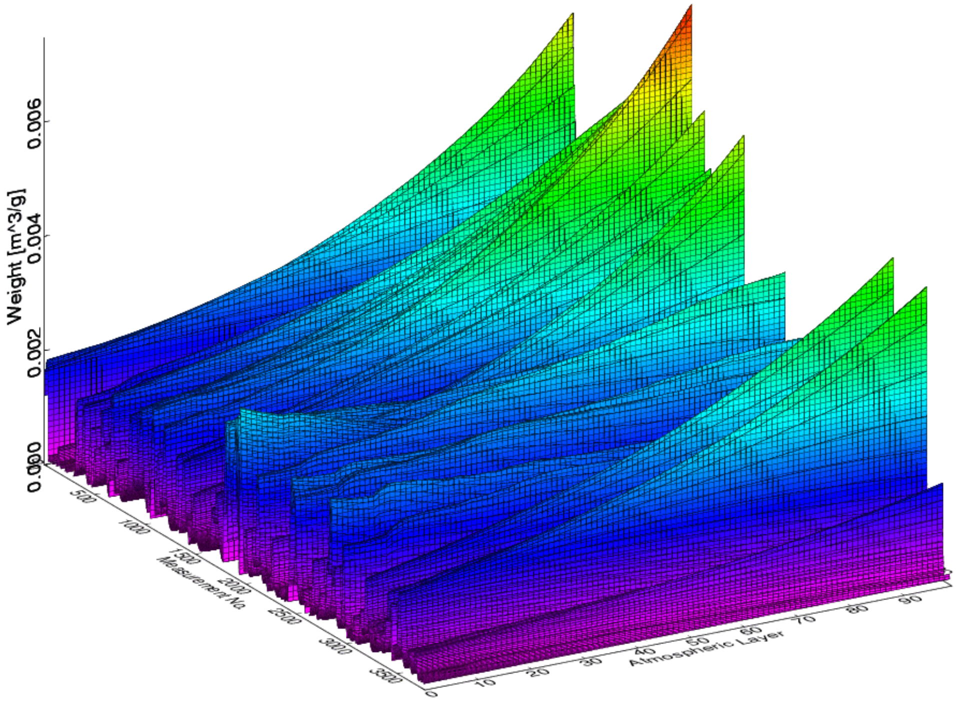

Figure 7.48: Weighting function matrix **K** for all wavelengths included in the analysis.

This analysis has been carried out for the inversion problem at hand. The weighting function matrix has been recalculated according to Eq. 4.17 using 100 equidistant atmospheric layers. Only the wavelength windows within the measurement intervals which were found to be suited for PW retrieval in section 6.3.3 were considered. The entire set of spectral measurements with a resolution of 1 *pm* amounts to more than 5000 wavelengths. The resulting weighting function matrix is plotted in Fig. 7.48. It corresponds to Fig. 4.6 and Fig. 4.7 in section 4.3.4 with the difference that it comprises all measured absorption lines. The covariance matrix $\mathbf{S}_{\mathbf{a}}$ for the absolute humidities ρ_j has been calculated using the 112 radiosondes of the MAP dataset. The measurement errors of the detector pixels were assumed to be independent, so the covariance matrix $\mathbf{S}_{\epsilon}$ is diagonal with $\sigma = 0.008$. The singular values of $\tilde{\mathbf{K}} = \mathbf{S}_{\epsilon}^{-\frac{1}{2}}\mathbf{K}\mathbf{S}_{\mathbf{a}}^{-\frac{1}{2}}$ are tabulated in table 7.8. It can be seen, that only the first

SV No.	value
1	37.6875
2	2.6395
3	0.3155
4	0.0498
5	0.0161
6	0.0057
7	0.0013
8	0.0005
9	0.0002
10	0.0001

Table 7.8: Singular values of the matrix $\mathbf{S}_\epsilon^{-\frac{1}{2}}\mathbf{K}\mathbf{S}_\mathbf{a}^{-\frac{1}{2}}$. Only the first two values are greater than 1, indicating the number of retrievable parameters is not greater than 2.

two singular values are greater than unity, implying that only two parameters can be estimated from the set of spectral measurements to better than measurement error. This result confirms the negative expectations expressed in the line selection (section 4.3.4) and in the accuracy analysis (section 7.4.4). We finally have to come to the conclusion, that a complete profile retrieval is not feasible with SAMOS measurements.

8 Discussion

8.1 Summary and Conclusions

The development of a dedicated DOAS system for remote sensing of tropospheric water vapor has been reported in this study. The investigations comprise theoretical aspects of retrieval, software developments for simulations and processing instrumental design and construction, as well as field measurements for comparison with other techniques. For simulations of the measurement process and data processing a numerical radiative transfer model was implemented which simulates the process of molecular line absorption. The algorithm is based on a line-by-line calculation of superposed absorption transitions. The line parameters describing the properties of the individual transitions were taken from the molecular database HITRAN. The model was used to select optimum measurement windows in the visible and near infrared spectral region in terms of suitability for DOAS measurements.

A spectrometer system was developed to measure solar absorption spectra in the selected wavelength intervals. The prototype called SAMOS (Solar Atmospheric MOnitoring Spectrometer) was designed as a field instrument using an Echelle grating with an extreme blaze angle of 82° in a Littrow mounting. Because of the high angular dispersion the instrument reaches a spectral resolution of better than 2 picometers over the entire spectral range, which enables to monitor the line shapes of individual H_2O-transitions. An absolute wavelength calibration of the measured spectra was achieved by means of neon reference spectra, which are measured in different diffraction orders from shifted entrance slits. The apparatus function of spectrometer was determined in laboratory measurements utilizing a narrow band Titanium-sapphire laser. In field operation, the sunlight is collected by a tracking solar telescope, which integrates a pre-monochromator stage consisting of narrow band interference filters. These can be fine adjusted to the measurement wavelengths by varying the incidence angle of solar radiation. The telescope also incorporates a halogen calibration lamp which generates flatfield spectra for baseline definition in the DOAS- processing.

The processing software comprises a pre-processing stage, in which each spectrum is associated to a wavelength scale by means of the simultaneously acquired neon spectra. In the subsequent normalization procedure, the flatfield spectra are utilized to define the normalization baseline. In this procedure the stray light levels of the flatfield spectra are determined in a least squares adjustment to the baseline interval of the solar spectra. An estimate of the solar stray light is obtained from measurements of saturated oxygen lines. The radiative transfer model is the basis for the final processing step, in which the tropospheric water vapor content is retrieved from the pre-processed SAMOS spectra. A least squares adjustment of the calculated transmission functions to the measured solar spectra is performed. In this procedure distribution models of atmospheric pressure, temperature and humidity are assumed and the fit parameter PW is determined.

The first measurements with SAMOS revealed that the retrieval of precipitable water vapor (PW) yielded large discrepancies between some of the different wavelength windows. These were interpreted as the result from significant errors in the spectral line parameters from HITRAN. As a consequence, one could have excluded the obviously erroneous intervals displaying the largest deviations from the average value of retrieved PW and find intervals with optimum agreement and redundancy. This would have meant abandoning the results of the interval selection and a considerable effort to perform measurements and retrievals over the entire observable spectral range. This was not feasible, since SAMOS was designed to operate at fixed wavelengths. Instead, the radiative transfer model was utilized in order to improve the spectral parameters of the selected transitions. First the line positions were corrected using the absolute wavelength calibration of the solar spectrometer. After that the line strength parameters were determined on the basis of a radiosonde dataset, which was acquired during a meteorological field campaign in which SAMOS was continuously operated at the launch site. Model transmission functions were fitted to the measured SAMOS spectra by adjusting the line intensity for each measured transition. In most cases, the fit results yielded improvements which were greater than the parameter errors specified in the database, although the largest adjustments were applied to the least accurately determined lines. The accuracy indices given in HITRAN are rough estimates and systematic errors have been recently discovered in the spectral region considered. Therefore it was decided to use the line strength parameters determined on the basis of a radiosonde dataset. This decision meant abandoning the postulation of independence from radiosonde calibration, which was pointed out as an advantage of the DOAS- approach over water vapor radiometry. However, the technique still offers the potential of external calibration in the laboratory and the line parameters available in molecular databases are likely to be improved in the future. WVRs are tuned to climate conditions for each area of deployment by a statistical dataset of radiosondes from that area. Line strength parameters, in contrast, have a universal validity as they correspond to the quantum mechanical transition probabilities (expressed by the Einstein coefficients), which are physical constants. Once they are determined, they can be applied everywhere on Earth (and in space). The retrieval results using the improved line parameters showed a satisfactory agreement between the different intervals within 0.5 kg/m^2 of PW.

Another observation from the comparison between radiative transfer model and measured solar spectra was the presence of additional absorption features which were not included in the model. Most of these could be identified as Fraunhofer lines by comparing spectra recorded at different solar elevation angles. In one case the comparison revealed the presence of atmospheric transitions that have not been incorporated in the spectral database. Nevertheless it could be demonstrated that the measurement windows exhibiting these features could be used for water vapor retrieval by considering only subintervals in which their influence can be neglected.

The SAMOS-system was deployed during three field campaigns in the USA (Hawaii), Switzerland and Germany. In all of these campaigns, collocated WVRs and GPS receivers were operated for comparing the results from independent techniques. To allow the comparison of the slant PW (SPW) retrievals from solar spectra with the zenith (ZPW) estimates of the other techniques they were related to the zenith value by integrating the modeled water vapor profile over height. The time series of ZPW showed different levels of agreement between the three remote sensing techniques with varying offsets. The statistically best match was obtained between the time series derived from SAMOS and GPS measurements. However, systematic deviations were observed which were interpreted as inherent effects of GPS meteorology. One observation is that the GPS estimates seem to react too slow on sudden changes in the troposphere´s water vapor content. This “inertial effect” is likely to arise from the relative constraints applied to the tropospheric parameters, which are necessary to keep the noise of GPS estimates within reasonable limits. This might also be the reason for the observed “exaggerating effect”: GPS estimates continue to fall or rise, respectively, after periods of steep drop or increase of PW, when SAMOS (and mostly WVR) already detected the turning point. Probably more problematic are periods of large deviations of more than 3 kg/m^2 between GPS and the other techniques, which are beyond the error limits of SAMOS and WVR (which are on the order of 1 kg/m^2). Part of the discrepancies with respect to SAMOS can be interpreted as azimuthal gradients of the water vapor content. While SAMOS retrievals are slant PW values in the direction to the Sun, GPS averages over the entire hemisphere. However, the observed discrepancies are too large to be fully explained by different viewing geometry. More recently, GPS software packages have been further developed to allow the estimation of tropospheric gradients in azimuth (Bar-Sever et al. [1998], Ruffini et al. [1999]). Such estimates can be compared with SAMOS slant PW retrievals in future investigations.

Another source of error in GPS estimates could be inappropriate mapping functions used in the GPS forward model, which are derived from standard atmospheres. These may not represent the atmospheric conditions in the presence of extreme meteorological profiles (e.g. temperature inversions). Such exotic humidity and temperature profiles (trade wind inversions) were frequently encountered on Hawaii, where the largest deviations were observed.

A surprising result of the comparisons were the discrepancies between the PW estimates from two identical GPS receivers at the Geofundamental Station in Wettzell, Germany. The two collocated receivers, which both are official IGS stations, exhibited variable offsets in PW reaching up to 3 kg/m^2 during short periods. Although the overall statistics of the comparison suggest a good agreement (bias and standard deviation ≈ 0.6 kg/m^2), these occasional periods of large discrepancies are likely to cause problems when introducing GPS estimates into numerical weather models for real-time forecasting. Therefore the external calibration and validation of such GPS retrievals with independent techniques will be a necessity in the operation of meteorological GPS networks, which are currently being established. The results of the test campaigns reported herein show that the solar spectrometry technique is feasible to perform this task.

One reason which makes the new technique especially suited as an absolute calibration standard is the excellent stability of the measurements. The error analysis revealed that the greatest part of the retrieval error for PW arises from uncertainties in the line strength parameters. The influence of meteorological profiles contributes about 20% of the total error while the impact of measurement noise of about 1 % differential transmission is neglectable. As mentioned above, line parameters can be improved by dedicated laboratory measurements, providing potential for further enhancement of absolute accuracy. The error budget of solar spectrometry differs significantly from that of WVR, where errors in the observed brightness temperatures have the largest impact (e.g.Kruse [2000]). The simultaneous deployment of both techniques is the best strategy for validating and calibrating GPS meteorological networks, since it combines the high stability of SAMOS retrievals with the capability of WVR for continuous omnidirectional operation under (almost) all weather conditions. The combined operation can mitigate the fundamental disadvantage of solar spectrometry to rely on Sun visibility.

The feasibility of deriving information on the vertical water vapor distribution from solar spectra was investigated taking into account the error analysis of the SAMOS measurements. Comparison of simulated spectra corresponding to real and modeled atmospheric profiles revealed that the signal for profile retrieval is on the order of 2-3 % differential transmission. While the measurement noise of approximately 1 % does not significantly affect the retrieval of column water vapor content, it renders the retrieval of humidity profiles impracticable. This was confirmed by an analysis of the weighting function matrix of the measurements taking into account the covariance of absolute humidity in different atmospheric layers.

8.2 Outlook

The feasibility of solar spectrometry-DOAS for stable and accurate retrieval of tropospheric water vapor abundance has been demonstrated. However, the technique has considerable potential for further improvements. In order to fully exploit the potential of the technique several instrumental and model parameters can be optimized. The most important non-instrumental optimization will be the improvement of spectral line parameters. The line selection process can be revised under the aspect of finding optimum measurement intervals for PW retrieval. In addition, the selected lines can be explicitly determined in dedicated laboratory measurements using long-path absorption cells.

Also on the instrumental side various optimizations can be achieved. The SAMOS prototype was optimized in terms of spectral resolution in order to study the information content of line shapes for profile retrieval. For the purpose of PW retrieval, the resolution power can be reduced to an extent which has to be investigated in future simulation studies. Loosening the requirements on resolution power would allow to use smaller Echelle gratings with lower blaze angles. This would significantly reduce the size and costs of new spectrometer prototypes. Since also the throughput is likely to be enhanced when working in lower diffraction orders, a tunable pre-monochromator could be used instead of fixed interference filters. A miniature pre-spectrometer with a holographic grating could perform the separation of Echelle orders. This would enhance the flexibility to change measurement frequencies over the entire observable spectral range.

Not only the technique bears potential for improvement, but also its spectrum of applications can be extended. As already pointed out in the previous section, solar spectrometry could serve as a calibration method for meteorological GPS networks. Such a calibration is especially important in real-time GPS meteorology. The use of predicted or simultaneously estimated GPS orbits has a strong impact on the absolute accuracy of tropospheric parameters, while the relative accuracy between PW estimates in such a network is less affected (Kruse et al. [1999]). By “binding” the absolute values of PW retrieved from a single GPS receiver to the measurements of a collocated solar spectrometer, and estimating relative tropospheric parameters with respect to this receiver, the entire network could be calibrated.

Another important advantage of the solar spectrometry approach is the capability of measuring at very low solar elevation angles. Retrievals of PW from spectra recorded at elevations down to 2° were demonstrated during the Wettzell campaign. This ability of the technique offers the possibility to investigate the impact of low elevation GPS measurements on the accuracy of estimated tropospheric parameters. While low elevation measurements are usually cut off in standard GPS processing they are of special importance in the context of GPS tomography, where they are required to constrain the three-dimensional water vapor fields in the tomographic analysis. On the other hand GPS low elevation observations suffer from increasing multipath errors arising from signal reflections at the ground. Microwave radiometry not suited to assess the error contribution, since the antenna side lobes of WVRs introduce contributions from the ground radiation resulting in dramatically increasing errors below roughly 15 degrees elevation. Solar spectrometer measurements offer the possibility to study the impact of ground-scattered multipath, which is a significant source of error in high accuracy GPS surveying and atmospheric sensing. There is considerable potential for reducing this error and the spectrometric technique may be useful for validation of multipath mitigation methods. Also spectrometer data will allow separation of delays induced by water vapor and by pressure gradients since SAMOS is sensitive only to water vapor while GPS is sensitive to refractivity (water vapor plus dry air). This is likely to be useful in error partitioning when GPS slant delays are assimilated into mesoscale models.

Some of the above mentioned topics will be investigated in the framework of a future ETH-project on solar spectrometry, which has recently been accepted. The project named GEMOSS (GEodetic Monitoring Solar Spectrometer) is the continuation of the SAMOS project and aims on the development and deployment of new spectrometer prototypes optimized for geodetic applications.

Bibliography

Bar-Sever, Y., Kroger, P., and Borjesson, J. (1998). Estimating horizontal gradients of tropospheric path delay with a single GPS receiver. *J. Geophys. Res.*, 103(B3):019–5036.

Becker, M., Zerbini, S., Baker, T., Bürki, B., Galanis, J., Garate, J., Georgiev, I., Kotzev, V., Lobazov, V., Marson, I., Negusini, M., Richter, B., Veis, G., and Yuzefovich, P. (2000). Assesment of Height Variations by GPS at the Mediterranean and Black Sea Coast Tide Gauges from the SELF Project. *Submitted to Global and Planetary Change.*

Becker-Ross, H., Florek, S., Franken, H., Radziuk, B., and Zeiher, M. (2000). A scanning monochromator for ICP-OES with dynamic wavelength stabilization and CCD detection. *J. Anal. At. Spectrom.*, 15:851–861.

Bevis, M., Businger, S., Herring, T., Rocken, C., Anthes, R., and Ware, R. (1992). GPS Meteorology: Remote Sensing of Atmospheric Water Vapor Using the Global Positioning System. *Geophys. Res. Lett.*, 97:15,787–15,801.

Bürki, B., Cocard, M., Geiger, A., Gyger, R., and Kahle, H.-G. (1992). Development of a portable dual frequency microwave water vapor radiometer for geodetic applications. *Proceedings Symposium Refraction of transatmospheric signals in Geodesy, J.C. De Munck and T.A.Th. Spoelstra (ed.), Netherlands Geodetic Commission*, 36:175–178.

Budden, K. (1961). *Radio Waves in the Ionosphere.* Camebridge University Press, Camebridge.

Camy-Peyret, C., Flaud, J.-M., Mandin, J.-Y., Chevillard, J., J.Brault, D. R., Vervloet, M., and Chauville, J. (1985). The High-Resolution Spectrum of Water Vapor between 16500 and 25250 cm-1. *J.Mol.Spectrosc.*, 113:208–228.

Chandrasekhar, S. (1960). *Radiative Transfer.* Dover Publications, Inc., New York.

Chevillard, J., Mandin, J.-Y., Flaud, J.-M., , and Camy-Peyret, C. (1989). H216O: line positions and intensities between 9500 and 11500 cm-1. The (041), (220), (121), (201), (102), and (003) interacting states. *Can.J.Phys.*, 67(1065-1084).

Clough, S., Kneizys, F., Anderson, G., Shettle, E., Chetwynd, J., Abreu, L., Hall, L., and Worsham, R. (1988). FASCOD3D: Spectral Simulation. In *Proceedings of the International Radiation Symposium ´88*, pages 372–375. A. Deepak Hapton, Va.

Dabberdt, W. F. and Schlatter, T. W. (1996). Research opportunities from emerging atmospheric observing and modeling capabilities. *Bull.Amer. Meteor. Soc.*, 77:305–323.

Davis, S. (1970). *Diffraction Grating Spectrogrphs.* Holt, Rinehart and Winston, New York.

Demoulin, P., Schmid, B., Roland, G., and Servais, C. (1996). Vertical column abundance and profile retrievals of water vapor above the Jungfraujoch,. *Proceedings of Atmospheric Spectroscopy Applications, ASA 96, Reims, September 4-6*, pages 131–134.

Dodson, A. and Baker, H. (1998). Accuracy of Orbits for GPS Atmospheric Water Vapour Estimation. *Phys. Chem. Earth*, 23:119–124.

Dodson et al., A. H. (1999). Final report on the wavefront project. *European Commission contract no ENV4-CT96-0301.*

Elgered, G. (1993). Tropospheric radio path delay from ground-based microwave radiometry. *Atmospheric Remote Sensing by Microwave Radiometry*, pages 215–258.

Emanuel, K., Raymond, D., Betts, A., Bosart, L., Bretherton, C., Droegemeier, K., Farrell, B., Fritsch, J. M., Houze, R., LeMone, M., Lilly, D., Rotunno, R., Shapiro, M., Smith, R., and Thorpe, A. (1995). Report of the first prospectus development team of the U.S. Weather Research Program to NOAA and the NSF. *Bull. Amer. Meteor. Soc.*, 76:1194–1208.

Eriksson, P. (1999). *Mircowave Radiometric Observations of the Middle Atmosphere: Simulations and Inversions.* PhD thesis, Chalmers University of Technology.

Essen, L. and Froome, K. (1951). The refractive indices and dielectric constants of air and its principal Constituents at 24 GHz. *Proc Phys Soc*, B-64:862–875.

Fiedler, M., nad T. Gomer, H. F., M.Hausmann, Pfeilsticker, K., and Platt, U. (1993). Groundbased spectroscopic measurements of stratospheric NO2 and OClO in the arctic winter 1989/90. *Geophys. Res. Lett.*, 20(10):963–966.

Florek, S. and Becker-Roß, H. (1995). High resolution spectrometer for atomic spectrometry. *J. Anal. At. Spectrom.*, 10:145 ff.

Flores, A., Ruffini, G., and Rius, A. (2000). 4D tropospheric tomography using GPS slant wet delays. *Annales Geophysicae*, 18(2):223–234.

Foster, N. and Foskett, L. (1945). A spectrometer for the determination of the water vapor in a vertical column of the atmosphere. *J. Opt. Soc. Am.*, 35:149–162.

Fowle, F. (1912a). The spectroscopic determination of aqueous vapor. *Astrophys. J.*, 35:149–162.

Fowle, F. (1912b). The transparency of aqueous vapor. *Astrophys. J.*, 42:394–411.

Gamache (2000). Total internal partition sums for molecules in the terrestrial atmosphere. *Journal of Molecular Structure*, 517-518:407–425.

Geiger, A. (1987). Einfluss richtungsabhängiger Fehler bei Satellitenmessungen. Technical Report 130, Institute of Geodesy and Photogrammetry, ETHZ, Zürich.

Gersitz, S. (1998). *Investigation Of the elastic Properties of Crystals by Near Infrared Brillouin Scattering.* PhD thesis, PSI / ETH Zürich.

Giver, L., C. Chackerian, J., and Varanasi, P. (1999). Long-Path near-Infrared Line Intensities for H2O. *Proceedings of the 5th ASA Conference, Reims, France*, page 141.

Glaus, R., Bürki, B., and Kahle, H.-G. (1994). Recent results of WVR radiometry in assessing vertical lithospheric movement by using spaec geodetic radio wave techniques. *Journal of Geodynamics*, 20:31–39.

Goody, R. (1964). *Atmospheric radiation I: Theoretical basis.* Clanderon Press, Oxford.

Gutman, S., Feng, P., Bock, Y., Bevis, M., Businger, S., and Holub, K. (2000). Operational ground-based gps water vapor observing system strategies. *Proceedings of the Fourth Symposium on Integrated Observing Systems*, pages 58–61.

Haase, J., Calais, E., Talaya, J., Rius, A., Vespe, F., Santangelo, R., Huang, X.-Y., Davila, J., Ge, M., Flores, A., Vedel, H., Mogensen, K., and Yang, X. (April 1999). The MAGIC Project: GPS Meteorology in the Mediterranean and Requirements for Data Consistency and Quality. *EGS Meeting, The Hague.*

Heitmann, U., M.Schütz, Becker-Roß, H., and Florek, S. (1996). Measurements on the Zeeman-splitting of analytical lines by means of a continuum source graphite furnace atomic absorption spectrometer with a linear charge coupled device array. *Spectrochim Acta*, B 51:1095 ff.

Herring, T. (1992). Modelling Atmospheric Delays in the Analysis of Space Geodetic Data. In *Refraction of Transatmospheric Signals in Geodesy, Proceedings of the Symposium*, volume Publ. Geod. 36, pages 157–164.

Herzberg, G. (1945). *Molecular spectra and molecular structure. Infrared and Raman spectra of polyatomic molecules.* D. van Nostrand Comp., Princeton, N.J.

Higgins, M. (2000). 3D-variational analysis with ground based GPS estimates of Total Zenith Delay. *Proceedings og the XXV. EGS General Assembly*, (in print).

Humlicek, J. (1982). Optimized computation of the Voigt and complex probability function. *JQSRT*, 57:819–824.

Ingold, T., Schmid, B., Mätzler, C., Demoulin, P., and Kämpfer, N. (2000). Modeled and Empirical Approaches for Retrieving Columnar Water Vapor from Solar Transmittance Measurements in the 0.72, 0.82 and 0.94 μm Absorption Bands. *J. Geophys. Res.*, in press.

Jarlemark, P. (1997). *Analysis of Temporal and Spatial Variations in Atmospheric Water Vapor Using Microwave Radiometry.* PhD thesis, School of Electrical and Computer Engineering Chalmers University of Technology. Technical Report 308.

Johansson, J., Elgered, G., and Davis, J. L. (1993). Wet Path Delay Algorithms for Use with Microwave Radiometer Data. *Contributions of Space Geodesy to Geodynamics Technology*, 25:81–98.

Kahle, H.-G., Cocard, M., Peter, Y., Geiger, A., Reilinger, R., McClusky, S., King, R. W., Barka, A., and Veis, G. (1999). GPS derived strain field in the Eastern Mediterranenan and Near East. *JGR*. submitted.

Kouba, J. and Mireault, Y. (1998). Analysis coordinator report. *IGS 1997 Technical Reports*, pages 23–69.

Kruse, L. (2000). *Spatial and Temporal Distribution of Atmospheric Water Vapor using Space Geodetic Techniques.* PhD thesis, ETH Zurich, Geodesy and Geodynamics Laboratory.

Kruse, L., Sierk, B., Springer, T., and Cocard, M. (1999). Gps-meteorology: Impact of predicted orbits on precipitable water estimates. *Geophys. Res. Lett.*, 26:2045–2048.

Mandin, J.-Y., Chevillard, J., and andand C. Camy-Peyret, J.-M. F. (1988). H216O: Line positions and intensities between 8000 and 9500 cm-1: the second hexad of interacting vibrational states:(050),(130),(031),(210),(111),(012). *Can.J.Phys.*, 66:997.

Mandin, J.-Y., Chevillard, J.-P., Camy-Peyret, C., Flaud, J.-M., and Brault, J. (1986). The High-Resolution Spectrum of Water Vapor between 13200 and 16500 cm-1. *J.Mol.Spectrosc.*, 116:167–190.

Maurellis, A., Lang, R., van der Zande, W., Aben, I., and Ubachs, W. (2000). Precipitable water column retrieval from GOME data. *submitted to Geophysical Research letters.*

McClusky, S., Balassanian, S., Barka, A., Demir, C., Georgiev, I., Hamburger, M., Hurst, K., Kahle, H.-G., Kastens, K., Kekelidze, G., King, R. W., Kotzev, V., Lenk, O., Mahmoud, S., Mishin, A., Nadariya, M., Ouzoun is, A., Paradissis, D., Peter, Y., Prilepin, M., Reilinger, R., Sanli, I., Seeger, H., Tealeb, A., Tokzoz, M., and Veis, G. (2000). GPS constraints on crustal movements and deformations in the Eastern Mediterranean (1988-1997): Implications for plate dynamics. *JGR*. In press.

Noel, S., Buchwitz, M., Bovesmann, H., Hoogen, R., and Burrows, J. (1999). Atmospheric water vapor amounts retrieved from GOME satellite data. *Geophysical Research letters*, 26(13):1841–1844.

Peckham, G. (1974). Information content and optimisation of high spectral resolution remote sensing measurements by satellite IR radiometry and optimum radiometer configurations. *Quart. J. R. Meteorol. Soc.*, 100:ff. 406.

Peter, R. and Kämpfer, N. (1992). Determination of water vapor and liquid water and its validation with other techniques. *JGR*, 97(D16):19'173 – 19'183.

Pfeilsticker, K., Erle, F., Funk, O., Marquard, L., Wagner, T., and Platt, U. (1998). Optical path modifications due to tropospheric clouds: Implications for zenith sky measurements of stratospheric gases. *J. Geophys. Res.*, 103:25323 – 25335.

P.Giver, L., Jr., C. C., and Varanasi, P. (2000). Visible and near-infrared H_2O line intensity corrections for HIRTAN96. *J. Quant. Spec. Rad. Trans.*, 66:101–105.

Platt, U. (1994). *Differential Optical Absorption Spectroscopy (DOAS), in Air Monitoring by Spectroscopic Techniques.* John Wiley & Sons, Inc., 605 Third Avenue, New York.

Quenzel, H. (1965). Ein Interferentfilter-Aktinograph zur optischen Bestimmung des atmosphärischen Gesamtwasserdampfgehaltes. *Beiträge zur Physik der Atmosphäre*, 39:2–4.

Reagan, J., Thome, K., Herman, B., and Gall, R. (1987). Water vapor measurements in the 0.94 micron absorption band: Calibration, measurements, and data applications. *IEEE Proceedings of the International Geoscience and Remote Sensing Symposium, Ann Arbor*, pages 63–67.

Richner, H. and Viatte, P. (1995). The hydrostatic equation in the evaluation algorithm for radiosonde data. *Journal of Atmospheric and Ocean Tec.*, 12:649 – 656.

R.McIlven (1989). *Basic Meteorology, a physical outline.* Van Nostrand Reinhold, ISBN 0 442 31769 7, UK.

Robinson, S. (1986). A new algorithm for microwave delay estimation from water vapor radiometer data. *TDA Progess report*, pages 42–87.

Rocken, C., Hove, R., Johnson, J., Solheim, F., Ware, R., Bevis, M., Businger, S., and Chiswell, S. (1995). GPS Storm –GPS Sensing of Atmospheric Water Vapor for Meteorology. *Journal of Oceanic and Atmospheric Technology*, 12:468–478.

Rocken, C., Hove, R., and Ware, R. (1997). Near real-time gps sensing of atmospheric water vapor. *Geophys. Res. Lett.*, 24:3221–3324.

Rodgers, C. (1996). Information content and optimisation of high spectral resolution measurements. In *Optical Spectroscopic Techniques and Instrumentation for Atmospheric and Space Research II*. SPIE.

Rodgers, C. (2000). *Inverse methods for atmospheric sounding: Theory and practice.* unpublished, see http://www.atm.ox.ac.uk/user/rodgers/.

Rothacher, M. and Mervart, L. (1996). *The Bernese GPS software version 4.0 user manual.* report, Astron. Inst., Univ. of Bern, Bern Switzerland.

Rothman, L., Rinsland, C., Goldman, A., Massie, S., Edwards, D., Flaud, J.-M., Perrin, A., Donna, V., Mandin, J.-Y., Schroeder, J., McCann, A., Gamache, R., Wattson, R., Yoshino, K., Chance, K., Jucks, K., Brown, L., Nemtchinov, V., and Varanasi, P. (1998). The HITRAN molecular database and HAWKS (HITRAN Atmospheric Workstation. *J. Quant. Spectrosc. Radiat. Transf.*, 60:665–710.

Ruffini, G., Kruse, L. P., Rius, A., Bürki, B., and Cucurull, L. (1999). Estimation of Tropospheric Zenith Delay and Gradients over the Madrid Area Using GPS and WVR data. *Geophysics. Res. Lett.*, 26(4):447–450.

Saastamoinen, J. (1973). Contributions to the Theory of Atmospheric Refraction / Introduction to Practical Computation of Astronomical Refraction. Bulletin géod ésique Nrs 105, 106, 107, pp.50.

Savigny, C., Davis, A., Funk, O., , and Pfeilsticker, K. (2000). Multi-fractal Characteristics of zenith-scattered Skylight transmitted through optically thick Clouds to the Ground. *J. Geophys. Res.*, submitted.

Schaer, S. (1999). *Mapping and Predicting the Earth's Ionosphere Using the Global Positioning System.* PhD thesis, University of Berne, Astronomical Institute University of Berne.

Schmid, B., Thome, K., Demoulin, P., Peter, R., Mätzler, C., and Sekler, J. (1996). Comparison of modeled and empirical approaches for retrieving columnar water vapor from solar trnasmittance measurements in the 0.94-μm region. *J. Geophys. Res.*, 101(D5):9345–9358.

Schmid, B. and Wehrli, C. (1995). Comparison of sun photometer calibration by use of the Langley technique and a standard lamp. *Applied Optics*, 34:4500–4512.

Schwenke, D. (1998). New H2O Rovibrational Line Assignments. *J.Mol.Spectrosc.*, 190:228–397.

Seeber, G. (1993). Satellite Geodesy: Foundations, Methods and Applications. de Gruyter, ISBN 3-11-012753-9.

Shannon, C. and Weaver, W. (1949). *Mathematical Theory of Communication.* University of Illinois Press, 1949.

Sierk, B., Bürki, B., Becker-Ross, H., Florek, S., Neubert, R., Kruse, L., and Kahle, H.-G. (1997). Tropospheric water vapor derived from solar spectrometer, radiometer, and GPS measurements. Journal of Geophysical Research, Vol. 102, No. B10, p. 22411 - 22424.

Sigrist, M. (1994). *Air Monitoring by Spectroscopic Techniques.* John Wiley & Sons, Inc., 605 Third Avenue, New York.

Solheim, F., Godwin, J., and Ware, R. (1998). Passive ground-based remote sensing of atmospheric temperature, water vapor, and cloud liquid water profiles by a frequency synthesized microwave radiometer. *Meteorologische Zeitschrift*, (7):370–376.

Teunissen, P. and Kleusberg, A. (1998). GPS for Geodesy. Springer, ISBN 3-540-63661-7.

Thayer, G. (1974). An improved equation for the radio refractive index of air. *Radio Sci.*, 9:803–807.

Thome, K., Herman, B., and Reagan, J. (1992). Determination of precipitable water from solar transmission. *J. Appl. Meteorol.*, 31:157–165.

Thorne, A. (1974). *Spectrophysics.* John Wiley & Sons, Inc., New York.

Tomasi, C. and Guzzi, R. (1974). High precision atmospheric hygrometer using the solar infraerd spectrum. *J. Phys. E. Sci. Instrum.*, 7:647–649.

Twomey, S. (1977). *Introduction to the Mathematics of Inversion in Remote Sensing and Indirect Measurements.* Elsevier Scientific Publ. Co., Amsterdam.

Vleck, J. V. and Huber, D. (1974). Absorption, emission and linebreadths: A semihistorical perspective. *Reviews of Modern Physics*, 49(4):939 – 959.

Volz, F. (1974). Economical multispectralSun photometer for measurements of aerosol extinction from 0.44 μm to 1.6 μm and precipitable water. *Appl. Opt.*, 13:1732–1733.

Ware, R., Fulker, D., Stein, S., Anderson, D., Avery, S., Clark, R., Droegemeier, K., Juettner, J., and Sorooshian, J. M. S. (2000). SuomiNet: A Real-Time National GPS Network for Atmospheric Research and Education. *Bulletin of the American Meteorological Society*, in press.

Westwater, E. and Strand, O. (1968). Statistical information content of radiation measurements used in indirect sensing. *J. Atmos. Sci.*, 25:750–758.

Wu, S. (1979). Optimum Frequencies of a passive Microwave Radiometer for Tropospheric Path-Length Correction. *IEEE Trans. Ant and Prop.*, AP-27,No. 2:233 – 239.

Yamamoto, G., Tanaka, M., and Aoki, T. (1968). Estimation of Rotational Linewidths of Carbon Dioxide Bands. *JQSRT*, 9:371–382.

Zuev, V. E. (1974). *Propagation of visible and infrared radiation in the atmosphere.* John Wiley & Sons, New York.

9 Appendix

9.1 SAMOS data acquisition software

The data acquisition software for the Solar Atmospheric Monitoring spectrometer has been written in Labview 5.1. In the following the general structure of the measurement program, the measurement cycle, the input files and some screen shots will be presented.

The measurement wavelengths to be adjusted by the computer are specified in the input file, whose format is shown in table. 9.1. In the first column the centers of the measurement windows are assigned. The second column determines the position of the corresponding interference filter on the wheel attached to the tracking telescope. In the third column the user specifies the filename of the solar spectra within the directory tree generated by the program. With the figures in column number four the exposure times for measuring the flat field spectra are adjusted. Column number five designates the neon entrance slit which is used for the absolute wavelength calibration (left or right from the central slit, see section 6.2.1). In the last column the theoretical center position of the neon line as calculated using Eq. 6.8 is given. This number could be used to correct the angle of the Echelle grating, in order to avoid the wavelength drift of the measured spectra. Furthermore the exposure times for the neon and dark current spectra as well as the maximum exposure time for solar spectra can be specified. If the minimum intensity for the solar spectra is not reached while using the maximum exposure time, the measured spectrum is not saved and the acquisition is repeated, until the intensity is sufficient.

In Fig. 10.2 a screen shot of the main window of the data acquisition program is displayed. Several parameters can be interactively adjusted during operation, e.g. the minimum and the maximum peak intensity of a measured solar spectrum. The exposure time is automatically adjusted to keep the measured intensity within these limits. The station coordinates are given to calculate the solar elevation and azimuth. These values can be automatically corrected by scanning the telescope in both directions and finding the telescope position with maximum solar intensity.

The last measured spectrum is continuously plotted in an additional window. Fig. 10.3 and 10.4 show raw spectra for a flatfield and a neon emission line measurement.

Wavelength nm	Filter number	File name	Flatfield exposure	Neon lamp	Center pixel
H_2O-lines					
601.300	10	6013	30	left	244
839.400	3	8394	30	right	233
825.450	8	8254	30	right	496
659.370	5	6593	30	left	821
836.700	3	8367	30	right	766
836.200	3	8362	30	right	539
892.720	7	8927	30	right	777
834.190	3	8341	30	right	479
819.850	6	8198	30	right	581
738.980	2	7389	30	right	632
845.980	4	8459	30	left	490
O_2-lines					
765.000	1	7560	30	right	819
765.500	1	7655	30	right	297
766.000	1	7660	30	left	319
766.500	1	7665	30	right	102

Table 9.1: Format of the input file for the SAMOS data acquisition software.

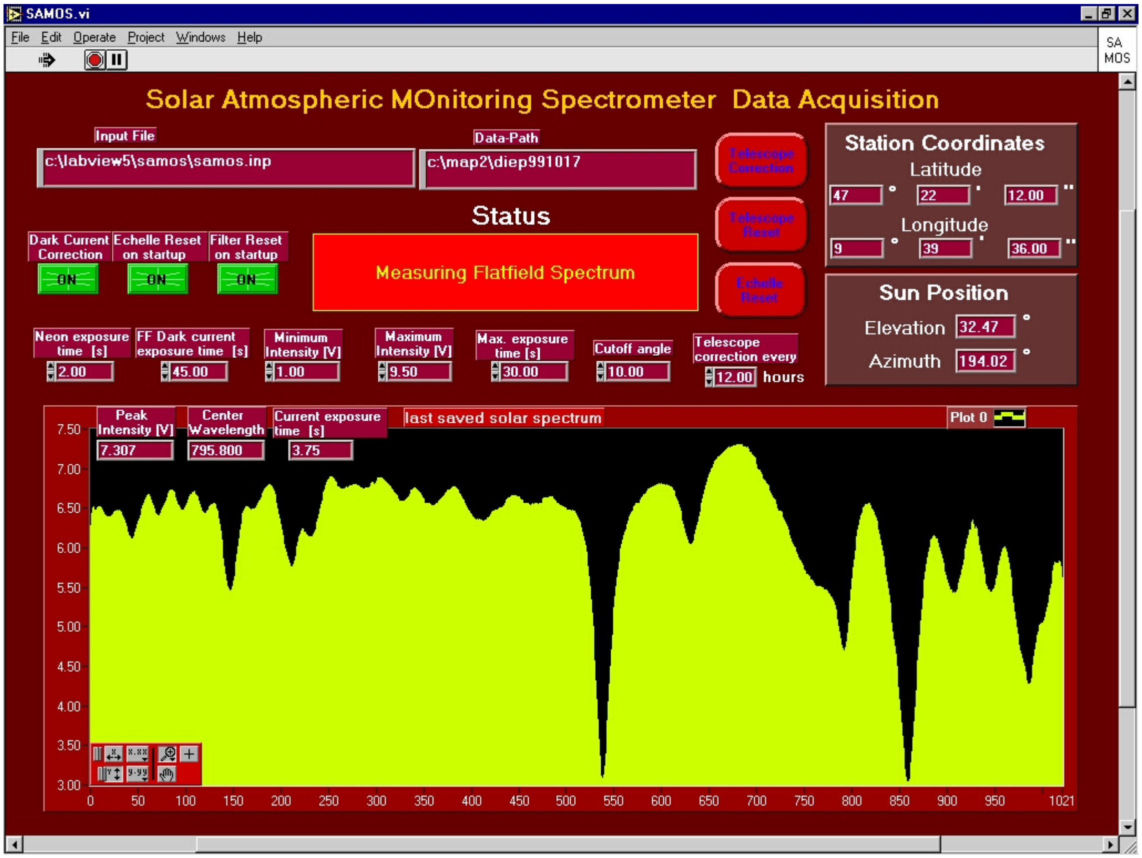

Solar Atmospheric MOnitoring Spectrometer Data Acquisition

Input File: c:\labview5\samos\samos.inp

Data-Path: c:\map2\diep991017

Status: Measuring Flatfield Spectrum

Dark Current Correction: ON

Echelle Reset on startup: ON

Filter Reset on startup: ON

Station Coordinates

Latitude: 47 ° 22 ' 12.00 "

Longitude: 9 ° 39 ' 36.00 "

Sun Position

Elevation: 32.47 °

Azimuth: 194.02 °

Neon exposure time [s]: 2.00

FF Dark current exposure time [s]: 45.00

Minimum Intensity [V]: 1.00

Maximum Intensity [V]: 9.50

Max. exposure time [s]: 30.00

Cutoff angle: 10.00

Telescope correction every 12.00 hours

Peak Intensity [V]: 7.307

Center Wavelength: 795.800

Current exposure time [s]: 3.75

last saved solar spectrum

Figure 9.1: Screen shot of the data acquisition software. The main window displays all parameters of measurement process (acquisition times, actual wavelength, Sun position, etc.) The last detector scan (raw spectrum) is plotted for visual control of the data.

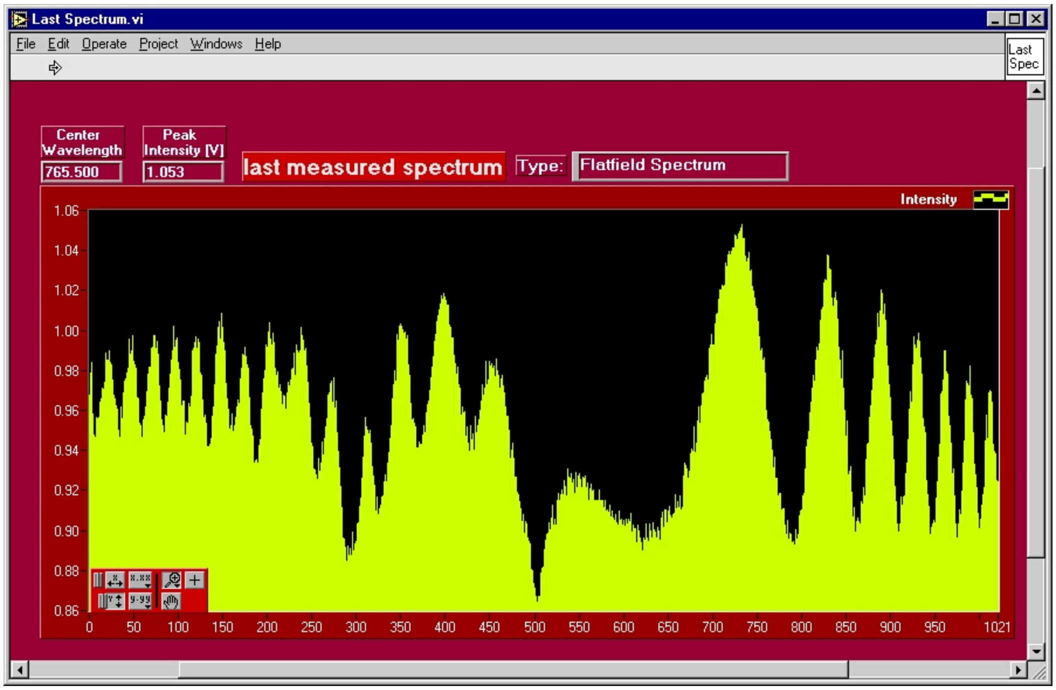

Center Wavelength: 765.500

Peak Intensity [V]: 1.053

last measured spectrum

Type: Flatfield Spectrum

Figure 9.2: Halogen lamp spectrum measured using the flatfield box. Instead of a flat intensity distribution periodic structures are visible, as a result of instrumental effects. Their origin is explained in 6.2.2

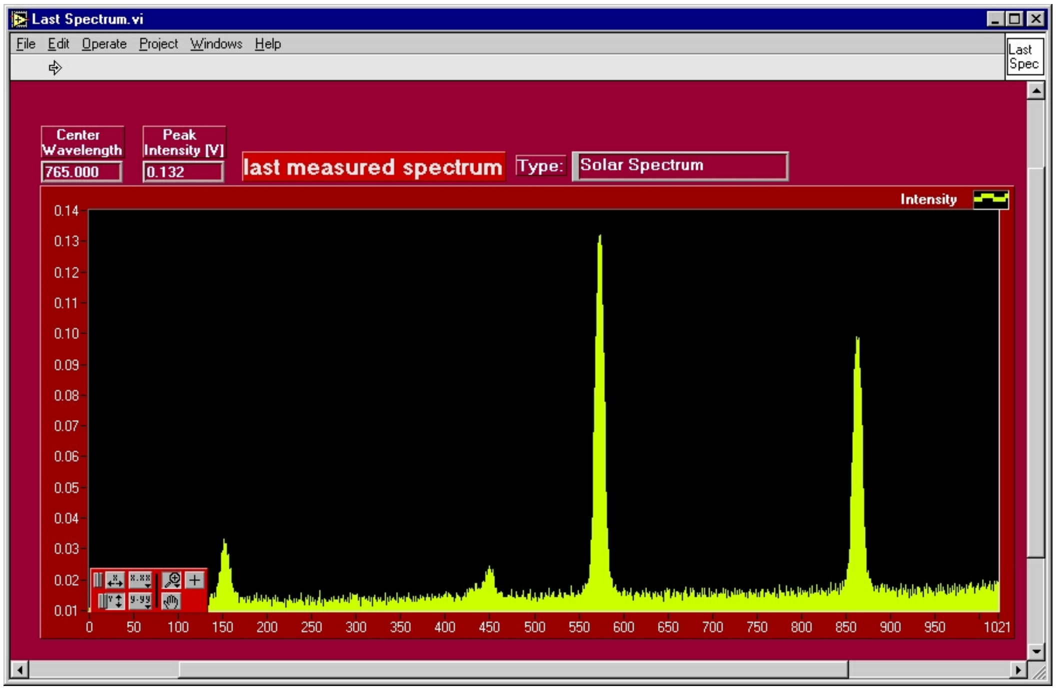

Center Wavelength: 765.000

Peak Intensity [V]: 0.132

last measured spectrum

Type: Solar Spectrum

Figure 9.3: Emission spectrum of neon lamps inside the spectrometer. Since the line positions of these transitions are well known, they can be used to define the wavelength scale (see 6.2.1)

9.2 Overview of the SAMOS system

In the following a schematic overview of the SAMOS system is presented. The communication between the control computer and the telescope/spectrometer system is performed using two interfaces: The RS232 serial port and a multi-functional PCMCIA card (LabView DAQCard-AI-16XE-50) which serves as an AC/DC converter and a digital control unit. The schematic structure of the sensor system is illustrated in Fig. 9.4. Four servo motors move the two telescope axes, the filter wheel and the Echelle grating. They are controlled by digital motor controllers (Motion Control System MCS751C, Gysling Engineering Office, Zurich, Switzerland) which are connected to the RS232 port. The turnable flatfield box (see 5.3.1) is moved by a servo controller. The remaining system components, the photodiode detector head (Hamamatsu C5964), the neon lamps and the entrance slit shutter are controlled by the PCMCIA card. For operating the detector a continuous pulse train of 375 kHz is generated which serves as a clock signal. After sending a start signal the detector returns a video signal (62.5 kHz), which is digitalized at the analog inputs of the PCMCIA card. The timing of the digitalization process is determined by a trigger signal sent by the detector head. The neon lamps and the shutter are switched by the digital lines of the PCMCIA card.

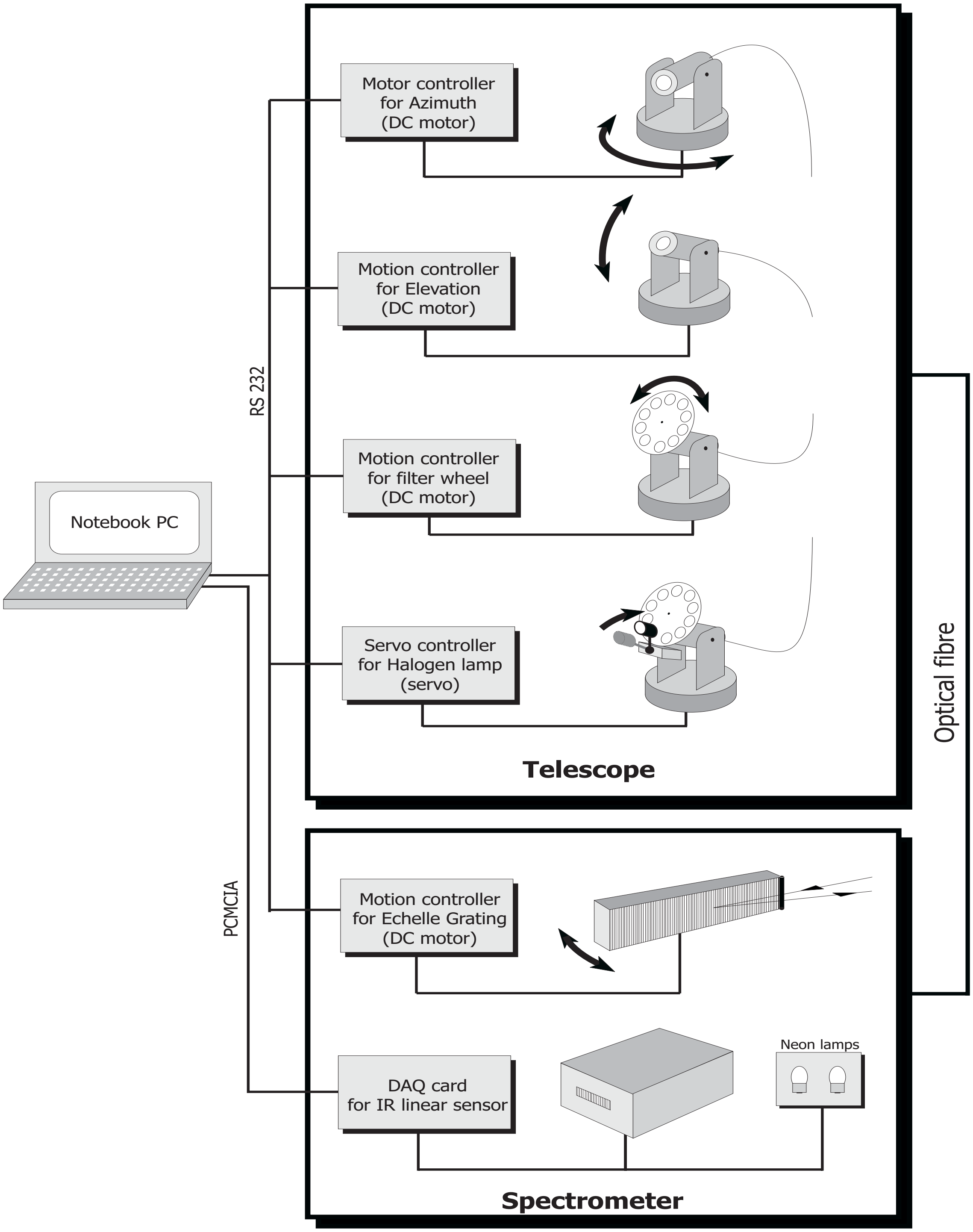

Figure 9.4: Schematic sketch of the SAMOS sensor components. The telescope as well as the Echelle grating are moved by DC motors and a motion controller connected to the RS232 serial port of a notebook PC. The detector head and the neon lamps are controlled by a multi-functional PCMCIA card for data acquisition (DAQ card).

“Geodätisch-geophysikalische Arbeiten in der Schweiz”

(Fortsetzung der Publikationsreihe ”Astronomisch-geodätische Arbeiten in der Schweiz”) der Schweizerischen Geodätischen Kommission (ab Bd. 40):

40 1989 Integrale Schwerefeldbestimmung in der Ivrea- Zone und deren geophysikalische Interpretation. B. Bürki. 186 Seiten.

41 1990 ALGESTAR satellitengestützte Geoidbestimmung in der Schweiz. U. Marti. 61 Seiten plus Punktprotokolle.

42 1990 Höhensysteme, Schwerepotentiale und Niveauflächen: Systematische Untersuchungen zur zukünftigen terrestrischen und GPS-gestützten Höhenbestimmung in der Schweiz. B. Wirth. 204 Seiten.

43 1990 Gravimetrisches Geoid der Schweiz: Potentialtheoretische Untersuchungen zum Schwerefeld im Alpenraum. A. Geiger. 231 Seiten.

44 1991 Rapid Differential Positioning with the Global Positioning System (GPS). E. Frei. 178 Seiten.

45 1992 Dreidimensionales Testnetz Turtmann 1985-1990 Teil I. F. Jeanrichard (Hrsg.)
Autoren: A.Geiger, H.-G. Kahle, R. Köchle, D. Meier, B. Neininger, D. Schneider, B. Wirth. 183 Seiten.

46 1993 Orbits of Satellite Systems in Space Geodesy. M. Rothacher. 243 Seiten.

47 1993 NFP 20. Beitrag der Geodäsie zur geologischen Tiefenstruktur und Alpendynamik. H.-G. Kahle (Hrsg.) Autoren: I. Bauersima, G. Beutler, B. Bürki, M. Cocard, A. Geiger, E. Gubler, W. Gurtner, H.-G. Kahle, U. Marti, B. Mattli, M. Rothacher, Th. Schildknecht, D. Schneider, A. Wiget, B. Wirth. 153 Seiten plus 90 Seiten Anhang.

48 1994 Ionosphere and Geodetic Satellite Systems: Permanent GPS Tracking Data for Modelling and Monitoring: Urs Wild, 155 Seiten.

49 1994 Optical Astrometry of Fast Moving Objects using CCD Detectors: Thomas Schildknecht, 200 Seiten.

50 1995 Geodätische Alpentraverse Gotthard: A. Elmiger, R. Köchle, A. Ryf und F. Chaperon. 214 Seiten.

51 1995 Dreidimensionales Testnetz Turtmann 1985-1993, Teil II (GPS-Netz).
F. Jeanrichard (Hrsg.) Autoren: G. Beutler, A. Geiger, M. Rothacher, Stefan Schaer, D. Schneider, A. Wiget, 173 Seiten.

52 1995 High Precision GPS Processing in Kinematic Mode: M. Cocard. 139 Seiten.

53 1995 Ambiguity Resolution Techniques in Geodetic and Geodynamic Applications of the Global Positioning System. L. Mervart. 155 Seiten.

54 1997 SG 95: Das neue Schweregrundnetz der Schweiz: F. Arnet und E. Klingelé. 37 Seiten.

55 1997 Combination of Solutions for Geodetic and Geodynamic Applications of the Global Positioning System (GPS). Elmar Brockmann, 211 Seiten.

56 1997 Geoid der Schweiz 1997. Urs Marti, 140 Seiten.

57 1998 Astrometry and Satellite Orbits: Theoretical Considerations and Typical Applications. Urs Hugentobler, 209 Seiten.

58 1998 Systematic Investigations of Error- and System-Modelling of Satellite Based Flight Approaches and Landings in Switzerland. Maurizio Scaramuzza, 165 Seiten.

59 1999 Mapping and Predicting the Earth’s Ionosphere Using the Global Positioning System. Stefan Schaer, 205 Seiten.

60 2000 Modeling and Validating Orbits and Clocks Using the Global Positioning System.
Timon Anton Springer, 154 Seiten.

61 2001 Spatial and Temporal Distribution of Atmospheric Water Vapor using Space Geodetic Techniques. Lars Peter Kruse, 128 Seiten.

62 2001 Solar Spectrometry for Determination of Tropospheric Water Vapor. Bernd Sierk, 212 Seiten.